

THE IMPULSIVE HARD X-RAYS FROM SOLAR FLARES

by

John Leach

National Aeronautics and Space Administration
Grant NSG-7092

CSSA-ASTRO-84-06

February 1984

Center for Space Science and Astrophysics
Stanford University
Stanford, California

THE IMPULSIVE HARD X-RAYS FROM SOLAR FLARES

by

John Leach

National Aeronautics and Space Administration
Grant NSG-7092

CSSA-ASTRO-84-06

February 1984

Center for Space Science and Astrophysics
Stanford University
Stanford, California

Page intentionally left blank

Page intentionally left blank

Abstract

Solar flares have been observed intensively for more than two decades at X-ray energies in excess of 10 kilovolts. We develop a technique for determining the physical arrangement of a solar flare during the impulsive phase, based upon a non-thermal model interpretation of the emitted hard X-rays. Our technique allows us to obtain accurate values for the flare parameters, including those which describe the magnetic field structure and the beaming of the energetic electrons, parameters which have hitherto been mostly inaccessible.

Our technique follows the evolution of streaming energetic electrons within the flare structure. The evolution of the electron number distribution, which is primarily controlled by Coulomb collisions, is evaluated using a steady-state Fokker-Planck Equation. From the evaluated electron distribution we calculate the emitted bremsstrahlung X-rays. The power of our technique lies in our ability to correlate the characteristics of these hard X-rays with the values of the model parameters describing the flare.

We find that the X-ray intensity height structure can be described readily with a simple expression based upon a semi-empirical fit to the results from many models. We also find that the degree of linear polarization of the X-rays from a flaring loop does not exceed 25 percent and can easily and naturally be as low as the polarization expected from a thermal model. This is a highly significant result in that it supersedes those based upon less thorough calculations of the electron beam dynamics and requires that we reevaluate our hopes of using polarization measurements to discriminate between categories of flare models.

We also confirm that one cannot determine satisfactorily flare model parameters solely on the basis of spatially unresolved observations. We show how the full power of our modeling technique enables us to use the recent high resolution X-ray observations to obtain values for the model parameters appropriate to each flare, in particular for those parameters which describe the injected electron beam and which are essential to furthering our understanding of the electron acceleration mechanisms.

Acknowledgements

It is with pleasure that I acknowledge the assistance, support and encouragement of my colleagues and friends. I would like to thank Dr. Vahé Petrosian for his guidance during my graduate studies and during the preparation of this manuscript; without the motivation he provided this report would not have been as complete a document as it is. For the many discussions and for their opinions I would like to thank Drs. Gordon Emslie, Spiro Antiochos and Steven Langer, and for his example Dr. Joshua Knight. But most of all I owe my greatest thanks to my wife Margaret for her patience and strength in those long final days of my stay at Stanford.

I thank Drs. Walt, MacDonald and Francis at Lockheed Missile and Space Company in Palo Alto for providing the computer code with which this work began. This work was supported by the National Aeronautics and Space Administration under grant NSG-7092.

Table of Contents

Signatures	ii
Abstract	iii
Acknowledgements	v
Chapter	page
I. Introduction	1
Flare structure	3
Thermal and non-thermal models	8
Flare emissions	14
Impulsive hard X-rays	16
The study conducted	21
II. The Fokker–Planck Equation	24
The general non-thermal model	24
Mathematical development	36
III. Solving the Equation both Analytically and Numerically	60
The reduced and approximate equations	61
The numerical treatment	71
Some results on the evolution of the electron beam	83
IV. X-ray Bremsstrahlung Theory	100

	Stokes Parameter formalism	101
	X-ray bremsstrahlung cross-sections	107
V.	The X-ray Results	115
	Literature survey	116
	X-ray characteristics from non-thermal models	129
	<i>Model 1</i>	144
	<i>Models 2 and 3</i>	174
	<i>Models 4 and 5</i>	187
	<i>Model 6</i>	197
	<i>Models 7 through 11</i>	200
VI.	Studies of X-ray Observations	211
	X-ray height structures	212
	The flare of April 10, 1980	218
	Stereoscopic observations of the flare of October 5, 1978	230
	The three similar flares of November 5, 1979	237
	Some recent polarization results	244
	Summary	249
VII.	Summary and Conclusions	251
	Summary	251
	Conclusions	259
	References	272

List of Tables

Table		page
I.	Some typical values for the collision logarithms	58
II.	The values of the model parameters	145
III.	The X-ray spectral indices for each model	163
IV.	The X-ray anisotropy for <i>Model 1</i>	168
V.	The maximum x-ray polarization for <i>Model 1</i>	172
VI.	The anisotropy of the whole loop (spatially integrated) X-rays for all models	183
VII.	The maximum degree of X-ray polarization for all models	188
VIII.	The coronal emission for <i>Model 4</i> , <i>Model 7</i> , <i>Model 8</i> and <i>Model 9</i> .	204
IX.	The flare of April 10, 1980	222
X.	The maximum degree of polarization at 16 keV	268

List of Figures

Figure	page
1.1	The structure of the solar atmosphere 4
1.2	A sketch of a flaring loop 6
2.1	The Coulomb collision process in the rest frame of the test particle 52
2.2	The Coulomb collision process in the rest frame of the field particles 54
3.1	The rate at which electrons lose energy 65
3.2	The domain of the solutions to the Fokker–Planck Equation . . . 76
3.3	Testing the code with the collision terms switched off 80
3.4	Testing the code with only the diffusion term switched on 82
3.5	The pitch angle evolution with depth for a narrow injected beam ($\alpha_0^2 = 0.04$) 86
3.6	As Figure (3.5) but for $\alpha_0^2 = 0.4$ 88
3.7	As Figure (3.5) but for $\alpha_0^2 = \infty$ 89
3.8	The evolution of the energy spectrum with depth 91
3.9	The pitch angle evolution for a model with a narrow injected beam and a converging magnetic field 93
3.10	The variation of the downward electron current with rates of convergence of the magnetic field 97
3.11	The variation of the downward electric current with α_0^2 for one magnetic bottle strength 98

5.1	The orientation of the flare loop within the global observation frame	130
5.2	The division of the loop into segments	134
5.3	$I(k, \tau)$ vs. τ for <i>Model 1</i>	146
5.4	The ratio between $I(k, \tau)$ from the numerical results for <i>Model 1</i> and from equation (5.2.12)	149
5.5a	The X-ray spectrum for a flare visible down to a depth τ_0 . . .	154
5.5b	Similar to Figure (5.5a) but with the whole loop spectrum folded out	155
5.6	$I(k, h)$ vs. h for <i>Model 1</i>	156
5.7	The X-ray spectrum in three orthogonal directions for <i>Model 1</i> .	160
5.8	The variation of the X-ray spectrum with depth for <i>Model 1</i> . .	161
5.9	The X-ray directivity for <i>Model 1</i>	166
5.10	The X-ray polarization for <i>Model 1</i>	171
5.11a,b	$I(k, \tau)$ vs. τ for <i>Model 1</i> and <i>Model 2</i>	179
5.11c	$I(k, \tau)$ vs. τ for <i>Model 3</i>	176
5.12a,b	As Figure (5.4) but for <i>Model 1</i> and <i>Model 2</i>	179
5.12c	As Figure (5.4) but for <i>Model 3</i>	180
5.13a,b	The X-ray directivity for <i>Model 1</i> and <i>Model 2</i>	181
5.13c	The X-ray directivity for <i>Model 3</i>	182
5.14a,b	The X-ray polarization for <i>Model 1</i> and <i>Model 2</i>	185
5.14c	The X-ray polarization for <i>Model 3</i>	186
5.15	$I(k, \tau)$ for <i>Model 1</i> , <i>Model 4</i> and <i>Model 5</i>	189
5.16,a,b	The X-ray directivity for <i>Model 1</i> and <i>Model 4</i>	192

5.16c	The X-ray directivity for <i>Model 5</i>	193
5.17a,b	The X-ray polarization for <i>Model 1</i> and <i>Model 4</i>	195
5.17c	The X-ray polarization for <i>Model 5</i>	196
5.18	The X-ray polarization for <i>Model 6</i>	198
5.19	$I(k, \tau)$ for <i>Model 4</i> , <i>Model 7</i> , <i>Model 8</i> and <i>Model 9</i>	203
5.20a	The X-ray directivity for <i>Model 5</i>	205
5.20b,c	The X-ray directivity for <i>Model 10</i> and <i>Model 11</i>	206
5.21a	The X-ray polarization for <i>Model 5</i>	207
5.21b	The X-ray polarization for <i>Model 10</i>	208
5.21c	The X-ray polarization for <i>Model 11</i>	209
6.1	The flare of April 10, 1980 as seen by HXIS	220
6.2	A comparison between the Tramiel, Chanan and Novick data and our non-thermal models	248

Chapter I

Introduction

“Solar flares are complex, transient excitations of the solar atmosphere above magnetically active regions of the surface involving enhanced thermal and radio emission, hard X-rays, cosmic rays and plasma ejection. Their origin is not yet understood after more than a century of study since the first recorded observations.” (Sweet 1969).

Solar flares have been studied for an extended period of time and have been under intensive study for at least the last twenty years. Yet they still represent somewhat of an enigma, and this despite the fact that the field has seen some major advances in the years since Sweet’s comments were written in 1969. Many of the fundamental physical processes are far from being understood, including those which initiate and power the flare. For this reason the study of solar flares will remain one of the more active programs in Astrophysics for many years to come.

Sweet described solar flares as being complex, transient and energetic. They are indeed all of these things. They are manifestations of the diverse physics of inhomogeneous plasmas with strong magnetic fields. They typically involve the

Chapter I: Introduction

bulk motion of up to 10^{16} g of plasma (Rust *et al.* 1980) – the equivalent of a small terrestrial mountain. Solar flares are known to accelerate elementary particles to energies of hundreds of *MeV* (Švestka 1975; Brown and Smith 1980; Ramaty *et al.* 1980), to heat huge volumes of plasma to temperatures of tens of millions of degrees Kelvin (Moore *et al.* 1980) and to generate electromagnetic radiation across a sixteen decade wavelength span from kilometric wavelengths to γ ray energies. The total energy budget of a solar flare can, for a typical large flare, exceed 10^{32} *ergs* (Zirin 1966, p455; Brown and Melrose 1977).[†] The flare is activated over timescales of seconds to minutes (Kane *et al.* 1980b), the energy is distributed throughout a structure which is tens of thousands of kilometers in size and is detectable as thermal radiation from a hot plasma for many hours thereafter.

Owing to the wide range of size scales from meters to thousands of kilometers, the wide range of timescales from seconds to many hours, and the huge quantities of energy involved, solar flares provide the scientist with a unique physical laboratory, obviously impossible to reproduce on earth. The sheer complexity and number of processes which are active at any one time plus the inherent inaccessibility of the experimental subject, provide ample justification for why so much data has been collected pertaining to solar flares, why so much uncertainty as to how they work still exists and why so much attention will continue to be directed toward their study.

[†] $\sim 10^{32}$ *ergs* dwarfs the most destructive of manmade devices – an SS18 missile can deliver a warhead with more than 10^{24} *ergs* of explosive power (Donley 1979, p71) – and easily exceeds nature's terrestrial limits. A large volcano might produce 10^{26} *ergs* of energy over many, many hours and a large earthquake might release 10^{29} *ergs* over very much shorter timescales.

Chapter I: Introduction

1.1 Flare structure.

The early ideas about solar flares (*cf.* review by Švestka 1966) were formed from observations taken at optical wavelengths, primarily $H\alpha$ (the transition from $n = 3$ to $n = 2$ in the Hydrogen atom, wavelength 6562 \AA , characteristic of temperatures $\sim 8000 \text{ K}$ (Zirin and Tanaka 1973)). The $H\alpha$ emission can depict events occurring in the chromosphere which is the level of the atmosphere immediately above the visible surface of the sun (*cf.* Figure (1.1)). $H\alpha$ observations show (*cf.* Vorpahl 1973; Canfield *et al.* 1980) diffuse regions of enhanced emission covering an area of several times 10^{19} cm^2 and lasting from minutes to hours. Embedded within these enhancements are small, very bright knots covering, usually, less than 10^{18} cm^2 and having a shorter duration with a lifetime of a few minutes. Alternately, the largest flares, known as two ribbon flares, show the bright knots connected together to form two long ribbons which lie parallel to each other. These ribbons can be 10^5 km or more long and $2 \times 10^4 \text{ km}$ wide each (Moore *et al.* 1980), giving a total area in $H\alpha$ brightening of several times 10^{19} cm^2 . (See also Zirin 1966, pp 390-406; Tanaka and Zirin 1973; Zirin and Tanaka 1973; and see the frontispiece of Sturrock *et al.* 1980 for an $H\alpha$ picture of a large two-ribbon flare).

The earliest observations were all made from ground-based instruments and this restricted the observations to visible and radio ($\sim 10 \text{ m} - 1 \text{ cm}$) wavelengths which could pass easily through the earth's atmosphere. The early observations at other wavelengths were made from high altitude balloons. Then, beginning after World War II, increasing use was made of rockets and, nowadays, these observations are frequently made from satellites or space vehicles such as Skylab

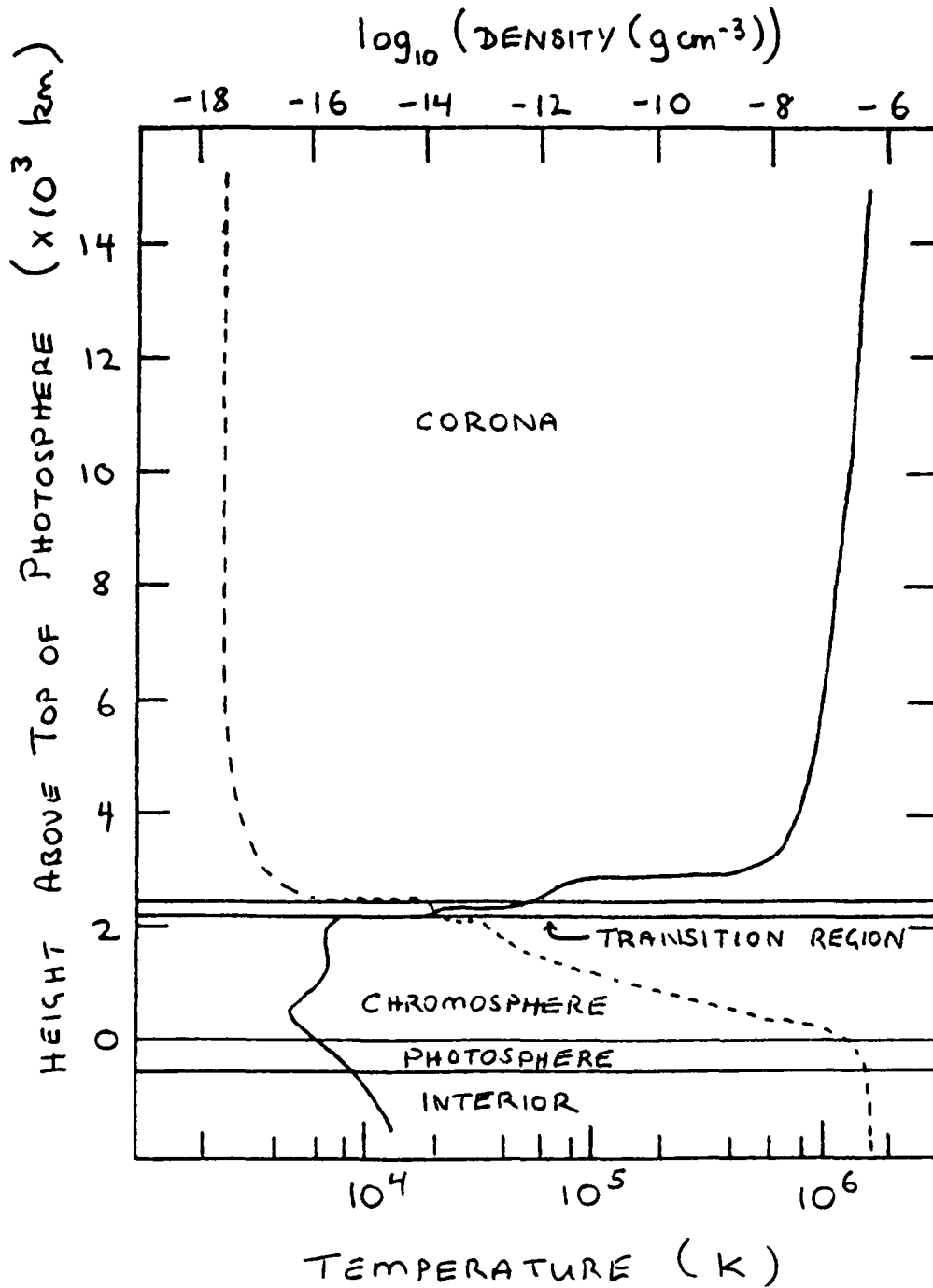


Figure 1.1. The structure of the atmosphere for the quiet (*i.e.*, non-flaring) sun. The photosphere is the visible surface of the sun. One solar radius is equal to 6.95×10^5 km. The solid curve shows the atmosphere's temperature structure and uses the bottom scale; the dotted curve shows the atmosphere's density structure and uses the top scale.

Chapter I: Introduction

or the Space Shuttle. Though widening the observational window, until recently none of the non-ground-based instruments had comparable spatial resolution to the $H\alpha$ instruments. In 1973 Skylab was launched and carried with it several telescopes which could collect radiation across most of the range $3 - 3940 \text{ \AA}$ with an angular resolution $\sim 2''$, which corresponds to a spatial resolution $\sim 1500 \text{ km}$ on the surface of the sun. These telescopes sent back thousands of images showing, for the first time, the geometric structure containing the hot plasma which remains and gradually cools after the shorter lived impulsive bursts have ceased. The observations, particularly the Extreme Ultra Violet (EUV) ($10 - 1030 \text{ \AA}$) and X-ray pictures, showed that flares generally occur in loop like structures which are rooted in the deep levels of the chromosphere and which project up into the solar corona (Widing and Cheng 1974; Cheng and Widing 1975; Vorpahl *et al.* 1975; Spicer 1977. *cf.* Figure (1.2)). The loop structure is a curved tube delineated by the magnetic field and, for the most part, survives throughout the lifetime of a solar flare (Vorpahl *et al.* 1975). Flare loops vary immensely in size but are frequently found to be between 4×10^3 and $20 \times 10^3 \text{ km}$ in length and about half as high as they are long (Cheng and Spicer 1975; Cheng and Widing 1975; Vorpahl *et al.* 1975). The footpoints of the loops are generally coincident with the knots of $H\alpha$ brightening (Spicer 1977). Large flares are often associated with arcades of these loops stacked closely together. In such cases the $H\alpha$ knots from adjacent loops merge to form the two long ribbons.

Early observations at wavelengths other than optical may not have had the spatial resolution of the $H\alpha$ images but they did allow the measurement of flare radiation emitted by many different processes and coming from widely different

Chapter I: Introduction

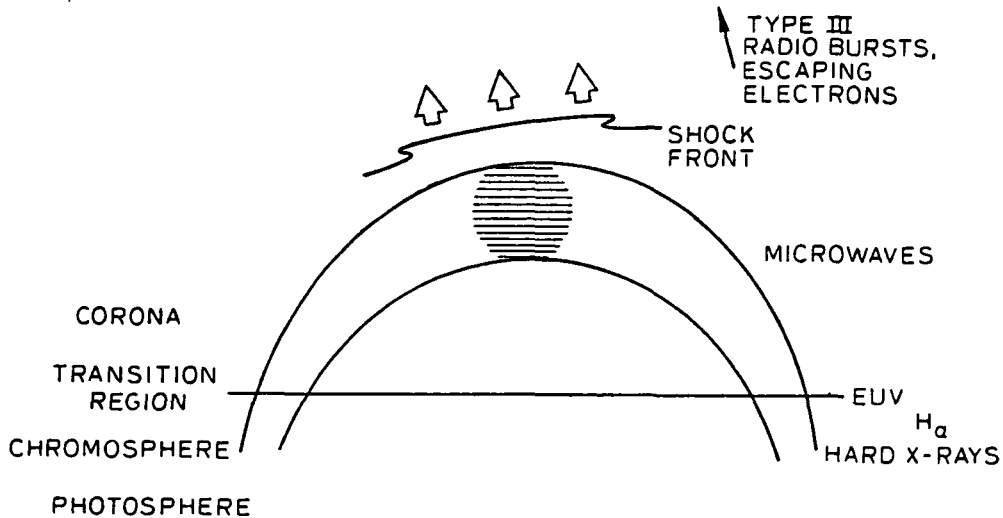


Figure 1.2. A sketch of a flaring loop showing the region of hottest plasma (shaded region) at the top of the loop and the source regions for the various burst emissions. A typical height for a flaring loop is 2×10^4 km.

parts of the flare structure, and they were able to show the synchrony of different emissions to within the relative timing calibration of the independent instruments. As seen in many of these emissions, there are primarily two timescales in the temporal development of a flare (*cf.* Kane 1969, 1974; de Feiter 1975, Haug 1982). One of these corresponds to the gradual phase during which the brightness of the flare increases over many minutes and then decays slowly, often over hours. This has the appearance of the bulk heating and slow cooling of a large volume of plasma. The flaring plasma can reach temperatures of tens of millions of degrees Kelvin, which is hot enough that the spectrum of continuum emission extends into the X-ray region. It was such X-rays from extremely hot plasmas in which the Skylab X-ray images were made.

Chapter I: Introduction

The other timescale in the temporal development of a flare corresponds to the impulsive phase. This is always accompanied by gradual phase emission though the converse does not always hold (Švestka 1975; Haug 1982). The gradual phase can occur with no detectible impulsive phase, though this may be an instrument threshold effect. The impulsive phase occurs during the early stages of the gradual phase. Flares sometimes show what is known as preheating for several minutes before the impulsive phase and this is seen as a slow and steady increase in the thermal emission of the preflare plasma (Kane 1974; Vorpahl *et al.* 1975; Haug 1982). The impulsive stage can last for a few seconds in small flares or for many minutes in large flares and during this time the intensity of the flare emissions varies rapidly and widely. The temporal structure of the impulsive phase is seen most distinctly at hard X-ray energies (> 10 keV X-rays), where the impulsive emission appears as a sequence of short lived bursts. In relatively small flares the impulsive stage can be decomposed into discrete bursts, which have similar structures (van Beek, de Feiter and de Jager 1974, 1976; de Jager and de Jonge 1978). These individual bursts can represent a contrast of up to a factor of three against the remaining hard X-ray profile, and for them the intensity rises and falls with an e-folding time of just three or four seconds (Vorpahl and Takakura 1974, 1975; de Jager and de Jonge 1978). Large flares have too complex a time structure for the decomposition into discrete bursts to be unambiguous (Brown 1975). The combined effect of many overlapping bursts is to give an X-ray intensity which is orders of magnitude above the preflare background (*cf.* Hoyng, Brown and van Beek 1976).

Some of the emissions at other than hard X-ray energies show a similar burst or impulsive stage structure, for example microwave bursts ($\lambda \leq 30$ cm. de Feiter

Chapter I: Introduction

1975; Takakura 1975) and Type III radio (meter) bursts (Smith 1974; Lin 1975; Rosenberg 1976). Yet other emissions are produced by the response of the solar atmosphere to the physical activity in a flare. For these the fine structure of the bursts is smoothed into slower varying but still burst-like brightenings. This is the appearance in both EUV and $H\alpha$.

1.2 Thermal and non-thermal models.

All the emissions associated with the impulsive phase are seen to be well correlated. The impulsive $H\alpha$, EUV, microwave and X-ray emissions show synchrony on timescales of seconds and often show good correlations between the size of their respective fluxes. The $H\alpha$ and hard X-ray bursts are simultaneous to within seconds and have broadly correlated fluxes (Zirin, Pruss and Vorpahl 1971; Zirin 1978). Acton (1968) found that $H\alpha$ flashes occurred only in flares which have a non-thermal (that is, an excess above thermal) X-ray component and Kane (1973) estimated that only about 10% of small $H\alpha$ flares ($H\alpha$ importance ≤ 1 ; cf. Zirin 1966, p391) have a clearly discernable impulsive hard X-ray component. At the other end of the size scale, large flares show white light flashes which are an enhancement of the broad band emission from the deep layers of the chromosphere. White light flashes tend to occur in flares which have a sizeable amount of $H\alpha$ emission (Zirin and Tanaka 1973; Zirin 1978).

Numerous studies have found close correlations between the impulsive hard X-rays and the microwaves, both in time and in flux (Peterson and Winckler 1959;

Chapter I: Introduction

Kundu 1961; Anderson and Winckler 1962; de Jager and Kundu 1963; Kundu 1963; Bowen *et al.* 1964; McKenzie 1972; Vorpahl 1972; Kane 1973; Zirin and Tanaka 1973; de Feiter 1975; Takakura 1975). Similarly between hard X-ray bursts, microwaves and interplanetary particles (Arnoldy, Kane and Winckler 1967; Acton 1968; Kane 1972b), and between the hard X-ray bursts and EUV emissions (Kane and Donnelly 1971; Wood and Noyes 1972; Donnelly and Kane 1978; Kane, Frost and Donnelly 1979). Type III radio emission occurs in “bursts” (starting frequency ~ 100 MHz or higher) and “storms” (starting frequency ~ 80 MHz or below) (Rosenberg 1976) of which bursts are strongly flare associated and storms are not (Kundu 1961; Anderson and Winckler 1962; de Jager and Kundu 1963; Kane 1972a; Fainberg and Stone 1974; Rosenberg 1976).

These impulsive emissions are strongly correlated and yet they are known to be generated in different regions of the flare (*cf.* Figure (1.2)). The H α and EUV come from material in the chromosphere (Falciani *et al.* 1968; Brown 1973b). The X-rays are predominantly chromospheric but can be distributed throughout the coronal loop as well. The microwaves come from the very top of the loop (Marsh and Hurford 1980; Marsh, Hurford and Zirin 1980; Marsh *et al.* 1980, 1981; Kundu, Schmahl and Velusamy 1982; Petrosian 1982; Kundu 1983) and the Type III radio bursts and interplanetary particles originate above the flaring loop in the corona (de Jager and Kundu 1963; Wild, Smerd and Weiss 1963; Kuiper 1973; Lin, Evans and Fainberg 1973). The synchrony to within seconds of emissions coming from regions which can be as much as 10^5 km apart requires that the agent transporting the source energy throughout the flare must move rapidly, much more rapidly than the plasma electron or ion thermal speeds and maybe as fast as a

Chapter I: Introduction

significant fraction of the speed of light. This excludes conduction and convection as the means of energy transport (Emslie, Brown and Donnelly 1978) and strongly indicates the presence within the flare of electrons which are accelerated to strongly suprathermal energies (Brown 1973b, 1975). These energetic electrons then stream along the magnetic field lines from the acceleration site into the chromosphere or out into the higher corona and give rise to the various impulsive emissions. Such particles are often seen arriving at the earth and have been clearly identified with the occurrence of flares (Lin 1974a,b).

The mechanisms by which these electrons are accelerated is not yet clearly understood. The Skylab X-ray images of flare loops showed that the hottest plasma was usually found at the apex of the loop (Cheng and Widing 1975; Spicer 1977) which might suggest that that is where the acceleration region is to be found. The total amount of energy released by a flare is so large in comparison to its volume that there is only really one source for all that energy. The thermal energy density of the hottest regions of the flare and the gravitational potential energy of the flare material fall well short of that required to power a flare (Brown and Smith 1980). Though there are no accurate measurements of the strength of the magnetic fields in flaring loops (but see Kundu 1973; Rust and Bar 1973) it is thought that the energy density of the magnetic field is sufficient (Brown and Smith 1980). The energy of a flare almost certainly originates as free energy stored in the non-potential magnetic field of the flare loop structure. It is released through the annihilation of the magnetic field, a process known as magnetic reconnection. Several geometries have been proposed for the reconnection process (Cheng and Spicer 1975; Spicer 1976; Kahler *et al.* 1980; Sturrock 1980) though it is not clear

Chapter I: Introduction

which is the most applicable to the solar flare problem. For all the geometries the actual magnetic reconnection occurs on size scales which are far too small for there to be any real chance of the reconnection geometry being seen directly in the foreseeable future. Instead we are limited to observing secondary phenomena, *i.e.*, the radiations produced by the accelerated particles.

To test the acceleration theories with observations the theories would have to be developed to a point where they could predict the properties of the electron populations they produce. Actual electron populations could then be calculated from the observations and comparisons made. However, theories of the acceleration mechanism are not yet advanced enough for such predictions to be made. Observations can only be used to give requirements on the acceleration mechanisms in order that these mechanisms be compatible with experimental data. If the accelerated electrons form a beam which passes from the top of the coronal loop down to the chromosphere, the amount of energy that the electrons need to carry in order to produce the observed radiations can be calculated. Of the various impulsive emissions, the X-rays place the most stringent demands upon the electron beam. The beam strengths required to produce the observed EUV (Donnelly and Kane 1978, Emslie, Brown and Donnelly 1978; Emslie and Noyes 1978), H α (Zirin and Tanaka 1973; Brown, Canfield and Robertson 1978; Zirin 1978) and microwave (Acton 1968; Ramaty and Petrosian 1972; Anderson and Mahoney 1974; de Feiter 1975) emissions, and to account for the escaping interplanetary electrons (Lin and Hudson 1971; Lin 1974a,b) are not as high as those required to produce the impulsive hard X-rays. The X-ray data is therefore most frequently used to obtain estimates of the amount of energy which must pass into the electrons.

Chapter I: Introduction

One problem arises immediately and is supported by a wide range of X-ray observations. This is that the energy required of the beam of electrons, in order that it generate the observed impulsive X-rays, is a sizeable fraction of the total energy budget of the flare (Lin and Hudson 1971; Brown 1973b; Kane 1973; Peterson, Datlowe and McKenzie 1973; Hoyng *et al.* 1975; Hudson, Jones and Lin 1975; Lin 1975; Hoyng, Brown and van Beek 1976; Lin and Hudson 1976; Brown, Melrose and Spicer 1979). This places an extremely high efficiency requirement on the acceleration mechanism if it is to release a large fraction of the liberated magnetic energy into the directed motion of the electrons in the beam without putting a lot of that energy into bulk heating of the coronal plasma (Smith 1980). An accompanying problem is that the number of electrons which are required to be accelerated throughout the lifetime of the impulsive burst can be as high as the total number of electrons in the entire flaring volume (Brown and Melrose 1977; Hoyng, Brown and van Beek 1976). This necessitates the bulk motion of electrons within the flare to continually resupply the acceleration region and it is not clear that this can be done without generating plasma instabilities which would throttle the passage of the injected electron beam (Hoyng, Brown and van Beek 1976; Melrose and Brown 1976; Brown and Melrose 1977; Hoyng, Knight and Spicer 1978; Brown, Melrose and Spicer 1979; Emslie 1980).

For these and other reasons (*cf.* Kahler 1975; Brown, Melrose and Spicer 1979 for reviews) many have begun to doubt the viability of non-thermal models, *i.e.*, models which require the presence of a beam of suprathermal electrons. The objections can all be brought down to the fact that such a beam of electrons is an inherently inefficient producer of hard X-rays. The electrons pass down through

Chapter I: Introduction

the flare loop and exchange their energy with the background, flaring plasma. Only about one part in 10^4 of the energy in the beam is given up to the hard X-rays (Brown 1971). If the electrons which produce the X-rays can be part of a thermal (and therefore very hot in order that high enough energy X-rays can be produced) distribution, then ideally all the electron energy could be used to generate radiation and many of the problems with the non-thermal models would be alleviated. This has been the motivation for the intensive study of the so called "thermal" models which has been conducted since the mid 1970's (Crannell *et al.* 1978; Mätzler *et al.* 1978; Brown, Melrose and Spicer 1979; Smith and Lilliequist 1979; Brown, Craig and Karpen 1980; Emslie and Brown 1980; Emslie and Vlahos 1980; Smith and Auer 1980; Brown and Hayward 1981; Emslie 1981a).

In thermal models the energy released by magnetic reconnection is used to bulk heat the flaring plasma. Ion-acoustic turbulent fronts bottle up the hot plasma allowing the electrons to acquire a distribution which is relaxed and nearly Maxwellian (Brown, Melrose and Spicer 1979) and hence be able to produce X-rays efficiently. In order to reproduce the time structure of the impulsive bursts the volumes in which the electrons are heated by reconnection must be small and the number of these heating kernels large (Brown, Craig and Karpen 1980). The local temperatures in each of the kernels is extremely high ($\geq 5 \times 10^8 K$) and the kernels cool by turbulent conduction. Those electrons in the hot quasi-Maxwellian distribution which have velocities greater than ~ 3 times the thermal velocity are able to escape through the confining turbulent fronts (Brown, Melrose and Spicer 1979). Therefore, thermal models produce not just volumes of hot plasma, but also streams of these highest energy electrons which pass through the confining fronts

Chapter I: Introduction

and act in a manner similar to the beams in non-thermal models (Emslie and Brown 1980). Therefore, when reproducing the time structure of short impulsive bursts, thermal models begin to lose their efficiency advantage over non-thermal models and cease to be as attractive (Brown, Craig and Karpen 1980; Brown and Hayward 1981).

1.3 Flare emissions.

If the energy requirements of the impulsive radiations cannot rule out one or the other type of model on theoretical grounds alone then we can look to the characteristics of the radiations in order to distinguish experimentally between what are two quite dissimilar distributions of source electrons. The presence of a suprathermal source for the impulsive radiations should be visible from the radiations themselves. Whether or not it is, is one of the most long standing of all the current controversies in solar flare physics.

The EUV emission is thermal emission no matter by what mechanism this part of the chromosphere is heated. The 10 – 1030 Å EUV emission is enhanced line and recombination emission from plasma with temperatures in the range $10^4 - 10^6$ K and density $\geq 10^{12} \text{ cm}^{-3}$ (Donnelly, Wood and Noyes 1973; Donnelly and Hall 1973; Kane 1973; Noyes 1973). Whatever mechanism provides the heating to this region (Emslie, Brown and Donnelly 1978) the atmosphere responds by radiating away the excess energy as EUV and does so synchronously with the rate at which energy is deposited there (Brown 1973b). The only requirement is that

Chapter I: Introduction

the heating mechanism be able to provide enough energy to the EUV radiating plasma and a suprathermal electron source seems to be more than able to do this (Wood and Noyes 1972; Brown 1973b; Donnelly and Kane 1978).

The microwave spectrum is only a distant reflection of the source electron distribution because there are so many operational physical processes in a magnetoactive plasma (*cf.* Holt and Cline 1968; Ramaty 1969, 1973). The microwaves are the gyro-synchrotron radiation from electrons in the energy range 10 – 100 keV. But, under solar conditions, the plasma medium exerts a strong influence upon the emission, absorption and transfer of gyro-synchrotron radiation. There are many absorption and suppression mechanisms which can dominate the microwave spectrum and it is difficult to do more than say that any given spectrum can be more or less easily obtained from a non-thermal as opposed to a thermal source (Arnoldy, Kane and Winckler 1968; Ramaty and Petrosian 1972; Takakura 1975).

Flare associated Type III radio bursts (Smith 1974; Lin 1975; Rosenberg 1976; Kane *et al.* 1980b) occur in compact groups during the impulsive phase. They last for a brief one or two seconds around 100 MHz, starting at a frequency of several hundred MHz and falling at an initial rate of about 100 MHz per second (Alvarez and Haddock 1973; de la Noë, Boishot and Aubier 1973). They are radiation at the coronal plasma frequency stimulated by electrons streaming out through the upper corona (Lin, Evans and Fainberg 1973). The rate at which the radio frequency falls can be translated into a velocity for the streaming electrons of roughly one third the speed of light (Wild, Sheridan and Neylan 1959; Stone and Fainberg 1973). Type III bursts have been well correlated with deka-keV interplanetary electrons (Alvarez, Haddock and Lin 1972) and both are associated with the impulsive phase

Chapter I: Introduction

of flares. The electrons which are injected into interplanetary space are probably not the same ones which are responsible for the impulsive X-rays though they may be accelerated simultaneously with them (de Jager and Kundu 1963; Kane 1972a; Lin 1975; Švestka 1975).

For one reason or another, then, impulsive bursts other than at hard X-ray energies are not well suited to measuring the details of the underlying source electrons. The impulsive hard X-rays, on the other hand, are a much more direct probe of the emitting particles (Kane 1973). They are bremsstrahlung from the electrons as they pass through the flaring plasma[†]. The emission process provides an instantaneous measure of the state of an electron and is well understood, and the solar atmosphere above the photosphere is completely transparent to the passage of the X-rays. The X-rays which travel directly to the observer can, therefore, be immediately traced back to the electron source and should provide a clear indication of it.

1.4 Impulsive hard X-rays.

The first observation of a solar hard X-ray burst was made in 1958 from a balloon over Cuba (Peterson and Winkler 1959). Shortly thereafter several more observations were reported (*cf.* Kundu 1961) and the number grew steadily throughout the 1960's. These early observations had low energy and time resolution. This

[†]The other contending mechanisms for the production of the X-rays: synchrotron from *MeV* electrons or the inverse Compton effect, are both unlikely candidates (Korčák 1967a,b, 1971; Kane 1973; Brown and Smith 1980).

Chapter I: Introduction

allowed a thermal interpretation to be put to the data (Chubb, Kreplin and Friedmann 1966) but the accumulated weight of opinion was in favor of the X-rays being characteristic of non-thermal sources (Winckler, May and Massey 1961; Anderson and Winckler 1962, 1963; Bowen *et al.* 1964; Culhane *et al.* 1964; Acton 1968; Arnoldy, Kane and Winckler 1968; Cline, Holt and Hones 1968; Kane 1969; Pounds 1970; to mention but a few).

In a review of the then available observations Kane and Anderson (1970) found that most impulsive hard X-ray bursts could be fit to a power law spectra over the range 10 *keV* to several hundred *keV*, often with a spectral break or steepening around 100 *keV* (See also Frost 1969; Cline, Holt and Hones 1968; Frost and Dennis 1971; and for later reviews of hard X-ray observations see Peterson, Datlowe and McKenzie 1973; Kane 1974; Brown 1975, 1976; Švestka 1976; Kane *et al.* 1980b; Haug 1982). The spectral index γ (where γ is defined as $d \ln J(k)/d \ln k$ for a photon flux $J(k)$ at energy k) is typically ~ 4 or 5 , and $\gamma < 3$ or $\gamma > 6$ are extremely rare (Datlowe *et al.* 1977; Haug 1982). There is some indication that very large flares may have appreciably harder spectra (lower γ) (Chupp, Forest and Suri 1975; Hoyng, Brown and van Beek 1976) but this is by no means certain (Kane 1973; Kane, Frost and Donnelly 1979).

A power law X-ray flux is usually taken to imply a power law (*i.e.*, non-thermal) electron energy spectrum (Haug 1982) though it is extremely important to remember that this is not a necessary implication, especially when considering the uncertainties in the data (Chubb 1971; Brown 1974, 1975, 1978). Owing to the steepness of the spectra many flares are not visible over a large dynamic range, and for observations spanning 10 – 100 *keV* the spectral resolution of many instruments

Chapter I: Introduction

is often rather poor (Kane *et al.* 1980b). A typical effective channel width for a scintillation counter detecting X-rays of an energy E (keV) is several times \sqrt{E} (Brown and Smith 1980). Consequently the fitting of a power law spectrum to the observations is often not unique. An alternate two parameter fit to X-ray data would be an isothermal spectrum, though these can often be ruled out on the basis of a power law spectrum being a better fit (Kane and Anderson 1970; Kahler 1975; Haug 1982). However, there is no reason to expect that the X-ray producing plasma would be isothermal and hence, a multi-temperature fit would be more appropriate (Chubb 1971). But, with no guidance as to how the amount of emitting, hot plasma would vary with temperature, a multi-temperature spectrum can be made to fit any X-ray data provided a satisfactory emission measure – temperature function can be found (Brown 1974). Again, the data often does not allow a unique fit to be made (Craig 1975, Brown 1978).

If the X-ray spectrum is unlikely to clearly discriminate between candidate distributions for the source electrons then we should look to other characteristics of the X-rays. One of these is the X-ray polarization and another is the X-ray height structure within the flare. The X-ray emission anisotropy, though theoretically a basis for distinguishing between models, is not, in practice, a useful discriminant (Brown 1975).

A directed beam of source electrons, such as is central to non-thermal models, has the potential to produce highly polarized X-rays (Elwert 1968), whereas a thermal distribution of electrons, being essentially undirected, would produce unpolarized X-rays. On this basis the X-ray polarization can be used to indicate a preference for thermal or non-thermal X-ray sources. The question of just how

Chapter I: Introduction

strongly polarized the hard X-rays from a non-thermal model would be has been the subject of quite some study in the last fifteen years (Elwert and Haug 1970, 1971; Haug 1972; Brown 1972; Hénoux 1975; Langer and Petrosian 1977; Bai and Ramaty 1978).

These treatments have been limited by the complexity that a thorough study would require (Korčák 1974; Brown 1975). They have tended to use simple, *i.e.*, idealistic, distributions for the source electrons and for this reason their calculated values for the X-ray polarization must be treated as upper limits. Their estimates of 30 – 40% polarization are certainly high enough that hard X-ray polarization measurements (Wolff 1973) could be expected to provide the sought for discrimination between models (Emslie and Brown 1980). However, there is not, currently, a body of clearly reliable observations upon which to rely (Brown 1975; Kahler 1975; Thomas 1975; Somov and Tindo 1978; Mandel'stam referenced in Emslie 1981b; Haug 1982), though there are hopes that this may change for the better in the near future (Emslie and Rust 1980; Lemen *et al.* 1982; Tramiel, Chanan and Novick 1984).

The alternate method of using hard X-ray burst data to provide the all important model discrimination is to investigate the spatial distribution of the hard X-rays within the source (de Feiter 1975; Emslie and Rust 1980). The general understanding of thermal and non-thermal models indicates that in thermal models the hard X-rays should come predominantly from the top of the coronal loop where the hottest plasma is contained by the turbulent fronts (Emslie 1981b; Brown and Hayward 1981). In non-thermal models the hard X-rays should come

Chapter I: Introduction

predominantly from the chromosphere where the background plasma density is high (Brown and McClymont 1975; Emslie 1981b).

Before the recent launching of the NASA Solar Maximum Mission (SMM) satellite in February 1980, the only means for obtaining any observational information about the X-ray height structure was from the occultation of flares occurring just behind the solar limb (McKenzie 1975). Most of the early reports of such observations were able to show that the hard X-ray source can extend to altitudes in excess of 20×10^3 km above the photosphere (Haug 1982) but they were not able to provide any accurate spectral information (Brown 1975). More recently, several stereoscopic observations of flares which are partially occulted to one of the two telescopes but which are in full view to the other have been reported (Kane 1983). Such stereoscopic observations resolve a flare into two spatially distinct source regions and provide hard X-ray measurements with the beginnings of spatial resolution.

Onboard the SMM satellite is the Hard X-ray Imaging Spectrometer (HXIS) (van Beek *et al.* 1980) which can image 3.5 – 30 keV X-rays with 8" angular resolution (corresponding to ~ 6000 km on the surface of the sun). HXIS is capable of resolving separately each loop footpoint and the coronal part of the loop for an average sized flare. The initial reports (*cf.* review by Haug 1982) have shown that the regions with the strongest emission of hard X-rays have the flattest spectra and tend to overly the brightest H α patches. Also, the regions of strongest soft X-ray emission are located between the regions of brightest hard X-rays. These HXIS observations provide support for the non-thermal interpretation of flare bursts (Duijveman, Hoyng and Machado 1982; Haug 1982).

Chapter I: Introduction

1.5 The study conducted.

Yet, as with the X-ray polarization estimates, calculations of the X-ray height structure in non-thermal models have suffered from the fact that a thorough study would require a complex and lengthy treatment of the dynamics of the electron beam. Idealized distributions for the electrons in the beam have been used and, consequently, the value of the calculated results has been primarily qualitative.

Because of the limited applicability of these qualitative results, there has been a great need for a full and thorough study of the impulsive hard X-rays from non-thermal models. With the launching of the SMM satellite carrying HXIS and the Hard X-ray Burst Spectrometer (HXRBS) (Orwig, Frost and Dennis 1980), the launching of the Hinotori satellite in February 1981 carrying the Imaging Hard X-ray Telescope (SXT) (Makishima 1982; Tanaka 1983; Takakura *et al.* 1983) and with the latest X-ray polarimeters promising accurate high resolution results there is a growing body of high quality data needing a comprehensive interpretation. This data can be used to further test the ability of flare theory to understand flare observations and, hence, to describe the physical processes active in flares, provided the theory has been developed to a level commensurate with the quality of the data. In this manner the data can provide the means for a discrimination between candidate models which has up to now been lacking.

But there has also been a need for a full study of non-thermal models which went beyond testing the viability of the theory. The study of solar flare impulsive hard X-rays has been motivated by a desire to measure the characteristics of the population of the energetic source electrons, and to use knowledge about the

Chapter I: Introduction

source electrons to further understand the acceleration mechanisms which power the flare.

We have conducted our study of non-thermal flare models with this view in mind. We have followed a method whereby we construct a general non-thermal model description of the solar flare physics and from this calculate the characteristics of the impulsive hard X-rays. The model description is very general in that it allows the geometric structure of the loop and the characteristics of the electron beam at the acceleration region to be flexibly specified by way of free parameters. From the description of the electron beam at the acceleration region a full description of the electron beam at all positions within the flaring plasma is calculated, and a complete description of the X-rays is obtained. We then correlate the characteristics of the X-rays with the values of the parameters describing the flare geometry and the electron beam, and we investigate how the characteristics of the X-rays change in response to a change in the model parameters. In this manner we are able to see how the X-rays convey information about the details of the flare models and the extent to which X-ray observations can be used to obtain a description of the source electrons.

In Chapter II we expand upon the non-thermal model paradigm and construct a mathematical description of the evolution of the electron beam within the flaring plasma. In Chapter III we obtain analytic and numerical solutions to our central equation and we present a sample of the results pertaining to the evolution of the electron beam. We do this in order that we may later understand the behavior of the X-rays in terms of that of the electron beam. In Chapter IV we describe how we incorporate the production of X-rays by the electron beam into the model

Chapter I: Introduction

paradigm. At this stage we have a complete description of the modelling technique and can proceed with calculating the X-ray characteristics.

In Chapter V we present our X-ray results. We set up a reference model and give the X-ray results for that model in detail. We then vary the model parameters and describe how the X-ray characteristics change in response to this. In Chapter VI we use our modelling technique to fit non-thermal models to the newly available data and show the extent to which the new data can be used to obtain descriptions of the population of source electrons in each case. In Chapter VII we summarize our study and recapitulate our major results.

Chapter II

The Fokker–Planck Equation

We now look more closely at the non-thermal model paradigm, and pare it down to make a workable description of our problem. In this chapter we step through the paradigm, elucidating the processes which play a role in the physical system and decide which of them we need to incorporate into a description of the flare physics. We see how the physics determines the mathematical approach to be followed, we construct the mathematical expression corresponding to our physical paradigm (the Fokker–Planck Equation) and we obtain the values of the various coefficients. In Chapter III we shall show how we solve this equation.

2.1 The general non-thermal model.

The physical structure of the loop:

The general physical paradigm comprises a magnetic structure, such as an arch or tube of magnetic flux, the body of which projects into the corona and which has footpoints descending through the chromosphere and into photospheric regions of opposite magnetic polarity (*cf.* Figure (1.2)). A typical length for the

Chapter II: The Equation

coronal part of the structure is 20 000 *km* (Vorpahl *et al.* 1975). The shape of the coronal loop is often not at all well determined. The Skylab soft X-ray loops frequently appeared more long than high though sometimes this may have been the result of observing an arcade of loops for which the individual loops were too small to be resolved (Spicer 1977). Loops seen on the limb of the sun suggest that a typical loop may be roughly half as tall as it is long (Vorpahl *et al.* 1975). In our modelling of flares we use loops which are semicircular and which are vertical upon meeting the transition region. The loops are then symmetric about the vertical through the top.

The acceleration region:

The mechanisms by which the magnetic energy is released into the plasma are poorly understood. The size scales over which the energy is liberated may be of the order of tens of centimeters (Sturrock 1968; Spicer 1976; Brown and Smith 1980), in which case the processes by which electrons are accelerated cannot be seen directly. Attempts to model the observed hard X-ray bursts have required that the accelerated electrons carry a large fraction of the total energy of the flare. A recent estimate is that at the peak of the bursts at least 20% of the flare power has to go into accelerating the beam electrons (Duijveman, Hoyng and Machado 1982). The acceleration mechanism therefore invests a large fraction of the liberated magnetic energy into the directed motion of the accelerated electrons and not into the bulk heating the flaring plasma. The understanding of how the acceleration mechanism can achieve such a high efficiency presents a major theoretical problem (Brown and Smith 1980; Smith 1980; Duijveman, Hoyng, and Machado 1982).

Chapter II: The Equation

The acceleration mechanism is also required to act at a rapid pace, releasing the flare energy on a timescale of only seconds to a few hundreds of seconds, and to act on a number of electrons which is of the order of the total number of electrons in the whole flare volume (Brown and Melrose 1977). The demands made upon the acceleration processes by the non-thermal model paradigm are prodigious. Confronted with such a poor understanding of the details of the acceleration processes, we must be satisfied with treating the energy release region as if it were a black box. This black box serves to produce the beams of accelerated electrons which are injected into both limbs of the magnetic arch. As we cannot derive the distribution in velocity space of the accelerated electrons, the characteristics of the injected beams are introduced into the problem through the use of free parameters. One of the results of this research is to show that the parameters describing the electron beam can be determined from the X-rays which are observed.

The black box acceleration region lies somewhere within the coronal loop (only $\simeq 0.1\%$ of the flare-accelerated electrons escape the solar atmosphere (Lin 1974a,b)) and could, in theory, be located at any point along its length. The observation of hard X-ray bursts coming from the two footpoints of a loop with a high degree of simultaneity need not suggest that the acceleration region is located halfway between the two footpoints, that is, at the top of the loop. The transit time for the energetic electrons to cross from one footpoint to the other along a loop of average length is measured in tenths of a second and, as such, is shorter than the time resolution of most observations. There is only one X-ray instrument which can see clearly such fast time structures: the Hard X-ray Burst Spectrometer (HXRBS) currently on the Solar Maximum Mission (SMM) satellite (Orwig, Frost

Chapter II: The Equation

and Dennis 1980). However, HXRBS has no spatial resolution capabilities and cannot separate the two footpoint sources from within its X-ray data.

Skylab soft X-ray observations showed that many post flare loops have the regions of hottest plasma located at the apex (Widing and Cheng 1974; Cheng and Widing 1975). This implies that the energy release region is localized and is near or at the apex of the loop. The emerging flux model of Heyvaerts, Priest and Rust (1977) and the triggering method of Leach and Emslie (1980) would both place the acceleration region at that point anywhere along the flaring loop where the triggering magnetic structure happens to touch first, implying that the acceleration region may occur at any position within the flare loop. One important parameter which is to some degree influenced by the position of the acceleration region is the thickness of flaring plasma between the acceleration region and the top of the chromosphere. This, however, is the product of the coronal density and the length of the loop, and these two variables can each range over at least a decade in magnitude. Consequently, the position of the acceleration region, as measured by its column depth above the chromosphere, is not narrowly confined, and should, in each instance, be derived from the observations rather than be imposed beforehand upon the flare models. We choose to place the energy release site at the apex of the flare loop and then select loop lengths and densities which give appropriate column thicknesses for the loops. Since the flare loop is symmetric about its apex, in our models we consider only one half of the loop, the acceleration region being located at the top. Since the distribution in velocity space of the accelerated electrons is to be introduced by way of free parameters, we incorporate

Chapter II: The Equation

this black box acceleration region in the form of an upper boundary condition to our problem.

The structure of the magnetic field:

The magnetic field geometry defining the flare loop is taken to be static, though the magnetic field itself is not necessarily of uniform strength throughout the length of the loop. As the beam electrons gyrating about magnetic field lines pass into regions of increasing field strength, they respond by increasing the pitch of their gyration and may well have their directions of travel along the field lines reversed. There is little information as to the strength of the flare magnetic fields in the corona (for a summary see the discussion preceding the results for models 7 through 11 in Chapter V), though the fields in an active region containing flares are known to be complex and to have strong gradients. Flare loops may, therefore, have a significantly varying cross-section throughout their length (Rust and Bar 1973, Withbroe 1978; Vesecky, Antiochos and Underwood 1979; Levine and Pye 1980). In our modelling we must allow for the magnetic field in the loop to increase its strength many fold in passing down through the loop. In such cases the field plays a significant role in the evolution of the electron beam. We therefore include the effects of the magnetic field in our analysis of the beam dynamics and allow for a wide range of possible field strengths.

The beam of high energy electrons (there is one beam in each limb, but we need to consider only one limb) passes down within the magnetic structure delineating the loop. The individual beam electrons gyrate as they move along the magnetic

Chapter II: The Equation

field lines. The gyroradius ($\approx 500 [B(\text{Gauss})]^{-1} \text{ cm}$ for a 20 keV electron) is much smaller than any of the geometric or dynamic size scales of the plasma. Cross field diffusion or drifting is therefore negligible (Krall and Trivelpiece 1973, Appendix I) and the beam electrons remain tied to the magnetic field lines. We consider each electron to be decoupled in its motions from the other beam electrons and we ignore any interactions between different electrons in the beam.

Coulomb collisions:

As the electrons move along the magnetic field lines, they interact with the ambient plasma constituents (electrons and protons). As they pass by the ambient particles, they undergo Coulomb collisions through which they lose energy and have their trajectories modified. It is, therefore, through these collisions that the electron beam evolves within the plasma. With the passage of the beam through a sufficient depth of plasma, the beam is completely dissipated. Coulomb collisions are, then, the dominant process controlling the motion of the electrons within the flaring plasma and are the principal process to be included into our modelling of a flare. Since this process is central to our non-thermal paradigm, we shall expand upon our description of it later in this chapter when we consider the mathematical formulation of our modelling approach.

Heating:

The beam electrons collide with the plasma constituents, electrons and protons alike, though the transfer of energy is greater to the plasma electrons than to

Chapter II: The Equation

the plasma protons in proportions given by the proton to electron mass ratio. The ambient electrons are heated by the beam and then slowly share their energy with the ambient protons. This heating of the ambient plasma undoubtedly gives rise to hydrodynamic motions within it. However, the timescale over which hydrodynamic effects become significant is large. Chromospheric material is evaporated into the corona as a rapid response to the impinging electron beam. But the timescale on which this hydrodynamic response affects the flaring loop is of the order of the time it takes a hydrodynamic signal to travel the length of the loop at the sound speed $c_s \sim 10^4 T^{1/2} \text{ cm sec}^{-1}$. For a loop length of 10^9 cm and a coronal temperature of 10^7 K , this time is $\sim 30 \text{ secs}$. Consequently, the timescale over which the effects of heating the ambient plasma by the electron beam arise is of the order of several tens of seconds. The timescale over which the beam electrons themselves travel from the top of the loop down into the photosphere is much shorter than this, being measured on scales of hundredths of a second. Consequently, we take the ambient plasma, as seen by the accelerated electrons, to be static and assume that the plasma particles remain cold.

Reverse currents:

The high electrical conductivity of the ambient plasma ensures that any local electric fields appearing within the plasma and associated with the passage of the electron beam remain small. There will, however, be an electric field generated across the whole length of the loop. The beam of high energy electrons constitutes an electric current passing between the top of the loop and its footpoints. Not only

Chapter II: The Equation

would this current have a self magnetic energy vastly exceeding its own kinetic energy but it would rapidly lead to a huge separation of electric charge within the plasma and would deplete the acceleration region of source electrons were it not for the reverse current set up in the plasma (Benford and Book 1971; and see Emslie 1980 and references within). This reverse current comprises a drift of ambient electrons toward the top of the loop and is of precisely the magnitude required to ensure exact local charge neutrality and zero local current density everywhere. This reverse current arises in response to the passage of the electron beam by way of the large scale electric field set up across the length of the arch by the attempted charge separation.

The electrons in the beam also experience this electric field and are slowed by it. In effect, energy is taken from the electron beam to drive the return current. Provided the current of suprathermal electrons is small, that is, provided the density of the electrons in the beam is much smaller than that of the ambient plasma, the reverse current can be maintained by a small electric field giving rise to a slow drift of the ambient plasma electrons. "Slow" is relative to the maximum velocity at which the plasma electrons can be driven before they begin to generate turbulence. This maximum velocity is a sensitive function of the electron to ion temperature ratio (Kindel and Kennel 1971; Emslie 1981c) and is characterised by the electron thermal velocity. If the current in the electron beam is low, only a slow drift of the ambient electrons is necessitated and only a small amount of energy is taken from the suprathermal beam. If the beam current is large, the density of the ambient electrons may no longer be high enough to provide the required reverse current without driving the plasma electrons faster than

Chapter II: The Equation

their thermal velocity. Any attempt to establish the reverse current then rapidly generates plasma turbulence which throttles the reverse current and prevents the passage of the initial electron beam.

Emslie (1980) has studied the effects of including the reverse current in the treatment of the electron beam and has obtained an upper limit to the size of the beam which can pass within the flaring plasma. However, his analysis is incomplete. He uses a mean scattering treatment to evaluate the evolution of the beam of electrons and does not consider fully the influence of the electrons which have been turned around by the combined effects of the electric field and Coulomb collisions and which are subsequently travelling back toward the top of the loop. When studying large reverse currents and large reverse current electric fields, it is no longer sufficient to think of the suprathermal electrons as being removed from the beam once their pitch angle has been increased to 90° and their forward motion has ceased. The transverse kinetic energy of the beam electrons will be greater than the thermal energy of the ambient plasma electrons and therefore the beam electrons will not immediately become a part of the background plasma. These electrons will more likely be accelerated back toward the top of the loop by the reverse current field and will comprise a returning beam of suprathermal electrons. This returning beam will be present at all depths within the flaring loop and, as such, will supplement the established reverse current. The presence of this returning beam will become increasingly significant for injected electron fluxes of increasing size. For very large fluxes of injected electrons, the current in the returning beam will be equal to a large fraction of the injected beam current. Taking this returning current into consideration will reduce the requirements on

Chapter II: The Equation

the ambient plasma and hence ease the stability constraints on the size of the electron beam.

Typically, the number density of the electrons in the beam is expected to be small compared to that of the ambient plasma (Smith and Lilliequist 1979). An analysis of the beam dynamics under the circumstances of plasma turbulence caused by a large beam current and an unstable reverse current would require a wholly different approach to the problem than is to be developed in this study and is not to be taken up here. We assume that the reverse current is weak and stable and that the effects of the reverse current electric field on the evolution of the beam are small and need not be taken into consideration.

Plasma turbulence:

The passage of the beam through the plasma may also be seen in terms of the total (beam + plasma) electron number distribution in velocity space. The presence of the beam may, if it is large enough, create a local minimum in the total distribution with a “gentle bump” to the high velocity side of it. Such a distribution may stimulate Langmuir turbulence and plasma waves and may redistribute energy among the electrons in the beam. The necessary and sufficient condition for the generation of such a two-stream instability is that the Penrose criterion be satisfied (Penrose 1960; Krall and Trivelpiece 1973 p472). This requires that the beam density be sufficiently high and that the “gentle bump” be sufficiently steep and separated from the main body of the number distribution, *i.e.*, that of the background plasma. It is uncertain whether the conditions exist

Chapter II: The Equation

within a flare to satisfy the Penrose criterion (Smith 1975; Emslie and Smith 1984), or, if they do, what the level of wave generation and turbulence would be and how the electron beam itself would be affected. Any analysis of this question would constitute a major body of research in itself and, as such, cannot be touched upon here. We assume, again, that the beam density is low enough in comparison with that of the background plasma and that the beam pitch angle distribution is sufficiently broad that the Penrose condition is not satisfied and that we need not consider the effects of the two-stream instability.

Radiative losses:

The electrons, by continuously changing their instantaneous direction of motion, will emit electromagnetic radiation, primarily through the synchrotron and bremsstrahlung processes. Both of these are extremely important mechanisms for providing observational information about the flare. However, the rate at which the electrons lose energy to radiation is insignificant in comparison with the rate at which they lose energy through collisions. The rates of energy loss to bremsstrahlung and synchrotron radiation are

$$\frac{\left. \frac{dE}{dt} \right|_{\text{Bremsstrahlung}}}{\left. \frac{dE}{dt} \right|_{\text{Coulomb}}} = 2.2 \times 10^{-4} \left(\frac{E}{m_e c^2} \right) \quad (2.1)$$

(Brown 1971) and

Chapter II: The Equation

$$\frac{\left. \frac{dE}{dt} \right|_{\text{Synchrotron}}}{\left. \frac{dE}{dt} \right|_{\text{Coulomb}}} = 9.2 \times 10^{-3} \frac{(B/100 \text{ Gauss})^2 \sin^2 \alpha}{(n_i/10^{10} \text{ cm}^{-3})} \left(\frac{E}{m_e c^2} \right)^{3/2} \quad (2.2)$$

(Kane 1973) for an electron of energy E and pitch angle α . B is the magnetic field vector and n_i the ambient plasma density. These energy loss rates to radiation are sufficiently low that the radiation processes need not be considered as contributing to the evolution of the electron beam.

All the physical processes which we omit from the treatment of the electron beam evolution either have a clearly negligible effect upon the beam (energy losses to radiation, hydrodynamic response of the flaring plasma, beam-beam interactions) or are extremely nonlinear (reverse currents, plasma turbulence and instabilities). Not only is the neglect of non-linear processes justified for a dilute electron beam, it is precisely their omission which makes the analysis of the beam evolution tractable. The remaining influential physical processes (Coulomb collisions and the variation of the magnetic field) are not lessened by the diluteness of the electron beam and must be retained in the treatment. To recapitulate, the paradigm is as follows (*cf.* Brown 1971, 1973b; Hudson 1972, 1973; Syrovat'skii and Shmeleva 1972; Petrosian 1973; Kane 1974; Melrose and Brown 1976; Donnelly and Kane 1978): electrons are injected with a range of energies and pitch angles into a static and passive flaring plasma from an acceleration region located at the apex of a semicircular loop. The electrons gyrate as they stream along the magnetic field lines which delineate the flare loop, and they experience the adiabatic scattering from the magnetic field and Coulomb collisions with the ambient plasma. The

Chapter II: The Equation

beam electrons lose energy to the ambient plasma and continually change their pitch angles. With the passage through a large enough thickness of the ambient plasma, the beam is completely absorbed. The high energy electrons emit X-ray bremsstrahlung radiation.

2.2 Mathematical development.

Because we are ultimately interested in using the evaluated details of the X-ray distribution as a diagnostic tool for probing the physical environment and the distribution of the electron beam, we need to calculate in detail the distribution of the beam electrons throughout the plasma. An equation satisfied by the electron number distribution is constructed in such a way as to describe the evolution of the collisionally modified beam as it passes from the top of the loop down through the footpoints. The effect of the acceleration region on the initial distribution of the beam is incorporated as a boundary condition. Once the full number distribution has been calculated we shall use it to obtain the characteristics of the X-rays.

The single-particle distribution function:

We now consider how we might best describe the evolution of the beam using an equation. According to our paradigm, the evolution of the beam is controlled by Coulomb collisions between the beam electrons and the ambient plasma. We conceive of the collisions as the interactions between the test particles (the beam electrons) of known positions and velocities, and the field particles (the background

Chapter II: The Equation

plasma) of random positions and velocities, the field being characterised by a number density n . It is impossible to know exactly the locations and velocities of each one of the background plasma particles. It is therefore just as impossible to calculate precisely the trajectory of each of the individual beam electrons even though the trajectory of a charged particle moving within the combined Coulomb field of the ambient plasma particles could, in theory, be calculated dynamically. This collisional interaction must be treated stochastically.

As we cannot calculate the trajectory of each individual electron we cannot construct a dynamical description of the beam evolution which would incorporate precise knowledge of the behavior of the beam electrons. We must instead deal with the electron beam by way of a probability function which describes the probability of finding an electron at a particular position \mathbf{x} within the flaring plasma and with a particular velocity \mathbf{v} (Chandrasekhar 1943). We study the electron beam by using a single-particle number distribution function in phase space, $f(\mathbf{x}, \mathbf{v}, t)$, a function which gives the probability of finding the test particle within an interval $d^3x d^3v$ about the coordinates (\mathbf{x}, \mathbf{v}) at any given time t as $f(\mathbf{x}, \mathbf{v}, t) d^3x d^3v$.

The system described by the number distribution is the beam of electrons moving through the background plasma where the beam may contain a flux upward of 10^{18} electrons $cm^{-2}sec^{-1}$. It is not immediately obvious that a single-particle distribution function will contain enough information to describe a system of N particles where N is such an extremely large number. That it may do so requires a discussion of the time intervals over which we are interested in having knowledge of the system.

Chapter II: The Equation

There are three significant time intervals for any real gas (Liboff 1969, pp 126; Wu 1966, pp 47):

1) The shortest time interval τ_0 is the “dynamical” time and is the characteristic time scale over which a test particle may be considered strongly influenced by any particular nearby field particle. τ_0 may be loosely equated with the duration of an individual electron-electron collision.

2) The intermediate time interval t_0 is the “kinetic” time and is the characteristic timescale over which the test particle will have undergone many collisions. The accumulated effect of the many random collisions is a change in the electron’s velocity by only a fractional amount which is small.

3) The longest timescale T_0 is the “hydrodynamic” time and is the characteristic timescale over which the beam would come to local thermodynamic equilibrium with the background plasma.

For a large system such as ours $\tau_0 \ll t_0 \ll T_0$ and the three timescales may be treated as defining three separate regimes. Over timescales $t \sim \tau_0$ each particle of an N-particle system is essentially isolated from the body of the system and is influenced only by those particles in the small volume immediately about it. Knowledge of the whole system of N isolated particles can only be obtained from the N-particle number distribution $F_N(\mathbf{x}^1, \dots, \mathbf{x}^N, \mathbf{v}^1, \dots, \mathbf{v}^N, t)$ which contains explicit information about all N particles.

Over the intermediate timescale $t \sim t_0$ a particle suffers many collisions and has its velocity \mathbf{v} changed by an amount $\Delta \mathbf{v} \ll \mathbf{v}$. $\Delta \mathbf{v}$ is the net effect of the independent impulses from many interactions. Over this timescale information as to the particular initial positions and velocities of the particles is lost and the

Chapter II: The Equation

particles become, to some degree, correlated. On this timescale the N-particle distribution function degenerates and may be written as the product of N one-particle distribution functions, *i.e.*,

$$F_N = \prod_{i=1}^N f(\mathbf{x}^i, \mathbf{v}^i, t). \quad (2.3)$$

On the kinetic timescale, therefore, knowing the single-particle distribution function $f(\mathbf{x}, \mathbf{v}, t)$ suffices in order to have complete knowledge about the system.

Finally, over the hydrodynamic timescale $t \sim T_0$ the system reaches local thermodynamic equilibrium and proceeds, by hydrodynamic processes, toward a global thermodynamic equilibrium. The system has attained a quasi-equilibrium distribution and is completely described by the first three moments of the one-particle distribution function, namely the local density $n(\mathbf{x})$, the local fluid velocity $\mathbf{v}(\mathbf{x})$ and the local temperature $T(\mathbf{x})$.

It is, then, the N-particle function which is required in order to describe the behavior of the beam over very small size and time scales, the one-particle function which is needed to describe the beam as it evolves, in this case under the influence of the collisional damping, in the direction of increasing entropy, and only the hydrodynamic moments which are needed to describe a beam locally in thermodynamic equilibrium with the plasma. Our interest is in the evolution of the beam as it approaches local equilibrium with the plasma from an initial distribution which is very far from equilibrium. We are interested in the earlier steps by which the beam evolves and we do not follow its evolution through to the later stages during which it merges with the background plasma. Because,

Chapter II: The Equation

ultimately, we shall be looking at the hard X-rays produced by the beam, we are not interested in the energetic electrons once their energy has fallen below hard X-ray energies ($\sim 10 \text{ keV}$). The beam electrons remain, throughout the energy interval of interest, suprathermal and quite distinct from the ambient plasma. Our interests are therefore best satisfied by the one-particle distribution.

Coulomb collisions:

The state of a purely dynamical system is governed by the Liouville equation which describes the conservation of extension in phase space as the system evolves. Without the collisional interactions between electrons, the beam would stream along the magnetic field lines and the trajectory of each electron would be governed by the conservation of the adiabatic invariants of its motion about the magnetic field. The trajectory of each electron could, therefore, be calculated precisely from a knowledge of its initial position and velocity. The Coulomb collisions are what introduces the non-dynamical behavior into the description of the electron beam. The effects of collisions on the electron trajectories must, therefore, be introduced by way of a separate *ansatz* which will allow us to calculate the additional non-dynamical terms to be used with the Liouville equation (Wu 1966).

The Coulomb interactions are mediated by the electromagnetic force which is long range in character. This fact severely complicates the analysis of multi-electron interaction problems. The nature of a long range force is such that the test electron is influenced more by its interactions with the large number of distant field particles than it is by its interactions with the few nearby field particles

Chapter II: The Equation

(Krall and Trivelpiece 1973 p294; Rosenbluth, MacDonald and Judd 1957). This manifests itself as a divergence in the value of the scattering cross-section for a long range force as the scattering angle goes to zero. We must therefore expect that any collision coefficients calculated on the basis of interactions in a pure Coulomb field would themselves contain this divergence and would become infinite as we include the incremental effects on the test particle of the increasing numbers of increasingly distant field electrons. This divergence can be removed when we consider the effects of the test particle on the distribution of the field particles.

The presence of the test particle perturbs the distribution of the field particles. A Fourier analysis of this perturbation shows that it gives rise to two types of density fluctuation (Pines and Bohm 1952). Those density perturbations which have a wavelength roughly greater than the Debye length manifest themselves as collective plasma oscillations. As mentioned above, we neglect in this analysis of the beam dynamics these oscillations or waves generated in the plasma. The shorter wavelength density perturbations manifest themselves as a co-moving (with the test particle) charge cloud which has the effect of screening the field particles from the test particle's electric charge. This screening arises from the Coulomb repulsion between test and field electrons and leads to a deficiency of negative charge with respect to positive charge in the immediate neighborhood of the test electron. The effective electric field arising from the test electron's charge then falls more rapidly than as the inverse square of the distance r away from the charge, and, as a consequence, the interactions between the test particle and distant field particles are weakened. The effective field is of the form $(e/r) \exp(-r/\lambda)$ (Pines and Bohm 1952) for an electric charge e where λ is a suitable scaling length. By using

Chapter II: The Equation

this interaction potential instead of the pure Coulomb potential, the resultant Coulomb collision terms are rendered finite. The end result is exactly equivalent to our calculating the collision terms using the pure Coulomb interaction potential and introducing a discrete cut-off in the range of the force at the distance λ . λ is frequently taken to be the Debye - Huckel distance λ_D (Debye and Huckel 1923) which is the appropriate screening distance for a plasma in thermal equilibrium and not containing an interspersed magnetic field. For a test particle which has a velocity well in excess of the plasma sound speed, more appropriate distance may be the mean free path or, in the presence of a strong magnetic field, the gyro-radius (Emslie 1978). For now we leave open the question of what value to use for λ . We shall see shortly that it occurs logarithmically in the collision terms and that this logarithmic term is, in general, not precisely known. The screening length λ need not be determined to better than approximate accuracy.

By introducing this screening of the test particle we are able to treat the test particle as if it had no interaction with any field particles which are farther away than a distance λ . There are, of course, many, many particles within this distance and with which the test particle is simultaneously interacting (of order 10^9 would be a characteristic number for the corona). The test electron also experiences large angle scattering from discrete encounters with the few very nearby field electrons but, if the test electron has a kinetic energy in excess of approximately 1 keV , the effects of these individual collisions may well be ignored (Banks, Chappell and Nagy 1974).

Chapter II: The Equation

The Fokker–Planck equation:

For the simultaneous interactions with many field electrons it is incorrect to think entirely in terms of discrete binary collisions. The very terms “collision” and “mean free path” are ambiguous (Wu 1966). We therefore hesitate before constructing our collision terms by invoking the usual Boltzmann *stosszahlensatz* and taking the path which leads to the Boltzmann collision integral. Because the Boltzmann collision integral focusses on discrete binary collisions, it is not quite appropriate for interactions based upon inverse square law forces and obscures the true physical situation. We prefer to obtain the collision terms by way of a different procedure.

Over a kinetic timescale, the modification of a beam electron’s trajectory is relatively small. The value of the distribution function $f(\mathbf{x}, \mathbf{v}, t)$ for a particular \mathbf{x} , \mathbf{v} and t is correlated only with those values of the function at the slightly earlier time $t - \Delta t$ and at the nearby positions \mathbf{x}_1 , \mathbf{v}_1 for which $\mathbf{x} - \mathbf{x}_1 = \mathbf{v} \Delta t$ and $|\mathbf{v} - \mathbf{v}_1| \ll \mathbf{v}$. The evolution of the distribution function then depends more upon the local velocity gradients $\partial f(\mathbf{x}, \mathbf{v}, t) / \partial \mathbf{v}$ about \mathbf{v} than on the value of the function $f(\mathbf{x}, \mathbf{v}, t)$ over the whole velocity range (Cohen, Spitzer and McRoutly 1950). Another method, then, by which we can calculate our collision terms, and the one which is followed in this analysis, is to assume that the evolution of the beam’s number distribution is controlled by a process which is Markovian. This then allows us to obtain the collision terms by using the Chapman–Kolmogoroff Equation. This path explicitly describes the effects of multiple simultaneous collisions in terms of the average rate of change of the electron’s position and velocity. However, when we actually calculate these rates of change we find that it is sufficient to

Chapter II: The Equation

use the cross-sections for two-body interactions provided we include the effects of particle correlations and use the shielded Coulomb potential. We do not in effect incorporate anything which is not already included in the calculation of the Boltzmann collision integral. The collision terms obtained by way of the Chapman-Kolmogoroff Equation in the end turn out to be obtainable from an expansion of the Boltzmann collision integral about the limit of small angle collisions. The end result, the Fokker-Planck Equation, may be obtained equivalently by either method (Lewis 1969, p 115 - 116; Wu 1966, p53).

To construct the collisional damping terms we require a way of incorporating the effects of collisions. We calculate the time rate of change over a kinetic timescale of the coordinates of an electron under the aggregate influence of many, many collisions. Over such an interval Δt , the electron suffers a mean displacement $\Delta \mathbf{v}$ where $\Delta \mathbf{v} \ll \mathbf{v}$ and is $O(\Delta t)$. This displacement is the sum of many independent impulses or displacements. To describe the quantity $\Delta \mathbf{v}$ by which \mathbf{v} changes we define a transition probability $\Psi(\mathbf{x}, \mathbf{v}, \Delta \mathbf{x}, \Delta \mathbf{v})$. This gives, as $\Psi(\mathbf{x}, \mathbf{v}, \Delta \mathbf{x}, \Delta \mathbf{v}) d^3x d^3v$ the probability of the electron going from an element $d^3x d^3v$ of phase space about (\mathbf{x}, \mathbf{v}) to a similar element about $(\mathbf{x} + \Delta \mathbf{x}, \mathbf{v} + \Delta \mathbf{v})$ in time Δt . Obviously, as the electron at no stage ceases to exist, the transition probability has to be normalized such that $\int \Psi(\mathbf{x}, \mathbf{v}, \Delta \mathbf{x}, \Delta \mathbf{v}) d^6\Delta \equiv 1$. This is the formal definition of $\Psi(\mathbf{x}, \mathbf{v}, \Delta \mathbf{x}, \Delta \mathbf{v})$ which is calculated later from a knowledge of the collision cross-sections and a description of the ambient background plasma.

We now use this transition probability to describe the evolution of $f(\mathbf{x}, \mathbf{v}, t)$ making the assumption that the modification process is Markovian. This assumption is that the evolution of the system depends only upon the instantaneous values

Chapter II: The Equation

of the system's physical parameters and not upon the system's history. We can obtain a description of the system at a time t from a full description of the state of the system at the slightly earlier time $t - \Delta t$. The evolution of the system can be seen as the gradual unfolding of the transition probability (Chandrasekhar 1943). The Markovian assumption is indeed an assumption (Gasirowicz, Neumann and Riddell 1956); if we were dealing with the N -particle distribution function $F_N(\mathbf{x}^1, \dots, \mathbf{x}^N, \mathbf{v}^1, \dots, \mathbf{v}^N, t)$ and if all the coordinates of the particles were known precisely, then we could take the Markovian assumption as being implied by the dynamical nature of the interactions. We are, however, dealing with a contraction of the total information of the system in the form of the one-particle distribution function; and that this contraction should obey the Markovian assumption need not necessarily follow (Vasiček 1973). That we take it to do so is our assumption.

The mathematical expression of this assumption on the nature of the evolution of $f(\mathbf{x}, \mathbf{v}, t)$ is given by the Chapman–Kolmogoroff Equation (Gasirowicz, Neumann and Riddell 1956):

$$f(\mathbf{x}, \mathbf{v}, t + \Delta t) = \int_{\Delta \mathbf{x}} \int_{\Delta \mathbf{v}} f(\mathbf{x} - \Delta \mathbf{x}, \mathbf{v} - \Delta \mathbf{v}, t) \Psi(\mathbf{x} - \Delta \mathbf{x}, \mathbf{v} - \Delta \mathbf{v}, \Delta \mathbf{x}, \Delta \mathbf{v}) d\Delta \mathbf{x} d\Delta \mathbf{v}, \quad (2.4)$$

where Δt is a kinetic time interval, *i.e.*, Δt is finite (long compared to the dynamical or “collision” timescale) but small (short enough that $\Delta \mathbf{v} \ll \mathbf{v}$).

The evolution of $f(\mathbf{x}, \mathbf{v}, t)$ is controlled predominantly by small angle collisions off the many distant field particles and, hence, $\Psi(\mathbf{x}, \mathbf{v}, \Delta \mathbf{x}, \Delta \mathbf{v})$ is strongly peaked about $(\Delta \mathbf{x}, \Delta \mathbf{v}) = 0$ and varies smoothly with \mathbf{x} and \mathbf{v} . We may then

Chapter II: The Equation

expand equation (2.4) in a Taylor series about $(\Delta \mathbf{x}, \Delta \mathbf{v}) = 0$ (Liboff 1969, p262).

$$\begin{aligned}
 f(\mathbf{x}, \mathbf{v}, t + \Delta t) = & \int_{\Delta \mathbf{x}} \int_{\Delta \mathbf{v}} d\Delta \mathbf{x} d\Delta \mathbf{v} \left([f(\mathbf{x}, \mathbf{v}, t) \Psi(\mathbf{x}, \mathbf{v}, \Delta \mathbf{x}, \Delta \mathbf{v})] \right. \\
 & - \Delta \mathbf{x} \cdot \frac{\partial}{\partial \mathbf{x}} \cdot [f(\mathbf{x}, \mathbf{v}, t) \Psi(\mathbf{x}, \mathbf{v}, \Delta \mathbf{x}, \Delta \mathbf{v})] \\
 & - \Delta \mathbf{v} \cdot \frac{\partial}{\partial \mathbf{v}} \cdot [f(\mathbf{x}, \mathbf{v}, t) \Psi(\mathbf{x}, \mathbf{v}, \Delta \mathbf{x}, \Delta \mathbf{v})] \\
 & + \frac{1}{2} \Delta \mathbf{x} \Delta \mathbf{x} : \frac{\partial^2}{\partial \mathbf{x} \partial \mathbf{x}} \cdot [f(\mathbf{x}, \mathbf{v}, t) \Psi(\mathbf{x}, \mathbf{v}, \Delta \mathbf{x}, \Delta \mathbf{v})] \\
 & + \frac{1}{2} \Delta \mathbf{v} \Delta \mathbf{v} : \frac{\partial^2}{\partial \mathbf{v} \partial \mathbf{v}} \cdot [f(\mathbf{x}, \mathbf{v}, t) \Psi(\mathbf{x}, \mathbf{v}, \Delta \mathbf{x}, \Delta \mathbf{v})] \\
 & \left. + \Delta \mathbf{x} \Delta \mathbf{v} : \frac{\partial^2}{\partial \mathbf{x} \partial \mathbf{v}} \cdot [f(\mathbf{x}, \mathbf{v}, t) \Psi(\mathbf{x}, \mathbf{v}, \Delta \mathbf{x}, \Delta \mathbf{v})] \right). \tag{2.5}
 \end{aligned}$$

Terms higher than second order may safely be ignored (Chandrasekhar 1943; Rosenbluth, MacDonald and Judd 1957).

We define the mean rates of change:

$$\begin{aligned}
 \left\langle \frac{\Delta \mathbf{v}}{\Delta t} \right\rangle &= \int_{\Delta \mathbf{x}} \int_{\Delta \mathbf{v}} \left(\frac{\Delta \mathbf{v}}{\Delta t} \right) \Psi(\mathbf{x}, \mathbf{v}, \Delta \mathbf{x}, \Delta \mathbf{v}) d\Delta \mathbf{x} d\Delta \mathbf{v}, \\
 \left\langle \frac{\Delta \mathbf{v} \Delta \mathbf{v}}{\Delta t} \right\rangle &= \int_{\Delta \mathbf{x}} \int_{\Delta \mathbf{v}} \left(\frac{\Delta \mathbf{v} \Delta \mathbf{v}}{\Delta t} \right) \Psi(\mathbf{x}, \mathbf{v}, \Delta \mathbf{x}, \Delta \mathbf{v}) d\Delta \mathbf{x} d\Delta \mathbf{v}. \tag{2.6}
 \end{aligned}$$

Similarly $\langle \Delta \mathbf{x} / \Delta t \rangle, \langle \Delta \mathbf{x} \Delta \mathbf{x} / \Delta t \rangle$.

$\Delta \mathbf{x}$ and $\Delta \mathbf{v}$ are integration variables and may be moved through the partial differentiation with respect to \mathbf{x} and \mathbf{v} . This then gives

Chapter II: The Equation

$$\begin{aligned}
 \frac{f(\mathbf{x}, \mathbf{v}, t + \Delta t) - f(\mathbf{x}, \mathbf{v}, t)}{\Delta t} &= -\frac{\partial}{\partial \mathbf{x}} \cdot \left[\left\langle \frac{\Delta \mathbf{x}}{\Delta t} \right\rangle f(\mathbf{x}, \mathbf{v}, t) \right] - \frac{\partial}{\partial \mathbf{v}} \cdot \left[\left\langle \frac{\Delta \mathbf{v}}{\Delta t} \right\rangle f(\mathbf{x}, \mathbf{v}, t) \right] \\
 &+ \frac{1}{2} \frac{\partial^2}{\partial \mathbf{x} \partial \mathbf{x}} : \left[\left\langle \frac{\Delta \mathbf{x} \Delta \mathbf{x}}{\Delta t} \right\rangle f(\mathbf{x}, \mathbf{v}, t) \right] + \frac{1}{2} \frac{\partial^2}{\partial \mathbf{v} \partial \mathbf{v}} : \left[\left\langle \frac{\Delta \mathbf{v} \Delta \mathbf{v}}{\Delta t} \right\rangle f(\mathbf{x}, \mathbf{v}, t) \right] \\
 &+ \frac{\partial^2}{\partial \mathbf{x} \partial \mathbf{v}} : \left[\left\langle \frac{\Delta \mathbf{x} \Delta \mathbf{v}}{\Delta t} \right\rangle f(\mathbf{x}, \mathbf{v}, t) \right] \\
 &= \frac{\partial f(\mathbf{x}, \mathbf{v}, t)}{\partial t} \Bigg|_{\text{Collisions}}.
 \end{aligned} \tag{2.7}$$

The path of an electron is continuous throughout a collision. Hence, in a time Δt , $\Delta \mathbf{v} = O(\Delta t)$, $\Delta \mathbf{x} = O(\Delta t^2)$, and to first order in the kinetic timescale Δt we can take

$$\left\langle \frac{\Delta \mathbf{x}}{\Delta t} \right\rangle = \left\langle \frac{\Delta \mathbf{x} \Delta \mathbf{x}}{\Delta t} \right\rangle = \left\langle \frac{\Delta \mathbf{x} \Delta \mathbf{v}}{\Delta t} \right\rangle = 0. \tag{2.8}$$

Then

$$\begin{aligned}
 \frac{\partial f(\mathbf{x}, \mathbf{v}, t)}{\partial t} \Bigg|_{\text{Collisions}} &= \\
 &= -\frac{\partial}{\partial \mathbf{v}} \cdot \left\langle \frac{\Delta \mathbf{v}}{\Delta t} \right\rangle f(\mathbf{x}, \mathbf{v}, t) + \frac{1}{2} \frac{\partial^2}{\partial \mathbf{v} \partial \mathbf{v}} : \left\langle \frac{\Delta \mathbf{v} \Delta \mathbf{v}}{\Delta t} \right\rangle f(\mathbf{x}, \mathbf{v}, t).
 \end{aligned} \tag{2.9}$$

Equation (2.9) is the formal expression for the collision terms and must be added to the Liouville Equation in order to give the Fokker-Planck Equation (Rosenbluth, MacDonald and Judd 1957). The result is:

$$\begin{aligned}
 \frac{\partial f(\mathbf{x}, \mathbf{v}, t)}{\partial t} + \mathbf{x} \cdot \frac{\partial f(\mathbf{x}, \mathbf{v}, t)}{\partial \mathbf{x}} + \dot{\mathbf{v}} \cdot \frac{\partial f(\mathbf{x}, \mathbf{v}, t)}{\partial \mathbf{v}} \\
 = -\frac{\partial}{\partial \mathbf{v}} \cdot \left\langle \frac{\Delta \mathbf{v}}{\Delta t} \right\rangle f(\mathbf{x}, \mathbf{v}, t) + \frac{1}{2} \frac{\partial^2}{\partial \mathbf{v} \partial \mathbf{v}} : \left\langle \frac{\Delta \mathbf{v} \Delta \mathbf{v}}{\Delta t} \right\rangle f(\mathbf{x}, \mathbf{v}, t).
 \end{aligned} \tag{2.10}$$

Chapter II: The Equation

The effects of collisions on the evolution of the beam are contained in the two terms on the right hand side. The first describes the slowing down of electrons owing to their sharing of their energy with the ambient plasma electrons. The second describes the diffusion of the beam electrons in velocity space. The slowing time and deflection time for suprathreshold electrons are of the same order of magnitude and are generally insensitive to the plasma temperature (Krall and Trivelpiece 1973, pp302).

The historical roots of the Fokker–Planck Equation can be traced back to 1891 when Lord Rayleigh studied the distribution function for heavy particles undergoing small velocity changes due to many collisions with light particles (Vasiček 1973). Einstein subsequently applied the method to Brownian motion in 1906. Einstein’s work was generalized in the years 1913 – 15 by Smoluchowski and paralleled by work in the years 1914 and 1917 by both Fokker and Planck. In 1940 it was realized that the Einstein–Smoluchowski Equation could be derived from the work by Fokker and Planck and from the 1950’s onwards the Fokker–Planck Equation has been applied to plasma calculations to obtain, among other things, energy exchange rates and relaxation times.

Before we evaluate the collision coefficients $\langle \Delta v / \Delta t \rangle$ and $\langle \Delta v \Delta v / \Delta t \rangle$, we can see what degrees of freedom the system has and express equation (2.10) in the form most natural to our problem. The electrons in the beam are constrained to move within a flare structure delineated by the magnetic field. The gyro-radius a of an electron is given by the expression (Jackson 1975, p581)

$$p_{\perp}(MeV/c) = 3 \times 10^{-4} B(Gauss) a(cm). \quad (2.11)$$

Chapter II: The Equation

If we take B as being of order 100 *Gauss*, we obtain

$$\begin{aligned} a &= 30 \text{ cm for a } 500 \text{ keV electron,} \\ &= 6.5 \text{ cm for a } 10 \text{ keV electron.} \end{aligned} \tag{2.12}$$

These distances of order tens of centimeters are generally much smaller than the size scales of the flare magnetic field variations. The electrons are, therefore, very efficiently tied to the magnetic field lines with any movement across the field lines being negligible. The position of an electron need then be given only in terms of the position of its guiding center along the field line, a distance s , say, from a reference point defined as $s = 0$. The guiding center approximation also means that the electron velocity \mathbf{v} has only two independent components. These we take to be the electron's total kinetic energy E (in units of $m_e c^2$) and the cosine of its pitch angle about the field line, μ . Our number distribution $f(\mathbf{x}, \mathbf{v}, t)$ thus becomes $f(E, \mu, s, t)$.

Another consideration with which we simplify the Fokker-Planck Equation comes from an inspection of the rise and fall times of hard X-ray bursts. The hard X-ray burst e-folding times are measured on timescales of a few seconds (de Jager and de Jonge 1978) and this may be assumed to be the timescale over which any variation in the total number of electrons present in the beam occurs[†]. The

[†]Recently there have been some reports of impulsive hard X-ray bursts having time structure measured in tens of milliseconds (Kiplinger *et al.* 1983). These are the fastest bursts ever reported though that has to be due to the fact that the instrument (HXRBS onboard the SMM satellite) has time resolution capabilities which far surpass any that were previously available (Orwig, Frost and Dennis 1980). These extremely fast events were clearly seen above the usual, more slowly varying X-ray components which were also present. These very fast spikes are rather rare and are not to be expected in all events; most of the events seen did not show time structure on scales of less than one second. These fast spikes may be due to small scale and short-lived structure in the loop magnetic field.

Chapter II: The Equation

interval for which any electron contributes to the beam is of the order of the time taken for that electron to travel the length of a coronal loop, a distance of, say, 10^9 cm. For electrons with energies sufficient to produce hard X-ray bursts, this timescale is of the order of 0.1 s or less. Therefore the beam evolutionary processes occur on timescales which are much less than the timescale over which the bursts normally rise and fall (Petrosian 1973). We take $\partial f(\mathbf{x}, \mathbf{v}, t) / \partial t$ to be small compared to the other terms in equation (2.10) and look for a steady state solution to the Fokker-Planck Equation.

We have $f(\mathbf{x}, \mathbf{v}, t) \equiv f(E, \mu, s)$, satisfying

$$\begin{aligned}
 \dot{s} \cdot \frac{\partial f(E, \mu, s)}{\partial s} + \dot{\mu} \cdot \frac{\partial f(E, \mu, s)}{\partial \mu} + \dot{E} \cdot \frac{\partial f(E, \mu, s)}{\partial E} = \\
 - \frac{\partial}{\partial \mu} \cdot \left\langle \frac{\Delta \mu}{\Delta t} \right\rangle f(E, \mu, s) - \frac{\partial}{\partial E} \cdot \left\langle \frac{\Delta E}{\Delta t} \right\rangle f(E, \mu, s) \\
 + \frac{1}{2} \frac{\partial^2}{\partial \mu^2} : \left\langle \frac{\Delta \mu \Delta \mu}{\Delta t} \right\rangle f(E, \mu, s) + \frac{1}{2} \frac{\partial^2}{\partial E^2} : \left\langle \frac{\Delta E \Delta E}{\Delta t} \right\rangle f(E, \mu, s) \\
 + \frac{\partial^2}{\partial \mu \partial E} : \left\langle \frac{\Delta \mu \Delta E}{\Delta t} \right\rangle f(E, \mu, s).
 \end{aligned} \tag{2.13}$$

The collision coefficients:

We shall now obtain the coefficients on the left hand side of equation (2.13). The homogeneous Fokker-Planck Equation (The Vlasov Equation) describes the collisionless evolution of the beam. The motion of an electron on a helical path about a magnetic field line involves no work being done on the electron ($\mathbf{v} \cdot (\mathbf{v} \times \mathbf{B}) \equiv 0$). Therefore $\dot{E} \equiv 0$. s is the velocity of the electron parallel to

Chapter II: The Equation

the field lines and is equal to $\mu v(E)$. The only agent (not including collisions) contributing to $\dot{\mu}$ is the convergence of the magnetic field; *i.e.*,

$$\dot{\mu} = \frac{d\mu}{dB} \cdot \frac{dB}{ds} \cdot \frac{ds}{dt}. \quad (2.14)$$

The adiabatic invariance of the electron's motion gives $(1 - \mu^2)/B = \text{constant}$.

Hence

$$\frac{d\mu}{dB} = \frac{1 - \mu^2}{-2\mu B} \quad (2.15)$$

and

$$\dot{\mu} = \frac{v \mu (1 - \mu^2)}{-2\mu B} \cdot \frac{dB}{ds} = -v \frac{(1 - \mu^2)}{2} \cdot \frac{d \ln B}{ds}. \quad (2.16)$$

The homogeneous (collisionless) equation would then be

$$v \mu \frac{\partial f(E, \mu, s)}{\partial s} - v \frac{(1 - \mu^2)}{2} \cdot \frac{d \ln B}{ds} \cdot \frac{\partial f(E, \mu, s)}{\partial \mu} = 0. \quad (2.17)$$

We need now to calculate the collision coefficients $\langle \Delta v / \Delta t \rangle$ and $\langle \Delta v \Delta v / \Delta t \rangle$. For this we need an expression for $\Psi(\mathbf{x}, \mathbf{v}, \Delta \mathbf{x}, \Delta \mathbf{v})$ which is now $\Psi(\mathbf{v}, \Delta \mathbf{v})$ under the elementary assumption that the collision mechanism in no way depends upon the particular location of the beam electron within the flare loop.

Figure (2.1) portrays schematically the collisional process in the rest frame of the test particle. The test electron sees the field particles streaming toward it with an average velocity $|\mathbf{v}|$. Because we treat the field plasma as being cold we may consider all the field particles to be approaching the test particle with the same velocity $|\mathbf{v}|$. The scattering cross-section $\sigma(\theta, v)$ in this frame is the probability of

Chapter II: The Equation

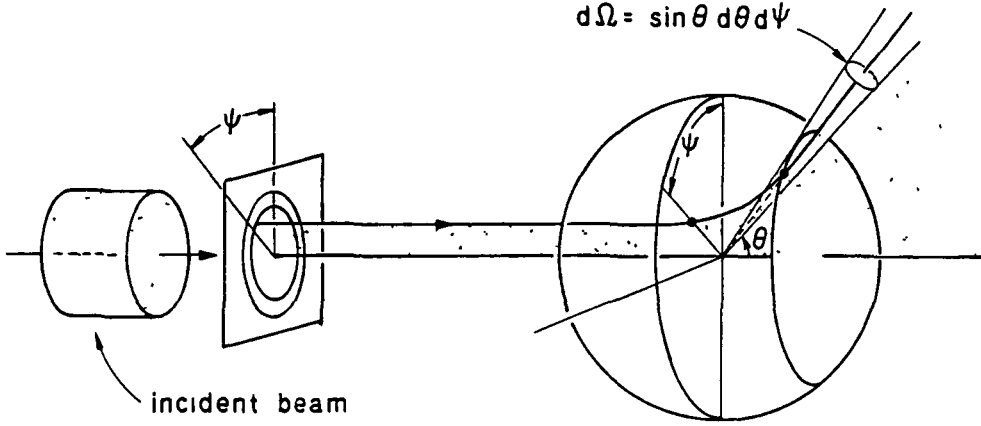


Figure 2.1. A schematic representation of the Coulomb collision process in the rest frame of the test particle (Taken from Liboff 1969, p193). Shown is θ , the angle of scattering for a field particle with impact parameter b .

a field particle at a distance b being scattered through an angle θ Hence,

$$b db d\psi = \sigma(\theta, v) d\Omega(\theta, \psi). \quad (2.18)$$

A field particle which is scattered into solid angle $d\Omega$ about (θ, ψ) gives an impulse $\{\Delta v\}$ to the test particle. The mean rate of change of v is given by the accumulated effect of the impulses from all the field particles, *i.e.*, by an integration over all b, ψ or all θ, ψ . Hence,

$$\left\langle \frac{\Delta v}{\Delta t} \right\rangle = \frac{1}{\Delta t} \int_{\Omega} v n \{\Delta v\} \sigma(\theta, v) d\Omega(\theta, \psi) \quad (2.19)$$

and

$$\left\langle \frac{\Delta v \Delta v}{\Delta t} \right\rangle = \frac{1}{\Delta t} \int_{\Omega} v n \{\Delta v \Delta v\} \sigma(\theta, v) d\Omega(\theta, \psi) \quad (2.20)$$

Chapter II: The Equation

where $\{\Delta \mathbf{v}\}$ and $\{\Delta \mathbf{v} \Delta \mathbf{v}\}$ correspond to the impulses from individual collisions. If the ambient plasma contains several constituents, we should add the effects of each. Then

$$\left\langle \frac{\Delta \mathbf{v}}{\Delta t} \right\rangle = \sum_i \frac{1}{\Delta t} \int_{\Omega} \mathbf{v} n_i \{\Delta \mathbf{v}\}_i \sigma_i(\theta, \mathbf{v}) d\Omega(\theta, \psi) \quad (2.21)$$

where the subscript i denotes quantities pertaining to particles of type i .

The cross-sections to be used are the fully relativistic Coulomb collision cross-sections for electrons on free electrons (Møller 1932; Evans 1955, p577; MacDonald and Walt 1961), for electrons on protons (Mott and Massey 1949; Evans 1955, p593), and for electrons on neutral atoms, predominantly Hydrogen and Helium (Snyder and Scott 1949).

As an example of how the collision terms are calculated, we shall demonstrate the evaluation of $\langle \Delta \mu / \Delta t \rangle$ for electron-proton collisions. The other collision terms all follow suit. We need two things: an expression for $\{\Delta \mu\}$ and a cross-section. The cross-section for electron-proton collisions is given by Evans as

$$\sigma(\theta, v) = \frac{1}{4} \left(\frac{e^2}{m_e c^2} \right)^2 \cdot \frac{1 - \beta^2 \sin^2(\theta/2) + \alpha \pi \beta (1 - \sin(\theta/2)) \sin(\theta/2)}{\gamma^2 \beta^4 (\sin^4(\theta/2))} \quad (2.22)$$

where θ is the scattering angle in both the lab frame and the center-of-mass frame owing to the fact that $m_p/m_e \gg 1$. α is the fine structure constant, approximately equal to 1/137.

$\{\Delta \mu\}$ is the change in the test particle's pitch angle cosine due to scattering in a direction θ, ψ about the incoming direction. Owing to the coincidence of the

Chapter II: The Equation

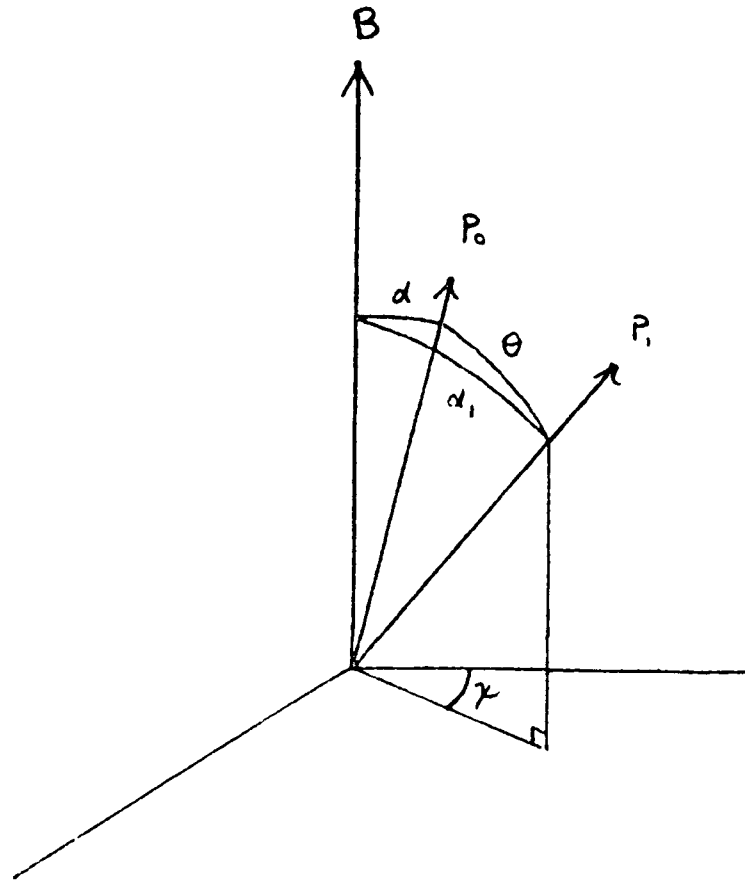


Figure 2.2. A schematic representation of the Coulomb collision process in the rest frame of the field particles. Shown are the magnetic field direction \mathbf{B} , the instantaneous direction of the incoming electron \mathbf{p}_0 and the instantaneous direction of the outgoing electron \mathbf{p}_1 . $\mathbf{B} \cdot \mathbf{p}_0 = \cos \alpha = \mu$, $\mathbf{B} \cdot \mathbf{p}_1 = \cos \alpha_1 = \mu_1$ and $\mathbf{p}_0 \cdot \mathbf{p}_1 = \cos \theta$

lab and center-of-mass frames, it is a straightforward exercise to obtain $\Delta\mu$. For electron-electron collisions we have to transform into the center-of-mass frame, follow through the collision and then transform back into the lab frame, a sequence which is more tedious than it is instructive.

Chapter II: The Equation

The coordinates for the scattering of electrons off protons are shown in Figure (2.2). The initial pitch angle cosine is $\mu = \cos \alpha$. The final pitch angle cosine is $\mu_1 = \cos \alpha_1$. From the geometry of the collision,

$$\cos \alpha_1 = \cos \alpha \cos \theta + \sin \alpha \sin \theta \cos(\pi - \psi), \quad (2.23)$$

giving

$$\mu_1 = \mu \cos \theta - (1 - \mu^2)^{1/2} \sin \theta \cos \psi. \quad (2.24)$$

Hence,

$$\{\Delta\mu\} = \mu_1 - \mu = \mu (\cos \theta - 1) - (1 - \mu^2)^{1/2} \sin \theta \cos \psi \quad (2.25)$$

(*cf.* MacDonald and Walt 1961). Performing the integration over ψ in equation (2.19) leaves

$$\begin{aligned} \left\langle \frac{\Delta\mu}{\Delta t} \right\rangle &= \frac{\mu v n_p}{\gamma^2 \beta^4} \cdot \frac{r_0^2}{4} \cdot \frac{1}{\Delta t} \int_{\theta_{\min}} (\cos \theta - 1) \sin \theta \\ &\quad \times \frac{1 - \beta^2 \sin^2(\theta/2) + \alpha \pi \beta (1 - \sin(\theta/2)) \sin(\theta/2)}{\sin^4(\theta/2)} \cdot d\theta \end{aligned} \quad (2.26)$$

where θ_{\min} is the smallest angle of scattering and corresponds to field particles at the screening distance λ . We keep only the dominant terms which are those terms which integrate to contain the Coulomb logarithm $\ln \Lambda \simeq -\ln \theta_{\min}$. The ratio between dominant and sub-dominant terms is of the order of $\ln \Lambda$ which has a value of $\sim 20 - 30$. This allows us to drop the sub-dominant, non-divergent terms

Chapter II: The Equation

(Spitzer 1962). Hence, we arrive at

$$\begin{aligned} \left\langle \frac{\Delta\mu}{\Delta t} \right\rangle &= \frac{\mu v n_p}{\beta^4 \gamma^2} \cdot \frac{r_0^2}{4} \cdot \frac{1}{\Delta t} \int_{\theta_{\min}} (\cos \theta - 1) \frac{\sin \theta}{\sin^4(\theta/2)} \cdot d\theta \\ &= -\frac{4\pi r_0^2}{\beta^4 \gamma^2} \cdot \frac{\mu v}{\Delta t} \cdot n_p \ln \Lambda. \end{aligned} \quad (2.27)$$

The Coulomb logarithm:

The Coulomb logarithm is $\ln \Lambda = \ln(\theta_{\min}/\theta_{\max})^{-1}$. θ_{\max} corresponds to large angle scattering off the few nearby field particles and is of the order of one radian. Its exact value need not be precisely evaluated because the value of θ_{\min} is so very uncertain. θ_{\min} corresponds to the maximum value of the impact parameter which is often taken to be the Debye length λ_D (Cohen, Spitzer and McRoutly 1950). The use of λ_D for the screening length is rigorous only for a plasma in thermal equilibrium and it would not normally be appropriate for a suprathermal beam of electrons passing through a relatively cold plasma. Spitzer (1962) quotes Marshak (1941) who gives the correction for a relativistic plasma, and offers the form

$$\ln \Lambda = \ln \left[\frac{3}{2e^3} \cdot \left(\frac{k^3 T^3}{\pi n_e} \right)^{1/2} \cdot \frac{2\alpha}{\beta} \right] \quad (2.28)$$

where T and n_e are the plasma temperature and electron number density, and $\beta = v/c$ for the fast electron. Again, α is the fine structure constant.

The applicability of this form could well be challenged but the uncertainty all around is large. Spitzer (1962) quotes observational agreement with this form for

Chapter II: The Equation

$\ln \Lambda$, though he suggests that this agreement may be a little fortuitous. Another form for $\ln \Lambda$ is given by Ginzburg and Syrovat'skii (1964) for cosmic rays passing through a detector and has been applied to the solar flare problem by Syrovat'skii and Shmeleva (1972) and Petrosian (1973). This form is

$$\ln \Lambda = \frac{1}{2} \ln \left[(2\pi)^3 \beta^4 \gamma / \left(\pi \alpha n (h/m_e c)^3 \right) \right]. \quad (2.29)$$

This form agrees, to within a constant of order unity inside the logarithm, with the form quoted by Spitzer, and is the form preferred here.

The full results, including collisions with protons, electrons, Hydrogen, and Helium are

$$\begin{aligned} \left\langle \frac{\Delta \mu}{\Delta t} \right\rangle &= -\mathcal{A} \mu v \left(n_e \ln \Lambda + n_p \ln \Lambda + n_H \ln \Lambda''_H + 4n_{He} \ln \Lambda''_{He} \right) \\ \left\langle \frac{\Delta \mu \Delta \mu}{\Delta t} \right\rangle &= \mathcal{A} (1 - \mu^2) v \left(n_e \ln \Lambda + n_p \ln \Lambda + n_H \ln \Lambda''_H + 4n_{He} \ln \Lambda''_{He} \right) \\ \left\langle \frac{\Delta E}{\Delta t} \right\rangle &= -\mathcal{A} v (\gamma^2 - 1) \left(n_e \ln \Lambda + n_H \ln \Lambda'_H + 2n_{He} \ln \Lambda'_{He} \right) \end{aligned} \quad (2.30)$$

with $\mathcal{A} = 4\pi r_0^2 / \beta^4 \gamma^2$ and

$$\begin{aligned} (\Lambda')^2 &= \beta^2 \gamma^2 (\gamma - 1) / I^2 && \text{(Evans 1955, p581)} \\ (\Lambda'')^2 &= \beta^2 \gamma^2 / 2Z^{2/3} \alpha^2 && \text{(Snyder and Scott 1949).} \end{aligned} \quad (2.31)$$

Here I is the ionization energy of either Hydrogen or Helium in units of $m_e c^2$ and Z is the atomic number (1 for Hydrogen and 2 for Helium). α is the fine structure constant. Typical values for these $\ln \Lambda$'s are expressed in Table I for $n_e = 10^9 \text{ cm}^{-3}$.

Chapter II: The Equation

Table I

Some typical values for the collision logarithms.

$E (keV)$	$\ln \Lambda$	$\ln \Lambda'_H$	$\ln \Lambda'_{He}$	$\ln \Lambda''_H$	$\ln \Lambda''_{He}$
20	24.9	7.82	6.53	3.31	3.08
100	26.4	9.46	8.18	4.15	3.92
500	27.5	11.2	9.94	5.11	4.88

Let us define two collision coefficients C_1 and C_2 as

$$\begin{aligned}
 C_1 &= 2\pi r_0^2 \left(n_e \ln \Lambda + n_H \ln \Lambda'_H + 2n_{He} \ln \Lambda'_{He} \right) \\
 \text{and} & \\
 C_2 &= 2\pi r_0^2 \left(n_e \ln \Lambda + n_p \ln \Lambda + n_H \ln \Lambda''_H + 4n_{He} \ln \Lambda''_{He} \right).
 \end{aligned} \tag{2.32}$$

Our equation (2.13) becomes

$$\begin{aligned}
 \mu v \frac{\partial f(E, \mu, s)}{\partial s} - \frac{v(1-\mu^2)}{2} \cdot \frac{d \ln B}{ds} \cdot \frac{\partial f(E, \mu, s)}{\partial \mu} = \\
 \frac{\partial}{\partial E} \left(\frac{2C_1 v}{\beta^2} f(E, \mu, s) \right) + \frac{2C_2 v}{\beta^4 \gamma^2} \frac{\partial}{\partial \mu} \left(\mu f(E, \mu, s) \right) + \frac{C_2 v}{\beta^4 \gamma^2} \frac{\partial^2}{\partial \mu^2} \left((1-\mu^2) f(E, \mu, s) \right)
 \end{aligned} \tag{2.33}$$

We can simplify this by using the relationships

Chapter II: The Equation

$$\frac{\partial}{\partial \mu} \left(\mu f(E, \mu, s) \right) + \frac{1}{2} \frac{\partial^2}{\partial \mu^2} \left((1 - \mu^2) f(E, \mu, s) \right) = \frac{1}{2} \frac{\partial}{\partial \mu} \left((1 - \mu^2) \frac{\partial f(E, \mu, s)}{\partial \mu} \right) \quad (2.34)$$

and

$$\frac{\partial}{\partial E} \left(\frac{2C_1 v}{\beta^2} f(E, \mu, s) \right) = \frac{2v}{\beta} \frac{\partial}{\partial E} \left(\frac{C_1 f(E, \mu, s)}{\beta} \right). \quad (2.35)$$

Our equation, in its final form, is then

$$\begin{aligned} \mu \frac{\partial f(E, \mu, s)}{\partial s} &= \frac{(1 - \mu^2)}{2} \cdot \frac{d \ln B}{ds} \cdot \frac{\partial f(E, \mu, s)}{\partial \mu} \\ &+ \frac{2}{\beta} \frac{\partial}{\partial E} \left(\frac{C_1 f(E, \mu, s)}{\beta} \right) + \frac{C_2}{\beta^4 \gamma^2} \frac{\partial}{\partial \mu} \left((1 - \mu^2) \frac{\partial f(E, \mu, s)}{\partial \mu} \right). \end{aligned} \quad (2.36)$$

This is the Fokker-Planck Equation in the form in which we use it. In the next chapter we shall solve it numerically to obtain the number distribution at each point in E, μ, s space. Ultimately we intend to use the electron number distribution to calculate the X-rays produced by the electrons in the beam. We can also attempt to solve this equation analytically, and in that way get a feel for how the solution behaves. In the next chapter we shall explain the method used to obtain the solution to equation (2.36) using the computer, and shall look at ways of checking that the numerical solution bears a good resemblance to the full analytic solution even though we do not have available an expression for that solution. We can approximate this full solution by obtaining the analytic solution to an equation which closely resembles equation (2.36), and this we do. Trusting that, if performed accurately, the analytic solution to the approximate equation and the numerical solution to the full equation will both resemble the unavailable analytic solution to the full equation, we compare the two solutions to see how much of a likeness they share.

Chapter III

Solving the equation both analytically and numerically

This chapter contains three sections. In § 3.1 we investigate the behavior of equation (2.36), the equation describing the evolution of the electron beam within the flaring plasma. From equation (2.36) we create three two-term “reduced” equations, each comprising the spatial derivative and one of the other three terms. Two of these reduced equations are easily solved. The third one contains the second order derivative in μ , and it is this term which prevents us from obtaining analytic solutions to the third reduced equation or to equation (2.36). We replace the second order derivative term by another term which has approximately the same behavior but which allows analytic solutions to be found. In this manner, therefore, we are able to obtain analytic solutions not to equation (2.36) but to an equation which approximates it.

Given that equation (2.36) cannot itself be solved analytically, we obtain its solutions numerically. In § 3.2 we give a schematic outline of the adopted numerical scheme and then we use the reduced equation solutions to test the scheme’s accuracy. In § 3.3 we give some numerical results pertaining to the evolution of the electron beam within the flaring plasma. These results are valuable

Chapter III: Solving the equation

in and of themselves and are an essential step to obtaining the X-ray results, for they allow simple expressions describing the beam evolution based upon the results of the full Fokker–Planck treatment. Understanding these electron results is prerequisite to understanding the X-ray results to be presented in later chapters. Also in this section, we compare our numerical results with the solution to the equation we obtained by approximating equation (2.36). This comparison helps us to understand the numerical results and shows the accuracy and usefulness of the approximate solution.

3.1 The reduced and approximate equations.

a) $C_1 = C_2 = 0$

We shall now investigate the behavior of equation (2.36). Let us consider first our Fokker–Planck Equation without the collision terms. This situation corresponds to the limit of very low plasma density when the evolution of the electron beam is determined only by the magnetic field structure. We have

$$\mu \frac{\partial f(E, \mu, s)}{\partial s} = \frac{(1 - \mu^2)}{2} \cdot \frac{d \ln B}{ds} \cdot \frac{\partial f(E, \mu, s)}{\partial \mu}. \quad (3.1.1)$$

In this case, the function $f(E, \mu, s)$ is independent of the electron energy and we can drop E as an explicit variable. We define

$$\bar{s} = \int_0^s \frac{d \ln B}{ds} ds = \ln \left(B(s)/B(0) \right). \quad (3.1.2)$$

Chapter III: Solving the equation

The distribution function then satisfies

$$\frac{\partial f(\mu, s)}{\partial \bar{s}} = -\frac{\partial f(\mu, s)}{\partial \ln(1 - \mu^2)} \quad (3.1.3)$$

over surfaces of constant E , and for $s \geq 0$ and $|\mu| < 1$. The characteristic curves for equation (3.1.3) are

$$\bar{s} - \ln(1 - \mu^2) = C \quad (3.1.4)$$

for constant C , and they show the invariance of $B/(1 - \mu^2)$ along an electron's trajectory. We specify initial values for the distribution function along the strip $s = \bar{s} = 0$, $1 > \mu \geq 0$ of the form $f(\mu, 0) = G_0(\mu)$, where $G_0(\mu)$ can be any function of our choice. Our solution becomes

$$f(\mu, s) = G_0 \left(\left[1 - (1 - \mu^2) \exp(-\bar{s}) \right]^{1/2} \right), \quad (3.1.5)$$

or

$$f(\mu, s) = G_0 \left(\left[1 - (1 - \mu^2) \frac{B(0)}{B(s)} \right]^{1/2} \right). \quad (3.1.6)$$

which is equivalent. This is the solution to the first of our reduced equations and shows that, if an electron's pitch angle is known at $s = 0$, then its pitch angle is known for all $s > 0$. The converse also holds, but note that we assumed that the magnetic field strength does not decrease as s increases. If $B(s) < B(0)$ for any $s > 0$, then not all values of μ are accessible. Note also that the solution is symmetric with respect to the reflection $\mu \rightarrow -\mu$.

Chapter III: Solving the equation

b) $d \ln B/ds = C_2 = 0$

Now we set $d \ln B/ds$ equal to zero and discard the term which describes the collisionally driven pitch angle diffusion. Retaining one collision term without the other means that this reduced equation does not describe a physical situation, though this will not hinder our finding its solution. We use this solution later to check the numerical code and to describe the evolution of the electron beam at sufficiently large depths by which the pitch angle distribution of the beam has relaxed to one which keeps the diffusion term small. We have, from equation (2.36),

$$\mu \frac{\partial f(E, \mu, s)}{\partial s} = \frac{2}{\beta} \frac{\partial}{\partial E} \left(\frac{C_1 f(E, \mu, s)}{\beta} \right), \quad (3.1.7)$$

or, rather

$$\mu \frac{\partial \phi(E, \mu, s)}{\partial s} = \frac{2C_1}{\beta^2} \frac{\partial \phi(E, \mu, s)}{\partial E}, \quad (3.1.8)$$

where we have used the definition

$$\phi(E, \mu, s) = f(E, \mu, s) / \beta \quad (3.1.9)$$

and the fact that the relative energy dependence of C_1 is slight. We now create two new independent variables. Let

$$d\eta = \beta^2 dE. \quad (3.1.10)$$

This integrates to give

$$\eta = \frac{E^2}{E + 1}. \quad (3.1.11)$$

Also, let

$$d\tau = 2C_1 ds. \quad (3.1.12)$$

Chapter III: Solving the equation

τ is then a collisional depth as measured along the magnetic field lines. Equation (3.1.8) now reads

$$\mu \frac{\partial \phi(E, \mu, s)}{\partial \tau} = \frac{\partial \phi(E, \mu, s)}{\partial \eta}. \quad (3.1.13)$$

The characteristics of equation (3.1.13) are the family of curves

$$\eta + \tau/\mu = C \quad (3.1.14)$$

for constant C . τ/μ is the collisional depth experienced by an electron which does not move parallel to the field lines but which has a pitch angle $\cos^{-1}\mu$. These characteristic curves describe approximately the rate at which an electron loses energy in passing down the flare loop, if μ is an average pitch angle taken along the electron's trajectory. They show that an electron starting with an energy E can penetrate through a depth $\tau = \mu\eta(E)$ of plasma, and that, at each depth $\tau' < \tau$, the electron has left an amount of energy E' where E' is the solution of

$$\eta(E') = \frac{E'^2}{E' + 1} = \frac{E^2}{E + 1} - \frac{\tau'}{\mu}. \quad (3.1.15)$$

The curves (3.1.14) are the relativistic extensions of the familiar expressions for the range of a beam electron, as given by Syrovat'skii and Shmeleva (1972, equation 6); Brown (1972, equation 7) and Emslie (1978, equation 24a). In Figure (3.1) we show the energy that an electron has at each depth, as given by equation (3.1.15) with $\mu = 1$. As we can see by the shape of the curves, once an electron has lost a significant fraction of its energy it stops thereafter very rapidly.

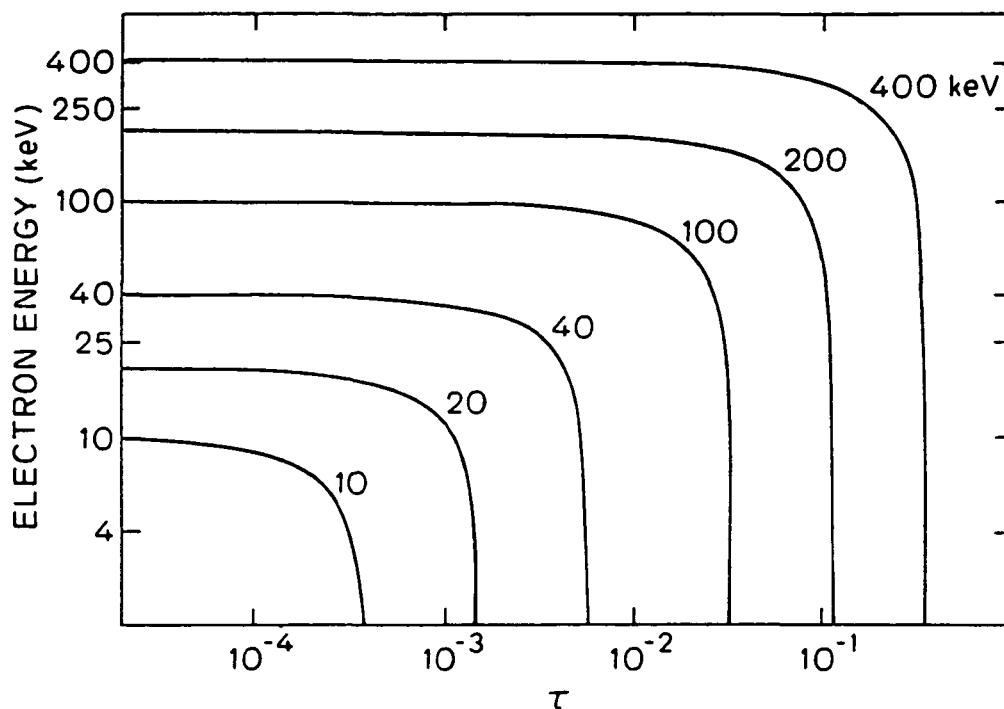


Figure 3.1. The rate at which electrons lose energy as a function of penetration depth within the flare plasma. The curves are obtained from equation (3.1.15) with τ defined by equation (3.1.12) and with $\mu = 1$.

If, for equation (3.1.13), we specify the initial values $\phi(\eta, \mu, 0) = \phi_0(\eta)\psi(\mu)$ for arbitrary functions ϕ_0 and ψ , our solution is

$$\phi(\eta, \mu, \tau) = \phi_0\left(\eta + \frac{\tau}{\mu}\right)\psi(\mu). \quad (3.1.16)$$

Again, we use this solution below when we check the accuracy of the numerical code.

Chapter III: Solving the equation

$$\text{c) } d \ln B/ds = C_1 = 0$$

Finally, we set $d \ln B/ds$ equal to zero and this time discard the term that describes the energy degradation of the electrons. From equation (2.36) we obtain

$$\mu \frac{\partial f(E, \mu, s)}{\partial s} = \frac{C_2}{\beta^4 \gamma^2} \frac{\partial}{\partial \mu} \left((1 - \mu^2) \frac{\partial f(E, \mu, s)}{\partial \mu} \right). \quad (3.1.17)$$

Again, only half the collisional effects are included, making the situation described by the solution unphysical. We show that the second order term which forms the right hand side of equation (3.1.17) can be approximated in such a way as to allow analytic solutions to the Fokker-Planck Equation. In these solutions, the pitch angle evolution of the electron beam is separated from its energy evolution. That this treatment gives an accurate description of the beam is borne out by our full numerical results. In this case, equation (3.1.17) provides a good description of the pitch angle evolution alone.

We define $d\tau = C_2 ds/\beta^4 \gamma^2$ and drop the explicit energy variable E . This leaves

$$\frac{\partial f(\mu, s)}{\partial \tau} = \frac{1}{\mu} \frac{\partial}{\partial \mu} \left((1 - \mu^2) \frac{\partial f(\mu, s)}{\partial \mu} \right). \quad (3.1.18)$$

Solutions to equation (3.1.18) can be obtained if we replace its right hand side by another term which, for the most part, has very similar behavior. This replacement term is obtained from the small pitch angle approximations $\mu \simeq 1$ and $1 - \mu^2 = (1 + \mu)(1 - \mu) \simeq 2(1 - \mu)$. Let us write $2(1 - \mu) = x^2$. The new variable x is then approximately equal to the pitch angle α . In equation (3.1.18) $-\partial/\partial \mu$ is replaced

Chapter III: Solving the equation

by $(1/x)\partial/\partial x$ and we obtain

$$\frac{\partial f(\mu, s)}{\partial \tau} = \frac{1}{x} \frac{\partial}{\partial x} \left(x \frac{\partial f(\mu, s)}{\partial x} \right). \quad (3.1.19)$$

The zeroeth order Bessel function $J_0(wx)$ satisfies

$$-w^2 J_0(wx) = \frac{1}{x} \frac{\partial}{\partial x} \left(x \frac{\partial J_0(wx)}{\partial x} \right). \quad (3.1.20)$$

Any solution to equation (3.1.19) may, therefore, be written as an expression in the Bessel functions $J_0(wx)$. A completely general expression is

$$f(\mu, s) = \int_0^{\infty} e^{-w^2 \tau} A(w) J_0(wx) dw. \quad (3.1.21)$$

$A(w)$ is a weighting term and is determined by the boundary conditions at $\tau = s = 0$.

Because we have used a small pitch angle approximation, we specify initial values which fall rapidly with increasing x away from zero. A suitable function is

$$f(\mu, 0) = f_0(x) = \frac{2}{x_0^2} \exp(-x^2/x_0^2). \quad (3.1.22)$$

We obtain $A(w)$ by solving equation (3.1.21) at $\tau = 0$:

$$\frac{2}{x_0^2} \exp(-x^2/x_0^2) = \int_0^{\infty} A(w) J_0(wx) dw. \quad (3.1.23)$$

This is satisfied by

$$A(w) = w \exp(-w^2 x_0^2/4) \quad (3.1.24)$$

Chapter III: Solving the equation

(Abramowitz and Stegun 1970). This, when put back into equation (3.1.21), gives

$$f(\mu, s) = \frac{2}{(4\tau + x_0^2)} \exp\left(-x^2/(4\tau + x_0^2)\right) \quad (3.1.25)$$

(Abramowitz and Stegun 1970) as the solution to equation (3.1.19). We see from equation (3.1.25) another reason why the form (3.1.22) was considered a suitable initial function. An electron beam which is initially Gaussian in pitch angle broadens with increasing depth and yet remains Gaussian throughout. We show later that this is a good general description of the beam evolution when we describe some of the numerical results to the full Fokker–Planck Equation.

$$\mathbf{d)} \quad d \ln B/ds = 0, \quad C_1 = C_2 = 2\pi r_0^2 n_e \ln \Lambda$$

We now apply our experience with the reduced equations to an examination of the Fokker–Planck Equation. We obtain a solution not to equation (2.36) but to another equation which is almost identical to it at small values of the pitch angle, repeating the procedure we found to be successful above.

We begin with

$$\mu \frac{\partial f(E, \mu, s)}{\partial s} = \frac{C_2}{\beta^4 \gamma^2} \frac{\partial}{\partial \mu} \left((1 - \mu^2) \frac{\partial f(E, \mu, s)}{\partial \mu} \right) + \frac{2}{\beta} \frac{\partial}{\partial E} \left(\frac{C_1 f(E, \mu, s)}{\beta} \right) \quad (3.1.26)$$

which is equation (2.36) with $d \ln B/ds$ set to zero. C_1 and C_2 may safely be taken to be independent of the electron's energy.

We define $d\tau = 4\pi r_0^2 n_e \ln \Lambda ds$ (*cf.* the definitions of C_1 and C_2 in Chapter II, equation (2.32)) and recall the definitions of ϕ and η given by equations (3.1.9)

Chapter III: Solving the equation

and (3.1.11). We rewrite equation (3.1.26) in the form

$$\mu \frac{\partial \phi}{\partial \tau} - \frac{\partial \phi}{\partial \eta} = \frac{1}{\beta^4 \gamma^2} \frac{\partial}{\partial \mu} \left((1 - \mu^2) \frac{\partial \phi}{\partial \mu} \right). \quad (3.1.27)$$

Using our small pitch angle approximation, this becomes

$$\beta^4 \gamma^2 \left(\frac{\partial \phi}{\partial \tau} - \frac{\partial \phi}{\partial \eta} \right) = \frac{1}{x} \frac{\partial}{\partial x} \left(x \frac{\partial \phi}{\partial x} \right). \quad (3.1.28)$$

Following our previous method, we look for a solution of the type

$$\phi(\eta, x, \tau) = \int_{w=0}^{\infty} g(w, \eta, \tau) J_0(wx) dw. \quad (3.1.29)$$

This requires that we solve

$$\beta^4 \gamma^2 \left(\frac{\partial g}{\partial \tau} - \frac{\partial g}{\partial \eta} \right) = -w^2 g. \quad (3.1.30)$$

We define $d\rho/d\eta = \beta^4 \gamma^2$ and obtain, modulo an integration constant,

$$\rho(\eta) = \frac{1}{2} \ln \left(\frac{E}{E+2} \right). \quad (3.1.31)$$

This gives

$$\beta^4 \gamma^2 \cdot \left(\frac{\partial g}{\partial \tau} \right) = -w^2 g + \frac{\partial g}{\partial \rho} = e^{w^2 \rho} \frac{\partial}{\partial \rho} \left(e^{-w^2 \rho} g \right), \quad (3.1.32)$$

which can be written

$$\frac{\partial}{\partial \tau} \left(e^{-w^2 \rho} g \right) = \frac{\partial}{\partial \eta} \left(e^{-w^2 \rho} g \right). \quad (3.1.33)$$

Let

$$g(w, \eta, \tau) = e^{w^2 \rho(\eta)} Z(w, \eta + \tau) \quad (3.1.34)$$

Chapter III: Solving the equation

where $Z(w, \eta + \tau)$ is any function of w and $\eta + \tau$ and is determined by the boundary conditions. We write the solution (3.1.29) in the form

$$\phi(\eta, x, \tau) = \int_{w=0}^{\infty} e^{w^2 \rho(\eta)} Z(w, \eta + \tau) J_0(wx) dw. \quad (3.1.35)$$

If we inject

$$\phi(\eta, x, 0) = \frac{2\phi_0(\eta)}{x_0^2} \exp\left(-x^2/x_0^2\right) \quad (3.1.36)$$

for any $\phi_0(\eta)$, we obtain (from equation (3.1.35) with $\tau = 0$)

$$Z(w, \eta) = w \phi_0(\eta) \exp\left(-w^2\left(\frac{x_0^2}{4} + \rho(\eta)\right)\right). \quad (3.1.37)$$

Putting this back into equation (3.1.35),

$$\phi(\eta, x, \tau) = \phi_0(\eta + \tau) \cdot \frac{2}{x_0^2 + \zeta(\eta + \tau)} \exp\left(-\frac{x^2}{x_0^2 + \zeta(\eta + \tau)}\right) \quad (3.1.38)$$

is the solution to (3.1.28), where

$$\zeta(\eta + \tau) = 4\left(\rho(\eta + \tau) - \rho(\eta)\right). \quad (3.1.39)$$

Equation (3.1.28) is an approximation to the Fokker-Planck Equation in the form (3.1.26), and its solution is the function (3.1.38). We needed to know whether or not (3.1.38) is close to the solution of equation (3.1.26) beyond the small pitch angle regime, for if it is, we would have, in equation (3.1.38), a very useful function for the further study of the electron beam dynamics. This expression describes the pitch angle evolution of the beam as well as the evolution of its energy spectrum,

Chapter III: Solving the equation

and both in very simple and manageable forms making their application most simple.

The next step was to obtain the solutions to the full Fokker-Planck Equation with the $d \ln B/ds$ term retained. Since we could not solve it analytically, we had to obtain its solutions numerically. These numerical results were then used for later calculations of the X-rays emitted by the electrons in the beam. We also used the numerical results to discover just how well equation (3.1.38) describes the beam over the full range of E , μ and τ and, hence, to find out how useful (3.1.38) can be.

3.2 The numerical treatment.

The equation we wish to solve is (*cf.* equation (2.36))

$$\begin{aligned} \mu \frac{\partial f(E, \mu, s)}{\partial s} = & \frac{(1 - \mu^2)}{2} \cdot \frac{d \ln B}{ds} \cdot \frac{\partial f(E, \mu, s)}{\partial \mu} \\ & + \frac{2}{\beta} \frac{\partial}{\partial E} \left(\frac{C_1 f(E, \mu, s)}{\beta} \right) + \frac{C_2}{\beta^4 \gamma^2} \frac{\partial}{\partial \mu} \left((1 - \mu^2) \frac{\partial f(E, \mu, s)}{\partial \mu} \right). \end{aligned} \quad (3.2.1)$$

This equation is linear, is first order in the derivatives of both E and s , and is second order in the derivatives of μ . In order to construct a numerical scheme for solving this equation we can use the natural properties of the physical system to our advantage. Electrons are able to travel in both directions in s space (both up and down the flare loop) but they can only travel in one direction in E space. In our paradigm, there is no mechanism by which an electron can be accelerated to higher

Chapter III: Solving the equation

values of E . We can use this by rewriting equation (3.2.1) with the derivative in E on the left hand side and by using the electron energy as the stepping variable by which we march forward (downward in E) over the three dimensional surface containing the solution.

We recall the definition $\phi(E, \mu, s) = f(E, \mu, s) / \beta(E)$. Equation (3.2.1) becomes

$$\begin{aligned} \frac{\partial}{\partial E} \left(2C_1 \phi(E, \mu, s) \right) = & \mu \beta^2 \frac{\partial \phi(E, \mu, s)}{\partial s} - \frac{(1 - \mu^2)}{2} \cdot \frac{d \ln B}{ds} \cdot \beta^2 \frac{\partial \phi(E, \mu, s)}{\partial \mu} \\ & - \frac{C_2}{\beta^2 \gamma^2} \frac{\partial}{\partial \mu} \left((1 - \mu^2) \frac{\partial \phi(E, \mu, s)}{\partial \mu} \right). \end{aligned} \quad (3.2.2)$$

This is of the functional form

$$\frac{\partial}{\partial E} \left(2C_1 \phi(E) \right) = \mathcal{F} \left[s, \mu, E, \phi(E), \frac{\partial \phi(E)}{\partial s}, \frac{\partial \phi(E)}{\partial \mu}, \frac{\partial^2 \phi(E)}{\partial \mu^2} \right] \quad (3.2.3)$$

which we write in shorthand notation as

$$= \mathcal{F} \left[\phi(E) \right],$$

where $\phi(E)$ is just a shorthand form for $\phi(E, \mu, s)$ which we use when the dependence on μ and s can remain implicit.

Equation (3.2.3) can be solved by the trapezium method. This is a one-step method for obtaining the solution at an energy E_0 once the solution is known at an earlier energy E_1 . We use this method in the form

$$2C_1(E_0)\phi(E_0) = 2C_1(E_1)\phi(E_1) - (E_1 - E_0)\mathcal{F} \left[\phi(E_{1/2}) \right] \quad (3.2.4)$$

Chapter III: Solving the equation

where $E_1 > E_0$ and $E_{1/2} = (E_1 + E_0)/2$. We require that the stepping distance $E_1 - E_0$ be small enough that we can accurately replace the expression for $\mathcal{F}[\phi(E)]$, $E_1 \geq E \geq E_0$, by the linear one connecting $\mathcal{F}[\phi(E_1)]$ and $\mathcal{F}[\phi(E_0)]$. Then

$$\mathcal{F}[\phi(E_{1/2})] = \frac{1}{2} \left(\mathcal{F}[\phi(E_1)] + \mathcal{F}[\phi(E_0)] \right) \quad (3.2.5)$$

and

$$2C_1(E_1)\phi(E_1) - \frac{(E_1 - E_0)}{2} \mathcal{F}[\phi(E_1)] = 2C_1(E_0)\phi(E_0) + \frac{(E_1 - E_0)}{2} \mathcal{F}[\phi(E_0)]. \quad (3.2.6)$$

If the solution $\phi(E_1)$ is known, then we are able to obtain the solution at the lower energy E_0 by solving the difference equation (3.2.6). We begin by specifying an initial solution $\phi(E_{\max})$ at the highest energy point $E = E_{\max}$, and then begin stepping down, obtaining the solution at each point E_i , until we reach our lowest energy E_{\min} .

In practice, what we have labelled a point at a value E_i is a two dimensional surface of constant energy. Our solution $\phi(E_i)$ is a solution obtained at an energy E_i and for all s and μ . Our one-step method for obtaining $\phi(E_0)$ by solving equation (3.2.6) contains an implicit multi-step method for obtaining the function values over the whole of that surface. The left hand side of equation (3.2.6) is known at E_1 for all s and μ . Let it be equal to $B_{E_1}(s, \mu)$, and let us separate $\mathcal{F}[\phi(E_0)]$ into two components which we denote as $\zeta_\mu[\phi(E_0)]$ and $\eta_s[\phi(E_0)]$:

Chapter III: Solving the equation

$$\zeta_{\mu}[\phi(E_0)] = -\frac{(1-\mu^2)}{2} \cdot \frac{d \ln B}{ds} \cdot \beta^2 \frac{\partial \phi(E_0)}{\partial \mu} - \frac{C_2}{\beta^2 \gamma^2} \frac{\partial}{\partial \mu} \left((1-\mu^2) \frac{\partial \phi(E_0)}{\partial \mu} \right)$$

and

$$\eta_s[\phi(E_0)] = \mu \beta^2 \frac{\partial \phi(E_0)}{\partial s}. \quad (3.2.7)$$

We have

$$B_{E_1}(s, \mu) = 2C_1(E_0)\phi(E_0) + \frac{(E_1 - E_0)}{2} \left(\zeta_{\mu}[\phi(E_0)] + \eta_s[\phi(E_0)] \right). \quad (3.2.8)$$

ζ_{μ} contains the second order derivative in μ and requires a multi-step procedure. This procedure can be either explicit or implicit, though implicit methods are generally more accurate than explicit methods of the same order. We choose to use an implicit method and, hence, to solve equation (3.2.8) by successive iterations. We obtain the sequence of solutions $\phi^m(E_0)$ for $m = 0, 1, \dots$ and check for convergence after each iteration. We continue until we are satisfied that $\phi^n(E_0)$ is close enough to $\phi^{n-1}(E_0)$. $\phi^n(E_0)$ is then our desired solution $\phi(E_0)$ to equation (3.2.8) and we can proceed to the next, lower energy level.

At the m^{th} iteration we need to solve (3.2.8) afresh using our most recently obtained solution $\phi^{m-1}(E_0)$ as a starting function. We halve the right hand side of (3.2.8), evaluate one half using the known function $\phi^{m-1}(E_0)$ and then transfer it to the left hand side. The residual half remains on the right hand side and is to be solved to give the next solution in the sequence, namely $\phi^m(E_0)$. At this iteration we have to solve

Chapter III: Solving the equation

$$\begin{aligned}
 B_{E_1} - C_1(E_0)\phi^{m-1}(E_0) - \frac{(E_1 - E_0)}{4} \left(\zeta_\mu \left[\phi^{m-1}(E_0) \right] + \eta_s \left[\phi^{m-1}(E_0) \right] \right) \\
 = C_1(E_0)\phi^m(E_0) + \frac{(E_1 - E_0)}{4} \left(\zeta_\mu \left[\phi^m(E_0) \right] + \eta_s \left[\phi^m(E_0) \right] \right)
 \end{aligned} \tag{3.2.9}$$

for $\phi^m(E_0)$. All the known information from the solution to the previous iteration ($\phi^{m-1}(E_0)$) and from the solution at the previous energy level ($\phi(E_1)$) is contained on the left hand side. Let the left hand side of equation (3.2.9) be denoted by b_E^{m-1} . Equation (3.2.9) is, in essence, still the one-step difference equation (3.2.6), but we have rewritten it so that we can now focus on the iterations over the μ, s surface instead of on the stepping down through E .

We solve equation (3.2.9) by approaching it successively at three levels. The first level solves the equation over lines of constant E and s ; the second level expands this to cover the whole surface of constant E , *i.e.*, for all s ; and the third level is that which steps down through surfaces of decreasing E (*cf.* Figure (3.2)).

Level 1:

At each level of constant E , and for each line of constant s , we replace the $\eta_s \left[\phi^m(E_0) \right]$ component by its two finite difference equivalents

$$\begin{aligned}
 \eta_s^+ \left[\phi^m(E_0, \mu, s) \right] &= \mu \beta^2 \cdot \frac{\phi^m(E_0, \mu, s + \Delta s^+) - \phi^m(E_0, \mu, s)}{\Delta s^+} \\
 \text{and} & \\
 \eta_s^- \left[\phi^m(E_0, \mu, s) \right] &= \mu \beta^2 \cdot \frac{\phi^m(E_0, \mu, s) - \phi^m(E_0, \mu, s - \Delta s^-)}{\Delta s^-},
 \end{aligned} \tag{3.2.10}$$

where Δs^+ and Δs^- are the forward and backward stepping distances in s . Our iterations to obtain ϕ^m from ϕ^{m-1} are in the form of a sweep from $s = 0$ to

Chapter III: Solving the equation

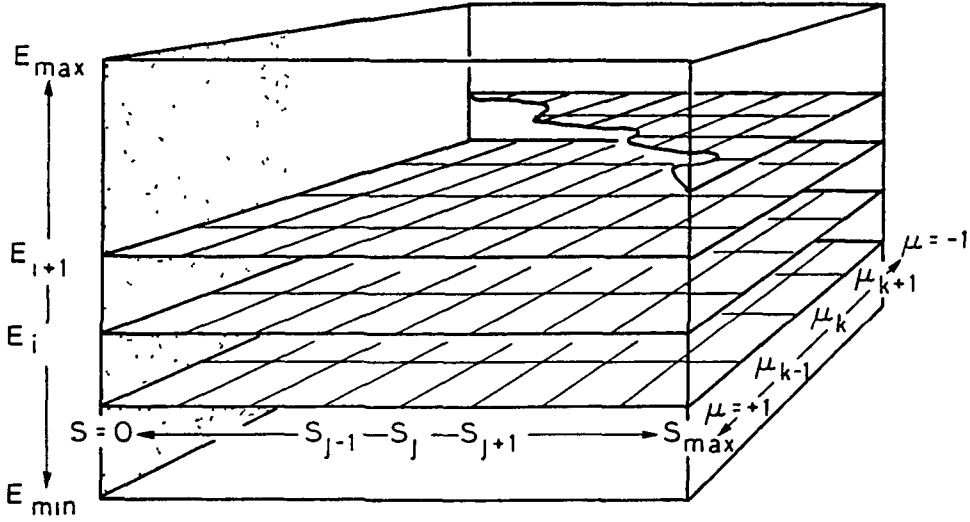


Figure 3.2 A schematic representation of the domain spanned by the independent variables in the Fokker-Planck Equation (equation (2.36)) and over which the solution is obtained. The pitch angle cosine μ covers $-1 \leq \mu \leq +1$ in K_{MAX} steps, the depth s covers $0 \leq s \leq s_{max}$ and the energy E covers $E_{min} \leq E \leq E_{max}$. The solution is obtained on a surface of constant E with the injected beam distribution specified on the line $s = 0$, $0 < \mu \leq +1$. The numerical code then steps down through E obtaining the solution at successively lower values of E .

$s = s_{max}$ followed by a return sweep from $s = s_{max}$ to $s = 0$ (*cf.* Figure (3.2)).

We use η_s^- on the sweep down and η_s^+ on the return. We solve either

$$\begin{aligned}
 b_E^{m-1} + \frac{E_1 - E_0}{4} \mu \beta^2 \cdot \frac{\phi^m(E_0, \mu, s - \Delta s^-)}{\Delta s^-} \\
 = C_1 \phi^m(E_0, \mu, s) + \frac{E_1 - E_0}{4} \cdot \left(\zeta_\mu \left[\phi^m(E_0, \mu, s) \right] + \mu \beta^2 \cdot \frac{\phi^m(E_0, \mu, s)}{\Delta s^-} \right)
 \end{aligned}
 \tag{3.2.11-}$$

when we sweep down, or

Chapter III: Solving the equation

$$\begin{aligned}
 b_E^{m-1} - \frac{E_1 - E_0}{4} \cdot \mu \beta^2 \cdot \frac{\phi^m(E_0, \mu, s + \Delta s^+)}{\Delta s^+} \\
 = C_1 \phi^m(E_0, \mu, s) + \frac{E_1 - E_0}{4} \cdot \left(\zeta_\mu \left[\phi^m(E_0, \mu, s) \right] - \mu \beta^2 \cdot \frac{\phi^m(E_0, \mu, s)}{\Delta s^+} \right)
 \end{aligned}
 \tag{3.2.11+}$$

when we sweep back, where, as before, everything known is kept on the left hand side.

$\zeta_\mu \left[\phi^m(E_0, \mu, s) \right]$ is a second order expression in derivatives of μ . At each value of μ it relates $\phi(E_0, \mu, s)$ to $\phi(E_0, \mu - \Delta\mu, s)$, $\phi(E_0, \mu, s)$ and $\phi(E_0, \mu + \Delta\mu, s)$. Hence, equations (3.2.11 -) and (3.2.11 +) can be solved in the form of a matrix equation $\mathbf{y} = A\mathbf{x}$. This equation is solved for \mathbf{x} , where \mathbf{x} is the vector of K_{MAX} values $\phi^m(E_0, \mu, s)$ along the line of constant E and s , from $\mu = \mu_1 = 1.0$ to $\mu = \mu_{KMAX} = -1.0$ (*cf.* Figure (3.2)). A is a $K_{MAX} \times K_{MAX}$ tridiagonal matrix and \mathbf{y} is the left hand side of (3.2.11 -) or (3.2.11 +). This matrix equation may be solved by factorizing A into upper- and lower- diagonal matrices and then obtaining \mathbf{x} by using Gaussian Elimination.

Level 2:

Level 1 gave the values of $\phi^m(E_0, \mu, s)$ along the lines of constant E and s . We now solve level 1 at successive values of the variable s . We begin at $s = 0$ (which corresponds to the top of the flare loop) and make our way down toward $s = s_{max}$ (*cf.* Figure (3.2)), solving equation (3.2.11 -) at each step. We then return and make our way back to $s = 0$, solving equation (3.2.11 +) at each step. The initial values $\phi^m(E_0, \mu \geq 0, s = 0)$ are set by the pitch angle distribution of

Chapter III: Solving the equation

the injected beam and constitute an upper boundary condition. The solution then generates the values $\phi^m(E_0, \mu < 0, s = 0)$. At $s = s_{\max}$ we use a free boundary condition. s_{\max} is large enough that the solution values there are negligibly small compared to those near the top of the domain and can be set effectively to zero.

Level 3:

Having solved level 2 in two sweeps, one down and one up, and having obtained a solution $\phi^m(E_0)$ for all values of s and μ , we compare $\phi^m(E_0)$ with $\phi^{m-1}(E_0)$. If they are sufficiently close, we proceed to the next energy level down; if not, we run another iteration on level 2 and check again, repeating this until we are satisfied that convergence has been obtained. To proceed to the next energy level down we take our final solution $\phi^n(E_0, \mu, s)$ and multiply it by a suitable scaling factor to give $\phi^0(E_{-1}, \mu, s)$, our first approximation to the solution at our new energy level $E_{-1} < E_0$. We then start the whole process again at this new energy level, sweeping from $s = 0$ to $s = s_{\max}$ and back to $s = 0$, solving equations (3.2.11 -) and (3.2.11 +), and obtaining $\phi^{1,2,\dots}(E_{-1})$. We continue in this manner until we have obtained the solution at our final energy level $E = E_{\min}$, by which time we have solved the Fokker-Planck Equation over the whole volume

$$\begin{aligned} E_{\max} &\geq E \geq E_{\min} \\ s_{\max} &\geq s \geq 0 \\ 1 &\geq \mu \geq -1. \end{aligned}$$

It is necessary to check that the numerical code is obtaining a satisfactory solution to the Fokker-Planck Equation. We can isolate the individual terms of

Chapter III: Solving the equation

the Fokker–Planck Equation when we run our numerical code on the computer. We can then compare these one-term numerical results with the three solutions (3.1.6), (3.1.16) and (3.1.25), obtained from our analysis of the reduced equations in §3.1. Should they show good agreement, we make the quite reasonable assumption that the solution obtained from the full numerical code agrees with the (unknown) solution of the full Fokker–Planck Equation.

Test #1: If, in our numerical scheme, we set $C_1 = C_2 = 0$ and inject an electron beam with a pitch angle distribution $f(\mu, 0) = -k \ln(1 - \mu^2)$ for $1 > \mu > 0$, we should obtain a distribution at all depths $s > 0$ given by equation (3.1.6), namely

$$\begin{aligned} f(\mu, s) &= -k \ln \left((1 - \mu^2) \frac{B(0)}{B(s)} \right) \\ &= k \left(\bar{s} - \ln(1 - \mu^2) \right), \end{aligned} \tag{3.2.12}$$

where \bar{s} is defined in equation (3.1.2).

In Figure (3.3) we compare the numerical results for this case with the above solution, using $k = 2$. As we can see, the two results agree quite precisely, except in the wings (large $|\ln(1 - \mu^2)|$) at large \bar{s} . This is because we were unable to specify our initial distribution all the way through to $\mu = 1$. The function value becomes infinite as $(1 - \mu^2)$ approaches zero. The effect of chopping off the initial function near $\mu = 1$ appears in the numerical results as we reach larger τ .

Test #2: If we set $d \ln B / ds = C_2 = 0$ in our numerical scheme and inject an electron beam with an energy spectrum which is a power law in η (*cf.* equation (3.1.11)), *i.e.*, $\phi_0(\eta) = f_0(\eta) / \beta(\eta) = \eta^{-\delta}$, we should obtain a distribution at all

Chapter III: Solving the equation

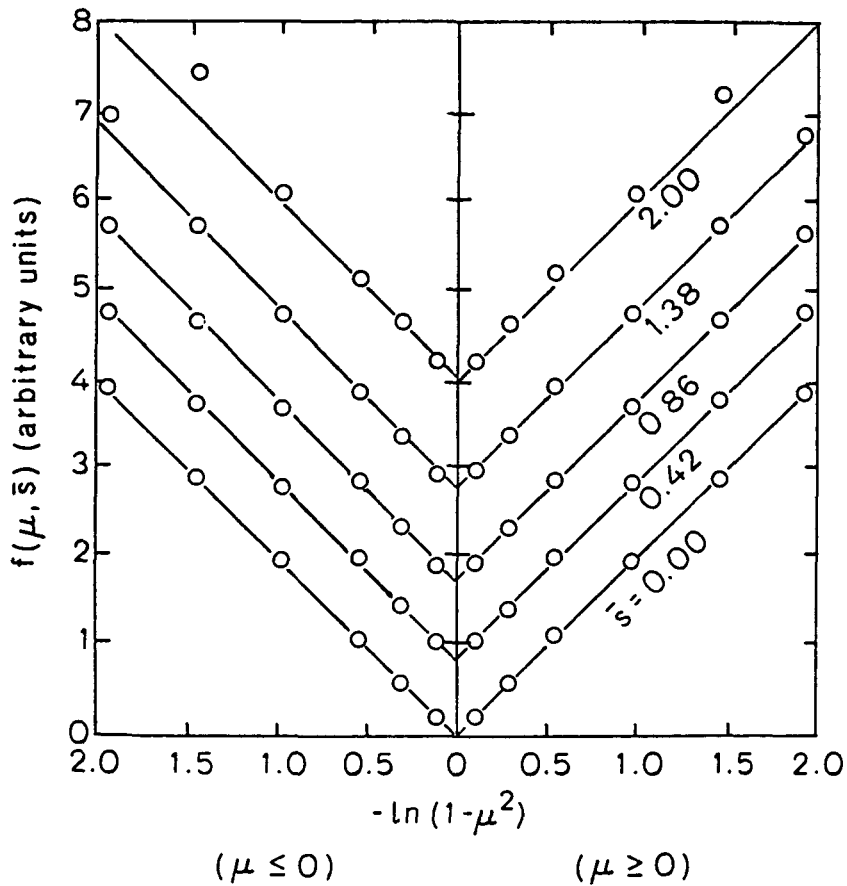


Figure 3.3 A comparison between the numerical results (dots) from running our code with the collisional terms switched off ($C_1 = C_2 = 0$) and the exact solution (equation (3.2.12)) (solid lines). \bar{s} is a measure of depth and is defined by equation (3.1.2). The injected ($\bar{s} = 0$) electron distribution is specified only for $\mu > 0$ (the right hand side of the diagram).

depths given by equation (3.1.16), namely

$$\phi(\eta, \mu, \tau) = (\eta + \tau/\mu)^{-\delta}, \quad (3.2.13)$$

with τ given by equation (3.1.12).

Chapter III: Solving the equation

We have compared the numerically obtained function $\phi(\eta, \mu, \tau)$ with equation (3.2.13). The two results agree perfectly.

Test #3: We now set $d \ln B / ds = C_1 = 0$ and inject an electron beam having a pitch angle distribution which is a narrow Gaussian centered about $\mu = 1$ ($x = 0$). We expect the pitch angle distribution to remain at least approximately Gaussian and to broaden with depth roughly in accordance with equation (3.1.25). For small values of x we may identify x with the pitch angle $\alpha = \cos^{-1}(\mu)$. In Figure (3.4) we compare our numerical results (dots) with equation (3.1.25) (solid lines). The agreement is very good for a wide dynamic range. Not only does our numerical code accurately solve the reduced equation (3.1.18), but also the approximation (3.1.19) would appear to hold well for values of μ distant from unity.

From our three checks we see that the numerical code gives very accurate solutions to the reduced equations. This means that our method handles well the individual terms of the Fokker-Planck Equation. We can then expect it to generate accurate solutions to the full equation with all the terms combined. We do not have an analytic solution to the full equation against which we can check the numerical code, though we do have the solution (3.1.38) to equation (3.1.28) which approximates the full equation with no magnetic field convergence. We can compare our numerical results with the approximate solution (3.1.38) and, if they are similar, expect both to be very close to the ideal (because unknown) solution of the full Fokker-Planck Equation.

Chapter III: Solving the equation

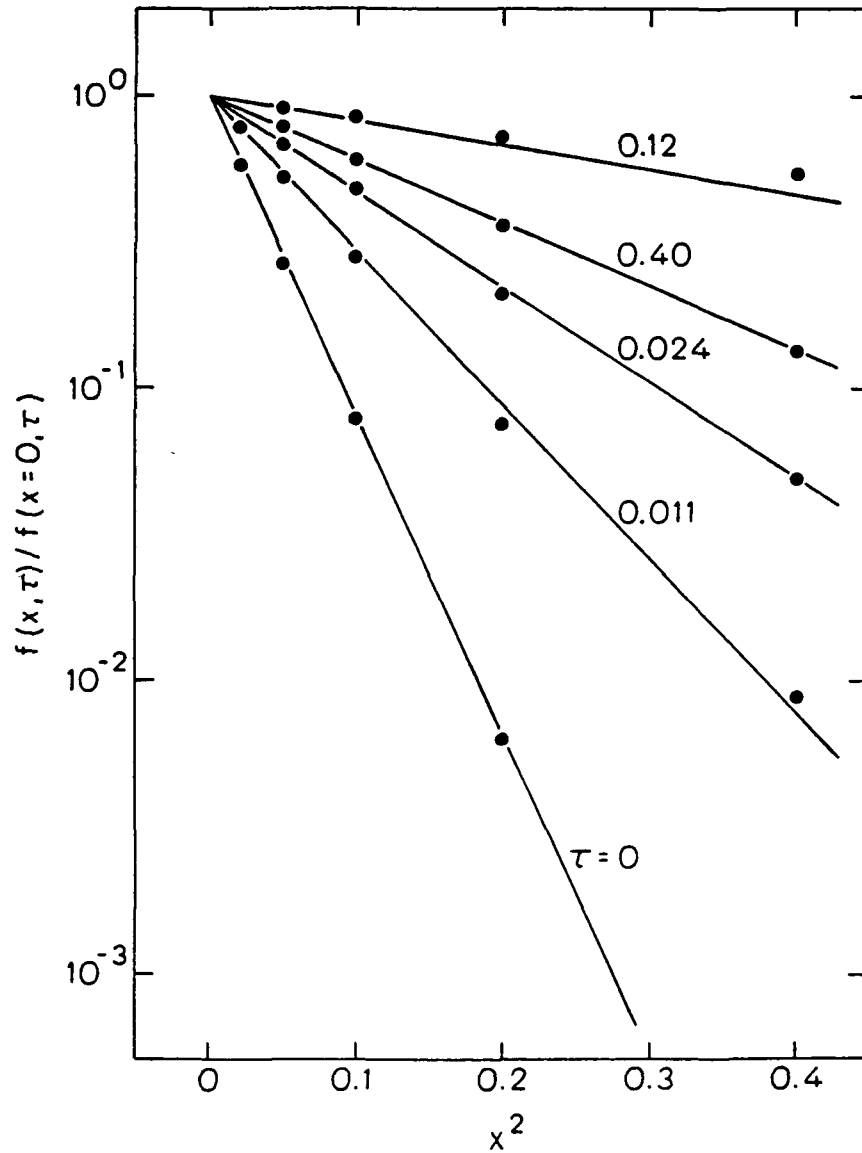


Figure 3.4 A comparison between the numerical results (dots) from running our code with only the diffusion term switched on ($C_1 = d \ln B / ds = 0$, $C_2 \neq 0$) and the exact solution (solid lines) to the equation approximating the diffusion equation, equation (3.1.25). x is our approximation to the pitch angle α near $\mu = 1$ and τ is the depth parameter (*cf* text above equation (3.1.19)). The injected distribution is Gaussian with $\alpha_0^2 = 0.04$.

3.3 Some results on the evolution of the electron beam.

In this section we present some results on the evolution of the electron beam within the flaring plasma. The primary use for these results is to obtain an understanding of the beam evolution, a prerequisite to looking at the X-ray results of Chapter V. The distribution of the X-rays will reflect the distribution of the emitting electrons, and knowing how the electron beam evolves as it passes down through the flare loop will enable us to correctly interpret the X-ray calculations and to draw strong conclusions accordingly. These results will also allow us to see how accurately our approximate solution (3.1.38) describes the evolution of the beam and to see how useful it can be for further studies of the beam dynamics, for example, in calculating the rate at which the beam heats the surrounding plasma or in calculating its ability to generate plasma turbulence.

We shall use equation (3.1.38) to guide us through the presentation of the electron results. For these results we assume the flaring plasma to be fully ionized Hydrogen and, in the definition of the depth parameter τ , we adopt a mean value of 20 for the Coulomb logarithm (*cf.* Table I, Chapter II). This simplifies the definition of τ , allowing us to replace equation (3.1.12) with

$$d\tau = 2 \times 10^{-23} n_e ds. \quad (3.3.1)$$

This integrates to give $\tau = N/N_0$ where N is the accumulated column thickness passed through, in units of particles cm^{-2} , and $N_0 = 5 \times 10^{22} cm^{-2}$.

When using the numerical code to solve equation (2.36) we use the pitch angle variable α instead of the variable x which was introduced by our approximation

Chapter III: Solving the equation

analysis. We inject an electron beam with a pitch angle distribution $\exp(-\alpha^2/\alpha_0^2)$ which, for small α_0^2 , is nearly indistinguishable from the form $\exp(-x^2/x_0^2)$ used in equation (3.1.36). We use the solution (3.1.38) but make the simple substitution of α for x . The energy spectrum of the injected electrons is always of the form $F_0(E) \sim E^{-\delta}$ where the spectral index δ is set for each model. In each case, therefore, we inject a flux

$$F(E, \mu, 0) = F_0(E, \mu) \sim E^{-\delta} \exp(-\alpha^2/\alpha_0^2). \quad (3.3.2)$$

The solution (3.1.38) is most directly applicable when expressed in terms of the electron flux $F(E, \mu, s)$ instead of the function $\phi(E, \mu, s)$. The two are simply connected, with $F(E, \mu, s) = c\beta^2(E)\phi(E, \mu, s)$. Our general solution is, then,

$$F(E, \mu, s) = \frac{\beta^2(\eta)}{\beta^2(\eta + \tau)} F_0(\eta + \tau) \cdot \frac{2}{\alpha_0^2 + \zeta(\eta + \tau)} \exp\left(-\frac{\alpha^2}{\alpha_0^2 + \zeta(\eta + \tau)}\right) \quad (3.3.3)$$

where $F_0(\eta)$ is the flux energy spectrum at $\tau = 0$. The units of the electron flux $F(E, \mu, s)$ are electrons $cm^{-2} sec^{-1} keV^{-1} ster^{-1}$.

Pitch angle evolution:

One of the first things to notice about solution (3.3.3) is that it separates the beam's pitch angle evolution from its energy evolution. This was the advantage gained from making a substitution for the second order derivative in μ in equation

Chapter III: Solving the equation

(2.36). For clarity let us write $F(E, \mu, s) = F_1(E, s) F_2(E, \mu, s)$ with

$$\begin{aligned} F_1(E, s) &= \frac{\beta^2(\eta)}{\beta^2(\eta + \tau)} F_0(\eta + \tau) \\ F_2(E, \mu, s) &= \frac{2}{\alpha_0^2 + \zeta(\eta + \tau)} \exp\left(-\frac{\alpha^2}{\alpha_0^2 + \zeta(\eta + \tau)}\right). \end{aligned} \quad (3.3.4)$$

$F_2(E, \mu, s)$ describes the pitch angle evolution of the beam. A beam which begins as a Gaussian of width α_0 broadens with increasing depth at a rate which depends upon the electron energy[†]. The broadening is controlled by $\zeta(\eta + \tau)$ which, for $Emec^2 \ll 2$ can be replaced by $\ln(1 + \tau/\eta)$. At $\tau = 0$, $\zeta(\eta + \tau) = 0$. The form of $F_2(E, \mu, s)$ shows that the beam's rate of broadening is similar for all energies E , provided we scale the depth correctly. For all but the highest energies, the correct depth scaling is by $\eta = E^2/(E + 1)$.

In Figures (3.5) through (3.7) we show the pitch angle evolution of the beam with depth for three different values of α_0^2 , as given by our numerical results. The curves are labelled according to their value of the scaled depth τ/η . Each diagram, therefore, represents the beam distribution across a wide range of energies, for the scaling of depth with η is found to be well supported by the numerical results. The first curve in each figure ($\tau/\eta = 0$) shows the injected distribution over $1 \geq \mu > 0$

[†]It is important to bear in mind the distinction between the concepts of the energy of an individual electron and the (electron) energy which is an independent variable in equation (3.1.26) and the solution (3.3.3). There is always the temptation to think of the evolution of the electron beam in terms of individual, real electrons which lose energy and change their pitch angles as they pass down the flare loop. The solution, however, does not follow the paths of individual electrons. The electrons described as having a given energy E at a depth s are not to be considered as having a direct connection with electrons of the same energy E at any other depth s' .

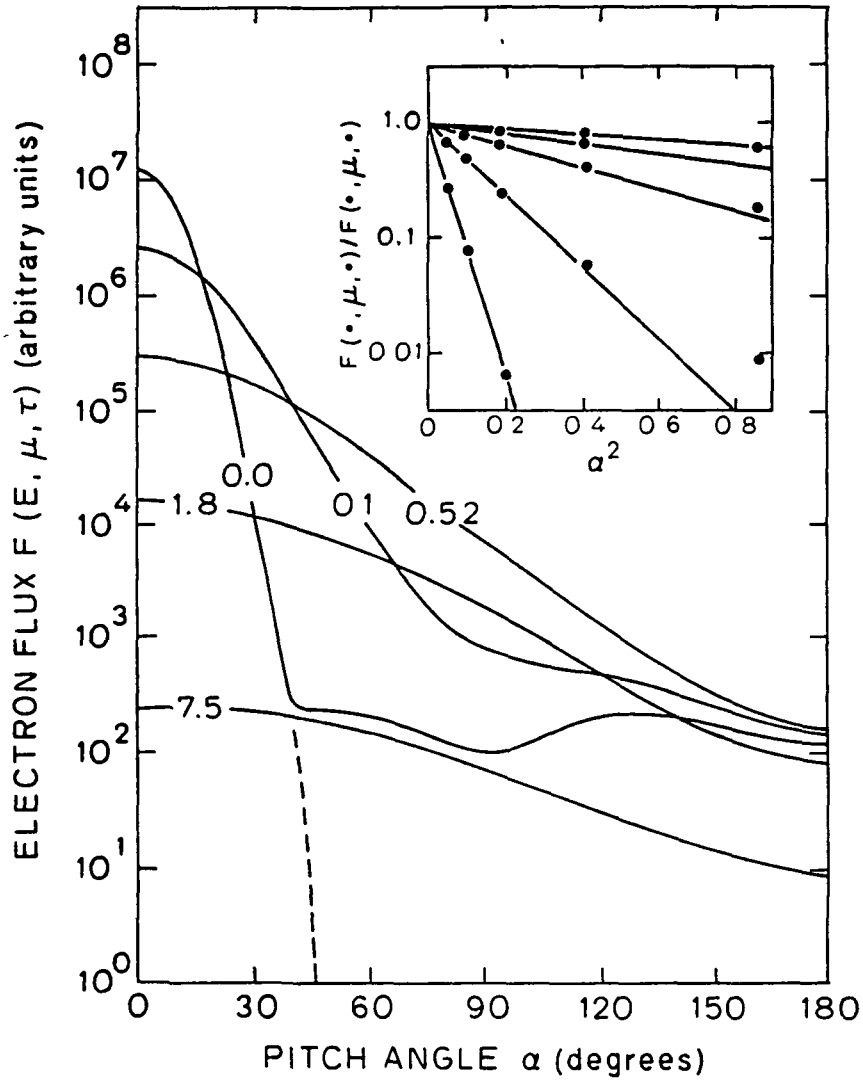


Figure 3.5. The pitch angle evolution with increasing depth of the electron beam for $\alpha_0^2 = 0.04$ (and $\delta = 5$, $d \ln B / ds = 0.0$). The curves are labelled according to their values of τ/η . For the first curve ($\tau/\eta = 0.0$) the continuation of the injected spectrum is shown by the dotted line. The flux at $\tau/\eta = 0.0$ with $90^\circ < \alpha \leq 180^\circ$ is reflected back into the loop with $0^\circ \leq \alpha < 90^\circ$ to mimic the symmetry of the flare loop about its apex. The inset shows the ratio $F(E, \mu, \tau)/F(E, \mu = 1, \tau)$ as obtained from the numerical results (dots) and equation (3.3.4) (solid lines).

Chapter III: Solving the equation

plus the distribution of electrons which are then calculated to have returned to the top of the loop with μ in the range $0 > \mu \geq -1$. To mimic the flare's symmetry about the top of the loop, the electrons which return to $\tau = 0$ with $\mu < 0$ are reflected back into the loop with a positive μ of equal magnitude. In Figure (3.5) we show, by the dotted line, the extension of the injected distribution below that of the reflected distribution. In Figure (3.7) the beam is injected with a uniform distribution over $1 \geq \mu > 0$, but the addition of the reflected component which is strongly concentrated at small values of $|\mu|$ gives rise to a maximum in the distribution at $\mu = 0$. Note that for small α_0^2 (Figure 3.5) the contribution of the reflected flux is negligible.

In Figure (3.5) the behavior predicted by equation (3.3.3) is evident. The beam broadens with increasing depth and the scaling of depth with η holds well. In the inset we show the ratio of $F(E, \mu, \tau)$ to $F(E, \mu = 1, \tau)$ as obtained from the numerical results (dots) and expression (3.3.4) for F_2 (straight lines). The beam is Gaussian upon injection, blends with the reflected flux as it broadens, becoming slightly wider than Gaussian, and then relaxes back to a distribution which is Gaussian, which broadens slowly with increasing τ/η as predicted and which falls steadily in magnitude.

One important effect evident in a comparison of Figures (3.5) through (3.7) needs to be stressed. The beam distribution at depths larger than $\tau/\eta \sim 1$ is identical in each figure and is independent of the narrowness of the injected beam. Turning to equation (3.3.4), at large τ/η , $\zeta(\eta + \tau)$ becomes larger than α_0^2 and the width of the beam is controlled by ζ independently of the narrowness of the beam at $\tau = 0$. Beyond $\tau/\eta \sim 1$, all information as to the narrowness of the injected

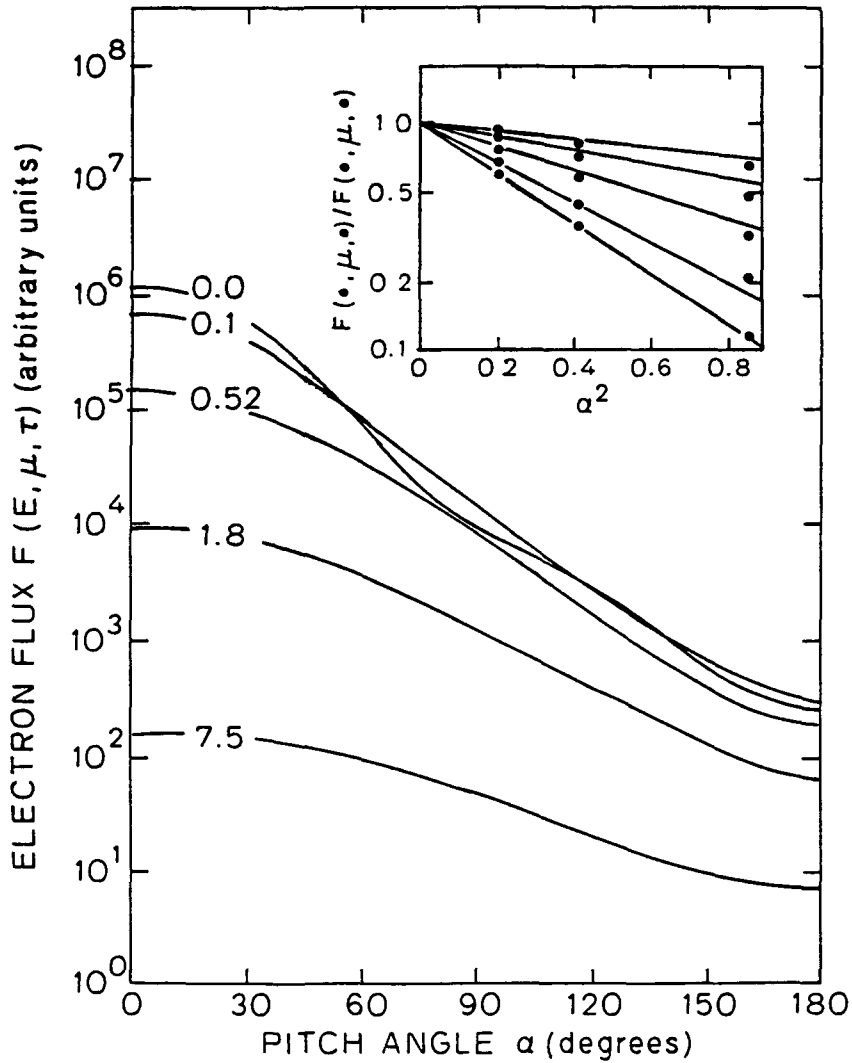


Figure 3.6 The same as Figure (3.5) but for $\alpha_0^2 = 0.4$. Note that the curves for $\tau/\eta = 1.8$ and 7.5 are identical to the curves for the same two τ/η values in Figure (3.5).

beam is lost. This is of significance when, later, we discuss the degree to which the X-ray results are able to give information about the source distribution of energetic electrons

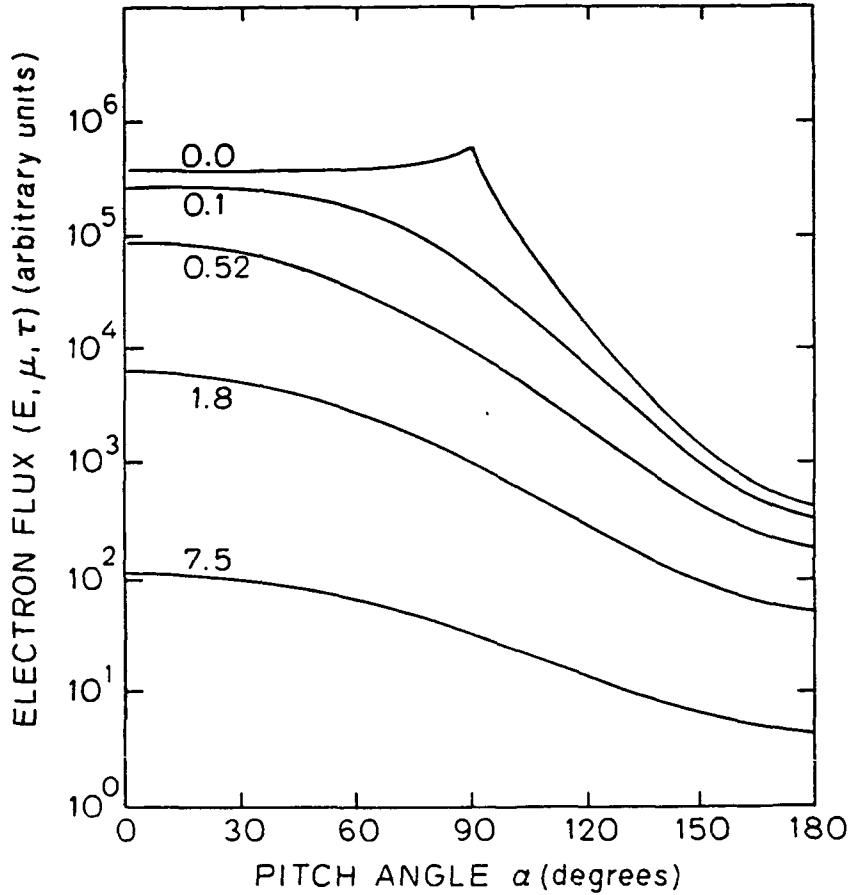


Figure 3.7. The same as Figure (3.5) but for $\alpha_0^2 = \infty$, that is, for an injected electron beam which is uniform over the range $0^\circ \leq \alpha < 90^\circ$. The flux which returns to $s = 0$ with $\mu < 0$ is reflected back into the loop. As this reflected flux is concentrated at small $|\mu|$, the total flux at $s = 0$ peaks at $\mu = 0$. Note, again, that the curves for $\tau/\eta = 1.8$ and 7.5 are identical to the curves for the same two τ/η values in Figures (3.5) and (3.6).

Spectral evolution:

We shall now look at the energy spectrum of the beam. If we integrate equation (3.3.3) over all pitch angles μ we see that the expression (3.3.4) for $F_2(E, \mu, s)$

Chapter III: Solving the equation

integrates to unity, leaving

$$\begin{aligned} F(E, s) &= \int_{\mu} F(E, \mu, s) d\mu \simeq F_1(E, s) \\ &= \frac{\beta^2(\eta)}{\beta^2(\eta + \tau)} F_0(\eta + \tau). \end{aligned} \tag{3.3.5}$$

Our injected energy spectrum $F(E, 0)$ equals $F_0(\eta) \sim E^{-\delta}$ electrons per unit energy E . From equation (3.3.5) we obtain $\partial F_1(E, s)/\partial E = 0$ at $E = E_{\max}$ where E_{\max} is given by

$$E_{\max}^2 \simeq \frac{2\tau}{\delta(\delta + 2)}. \tag{3.3.6}$$

The numerically obtained electron flux integrated over pitch angle is given in Figure (3.8) for $\delta = 5$ (from the model with $\alpha_0^2 = 0.04$). The injected flux falls steeply with increasing E . On penetrating through the flaring plasma, the lower energy electrons lose energy more rapidly than do the higher energy electrons. The number of low energy electrons is rapidly depleted, the spectrum begins to turn down and it develops a hump which then moves to higher E with increasing τ . The variation of the hump energy with depth should be as given by equation (3.3.6). In the inset in Figure (3.8) we show E_{\max}^2 as a function of τ as taken from the numerical results. Their relationship is linear, as expected.

Luhman (1976), in reference to auroral electrons in the earth's atmosphere, obtained the solution to a simplified electron transport equation which was derived from the Fokker-Planck Equation. His treatment of the pitch angle diffusion was rather crude and differed entirely from the treatment in effect here. Notwithstanding this dissimilarity, we may compare our energy spectra as given in Figure (3.8) with his results as presented in his Figure 1 (Luhman 1976). Though a direct

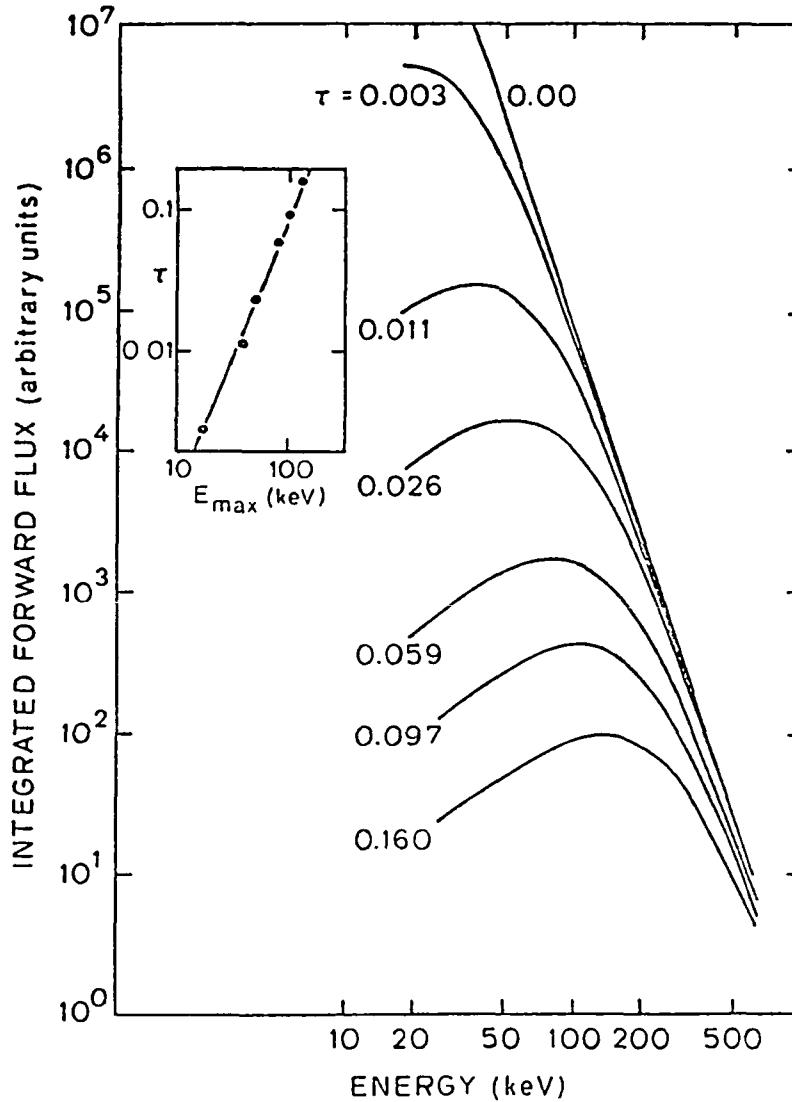


Figure 3.8 The electron energy spectrum at successive depths for the model with $\delta = 5$ (and $\alpha_0^2 = 0.04$, $d \ln B / d s = 0$). The curves are labelled according to their depths τ . The inset shows the energy of the spectral maximum as a function of depth (cf. equation (3.3.6)). The gradient to the right of the maximum is set by the value of δ , the gradient to the left is set by the Coulomb collision process.

Chapter III: Solving the equation

comparison of the two sets of spectra cannot easily be made their similarity is clear.

Changing the value of α_0^2 does not affect the spectral evolution as presented in Figure (3.8), just as changing the value of δ does not affect the shape of the curves in Figures (3.5) through (3.7) (though it will affect the variation of the relative magnitudes of the flux with depth). In Figure (3.8), using a different value of δ changes the gradient of the spectrum to the high energy side of the hump, but does not affect the slope on the low energy side.

The influence of a converging magnetic field:

If we now add a magnetic field of increasing strength along the loop, the effects on the pitch angle distribution of the beam are pronounced. Consider an injected beam which is narrow and peaked about the downward direction. As electrons enter regions of greater field strength, they swiftly move to larger pitch angles and can be reflected, after which their motion is directed toward the top of the loop. As these reflected electrons are then moving into regions of lower field strength, their pitch angle continues to increase toward 180° and their motion becomes increasingly anti-parallel to the field lines. In Figure (3.9) we show the numerical results for a model which has the same injected electron beam as the model used for Figure (3.5), but which in addition has a converging magnetic field. The model has a column thickness of $2.4 \times 10^{18} \text{ cm}^{-2}$ from the top of the loop (curve 1) to the transition region (curve 3). Over this distance the magnetic field strength increases by a factor of five. The curves are for an electron energy of 78 keV,

Chapter III: Solving the equation

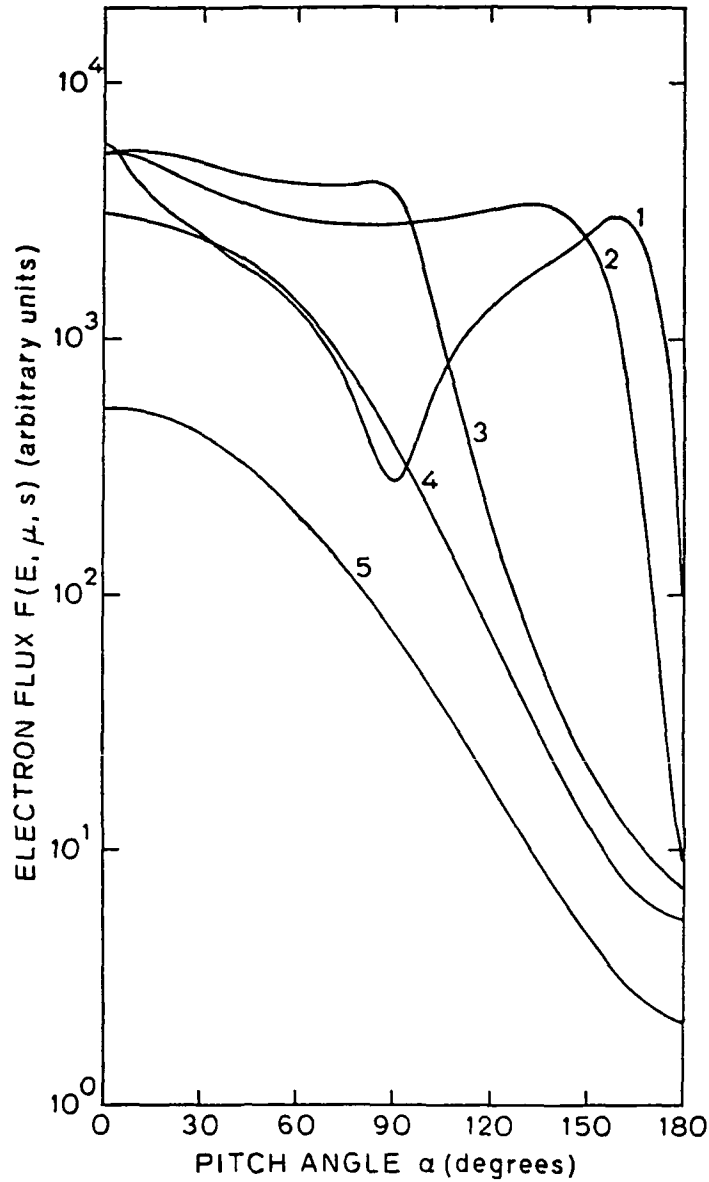


Figure 3.9. The pitch angle evolution of the electron beam for a model with a narrow injected beam ($\alpha_0^2 = 0.04$) and a converging magnetic field. The magnetic field converges by a factor of five from the top of the loop (curve 1) to the transition region (curve 3) which is at a column depth of $2.4 \times 10^{18} \text{ cm}^{-2}$. Curve 2 corresponds to the mid-point of the coronal loop. Below the transition region (curves 4 and 5) the magnetic field convergence no longer controls the electron beam evolution because the plasma density there is too high. The electron beam, under the influence of Coulomb collisions, establishes a smooth profile with behavior similar to that found in the models without converging magnetic fields.

Chapter III: Solving the equation

which means that, in the corona, Coulomb collisions are relatively unimportant. Curves 4 and 5 are for successively deeper levels of the chromosphere. For these the field convergence is no longer the dominant influence on the electron beam.

For a depth half way along the coronal loop (curve 2), the electron distribution is the sum of many contributions. Electrons with small pitch angles ($\mu \lesssim 1$) had even smaller pitch angles higher up and have yet to be strongly deflected by the magnetic field. Those with larger pitch angles are rapidly approaching their mirroring depth. Within a short distance they go from having positive μ to negative μ . Near to being mirrored an electron changes its pitch angle very rapidly and for this reason the distribution is symmetric immediately about $\mu = 0$. Electrons with μ less than but close to zero in curve 2 were recently mirrored, but those with more negative μ were mirrored in much lower levels of the coronal loop. When the mirroring depth falls below the transition region the electrons have to rely on Coulomb scattering to return them to the corona and for this reason the flux at $\mu \simeq -1$ is always well below that at $\mu \simeq 0$. All the electrons which are mirrored within the body of the coronal loop together form a beam which moves anti-parallel to the injected beam. Toward the top of the loop the electron distribution takes on a two-beam structure, as can be seen in curve 1. The relative size of the mirrored beam depends upon the relative importance of magnetic mirroring to Coulomb collisions. For the model shown in Figure (3.9) (the coronal section of the loop has a column thickness of $2.4 \times 10^{18} \text{ cm}^{-2}$ and the magnetic field strength increases

Chapter III: Solving the equation

five fold) and for 78 keV electrons, the ratio of mirrored to total[†] injected flux at the top of the loop is 0.89. For 400 keV electrons it is still 0.89 but for 10 keV electrons it is 0.51.

The magnetic field reflects the beam electrons without drawing energy from them. The field, therefore, tends to trap the electron beam in the upper reaches of the flare loop. Electrons escape from this magnetic bottle if they are continually scattered by the Coulomb collisions to smaller pitch angles. In this manner they can reach the lower regions of the coronal part of the loop and a few of them will reach the chromospheric regions where the plasma density is high enough that the electrons are no longer controlled by the magnetic field.

Just how effective the magnetic field can be at bottling up the beam is shown in Figures (3.10) and (3.11). Figure (3.10) shows the rate at which the downward flux falls with increasing magnetic field strength for three rates of increase of the field. The downward flux at any depth is the integral over positive μ of μF , i.e.,

$$F_B(E, s) = \int_{\mu=0}^1 \mu F(E, \mu, s) d\mu, \quad (3.3.7)$$

and is also integrated over the cross-sectional area of the loop. F_B is, therefore, a measure of the electron current passing through the loop, not the current density,

[†]The total injected flux is the sum of two components: the specified injected flux with a distribution $F_0(E, \mu)$ (cf. equation (3.3.2)) and the flux which exits the other half of the flare loop, crosses the top and passes into the half of the loop which we are considering. Owing to the reflection symmetry of the flare loop about its apex, this second component of the injected flux is identical to the flux which exits the top of this half of the loop. The magnitude and distribution of this component are obtained by solving equation (2.36) in a self-consistent manner.

Chapter III: Solving the equation

i.e., the current cm^{-2} . For each of the three cases shown, the magnetic field increases with constant $d \ln B/ds$. In terms of the scale depth z , the magnetic field strength relative to that at the top varies as 10^{bz} where $b = 0.0, 0.5$ and 1.0 for the dotted, dashed and solid lines, respectively. The column depth from $z = 0$ to $z = 3$, at 3×10^{18} , is insignificant, as shown by the $b = 0$ (dotted) lines. The downward flux falls in proportion to the magnetic field strengthening. The tighter the magnetic bottle, the smaller the fraction of the flux which escapes. Figure (3.11) shows that this behavior is not strongly sensitive to the value of α_0^2 .

Though Figure (3.10) shows that the bottling up of the downward flux is roughly the same for all energies, this does not mean that electrons of different energies have the same fate. If the escaping flux is, for example, one one-thousandth of the flux at the top of the loop, an average electron would be mirrored a thousand times before it escapes. In traveling up and down the loop this number of times, it passes through an accumulated depth of $6 \times 10^{21} cm^{-2}$. For a low energy (say, $30 keV$) electron, this is a large enough depth that the electron stands a greater chance of being stopped in the corona than of escaping to the chromosphere. On the other hand, a high energy electron can pass through this amount of material without being slowed significantly and will have a good probability of escaping eventually even if it has only a one in 10^3 probability of escaping at each try. This means that the magnetic field can trap very efficiently low energy electrons in the corona, but it would take an extraordinarily strong magnetic bottle to prevent most of the highest energy electrons from eventually reaching the chromosphere. The resulting effect upon the X-rays will be seen in Chapter V.

Chapter III: Solving the equation

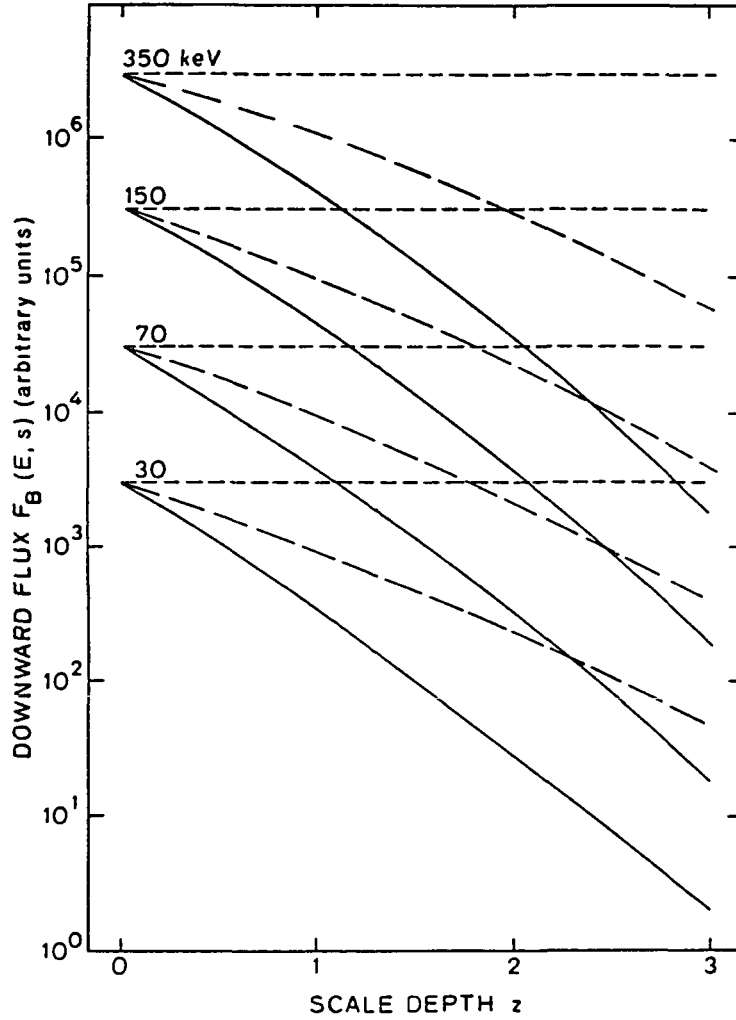


Figure 3.10. The downward moving electron current within the loop for three different rates of increase of the magnetic field strength and for $\alpha_0^2 = 0.4$. These curves show how effective the magnetic field is at bottling up the electron beam. The downward current is defined by equation (3.3.7). The magnetic field strength has the form $B(z) = B_0 10^{bz}$ for arbitrary B_0 . The dotted curves correspond to $b = 0.0$, the dashed curves to $b = 0.5$ and the solid curves to $b = 1.0$. The column depth at a scale depth of $z = 3$ is $3 \times 10^{18} \text{cm}^{-2}$. The effect on the electron beam of Coulomb collisions is, therefore, negligible compared with the effect of the magnetic trapping.

Chapter III: Solving the equation

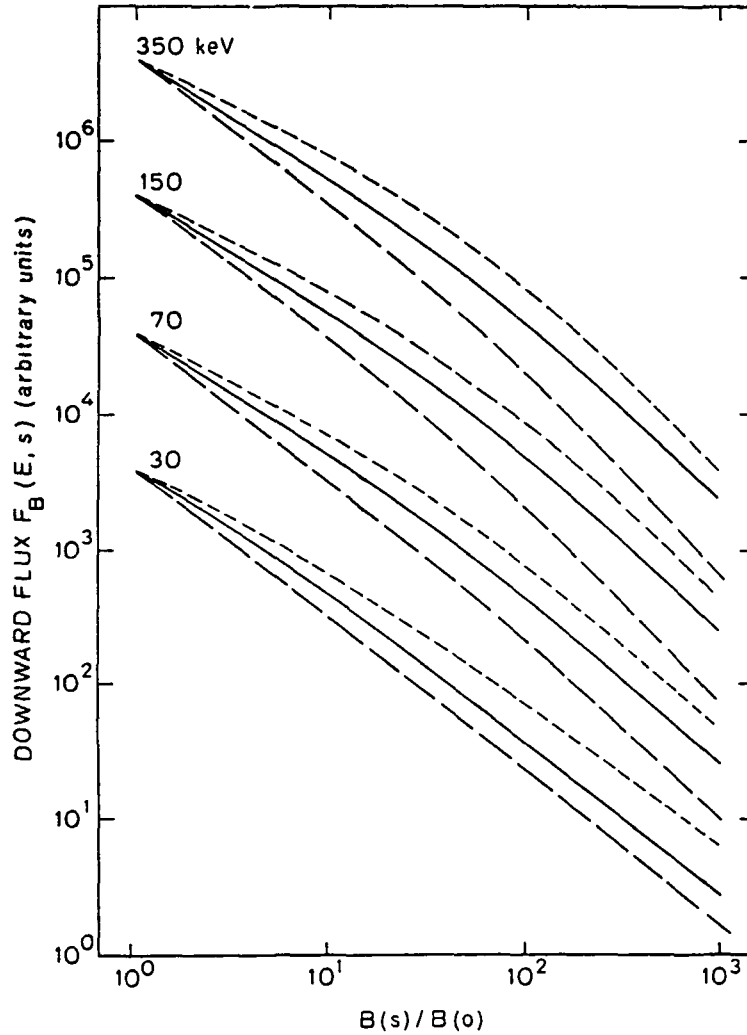


Figure 3.11 As Figure (3 10) but for one magnetic bottle strength ($b = 1.0$) and three values of α_0^2 . The dotted lines correspond to $\alpha_0^2 = 0.04$, the solid ones to $\alpha_0^2 = 0.4$ and the dashed ones to $\alpha_0^2 = \infty$. The effectiveness of the magnetic bottle is only slightly dependent upon α_0^2 .

In this chapter, we have taken the equation that describes the electron transport, we have looked at the individual terms to get an indication of how the electron beam evolves within the flare and we have described the method by which the equation is solved numerically. We then looked at these numerical results in

Chapter III: Solving the equation

order to learn how the electron beam actually behaves. We now need to include into our paradigm a description of the X-ray production by these energetic electrons so that we may calculate the X-ray characteristics associated with our models. This we shall do in Chapter IV.

Chapter IV

X-Ray Bremsstrahlung Theory

In the preceding chapters we structured the physical problem, obtained its mathematical expression and then looked at the solutions. We now have the function $f(E, \mu, s)$ which describes the number density of high energy electrons throughout the flare loop. Our next step is to combine this with information describing how the electrons produce the hard X-rays and to ensure that we have enough information about the X-rays that we can use them as a diagnostic tool to probe the physical conditions in a flare.

We are interested in X-rays with energies in the range $10 \sim 500 \text{ keV}$. There are three possible mechanisms by which the energetic electrons might produce continuum radiation in this interval:[†] the bremsstrahlung mechanism, the gyro-synchrotron mechanism and the inverse Compton mechanism. Investigating the viability of these three mechanisms for a broad range of conditions appropriate to a flare, Korčák (1967a,b; 1971) concluded that bremsstrahlung would be the primary mechanism producing hard X-rays in flares; this has since been widely accepted throughout flare X-ray studies (see also Brown 1976; Brown and Smith

[†] There is no line emission in this energy range. The highest energy line seen in the solar corona comes from fully ionized iron and has a line energy of $\simeq 6.9 \text{ keV}$

Chapter IV: X-Ray Theory

1980). The other two mechanisms will only become important should the energy spectrum of the fast electrons not extend down below several MeV .

Accepting that bremsstrahlung is the most likely emission mechanism, we can expect that unpolarized source electrons will emit only linearly polarized X-rays (Gluckstern, Hull and Breit 1953; Bannerjee 1958). The plane containing the polarization vector will be either parallel or perpendicular to the plane of emission, which is that plane containing the directions of propagation of the incoming electron and the outgoing photon. The production of the X-radiation is described by two cross-sections, each giving the probability of emission with one or other of these two polarizations. We denote the two cross-sections by $d\sigma_{\parallel}$ and $d\sigma_{\perp}$ respectively (suppressing for now their dependence on the photon energy, electron energy and η , the angle between the electron and the photon).

4.1 Stokes Parameter formalism.

Before we discuss these cross-sections in detail let us consider a method for describing the X-rays. We need to calculate the X-ray intensity and polarization for all viewing directions, for a range of photon energies and for all source positions along the length of the loop. A complete description of a beam of radiation (labelled according to its source position s , direction $\hat{k}(\Theta, \Phi)$, and energy k) contains information about its intensity, its degree of polarization, the orientation of its polarization plane and its ellipticity (Chandrasekhar 1960, p25). A very convenient parametric representation of such a description was formulated and

Chapter IV: X-Ray Theory

introduced by Sir George Stokes (Stokes 1852; see also Chandrasekhar 1946; 1960, p25; Tolhoek 1956; Bekefi 1966, p21). Under this parameterization an elliptically polarized beam of light is fully described by the four Stokes parameters I , Q , U and V . Such a representation derives its particular usefulness from the fact that the Stokes parameters are additive; that is, we obtain the Stokes parameters for (and hence a complete description of) any beam of radiation by simply adding together the Stokes parameters for the independent elements of which that beam is comprised. The Stokes parameterization is not unique and requires the specification of a reference plane with respect to which the direction of the polarization vector can be located. The Stokes parameters for the independent elements are additive only if all the elements use the same reference plane.

The X-radiation from any particular source position within the flare is the sum of the independent emissions from each electron in that source region. The problem of describing the radiation field, then, is reduced to that of obtaining a correct parametric description of the radiation from each element of the emitting volume. Obtaining these elemental Stokes parameters from the X-ray cross-sections is a straightforward process which we now demonstrate.

Consider that part of the radiation field which is emitted with a photon energy k , in a direction $\hat{k}(\Theta, \Phi)$ and from a source volume of electrons which is at a distance s from the top of the loop (*cf.* Figure (5.1)). For this part of the radiation field let the Stokes parameters be $I(k, \Theta, \Phi, s)$, $Q(k, \Theta, \Phi, s)$, $U(k, \Theta, \Phi, s)$ and $V(k, \Theta, \Phi, s)$. Consider now the element which is contributed to that beam of X-rays by those electrons in the source volume which have a kinetic energy E and which have an instantaneous direction of travel \hat{p}_0 which is at an angle η to the

Chapter IV: X-Ray Theory

beam direction \hat{k} . The first two Stokes parameters for that one element of the beam, ΔI , ΔQ , are given by (Haug 1972; Langer and Petrosian 1977)

$$\begin{aligned}\Delta I dk d\Omega_k ds dE d\Omega_p &= n_H(s) f(E, \mu, s) (d\sigma_{\perp} + d\sigma_{\parallel}) dk d\Omega_k ds dE d\Omega_p \\ \Delta Q dk d\Omega_k ds dE d\Omega_p &= n_H(s) f(E, \mu, s) (d\sigma_{\perp} - d\sigma_{\parallel}) dk d\Omega_k ds dE d\Omega_p\end{aligned}\quad (4.1)$$

where $d\Omega_k = d\Omega(\Theta, \Phi)$ is the element of solid angle about the photon direction $\hat{k}(\Theta, \Phi)$, $d\Omega_p$ is the element of solid angle about the electron direction \hat{p}_0 , and $n_H(s)$ is the local number density of heavy nuclei. The definition of the two cross-sections, $d\sigma_{\perp}$ and $d\sigma_{\parallel}$, specifies the emission plane as the plane with respect to which the polarization vector is located. Equation (4.1), then, employs the emission plane as the required reference plane in the definition of the Stokes parameters.

For our purposes here we consider the solar atmosphere to be a plasma of pure Hydrogen. Helium and elements with a higher atomic number Z have a relatively low abundance in the solar corona and chromosphere. The bremsstrahlung yield from the high Z elements is proportional to Z^2 ; hence a significant emphasis is placed on the contributions of the high Z elements despite their low abundances. Allowing for these other ions would amount to replacing the ambient plasma density n_H by $n_H + \sum_{Z \geq 2} Z^2 n_Z$. This has been estimated at $\sim 1.8 n_H$ by Elwert and Haug (1971), $1.36 n_H$ by Haug (1979) and $1.25 n_H$ by Duijveman, Hoyng and Machado (1982). The high Z elements do not affect the characteristics of the X-rays produced; they do no more than introduce a renormalization of the total X-ray flux. Because of this we do not need to include the high Z elements in our study.

The radiation, being bremsstrahlung from unpolarized electrons, has no circular polarization. This is easily understood if we think in terms of the classical

Chapter IV: X-Ray Theory

description of the emission mechanism. An electron emits because it is accelerated. During a collision the electron's trajectory remains within the plane of emission defined by the direction of motion of the incoming electron and the force vector pointing toward the scattering center. The physical system is then symmetric with respect to reflection in this plane and, therefore, so must be the emitted radiation. Any left circularly polarized radiation is matched by an exactly equal amount of right circularly polarized radiation. The sum of the two is always linearly polarized. This absence of any circularly polarized radiation means that the fourth Stokes parameter for the element of radiation, $\Delta\mathcal{V}$, is identically zero, and this result is independent of the reference frame (Chandrasekhar 1960, pp25). Henceforth, we shall work with only the first three Stokes parameters.

The third Stokes parameter for the element of radiation, $\Delta\mathcal{U}$, also happens to be zero. This is because, by the above physical symmetry, the X-ray polarization direction has to be either parallel or perpendicular to the plane of symmetry. This symmetry plane is the plane of emission which also serves as the reference plane in equation (4.1). It is this coincidence of the symmetry and reference planes which causes $\Delta\mathcal{U}$ to be zero (*cf.* equation (4.2) with $\psi = 0$.) When we change the reference plane, as we are about to do, the third Stokes parameter need no longer be zero. We must, therefore, retain it in order that the linear polarization be correctly described.

We now add together all the individual elements which contribute to that part of the radiation field we are considering. The Stokes parameters for each element are defined with respect to that element's plane of emission. These different elements of radiation all come from electrons with different directions of travel

Chapter IV: X-Ray Theory

and hence different reference planes. Before we can add the Stokes parameters for each element to give the Stokes parameters for the entire beam we must specify a common reference plane. For now we shall define this common reference plane to be that plane containing the beam direction \hat{k} and the direction \hat{r} , where \hat{r} is any well defined direction in space. If the three elemental Stokes parameters in the new reference plane are denoted by dI , dQ and dU respectively we obtain (Haug 1972),

$$\begin{aligned}
 dI dk d\Omega_k ds dE d\Omega_p &= n_H(s) f(E, \mu, s) (d\sigma_{\perp} + d\sigma_{\parallel}) dk d\Omega_k ds dE d\Omega_p \\
 dQ dk d\Omega_k ds dE d\Omega_p &= n_H(s) f(E, \mu, s) (d\sigma_{\perp} - d\sigma_{\parallel}) \cos 2\psi dk d\Omega_k ds dE d\Omega_p \\
 dU dk d\Omega_k ds dE d\Omega_p &= n_H(s) f(E, \mu, s) (d\sigma_{\perp} - d\sigma_{\parallel}) \sin 2\psi dk d\Omega_k ds dE d\Omega_p
 \end{aligned} \tag{4.2}$$

where ψ , the angle between the old reference plane and the new one, is given by

$$\cos \psi = (\hat{p}_0 \times \hat{k}) \cdot (\hat{r} \times \hat{k}) \tag{4.3}$$

Once this transformation has been performed, the Stokes parameters for the independent elements of the beam may be added together to yield the Stokes parameters for the whole beam. If we denote the aggregated Stokes parameters by $I(k, \Theta, \Phi, s)$, $Q(k, \Theta, \Phi, s)$ and $U(k, \Theta, \Phi, s)$, we can, with a little spherical trigonometry and by integrating over the correct populations, obtain a complete description of the X-rays in the form

Chapter IV: X-Ray Theory

$$\begin{aligned}
 \begin{pmatrix} I \\ Q \\ U \end{pmatrix} (k, \Theta, \Phi, s) dk d\Omega_k ds &= \int_{\eta=0}^{\pi} d\eta \oint_{\hat{\mathbf{p}}_0 \cdot \hat{\mathbf{k}} = \cos \eta} d\mu \int_{E=k}^{\infty} dE \\
 & n_H(s) f(E, \mu, s) \begin{pmatrix} 1 \\ \cos 2\psi \\ \sin 2\psi \end{pmatrix} \begin{pmatrix} d\sigma_{\perp} + d\sigma_{\parallel} \\ d\sigma_{\perp} - d\sigma_{\parallel} \\ d\sigma_{\perp} - d\sigma_{\parallel} \end{pmatrix} dk d\Omega_k ds
 \end{aligned} \tag{4.4}$$

What remains is to express the X-ray intensity and degree of polarization in terms of our three Stokes parameters. The intensity of radiation in the beam is given by the first parameter, I . The degree of linear polarization is given by $\Pi = (Q^2 + U^2)^{1/2} / I$ and the angle between the polarization plane and the reference plane, χ , is given by $\tan 2\chi = U/Q$ (Bekefi 1966, p22).

We note here that we have described a method by which we can obtain the intrinsic characteristics of the flare's X-rays, that is, the characteristics of the radiation at the source. We have not considered the possibility that these characteristics may be modified by scattering of the X-rays between source and observer. The X-rays can be either photo-absorbed or Compton scattered; though for energies above $\sim 15 \text{ keV}$ scattering is the primary mechanism (McKenzie 1975; Langer 1978). The cross-section for Compton scattering decreases with increasing photon energy and is no larger than the classical Thomson cross-section, which has a value of $6.6 \times 10^{-25} \text{ cm}^2$ (Tucker 1975, p153). For an X-ray in the 20 – 100 keV range to be scattered out of its original forward hemisphere it has to pass through at least 10^{24} cm^{-2} of solar material. This places the solar X-ray limb at an altitude of $\sim 300 \text{ km}$ above the visible limb or, which is much the same, in an

Chapter IV: X-Ray Theory

atmospheric region of density $\sim 6 \times 10^{14} \text{ cm}^{-3}$ (McKenzie 1975). The corona and chromosphere, having much smaller densities than this, are clearly transparent to hard X-rays, and those X-rays which are emitted away from the photosphere reach the observer unmodified.

However, flares do not sit very high above the photosphere and it is very difficult for any of the currently available X-ray telescopes to separate those X-rays which are seen directly from those which are seen only after they have been reflected by the solar photosphere. HXIS is the only hard X-ray telescope with the capability to image its source. Its fine field of view has a spatial resolution of $\sim 5000 \text{ km}$ on the sun's surface. This is not sufficient for HXIS to clearly resolve the albedo patch from the X-ray source, yet the albedo patch is bright enough that, at the low energy end of the hard X-ray range, its presence affects the data. An investigation of the effects this reflected contribution has on the measured characteristics is well beyond the scope of this present work and will be left to a later study (Leach, Langer and Petrosian 1984). All the results presented here are understood to refer only to the intrinsic X-rays.

4.2 X-ray bremsstrahlung cross-sections.

Earlier in this chapter we expressed the Stokes parameters in terms of the two cross-sections $d\sigma_{\perp}$ and $d\sigma_{\parallel}$ (*cf.* equation (4.4)). Let us now turn our attention to how these two cross-sections are obtained.

The bremsstrahlung process is one in which an electron makes a transition from an initial state of momentum \mathbf{p}_0 to a final state of momentum \mathbf{p} and, in so

Chapter IV: X-Ray Theory

doing, emits a photon of energy k . The final electron energy states are distributed continuously throughout energy phase space and hence the emission process gives rise to continuum radiation. The cross-section depends upon the square of the absolute value of the matrix element for the transition. The matrix element is an integral over the initial and final electron wave functions and the expression for the scattering potential field. The difficulty in evaluating exact expressions for the emission cross-sections arises from the difficulty of obtaining suitable electron wave functions.

Precise electron wave functions have been obtained only for the two extremes of non-relativistic and ultra-relativistic electrons. Sommerfeld (1931; see also Kirkpatrick and Wiedmann 1945) used the exact non-relativistic Coulomb wave functions and the dipole approximation to calculate the bremsstrahlung cross-sections, but the theory is only meant to apply for β_0 ($= v_0/c$ where v_0 is the incoming electron's velocity) $\ll 1$ (Koch and Motz 1959), so it is not appropriate when the initial electron kinetic energy is greater than a kilovolt or so. At the other extreme, the cross-sections have been calculated using fully relativistic Coulomb wave functions (Bethe and Maximon 1954; Olsen, Maximon and Wergeland 1957; Olsen and Maximon 1959), but these are applicable only to extremely relativistic electrons with energies in excess of about 50 MeV (Koch and Motz 1959; Lee *et al.* 1976).

Cross-sections for the intermediate range of electron kinetic energies (from a few keV to a few tens of MeV) have, so far, been obtained in two ways. The first was by using the Born approximation for the electron wavefunctions. The

Chapter IV: X-Ray Theory

second, and more recent, was by solving numerically the applicable form of the Dirac Equation.

The Born approximation treats the electron transition as being due to perturbations of the electron's wave function, generated by the photon and by the Coulomb field of the proton (Bethe and Heitler 1934; Heitler 1954, pp242). The electron wave functions which one then uses to evaluate the matrix elements are incoming and outgoing plane waves. The perturbation theory is taken to first order and is good provided the expansion parameter is small, *i.e.*, provided

$$\frac{2\pi\alpha Z}{\beta_0}, \quad \frac{2\pi\alpha Z}{\beta_1} \ll 1 \quad (4.5)$$

where $\alpha (= 2\pi e^2/hc)$ is the fine structure constant, $\beta_0 = v_0/c$, $\beta_1 = v_1/c$ and Z is the atomic number of the target material, in our case unity. Hence, the Born approximation formulae should become less reliable as either β_0 or β_1 decreases.

An electron with a kinetic energy of 10 keV has $2\pi\alpha/\beta = 0.24$, which means that we should hesitate before using Born approximation cross-sections with our lowest energy electrons or when the outgoing electron is left with $\lesssim 10 \text{ keV}$ of the initial kinetic energy. For such cases the Born approximation theory can be corrected. By comparing the Bethe-Heitler (1934) Born approximation results with Sommerfeld's exact, non-relativistic results, Elwert (1939) obtained the requisite correction term which has since become known as the Elwert Factor. The correction is given as a renormalization of the cross-sections arising from a renormalization of the electron wavefunctions, and it smoothly extends the use of the Born approximation into the non-relativistic regime.

Chapter IV: X-Ray Theory

The one restriction on the use of Elwert's correction is that, according to the original derivation, it is not designed for the high frequency ("tip") limit (Pratt and Tseng 1975). This limit arises when the photon takes almost all the electron's available kinetic energy and the outgoing electron is left with $\beta_1 \simeq 0$. This high frequency limit turns out to be a very important domain for our problem. A steep electron energy spectrum, such as is often implied by the X-ray observations (*cf.* § 5.1), means that, in general, photons of a particular energy k will tend to have been emitted by electrons with kinetic energies E which are not, on the whole, very much larger than k . An electron with $E \gg k$ has a greater probability of emitting a photon of energy k than does an electron with $E \simeq k$, though this probability is easily outweighed by the greater number of lower energy electrons implied by the observations. Consequently, it is in the tip region of the X-ray spectrum that we would like to have the most precise cross-sections.

The reason that the Born approximation theory cannot be used in the high frequency limit is that, in these situations, the field of the proton (or nucleus) strongly distorts the outgoing electron wave function from that of a plane wave (Elwert and Haug 1969). The Born approximation cross-sections vanish in the limit $k \rightarrow E$ whereas cross-sections based upon the exact point-Coulomb wave functions do not.[†] First order results correcting the Born approximation theory in this "tip" region were obtained by Fano, Koch and Motz (1958) and Fano (1959).

[†]Actually, for the more realistic case of a screened potential, the cross-sections eventually do vanish when the outgoing electron has a low enough energy. Calculations suggest that this does not occur until the outgoing electron energy is less than ~ 100 eV (Pratt and Tseng 1975). This behavior occurs over too small an energy interval to be of any significance to our current work.

Chapter IV: X-Ray Theory

Ten years later, Elwert and Haug (1969) extended Elwert's original (1939) results to take them into the high frequency limit. They re-evaluated the Elwert Factor and this time expressed it as a function of the emission angle η . They found that, for low Z elements and for k not too close to E , the re-evaluated correction is approximately constant for all values of η and has a value equal to that of the original Elwert Factor. As k approaches E , the correction remains constant and equal to the Elwert Factor for those values of η over which most of the photons are emitted. In the limits of forward and backward emission, the correction becomes larger than the Elwert Factor, though the overall cross-section remains relatively small. We conclude, then, that the Elwert Factor successfully extends the use of the Born approximation theory into the two important domains excluded by equation (4.5); that is, the high frequency and non-relativistic limits.

More recently, it has become possible to solve numerically the relativistic Dirac equation for an electron in a Coulomb field, and to do so with a high degree of accuracy. In a series of papers (Tseng and Pratt 1970; 1971; 1973; 1974; Pratt and Tseng 1975 and Lee *et al.* 1976) Tseng, Pratt and their co-workers evaluated the bremsstrahlung cross-sections for initial electron kinetic energies ranging from 1 *keV* up through 5 *MeV*. They compared their results with the Born approximation formulae at all values of the emission angle from 0 to π and for all values of x ($= k/E$) between 0 and 1. They believe that their numerical inaccuracies are no more than $\sim 1\%$ and that in most cases they are better than 0.5% (Tseng and Pratt 1971).

The outcome of their considerable body of work is that the corrected Born approximation formulae are shown to be good (to within a few percent in most

Chapter IV: X-Ray Theory

situations) for small values of Z and over a broad range of energies (Tseng and Pratt 1973; Lee *et al.* 1976). They claim good agreement of their many results with some recent experiments (Tseng and Pratt 1973; Kuckuck and Ebert 1973; Tseng and Pratt 1974), though there is a shortage of experimental data, especially polarization data, in the correct energy range suitable for such a comparison. They support the work of Elwert and Haug (1969), showing that the Elwert correction serves well in the high frequency limit, especially for low values of Z (Tseng and Pratt 1971; Pratt and Tseng 1975). They note that there is a discrepancy between the theory (Fano, Koch and Motz 1958; Fano 1959; Elwert and Haug 1969) and the experimental results (Starek, Aiginger and Unfried 1972) pertaining to emission at the tip of the spectrum, with the experiments indicating higher cross-section values than the theory by a factor of roughly 2 – 4 (Pratt and Tseng 1975). They note that their results, agreeing with the theory and not the experiments, leave the discrepancy unresolved.

The outcome of all this is that the Born approximation results seem able to serve our needs here. They have been thoroughly studied and would appear to have an accuracy which is commensurate with the accuracy of the electron results described in Chapters II and III. For the two bremsstrahlung cross-sections, then, what we need are Born approximation expressions which are appropriate for electrons in the range of several keV to MeV and which are differential in the incoming electron's energy, photon energy and emission angle. Suitable cross-sections have been obtained by Gluckstern and Hull (1953) and, notwithstanding the criticism of Starfelt and Koch (1956) who claim that the Gluckstern and Hull cross-sections do not hold well outside the low frequency limit, they have been

Chapter IV: X-Ray Theory

supported by the work of Fronsdal and Überall (1958) and by Tseng and Pratt (1973). The Gluckstern and Hull cross-sections do, still, require the Elwert Factor correction.

In addition to electron-proton bremsstrahlung there will be a contribution to the X-ray production from electron-electron bremsstrahlung (Joseph and Rohrlich 1958). However, the electron-electron system has no dipole moment and the bremsstrahlung cross-sections, evaluated by the usual dipole approximation, subsequently vanish. Calculations extending beyond the dipole approximation are exceedingly complicated because of the exchange character of the electron-electron interaction. The available results indicate that electron-electron bremsstrahlung will make a significant contribution (of order 25%) to the total X-ray output only at photon energies above several hundred keV, and then only for the forward photons produced by a highly anisotropic distribution of source electrons (Haug 1976). In all other cases the spectral index of the total X-ray flux does not significantly change (Starfelt and Koch 1956; Koch and Motz 1959; Haug 1976). Hence, we shall not need to consider further this uncertain contribution to the X-ray bremsstrahlung.

We now have our complete method. We have a flaring loop through which passes a beam of electrons. The beam is fully described at each point by the number distribution function $f(E, \mu, s)$ which is obtained numerically as the solution to our major equation, the Fokker-Planck Equation. These beam electrons generate X-rays according to the cross-sections described above and the X-ray information can be expressed in terms of a Stokes parameter representation. We are now

Chapter IV: X-Ray Theory

in a position where we can select any non-thermal model description of a flare, incorporate its physical characteristics into the coefficients in the Fokker-Planck Equation and calculate the corresponding characteristics of the X-rays produced.

Chapter V

The X-Ray Results

In this chapter, which is divided into two sections, we discuss hard X-rays within the framework of non-thermal models. In § 5.1 we survey the literature pertaining to the characteristics of the impulsive hard X-rays from a solar flare. We discuss the theoretical estimates of the X-ray polarization, directivity and spectrum, and the pertinent X-ray observations. We survey only that literature concerning the X-ray results for a spatially unresolved flare, leaving a discussion of theoretical and observational work on the X-ray spatial structure to the next chapter. In § 5.2 we present the hard X-ray characteristics as calculated for a series of flare models according to the method explicated in Chapters II, III and IV. We choose one model to act as a reference and for this we describe our X-ray results in some detail. We then discuss our other model results, focussing primarily on how the X-ray characteristics change in response to the difference in model parameters.

With this presentation of our results we greatly expand upon the hitherto available, primarily qualitative, theoretical understanding of non-thermal model impulsive hard X-rays. We give a quantitative evaluation of the correlations between the X-ray characteristics and the model parameters. We also demonstrate that each X-ray characteristic on its own has only a limited ability to indicate the

Chapter V: X-ray Results

values of the source model parameters. Thus we favor coordinated observational programs which simultaneously measure several of the X-ray characteristics over uncoordinated programs aimed at measuring just one of the flare's X-ray characteristics.

5.1 Literature Survey.

Much of the active dispute in the study of solar flares revolves around the question of whether the processes giving rise to the observed hard X-ray bursts are thermal or non-thermal in nature. Models of increasing sophistication have been studied and observations of increasing resolution and reliability have been collected. Despite this the major controversy (thermal or non-thermal?) still exists, partly because of the lack of a clear understanding of how to use the observations to put constraints upon the models. The literature contains some dispute as to the X-ray characteristics expected from non-thermal models, viz. how large a directivity and polarization to expect and what the X-ray spectrum can tell about the energy spectrum of the source electrons. We shall now survey briefly the literature pertaining to the X-ray characteristics from non-thermal models and shall compare the theoretical results with the experimental measurements where available.

Polarization and Directivity:

In 1968, Elwert recognized that the impulsive hard X-rays emitted by an anisotropic electron distribution would be polarized, and that X-ray polarization

Chapter V: X-ray Results

observations would be a suitable means of determining the nature of the source electron population (Elwert 1968). In a series of papers (Elwert and Haug 1970; 1971; Haug 1972) Elwert and Haug calculated the X-ray polarization and directivity from a beam of electrons in which all the electrons moved along a vertical magnetic field and had the same, unchanging pitch angle α^\dagger . For the particular case $\alpha = 0$ they obtained X-ray anisotropies (the anisotropy being expressed in the form J_{max}/J_{min} where J_{max} , J_{min} are the X-ray intensities in the directions of maximum and minimum emission, respectively) which increased from ~ 7.5 at 10 keV up to ~ 120 at 300 keV . The polarization changed only slightly with X-ray energy and was $\sim 70\%$ at 50 keV . The X-ray anisotropy fell as the electron's pitch angle was increased and it almost disappeared (was ~ 1.4 at 50 keV) for the case $\alpha = 90^\circ$. The degree of polarization also fell but not by as much. It stayed at $30 - 50\%$ reflecting the high anisotropy of an electron distribution where all the emitting electrons have the same pitch angle.

The next step forward in complexity was to allow for changing electron pitch angle. Brown (1972) used a mean scattering treatment to imitate the effects of Coulomb scattering of the beam electrons by the flaring plasma. The scattering treatment calculated a mean energy and pitch angle for the electrons at each

[†]The physical situation corresponding to unchanging electron pitch angle is known as the "thin-target" approximation. The electron beam is considered to be passing through a sufficiently tenuous background plasma that the effects of Coulomb collisions on the beam electrons are negligible. The corresponding X-ray results are known specifically as thin target results. The alternate situation, known as the "thick-target" case, considers the electron beam to pass through enough of the background plasma for the collisions to change the electrons' energies and pitch angles. In the limit of large plasma column thicknesses the electron beam is completely absorbed. The corresponding X-ray results are known as thick-target results.

Chapter V: X-ray Results

depth but could not introduce dispersion. Brown's beam electrons were injected with a pitch angle of zero degrees into a vertical magnetic structure. He obtained X-ray directivities ($J(\Theta = 0^\circ)/J(\Theta = 90^\circ)$ for viewing angle Θ) of ~ 2 at 10 keV increasing to ~ 6 at 150 keV and degrees of polarization ranging from $\simeq 30\%$ at 10 keV to 45% at 150 keV . By comparing the results he obtained for models with and without the inclusion of his scattering treatment, he estimated that the inclusion of scattering made the X-ray polarization fall to approximately half the values obtained for the models without scattering. He noted that the polarization also fell slightly with a flattening of the electron energy spectrum but he claimed that this did not have a significant effect upon his results.

These two studies form the principle bodies of work aimed at calculating the intrinsic X-ray polarization and directivity for the thin and thick target cases. Three more-recent studies included the contributions of the photospheric albedo (Hénoux 1975; Langer and Petrosian 1977; Bai and Ramaty 1978). Of the X-ray flux which is incident upon the photosphere, as much as 70% at peak reflection energies ($20 - 40 \text{ keV}$) and much less at higher and lower energies (Santangelo *et al.* 1973) can be turned around to join with the flux which was initially directed away from the solar surface. But if the original X-ray source directs many more times the number of X-rays down into the sun than it does away from it, the reflected contribution can have a large affect on the observed X-ray characteristics. All three studies found that the albedo contribution significantly reduced the X-ray directivity from that in the source, especially at photon energies of 50 keV or less, but that it had a smaller effect upon the degree of polarization. They obtained

Chapter V: X-ray Results

polarizations for the observed X-ray flux in the range 30 – 50% which was of the same order as that for the sources they used.

These early attempts to quantify the expected degree of polarization were, necessarily, based upon idealized flare models. They used highly anisotropic electron distributions and linear flare geometries, not because these are demanded by experimental data but because of the need to simplify the mathematical treatment. Together these works suggest that the impulsive hard X-rays should typically have an anisotropy of order 2 – 3 and polarizations of order 30 – 40%. However, the simplified loop geometries and electron distributions used must mean that these values can only be taken as upper limits and that they may not reflect the true potential of X-ray measurements from flares. Giving due allowance to the model simplifications Korčák (1974) suggested that a thorough and realistic treatment might obtain lower polarizations, closer to 20%. Hudson is reported to have been more skeptical (see Brown 1972, p443). He expected that a complete treatment which allowed for the total absorption of the electron beam by the flaring plasma would obtain much smaller, if not negligible, directivities and polarizations altogether.

Observations of flare impulsive hard X-ray directivities and polarizations, as they stand, are far from definite. It is not possible to surround an individual flare with many X-ray telescopes and to measure directly the variation of X-ray intensity with flare orientation. Kane and his co-workers have reported stereoscopic observations of eight flares using X-ray telescopes onboard the ISEE - 3 and PVO spacecraft (Kane *et al.* 1980). The difference in viewing angle of the two spacecraft varied from 13° to 79° among the eight flares. A comparison between

Chapter V: X-ray Results

the observations from the two telescopes showed that the sizes of the flares as measured by each telescope differed only slightly. These discrepancies could be accounted for by different albedo contributions and by the calibration uncertainties between the two spacecraft. The conclusion drawn from the study was that the observations were consistent with isotropic X-ray emission in the energy range 50 – 100 keV.

An alternative approach to measuring the X-ray directivity is to resort to a statistical study, using as many flares as possible, of the frequency of observation of flares at different positions on the disk. However, there is a wide variation in intrinsic flare parameters from flare to flare and there can be no certainty that a statistical study will tell much unless it draws upon an enormous base of data (Brown 1975). The earliest of such statistical studies used a small sample of X-ray flares seen at hard and soft X-ray energies. Two studies selecting from a common database (Ohki 1969; Pintér 1969) obtained different results. Ohki found a strong decrease in the number of observed hard X-ray flares with increasing heliographic angle whereas Pintér found the distribution to peak at a heliographic angle of 40° – 50°. In addition to this discrepancy, the X-ray observations did not themselves record the position of the flare on the solar disk. The times of occurrence of the X-ray bursts were compared with those of H α flares listed in *Solar-Geophysical Data*, and the X-ray bursts were associated with the H α flares on the basis of time coincidence. It is, therefore, important to allow for the distribution of H α flares across the sun's disk. The probability of seeing an H α flare varies quite strongly with the flare's central meridian distance (CMD) and decreases with increasing CMD (Drake 1971). Of the sizeable fraction of Ohki's and Pintér's initial sample

Chapter V: X-ray Results

of X-ray bursts which could not be associated with any of the reported $H\alpha$ flares, the chances are that many of them came from flares occurring near the solar limb. The distribution of $H\alpha$ associated X-ray bursts, therefore, does not represent the distribution of the X-ray burst frequency. Neither Ohki nor Pintér allowed for this $H\alpha$ CMD variation. Drake (1971) made this allowance and obtained no significant dependence of the X-ray burst occurrence on heliographic longitude. His conclusion was that there was no evidence for emission directivity. This was supported by two further studies both of which were, again, based upon rather a small number of flares (Phillips 1973; Pizzichini, Spizzichino and Vespignani 1974).

Kane, in summarising the pre-1974 studies, concluded that there was no clear indication of anisotropic emission for the impulsive hard X-rays (Kane 1974). Datlowe and his coworkers (Datlowe, Elcan and Hudson 1974; Datlowe and Hudson 1975) found no significant variation in the relative frequency of observation of hard X-ray bursts with longitude, using a collection of 123 bursts seen by OSO - 7. In a later, more thorough, study (Datlowe *et al.* 1977) an upper limit was put on the amount of limb brightening or darkening observed. Using measurements of the burst brightness at 20 keV, the estimate of the variation in flare brightness from disk center to limb was 1 (+63, -40)% at the 95% confidence level. All told, the consensus on the observed degree of anisotropy is that there isn't any, but the uncertainty in this result is high.

The polarization results are every bit as unclear. Early measurements of 20 - 40% polarizations made by instruments onboard the Intercosmos series of satellites (Tindo *et al.* 1970, 1972a,b; Tindo, Mandel'stam and Shuryghin 1973. See also Nakada, Neupert and Thomas 1974; Thomas 1975) were criticised by Brown,

Chapter V: X-ray Results

McClymont and McLean (1974) for the way that the in-flight calibration had been performed. The polarimeter was calibrated on the assumption that the gradual emission from the decay phase of flares would be unpolarized. The objection was that, though the intrinsic radiation might well be unpolarized, the albedo radiation would not be, and that the sum of the two would be polarized. The criticism was rejected by Mandel'stam, Beigman and Tindo (1975) on the basis that this effect would be too small. The rejection was supported by the calculations of Hénoux (1975) who showed that the resultant polarization from an isotropic source would be $\sim 5\%$, and by a later series of measurements (Tindo, Shuryghin and Steffen 1976) obtaining less than 5% polarization during the decay phase of a flare. But, though the initial criticism was illfounded, it is still not clear that the earlier Intercosmos results are at all reliable (Mandel'stam, quoted in Emslie 1981b, but see also Brown 1975 and Kahler 1975)

The most conclusive assessment of the Intercosmos polarization results has been given by Somov and Tindo (1978). They quoted the results from observations of thirteen flares and from these selected three which they claimed to be clean results. They reported polarizations of $40\% \pm 20\%$, $16\% \pm (5 - 8)\%$, and $21\% \pm (5 - 8)\%$. These can be taken to indicate that some polarization is present (at the 20% level) though just how much remains undetermined. The polarization vectors for these measurements were closely aligned with the directions connecting each flare to the center of the solar disk. This is in agreement with the predictions of non-thermal modelling and would indicate that the albedo contribution was not significant (Kahler 1975). But, in another review (Haug 1982), the polarization vector is reported to have shown large fluctuations in time and this is taken to

Chapter V: X-ray Results

indicate unreliability in the results. However, another interpretation of the large fluctuations could be that the individual bursts, occurring during the long integration time of the measurements, might have come from different loop structures and that this would have caused the vector's direction to fluctuate rapidly. Obviously, the Intercosmos results do not stand well alone and need to be either corroborated or refuted by other, more reliable, measurements.

We have recently been apprised of polarization measurements of solar flares made by an instrument onboard the Space Shuttle Columbia (Tramiel, Chanan and Novick 1984). The polarimeter resolved 5 – 21 keV X-rays into nine energy channels and had five second time resolution (Lemen *et al.* 1982). However, again, the in-flight calibration method is questionable. The device was calibrated on the assumption that the X-rays from a flare located at disk center would have to be unpolarized, and this need not be the case. The details of these observations and their interpretation by non-thermal flare modelling are given in Chapter VI. In brief, the measurements indicated flare polarizations of $3.4 \pm 2.2\%$ which were taken as being consistent with emission from either an isotropic thermal source or from a non-thermal model source with an isotropic injected beam.

X-Ray Spectrum:

Since the very earliest (balloon-borne) measurements of solar flare hard X-rays (Peterson and Winckler 1959; Vette and Casal 1961; Winckler, May and Massey 1961; Anderson and Winckler 1962, 1963; Bowen *et al.* 1964; Culhane *et al.* 1964) attempts have been made to determine the nature of the X-ray spectrum. Of

Chapter V: X-ray Results

concern was whether the X-rays came from a source of electrons with an isothermal Maxwellian or a power law spectrum, as this would be an indication of the type of physical processes active in a flare. The reasons for choosing these two types for categorizing the spectra is that they are the simplest types of spectra to use. They are both two parameter fits and the early data did not have sufficient energy resolution or accuracy to warrant better.

Reviews of the observations (Kane and Anderson 1970; Kane 1974; de Feiter 1975; Brown 1975; 1976; Kane *et al.* 1980b; Haug 1982) have concluded that most impulsive phase hard X-ray spectra are not indicative of an isothermal source. If a multi-temperature thermal plasma were to be invoked, then temperatures well in excess of $10^8 K$ would be required (Brown 1974; Crannell *et al.* 1978; Elcan 1978). Such high temperatures do not necessarily militate against thermal models. Given that enough energy is released to power the flare and that this energy is initially released in very small volumes, such high temperatures are plausible (Brown and Smith 1980).

However, neither are the X-ray spectra always simple power laws. The best fits are often to a double power law spectrum

$$\begin{aligned}
 J(k) &\sim k^{-\gamma_1} & 10 \text{ keV} \leq k \leq k_0 \\
 J(k) &\sim k^{-\gamma_2} & k_0 \leq k
 \end{aligned}
 \tag{5.1.1}$$

where $J(k)$ is the photon number spectrum per unit photon energy k . The break energy lies in the range $70 \text{ keV} \leq k_0 \leq 120 \text{ keV}$ (Kane and Anderson 1970), the low energy spectral index in the range $2 \leq \gamma_1 \leq 7.0$ with $\gamma < 3$ and $\gamma > 5.5$ being very rare (Kane and Anderson 1970; Lin and Hudson 1971; Frost and Dennis 1971;

Chapter V: X-ray Results

Peterson, Datlowe and McKenzie 1973; Datlowe *et al.* 1977; Kane *et al.* 1980b; Haug 1982), and the break in the index is $\gamma_2 - \gamma_1 \sim 2$ (Brown 1972). Occasionally the power law behavior is seen to extend down below 10 keV (Kahler and Kreplin 1971; Peterson, Datlowe and McKenzie 1973), and in a very large flare can extend to many hundreds of keV (Chupp, Forest and Suri 1975; Hoyng, Brown and van Beek 1976; Lin and Hudson 1976). There is some dispute as to whether or not very large flares generally have harder spectra. Several summaries have shown very little correlation between the peak flux and the spectral index (Kane, Frost and Donnelly 1979; Kane *et al.* 1980b). Despite this, the large events of August 1972 did have appreciably harder spectra (Chupp, Forest and Suri 1975; Hoyng, Brown and van Beek 1976).

The theory behind X-ray production is well understood and, consequently, obtaining the X-ray spectrum from a known distribution of source electrons is quite straightforward. If the flux distribution of the emitting electrons is $N(E) \sim E^{-\delta}$ per unit electron kinetic energy E , and if the non-relativistic Bethe-Heitler cross-section is used, then the X-ray spectrum is

$$J(k) \sim \int_{E=k}^{\infty} \frac{1}{kE^{\delta+1}} \ln \left(\frac{1 + \sqrt{1 - k/E}}{1 - \sqrt{1 - k/E}} \right) dE \sim k^{-\gamma_1} \quad (5.1.2)$$

with $\gamma_1 = \delta + 1$ (Holt and Ramaty 1969; Syrovat'skii and Shmeleva 1972; Brown and McClymont 1975). Alternately the X-ray spectrum may be obtained not from the distribution of the source electrons but from the distribution of the injected electrons. The injected distribution is related to the overall distribution of electrons in the source by the assumption that the energetic electrons eventually

Chapter V: X-ray Results

lose all their energy through Coulomb collisions. If the injected electrons have the distribution $F_0(E) \sim E^{-\delta_1}$, then the X-ray spectrum obtained is again $J(k) \sim k^{-\gamma_1}$ but with $\gamma_1 = \delta_1 - 1$ (Brown 1971; Hudson 1972; Brown and McClymont 1975). Consequently, a power law X-ray spectrum has come to indicate a power law spectrum for the electrons, either in the source or at injection (Haug 1982).

Improving the theoretical sophistication means that the X-ray spectrum calculated for the above electron distributions changes. If the relativistic X-ray cross-section is used and the spectrum is measured for different viewing angles, the relationship between γ_1 and δ/δ_1 can change by as much as $\simeq 1.0$ (Brown 1971, 1972; Petrosian 1973). If we allow for the presence of neutral Hydrogen in the chromosphere the collisional evolution of the electron beam is changed. This results in a small change in the X-ray spectrum (Brown 1973a).

Several affects can be included which will tend to produce a knee in the X-ray spectrum. The knee may arise from a cutoff in the electron number distribution at an energy of roughly 100 keV (Kane and Anderson 1970), an increased probability of escape for the higher energy electrons or their greater synchrotron losses (Elwert and Haug 1971), the relativistic beaming of high energy photons (Petrosian 1973) and/or the effects of the photospheric albedo (Tomblin 1972; Santangelo *et al.* 1973; Langer and Petrosian 1977; Bai and Ramaty 1978). The spectral knee may also arise if not all the source is fully visible. The visible part of a source which is partially obscured from view, such as can occur when the flare is located just behind the solar limb, will not necessarily have an electron energy distribution which is a single power law even if the injected and whole-source distributions are. The electron distribution for a partially occulted source will be steeper at high

Chapter V: X-ray Results

energies than at low energies and this will lead to a concomitant X-ray spectral break of $\gamma_2 - \gamma_1 \simeq 2$ (Brown and McClymont 1975). This may also be the source of the observed steepening of spectra as flares cross the limb (Datlowe, Elcan and Hudson 1974; Datlowe 1975; Datlowe and Hudson 1975; Roy and Datlowe 1975; but see also Datlowe *et al.* 1977; Hudson 1978).

The inverse problem, that of obtaining the electron spectrum from the observed photon spectrum, is not as trivial as the above studies would have us expect. It has been suggested that the inverse problem is comparatively ill-posed (Craig and Brown 1976; Brown 1978). A small uncertainty $\sim 5\%$ in the determination of the photon spectrum can translate into a large uncertainty $\sim 100\%$ in the derived electron spectrum (Craig and Brown 1976). This would imply that widely different electron distributions would be able to generate similar photon spectra. In this case a power law X-ray spectrum need not imply a non-thermal source for the electrons. Forms other than a simple two parameter fit for the electron spectrum can be satisfactorily applied to the observations (Brown 1974, 1975; Craig 1975). Though the overall electron spectrum for these multitemperature thermal fits is not widely different from a straight power law spectrum, they do imply different physical processes occurring in the flare. As the motivation behind studying the X-ray characteristics in the first place was to use them to determine the nature of these processes, it would appear that the X-ray spectrum is not a good source of information on the X-ray producing electrons. This has, indeed, been supported by Hoyng, Melrose and Adams (1979) who find that power law X-ray spectra are generated by many different electron distributions and that these spectra are, therefore, insensitive to the details of the processes active in a flare.

Chapter V: X-ray Results

This brief literature survey has shown several things. It was initially hoped that X-ray observations could be used to determine whether the processes active in a flare conformed more to the thermal or non-thermal type of model. Based upon studies having different degrees of simplicity and upon the available observational data it has been shown that:

the X-ray directivity is strongly affected by the photospheric albedo and is very difficult to measure satisfactorily, either directly or indirectly.

the X-ray spectrum is too general a characteristic and, tending to fall steeply with photon energy, is not easy to measure accurately.

the X-ray polarization may be as high as 30 – 40% but is probably lower. Theoretical polarization estimates suffer from the conflicting requirements of accuracy and tractability and there is no body of clearly reliable observations upon which to rely.

There may be hope for reliable polarization measurements in the near future and for these to be of any value they must be accompanied by a full and thorough theoretical analysis of the polarization which can be expected according to the models. Other than this, an alternate method by which the X-rays can be used to indicate a preference for one or the other type of model is to turn to the X-ray height distribution (Emslie and Rust 1980). In the following section we shall give the results of our study of the X-ray characteristics according to non-thermal models. We shall describe our results for the X-ray spectrum, directivity and polarization, and shall describe the behavior of these and the X-ray intensity as functions of source position within the flare. In Chapter VI we shall take up again

Chapter V: X-ray Results

the idea of using the X-ray height distribution to discriminate between models and shall show that it can, in fact, give much more information than simply categorize flares.

5.2 X-ray characteristics from non-thermal models.

We now look at the characteristics of the X-rays calculated from a variety of our flare models. In this manner we are able to obtain a general picture of the X-ray characteristics to be expected of flares, and to explore the correlations between the X-ray characteristics and the flare model parameters.

The reference frames:

Our information about the hard X-rays is obtained through the Stokes parameter formalism, as explained in Chapter IV. This requires the specification of an observation frame and a reference plane. We shall define a global reference frame for the observations, which is that frame containing the flare loop in the \hat{y}, \hat{z} plane and the (planar) photosphere in the \hat{x}, \hat{y} plane (*cf.* Figure (5.1)). We define the two viewing angles Θ and Φ as shown, with Θ being the polar and Φ the azimuthal angular coordinates of a photon having a direction of propagation \hat{k} and an energy k (in units of $m_e c^2$). The polar axis is the outward normal to the surface of the sun and zero azimuthal angle corresponds to the positive \hat{y} direction. The reference plane for locating the direction of the polarization vector is the one containing \hat{k} , or the direction of observation, and the surface normal \hat{z} .

Chapter V: X-ray Results

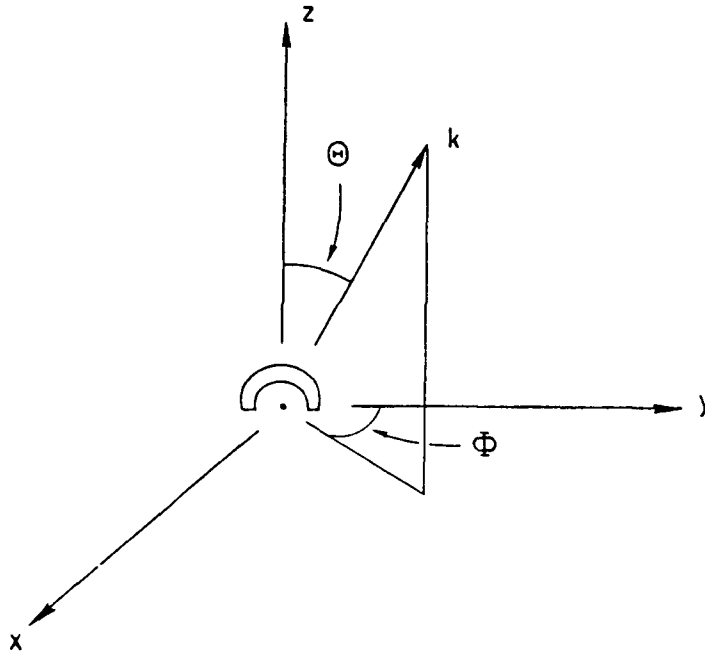


Figure 5.1. The orientation of the flare loop within the global observation frame. The (planar) solar surface is the x,y plane and the loop is in the y,z plane. Shown also are the observation angles Θ and Φ for a photon with direction k . The global observation frame is the frame used when discussing the spatially unresolved X-ray results for the whole loop.

Whenever we discuss the radiation from the loop as a whole we shall, implicitly, be talking about the radiation as measured in this global observation frame. In these cases we shall have no need for any spatial resolution of the flare loop and so we shall treat the whole loop as if it were a point source. We then obtain the Stokes parameters for the whole loop by simply adding together the Stokes parameters from each position along the loop, thereby ignoring the small source displacements (and the corresponding small variation in observation angles) which arise by virtue of the finite size of the loop.

Chapter V: X-ray Results

To investigate the behavior of the X-ray characteristics as functions of source depth we divided the whole loop up into adjoining segments. By virtue of the symmetry of the loop about the \hat{x}, \hat{z} plane we concern ourselves only with one half of the loop and we choose that half which projects into the positive \hat{y} half-space. We divide the coronal portion of the loop into m segments for which each segment is an arc of length $90/m$ degrees. At the end of the coronal portion (the end of the m^{th} segment) the magnetic field direction is vertical and remains vertical as the loop penetrates deeper in toward the photosphere. This chromospheric part of the loop is then divided into a number of contiguous vertical segments.

In the next chapter it will be necessary to ensure that the loop has length and density specifications which match the values indicated by observations. But, as we found in Chapter III, the best measure of location within the loop is not the spatial distance s (cm) of any point but its accumulated column depth N (cm^{-2}). We therefore specify the X-ray source heights by the source segment and to each segment we assign a mean column depth. This mean column depth is the column depth of a point half way along the length of the segment. Describing the radiation in terms of the overlying column depth N removes the obfuscating effects of the rapid change in background plasma density and hence emission intensity per unit volume or distance which is encountered upon crossing the transition region from the corona into the chromosphere (*cf.* Figure (1.1)).

At times we find it convenient to use a dimensionless measure of the column depth, just as we did in Chapter III. When looking at the evolution of the electron beam within the plasma we saw that its behavior at different energies was similar if the depth parameter was suitably scaled. The depth parameter we used we

Chapter V: X-ray Results

named τ and it was related to the column depth N by $\tau = 4\pi r_0^2 \ln \Lambda N$, with a mean value chosen for $\ln \Lambda$. The inspiration for this came from the equations (2.32) and (3.1.12) with $n ds$ replaced by dN . We now attempt a similar scaling of the column depth and we shall find that its usefulness is, indeed, borne out by the X-ray results themselves. As in Chapter III we use the scaling $\tau = N/N_0$ with $N_0 = 5 \times 10^{22} \text{ cm}^{-2}$.

We need to define the observation frames for each loop segment. The global observation frame defines a polar axis (the \hat{z} direction) for the loop as a whole, and is the most appropriate and yet versatile observation frame for when we compare our results with data from spatially unresolved flares. The source of the X-rays, however, is the electron beam and the direction in space which is the natural axis for describing the beam electrons is the direction of the loop magnetic field. The motion of the electrons is such that at each point along the flare loop we have azimuthal symmetry of the electron number distribution about the magnetic field direction. As shown by Haug (1972), when the electron distribution is symmetric about an axis, the third Stokes parameter \mathcal{U} , taken with reference to the frame containing the axis of symmetry, is identically zero. This condition implies that the plane of polarization is either in the plane containing the photon and the axis of symmetry or is perpendicular to it.

For the chromospheric part of the flare loop the polar axis of the global observation frame coincides with the axis of symmetry of the electrons, *i.e.*, the magnetic field direction. This is not so for the coronal part of the loop. In the corona the magnetic field changes direction continuously but smoothly. When we

Chapter V: X-ray Results

divide the coronal loop into its m segments, each segment has only a relatively small amount of curvature and has a mean magnetic field direction which is the direction of the magnetic field at the middle of the segment (*cf.* Figure (5.2)). Thus in each segment there is only a relatively small asymmetry about this mean direction. If we now define, for each segment, a local observation frame which takes the mean magnetic field direction as its polar axis, and if we refer the Stokes parameters for each segment to the plane containing the photon and the local polar axis, then we shall find that for each segment the third Stokes parameter is small relative to the second. The physical interpretation of this is that, in each local frame, the plane of polarization is close to being either parallel to or perpendicular to the local reference plane. Henceforth whenever we discuss the variation with source height of the X-rays we shall implicitly be referring to the local observation frames. For the chromospheric part of the loop the local and global frames coincide.

We shall not quote the results in the form of the values of the Stokes parameters themselves. Instead we shall present the results in the more usual forms employing the directivity, degree of linear polarization, spectral index and relative intensity of the radiation.

Directivity:

The directivity $\Delta(k, \Theta, \tau)$ is a measure of the anisotropy of the radiation intensity and, in the literature, can be found to be defined in any of several ways. The definition we shall adopt is

$$\Delta(k, \Theta, \tau) = \frac{I(k, \Theta, \Phi, \tau)}{\bar{I}(k, \tau)} \quad (5.2.1)$$

Chapter V: X-ray Results

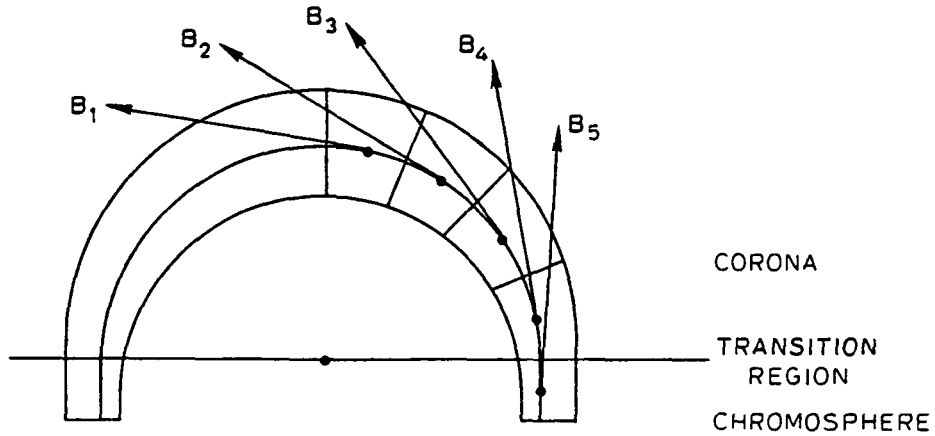


Figure 5.2 The division of the loop into segments, and the magnetic field directions at the mid-point of each segment. These directions are the polar axes of the local observation frames. Owing to the only small amount of loop curvature in each of the coronal segments the Stokes parameters in the local observation frames are essentially independent of the azimuthal angle Φ . These local observation frames are the ones used when we discuss the evolution of the X-ray characteristics with depth within the flare. For the chromosphere ($N > 2.4 \times 10^{18} \text{ cm}^{-2}$) the local and global observation frames coincide. For all local and the global frames the \hat{x} directions coincide.

where $I(k, \Theta, \Phi, \tau)$ is the first Stokes parameter and

$$\bar{I}(k, \tau) = \frac{1}{4\pi} \int_{\Omega} I(k, \Theta, \Phi, \tau) d\Omega(\Theta, \Phi). \quad (5.2.2)$$

Owing to the near azimuthal symmetry of the X-rays in the local observation frames, $I(k, \Theta, \Phi, \tau)$ barely depends upon Φ . The results do not warrant an exposition of their variation with this azimuthal angle and, when we give our results, we shall select for quotation the values at $\Phi = 90^\circ$ (the \hat{x} direction, which coincides for all the local and the global frames). We shall often find use for a directivity ratio $d(k, \tau)$, a more transparent measure of the radiation anisotropy. This

Chapter V: X-ray Results

we define as the ratio of the maximum to minimum values of $\Delta(k, \Theta, \tau)$ taken over the whole range of θ .

$$d(k, \tau) = \frac{\max_{0 \leq \Theta \leq \pi} (\Delta(k, \Theta, \tau))}{\min_{0 \leq \Theta \leq \pi} (\Delta(k, \Theta, \tau))}. \quad (5.2.3)$$

Using the directivity ratio allows us to more easily present the results for many models.

Polarization:

The degree of linear polarization $\Pi(k, \Theta, \tau)$, which is the percentage excess of the radiation which is polarized perpendicular to the plane of polarization above that which is polarized parallel to it, is obtained from the Stokes parameters in the form

$$\Pi(k, \Theta, \tau) = \pm \frac{\sqrt{Q^2(k, \Theta, \Phi, \tau) + U^2(k, \Theta, \Phi, \tau)}}{I(k, \Theta, \Phi, \tau)} \quad (5.2.4)$$

(Chandrasekhar 1960, p33). When quoting the results in the text we shall often refer only to the maximum value of the polarization, namely

$$p(k, \tau) = \max_{0 \leq \Theta \leq \pi} \Pi(k, \Theta, \tau). \quad (5.2.5)$$

The sign of Π is determined by the angle of inclination of the polarization vector to the reference plane. This angle we call χ and it is given by

$$\chi = \frac{1}{2} \tan^{-1} \left(U(k, \Theta, \Phi, \tau) / Q(k, \Theta, \Phi, \tau) \right) \quad (5.2.6)$$

Chapter V: X-ray Results

for $0 < \chi < \pi/2$ (Chandrasekhar 1960, p33). Owing to the definition of the local observation frames which we are using we find $|\mathcal{U}| \ll |\mathcal{Q}|$ and the polarization vector is either nearly perpendicular ($\chi \simeq \pi/2$) or nearly parallel ($\chi \simeq 0$) to the reference plane as \mathcal{Q} is either positive or negative. In equation (5.2.4) Π , therefore, has the sign of \mathcal{Q} .

One final word while we are setting up the terminology for the discussion of the X-ray results. In studies of X-ray cross-sections one of the primary variables in terms of which a photon is described is its hardness x , where x is the ratio between the energy k of the photon under consideration and the energy E of the particle which emitted it, *i.e.*, $x = k/E$. Cross-sectional results are as often presented in terms of x and E as they are in terms of k and E . The terminology describes photons for which $x \sim 1$ as being “hard” and photons for which $x \sim 0$ as being “soft”. Unfortunately, this terminology conflicts to some extent with solar physics terminology for which the terms “hard” and “soft” X-rays refers to X-rays of energy greater than or less than a characteristic energy usually taken to be 10 keV. This conflict in the terminology can be the source of some confusion and we shall, therefore, now specify the sense in which the words “hard” and “soft” are used in the coming discussion of our X-ray results.

When discussing the production of X-rays by the beam electrons there is no adequate substitute for the variable $x = k/E$. This variable is the one in terms of which the X-ray characteristics are most easily understood and upon which they most strongly depend. For this reason the terms “hard photons” and “soft photons” will always refer to photons for which $x \sim 1$ and $x \sim 0$, respectively. When discussing X-ray observations and particularly when comparing flare X-rays with

Chapter V: X-ray Results

other flare emissions, for example, microwaves or Type III bursts, the behavior of high energy ($\geq 10 \text{ keV}$) X-rays is markedly and significantly different from the behavior of low energy ($\leq 10 \text{ keV}$) X-rays. The vast body of literature devoted to the subject of flare X-ray emissions rather demands the use of the terms “hard X-rays” and “soft X-rays” when discussing either of these two types of X-ray behavior. For this reason hard and soft X-rays, when these terms are used, will always refer to X-rays of energy greater than or less than 10 keV , respectively. The key to keeping the two meanings of “hard” and “soft” apart (other than the context of the discussion) is their use with either the words “photon” or “X-rays”. Hard photons are always those for which $x \sim 1$. Hard X-rays are always those for which $k.m_e c^2 \geq 10 \text{ keV}$. Whenever possible the use of the terms hard or soft X-rays will be avoided in preference to the terms high energy or low energy X-rays.

Specifying solutions to the equation:

In order to completely specify a solution to the Fokker–Planck Equation (equation (2.36)) we must specify

- a) The ranges of the independent variables E, μ, s .
- b) The coefficients C_1, C_2 , and $d \ln B/ds$.
- c) The boundary conditions.

These are not much changed from those used for the electron results and discussed in Chapter III. Briefly:

Chapter V: X-ray Results

a) The distance s (cm) is measured along the magnetic field from the top of the flare loop which is designated $s = 0$. The bottom of the flare loop is embedded in the low chromosphere or photosphere and need only be deep enough that the flux of high energy electrons reaching the bottom is sufficiently attenuated from that injected at the top. For all of the models considered the domain of calculation was extended through a distance sufficient to give a total column depth in excess of $4 \times 10^{22} \text{ cm}^{-2}$, a depth sufficient to reduce the flux of 500 keV electrons by more than three orders of magnitude (*cf.* Leach and Petrosian 1981 and Chapter III).

The pitch angle cosine μ is measured relative to the direction of the magnetic field and $\mu = 0$ corresponds to motion directly away from $s = 0$. The electrons are allowed the complete range of pitch angles α ($= \cos^{-1} \mu$) from 0° to 180° throughout the whole of the loop. This is in contrast to the earlier work (Elwert and Haug 1970, 1971; Haug 1972; Brown 1972; Petrosian 1973) for which the electrons either had a fixed and unchanging pitch angle or for which the scattering treatment had no facility for incorporating those electrons which are scattered into $\mu < 0$ and which thereafter return toward the top of the loop. The range of μ is $-1 \leq \mu \leq +1$.

The electron kinetic energy E (in units of $m_e c^2$) varies in effect from a lowest energy E_{\min} upwards indefinitely but, in practice, from E_{\min} to an upper energy E_{\max} . The impulsive X-rays are occasionally observed in flares down to energies as low as 5 keV but in most cases are only unambiguously observed from 10 keV upwards (Kane 1974). We therefore take E_{\min} to correspond to electron energies

Chapter V: X-ray Results

of 10 keV ($E_{\min} = 0.01957 m_e c^2$). Few observations of the impulsive X-ray continuum extend to photon energies as high as 500 keV , and all the observed spectra above 100 keV are so steep that the flux of photons at 500 keV is negligible compared to the flux in the lower, more accessible, energy ranges. There is then no real need for us to take our X-ray calculations to energies of more than several hundred keV . Another consequence of the general steepness of X-ray spectra is that far and away the major source of photons with an energy k is electrons with energies of the same order and certainly with energies less than three or four times k (Korčak 1974). In all cases it is sufficient for us to impose an upper cutoff in the energy spectrum and to take our calculations no further than an upper electron kinetic energy E_{\max} which corresponds to 1 MeV ($E_{\max} = 1.957 m_e c^2$).

These domains over which the solutions, *i.e.*, the model flares, are taken, are kept constant from model to model.

b) The coefficients C_1 and C_2 (*cf.* equation (2-34)) require the specification of the background plasma's constituents and their number densities. A flaring plasma would consist primarily of Hydrogen with roughly a 20% relative abundance of Helium and trace amounts of all the heavy elements up to Iron. The heavy elements are important for radiative diagnostics but have too low an abundance to make any noteworthy contribution to C_1 and C_2 . The inclusion of Helium would not change the behavior of the coefficients C_1 and C_2 and would only lead to a renormalization of the order of 20%. This renormalization will not affect the correlations between electron and X-ray characteristics which are being investigated and, as such, we shall keep the model atmosphere simple by overlooking the presence of the Helium.

Chapter V: X-ray Results

We shall utilize model atmospheres which are 100% Hydrogen and 100% ionized throughout (see Brown (1973a) for the possible effects of changing the ionization levels deep within the chromosphere).

The number density $n_{e,p}(s) \text{ cm}^{-3}$ of the atmospheric constituents (electrons and protons) is of importance in conjunction with a measure of the size of the loop. The X-ray results will be given either in terms of the number column density $N (\text{cm}^{-2})$ for which

$$N(s) = \int dN = \int_0^s n_p(s) ds \quad (5.2.7)$$

or in terms of the dimensionless parameter $\tau = N/N_0$. Hence we need only take care to specify a particular form for the density when we have a non-constant magnetic field strength along the loop, *i.e.*, non-zero $d \ln B/ds$. For all the models $n_e = n_p = 10^9 \text{ cm}^{-3}$ in the corona and the coronal loop length is $2.4 \times 10^9 \text{ cm}$. We recall that the Skylab ATM results showed loop sizes ranging from as low as $3.6 \times 10^8 \text{ cm}$ up to $\sim 10^{10} \text{ cm}$, with $2 \times 10^9 \text{ cm}$ a good typical value (Vorpahl *et al.* 1975). Our loop length and coronal density give a coronal column depth to the transition region, N_{tz} , of $2.4 \times 10^{18} \text{ cm}^{-2}$. This value is typical for the quiet sun (Vernazza, Avrett and Loeser 1973) but not for flares. More typical values for solar active regions are $\sim 10^{19} \text{ cm}^{-2}$ (Basri *et al.* 1979) and as high as $\sim 10^{21} \text{ cm}^{-2}$ for solar flares late into the decay phase (Machado *et al.* 1980). The main reason for using a rather low value for N_{tz} is to facilitate our seeing the early evolution of the injected electrom beam, particularly the early pitch angle evolution, and the ways in which the X-rays respond. It also allows us to isolate the effects of the magnetic field structure on the beam electrons and, hence, on the X-rays. The coefficient

Chapter V: X-ray Results

$d \ln B/ds$ is specified in terms of the ratio of the magnetic field strength at the transition region to that at the top of the limb. We have little indication as to what values for $d \ln B/ds$ may be typical for flares (though see our discussion preceding the results for *Model 7*, *Model 8* and *Model 9* later on in this chapter) and we have therefore chosen values which allow us to see most clearly the nature of the relationship between the X-ray characteristics and the magnetic field convergence (*cf.* Table II for the values of $d \ln B/ds$ in our models).

c) For an upper boundary condition we need to specify the electron number distribution for the beam which is injected into the flare limb from the top ($s = 0$) and we should allow for the fact that our solution deals with one limb of a symmetric (two - limbed) flare loop. For a lower boundary condition we must know how to allow for electrons entering the domain of the solution from beneath (electrons with $90^\circ < \alpha \leq 180^\circ$ at the bottom of the loop) .

The electron number distribution which we specify at the top of the loop is a function $f(E, \mu, 0) = f_0(E, \mu)$. Early studies of the beam dynamics tended to assume a highly collimated injected beam primarily because such a distribution made the analyses tractable (Kane 1974). More recently it has been suggested that we should expect a broad distribution in pitch angle (Hoyng and Melrose 1977; Hoyng, Melrose and Adams 1979; Petrosian 1982). We see from the analysis in Chapter III that the electron number distribution, if given at $\tau = 0$ in the form of a Gaussian in pitch angle α , will relax to a Gaussian which continues to broaden with increasing depth. With this as an indication we shall inject electrons with a pitch angle distribution of the form $\exp(-\alpha^2/\alpha_0^2)$ and shall leave the value of

Chapter V: X-ray Results

α_0^2 to be specified for each flare model. In this manner we shall have access to a complete range of beaming from highly collimated ($\alpha_0^2 \ll 1$) to uniform ($\alpha_0^2 = \infty$).

Observations indicate that impulsive X-ray spectra can often be well fitted to a power law function in energy with a spectral index γ in the range $3 \leq \gamma \leq 5.5$ (*cf.* § 5.1) This suggests that the electron distribution at injection should be described by a power law energy spectrum with a spectral index δ in the range $3.5 \lesssim \delta \lesssim 6$ and with all values in this range being permissible. We shall inject electrons with a power law spectrum and we shall leave the value of δ to be specified for each flare model (*cf.* Table II). The injected flux distribution we use is, therefore,

$$F_0(E, \mu) \sim E^{-\delta} \exp(-\alpha^2/\alpha_0^2). \quad (5.2.8)$$

The Fokker-Planck Equation (equation (2.36)) will generate for us the flux of electrons which are scattered through large angles and which then return to the top of the limb with negative values of μ . This flux may be considered to supplement the flux which is injected into the other limb of the loop. We should not neglect these electrons which cross the plane of symmetry of the loop for their number can sometimes be large. We include these electrons by reflecting those which exit at $s = 0$ and with μ in the range $-1 \leq \mu < 0$ back into the loop. The flux which returns to $s = 0$ with a particular (negative) value of μ is simply added to the flux which is being injected into the loop at the pitch angle of equal magnitude. This mimicking of the symmetry of the loop we do for all our models.

Chapter V: X-ray Results

The final boundary condition pertains to the bottom of the domain of the solution. In a flare the electron beam passes down toward the photosphere until all of the beam electrons have been thermalized at which point the beam is no longer considered to exist. In our models we truncate the domain at a depth which is sufficiently great that the flux of high energy electrons there is several orders of magnitude below that which was injected at the top. Ideally, we should include the flux of suprathermal electrons which, at that bottom depth, would have negative pitch angle cosines and would enter our domain from the direction of the photosphere. In practice, again, this flux is sufficiently small at all electron energies that we may safely neglect it. This we do for all our models.

From the above discussion we can see that there are three parameters which we have left to be specified in our models. Two of these (α_0^2, δ) describe the injected electron distribution through equation (5.2.8) and the third ($d \ln B/ds$) describes the rate of convergence of the magnetic field. We can therefore categorise our models according to the values of these three parameters and can look at how the X-rays behave from one model to the next in order to correlate the behaviour of the X-ray characteristics with the values of these model parameters. In Table II we give the models, the results of which we are now ready to discuss.

Flare models:***Model 1***

Model 1 is the reference model against which the results of the other models are compared. We therefore discuss the results for *Model 1* in some detail.

X-ray intensity:

In Figure (5.3) we show the normalized X-ray intensity $I(k, \tau)$ as a function of depth τ and for several photon energies k . We define $I(k, \tau)$ to be the fraction of the total X-ray emission (the total number of photons produced) at a photon energy k (in units of the electron rest mass energy $m_e c^2$), emitted per unit of depth τ . The normalization for $I(k, \tau)$ is such that, for each photon energy k ,

$$\int_0^{\infty} I(k, \tau) d\tau = 1. \quad (5.2.9)$$

To obtain the true or unnormalised X-ray intensity as a function of depth, which we may call $J(k, \tau)$, one needs only to multiply $I(k, \tau)$ by the whole loop X-ray spectrum $J(k)$, which, for *Model 1*, is $\sim k^{-\gamma}$ where $\gamma = 4.3$ (*cf.* Table III).

The first thing to notice in Figure (5.3) is that the form of the curves at each energy is similar. At small column depths the intensity is nearly constant, declining only slowly with increasing depth. In the vicinity of a characteristic column depth which varies from $6 \times 10^{18} \text{ cm}^{-2}$ for 10 keV X-rays ($k = 0.0196 m_e c^2$) to $4 \times 10^{21} \text{ cm}^{-2}$ for 500 keV X-rays ($k = 0.978 m_e c^2$) the curves turn down and,

Chapter V: X-ray Results

Table II

The values of the model parameters.

MODEL	δ	α_0^2	$d \ln B/ds$	$B(N_{tz})/B(0)$
1	5	0.4	0.0	1.0
2	4	0.4	0.0	1.0
3	3	0.4	0.0	1.0
4	5	∞	0.0	1.0
5	5	0.04	0.0	1.0
6	3	0.04	0.0	1.0
7	5	∞	2.9 (-10)	2.0
8	5	∞	6.7 (-10)	5.0
9	5	∞	1.34 (-9)	25.0
10	5	0.04	6.7 (-10)	5.0
11	5	0.04	1.34 (-9)	25.0

The electrons are injected with a flux $F(E, \alpha, \tau = 0) \sim E^{-\delta} \exp\{-\alpha^2/\alpha_0^2\}$ for pitch angles $0 \leq \alpha \leq \pi/2$ and energy $10 \text{ keV} \leq E m_e c^2 \leq 1 \text{ MeV}$. $B(N_{tz})/B(0)$ is the ratio of the magnetic field strength at the transition region to that at the top of the loop.

from then on, have a constant gradient. The curves are parallel at large column

Chapter V: X-ray Results

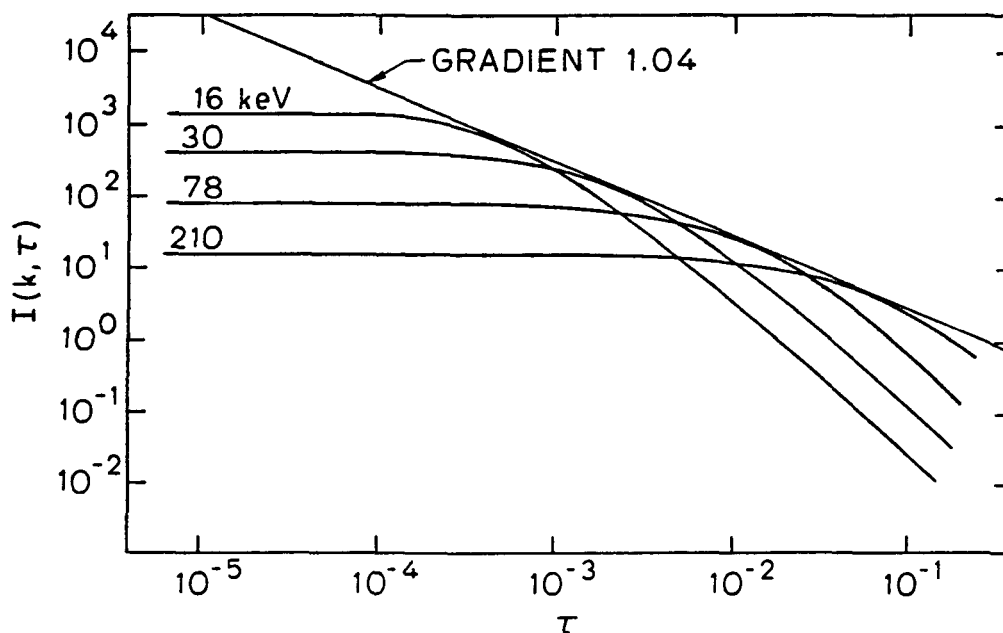


Figure 5.3 $I(k, \tau)$ vs τ for *Model 1*. $I(k, \tau)$ is the relative rate of emission with depth as given by the numerical results, in the form of the fraction of the total emission at that photon energy k per unit τ . τ is a dimensionless measure of the column depth and is equal to N/N_0 where N is the overlying column depth and $N_0 = 5 \times 10^{22} \text{ cm}^{-2}$. $I(k, \tau)$ is normalized so that $\int_0^\infty I(k, \tau) d\tau = 1$. At both large and small column depths the curves are parallel (gradients -2.5 and 0.0 , respectively) and the envelope to the curves has a gradient of -1.04 .

depths, each having a gradient $d \ln I(k, \tau) / d \ln \tau \simeq -2.5$. The tangent envelope has a gradient which is very nearly equal to -1.0 .

These X-ray intensity curves are taken from the results of the full Fokker-Planck treatment and yet their form suggests that we could possibly find a relatively simple expression for the function $I(k, \tau)$ which is good for a wide range of k and τ . These X-ray curves closely follow the evolution of the electron flux for a similar energy. This points to photons of an energy k coming predominantly from electrons of energy E , with $E \sim k$. One quick look at the X-ray bremsstrahlung

Chapter V: X-ray Results

cross-sections (*cf.* Koch and Motz 1959 for cross-sections without the Elwert correction and Pratt and Tseng 1975 for cross-sections with the exact Coulomb correction) shows that the cross-section actually falls as $x (= k/E)$ increases toward unity and is either zero or finite at $x = 1$ according to whether or not the Coulomb correction is included. However, this lessening of the cross-section as x approaches unity, or as E approaches k , is much less rapid than the corresponding increase in the number of electrons which become available for X-ray production. Owing to the quite considerable steepness of the electron energy spectrum inferred from almost all flare impulsive bursts, the excess in number of electrons with $E \sim k$ over those with $E \gg k$ more than compensates for the relative difficulty of producing hard (*i.e.*, $x \sim 1$) photons. The predominant source of photons k is then electrons E with $E \sim k$ and it is reasonable that the photon flux closely follows that of the electrons at a similar or slightly higher energy. The closeness of the correlation can be expected to increase with increasing electron spectral index. This is, indeed, borne out by our later X-ray results.

Let us now obtain the simple expression in k and τ which describes the curves for $I(k, \tau)$ in Figure (5.3). We take as a strong indication of the form of $I(k, \tau)$ that all the curves show the same gradient at large column depths, the value of the gradient being -2.5 , and that, at small column depths, the curves are nearly independent of τ . The cross over from the small to the large column depth regimes is energy dependent. Let us then suggest a form

$$I(k, \tau) = A(k) [1 + \tau \cdot g(k)]^{-2.5} \quad (5.2.10)$$

Chapter V: X-ray Results

where $g(k)$ controls the energy dependence of the transition from small to large column depth behaviour and $A(k)$ ensures the correct normalization. $A(k)$ gives the behaviour of $I(k, \tau)$ with k at $\tau = 0$ and $g(k)$ gives the scaling which makes the curves similar as functions of depth. The normalization requires that $A(k)$ be of order $g(k)^{-1}$. We recall that the energy scaling indicated by both the numerical results to and the analytic treatment of the Fokker-Planck Equation in Chapter III was by $\eta = E^2/(E+1)$ (*cf.* equation (3.1.11)). Plotting $I(k, 0)$ versus $k^2/(k+1)$ shows clearly that $A(k)$ behaves like $a(k+1)/k^2$ for constant a .

The normalization is

$$\begin{aligned} \int_0^{\infty} I(k, \tau) d\tau &= \int_0^{\infty} a \left(\frac{k+1}{k^2} \right) \left(1 + \tau \cdot g(k) \right)^{-2.5} d\tau \\ &= \frac{a}{1.5} \cdot \left(\frac{k+1}{k^2} \right) \cdot \frac{1}{g(k)} = 1.0 \end{aligned} \quad (5.2.11)$$

Let us then try $g(k) = (k+1)/bk^2$ and $a = 1.5/b$ for some constant b . The determination of b then comes from finding the correct normalisation N_0 in the equation relating our column depth variables τ and N . From Chapter III we found $N_0 = 5 \times 10^{22} \text{ cm}^{-2}$ to be well supported by the electron results and it would be the obvious choice for the depth scaling in these results as well. On the whole this scaling is well supported by the X-ray results and we shall continue to use it, pointing out as we go where a differently valued or energy dependent scaling would be preferable. If we retain $N_0 = 5 \times 10^{22} \text{ cm}^{-2}$, then $b \equiv 1$. We arrive at

$$I(k, \tau) = 1.5 \left(\frac{k+1}{k^2} \right) \left(1 + \tau \cdot \frac{k+1}{k^2} \right)^{-2.5} \quad (5.2.12)$$

for the variation with column depth of the fractional X-ray intensity for *Model 1*.

Chapter V: X-ray Results

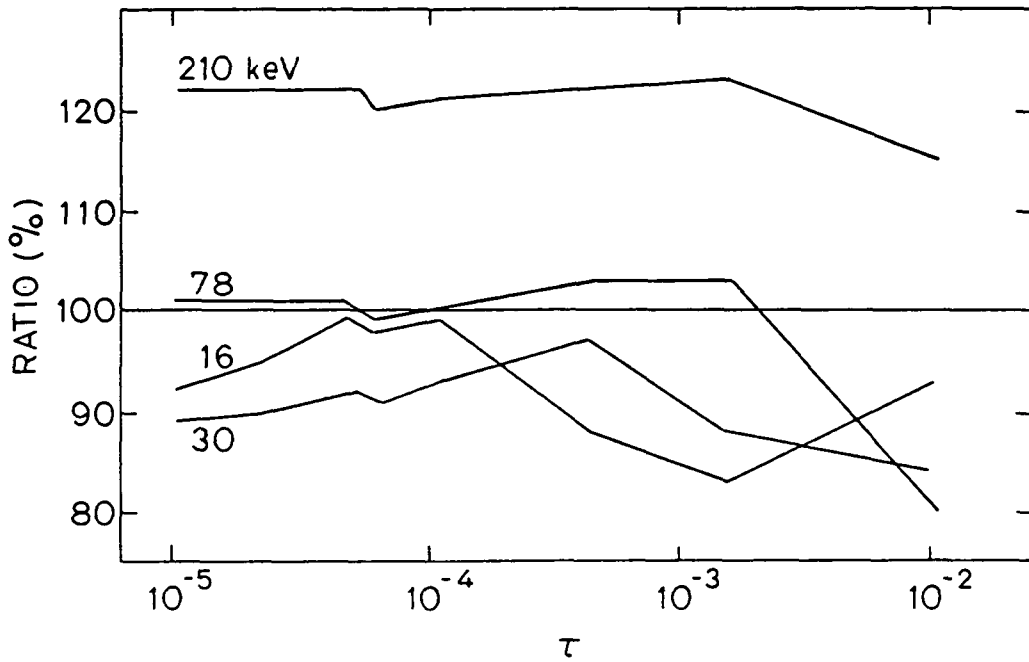


Figure 5.4 The ratio between $I(k, \tau)$ as given by the numerical results for *Model 1* and $I(k, \tau)$ as given by equation (5.2.12) for the intermediate range of τ over which the $I(k, \tau)$ curves turn down. Equation (5.2.12) is obtained from a semi-empirical fit to the full numerical results.

To see how well this expression fits the X-ray curves of Figure (5.3) we show, in Figure (5.4), the ratio between the numerical values of the X-ray intensity (as plotted in Figure (5.3)) and the values from equation (5.2.12), for the middle range of τ where the curves are changing from small τ to large τ behavior. Two remarks can be made about Figure (5.4). The raggedness of the curves arises from the difficulty of selecting an appropriate value of τ for each loop segment. Some of the high τ segments are wide enough that the X-ray flux can drop as much as a decade from the beginning to the end of the segment. This presents a problem which is similar to the deconvolution problem one meets when trying to fit a spectrum to a series of X-ray count rates, one from each channel of a detector. In our case,

Chapter V: X-ray Results

to select a representative value of τ for each loop segment, we need to know the variation of the X-ray intensity within each segment, and that variation is different for different X-ray energies. Hence, no one value of τ can satisfactorily represent each segment at all energies. The value of $I(k, \tau)$ calculated from equation (5.2.12) depends quite sensitively on the value of τ used, at least once the curves have begun to fall and τ is no longer very much less than $k^2/(k+1)$. Therefore, a small discrepancy between the value of τ used and the optimal value for that segment and k can produce the raggedness seen in Figure (5.4) even though both the numbers plotted in Figure (5.3) and the numbers obtained from equation (5.2.12) vary smoothly with τ .

The second remark on Figure (5.4) is that the curve for 210 keV is consistently high for all τ . We may expect the best fit value for N_0 to vary slightly with k as does $\ln \Lambda$ with E and, indeed, the fact that the curve for 210 keV is consistently high suggests that a lower value of N_0 would be more appropriate. The numerical results are in the form of a number of X-ray photons emitted per loop segment of known column thickness in N . This has to be converted into a fraction of the total emission per unit τ before Figures (5.3) and (5.4) can be drawn. Using a lower value of N_0 would decrease the thickness of unit τ as measured in terms of N , and would decrease the estimate of the fraction of the X-rays emitted per unit τ . Hence the 210 keV curve in Figure (5.4) would be lowered.

We conclude that, for a wide range of photon energies, equation (5.2.12) accurately describes the numerical results obtained from the full treatment. Even if we ignore the slight energy dependence of N_0 , the equation stays within roughly 20% of the computed X-ray intensities at both large and small column depths.

Chapter V: X-ray Results

This accuracy is itself the order of the general accuracy of the computed X-ray values.

When, later on in this section, we analyse the results for our other models we shall be able to observe how broad or how limited is the use of an equation of the form (5.2.12) for a range of model parameters. We shall see that the exponent, given as -2.5 in equation (5.2.12), is directly related to the electron spectral index and that it behaves as $-\delta/2$ for our entire range of δ . We shall, for now, assume this general form for the exponent and shall leave its verification until we have had the opportunity to look at the X-ray results from other models.

Let us note here a few of the results which we can draw from equation (5.2.12) with 2.5 replaced by $\delta/2$. If the X-ray spectrum for the loop as a whole is of the form $J(k) \sim k^{-\gamma}$ counts per unit k , then the X-ray emission at each height τ is of the form

$$\begin{aligned}
 J(k, \tau) &= J(k) \cdot I(k, \tau) \\
 &\sim \left(\frac{k+1}{k^{2+\gamma}} \right) \cdot \left(1 + \tau \cdot \frac{k+1}{k^2} \right)^{-\delta/2}.
 \end{aligned}
 \tag{5.2.13}$$

This implies that the spectrum at the very top of the loop (such as may be seen for a heavily occulted flare or for a large flare seen with very good X-ray imaging) is

$$J(k, \tau \simeq 0) \sim \frac{k+1}{k^{2+\gamma}}
 \tag{5.2.14}$$

For $k \ll 1$, (*i.e.*, for deka keV X-rays), $J(k, \tau \simeq 0) \sim k^{-(2+\gamma)}$, which is two orders of magnitude steeper than the spectrum for the whole flare. This is in agreement with the observed steepening of the X-ray spectrum as flares cross the solar limb (*cf.* § 5.1) and the earlier modelling of Brown and McClymont (1975).

Chapter V: X-ray Results

Equation (5.2.14) indicates a flattening of the X-ray spectrum with increasing photon energy. Alternately, if we assume a power law spectrum for the top of the loop, for example $J(k, \tau \simeq 0) \sim k^{-\gamma'}$, then equation (5.2.14) indicates a spectrum for the whole flare of the form

$$J(k) = \sim \frac{k^{-\gamma'+2}}{k+1} \quad (5.2.15)$$

This spectrum displays a “knee” reminiscent of the knee which is often to be found in spectra drawn from X-ray observations of solar flares (*cf.* §5.1). However, this behaviour does not contribute to the observed spectral knee because the steepening shown in equation (5.2.15) occurs rather too slowly and would lead to a knee energy $k \simeq 1$, (corresponding to ~ 500 keV X-rays) which is in disagreement with the above mentioned observations.

Returning to (5.2.13) we can obtain the expected X-ray spectrum should the sources be visible only down to a column depth N_0 (or τ_0). We have

$$\begin{aligned} J(k, \tau \leq \tau_0) &= \int_0^{\tau_0} J(k, \tau) d\tau \\ &= J(k) \cdot \left(1 - \left[1 + \tau_0 \cdot \frac{k+1}{k^2} \right]^{1-\delta/2} \right) \end{aligned} \quad (5.2.16)$$

For a particular value of τ_0 and for relatively small k , $\tau_0(k+1)/k^2 \gg 1$ and

$$J(k, \tau \leq \tau_0) \simeq J(k). \quad (5.2.17)$$

For the same value of τ_0 but for relatively large k , $\tau_0(k+1)/k^2 \ll 1$ and

$$J(k, \tau \leq \tau_0) \simeq J(k) \cdot \frac{k+1}{k^2}. \quad (5.2.18)$$

Chapter V: X-ray Results

If k is still small, though larger than τ_0 , then $k \ll 1$, $\tau_0(k+1)/k^2 \ll 1$ and

$$J(k, \tau \leq \tau_0) \simeq J(k)/k^2. \quad (5.2.19)$$

A comparison between equations (5.2.17) and (5.2.19) indicates that the spectrum for a flare which can only be observed down to a column depth τ_0 will show a spectral knee, this time with the break being a change of order two in the spectral index. The knee occurs around $\tau_0(k+1)/k^2 \simeq 1.0$. For a photon energy of, say 80 keV , $(k+1)/k^2 \simeq 50$ which would indicate a value of $\tau_0 \simeq 1/50$ or $N_0 \simeq 10^{21} \text{ cm}^{-2}$. This is to be found near the upper chromosphere. Figure (5.5) shows equation (5.2.16) evaluated at a range of values τ_0 with and without the whole loop spectrum $J(k)$ folded out. For $\tau_0 = 10^{-2}$ Figure 5.5a shows that the spectral knee occurs somewhere between 30 and 80 keV . Setting $\tau_0(k+1)/k^2 = 1$ for $\tau_0 = 10^{-2}$ gives $k \simeq 54 \text{ keV}$. This is shown as the vertical mark on the $\tau_0 = 10^{-2}$ curve in Figure (5.5b).

Let us now return to *Model 1* and the numerical X-ray results. In Figure (5.6) we show the normalised X-ray emission $I(k, h)$ which is the fraction of the total X-ray emission per unit height as a function of source altitude h (km). Coronal sources have positive altitudes, chromospheric ones have negative altitudes and note the change of altitude scale on passing through the transition region. Figure (5.6) is a combination of Figure (5.3) and the density-height structure which is shown in the inset.

The coronal density is constant and the total column depth to the transition region is small for all energies shown. Consequently the coronal emission is flat.

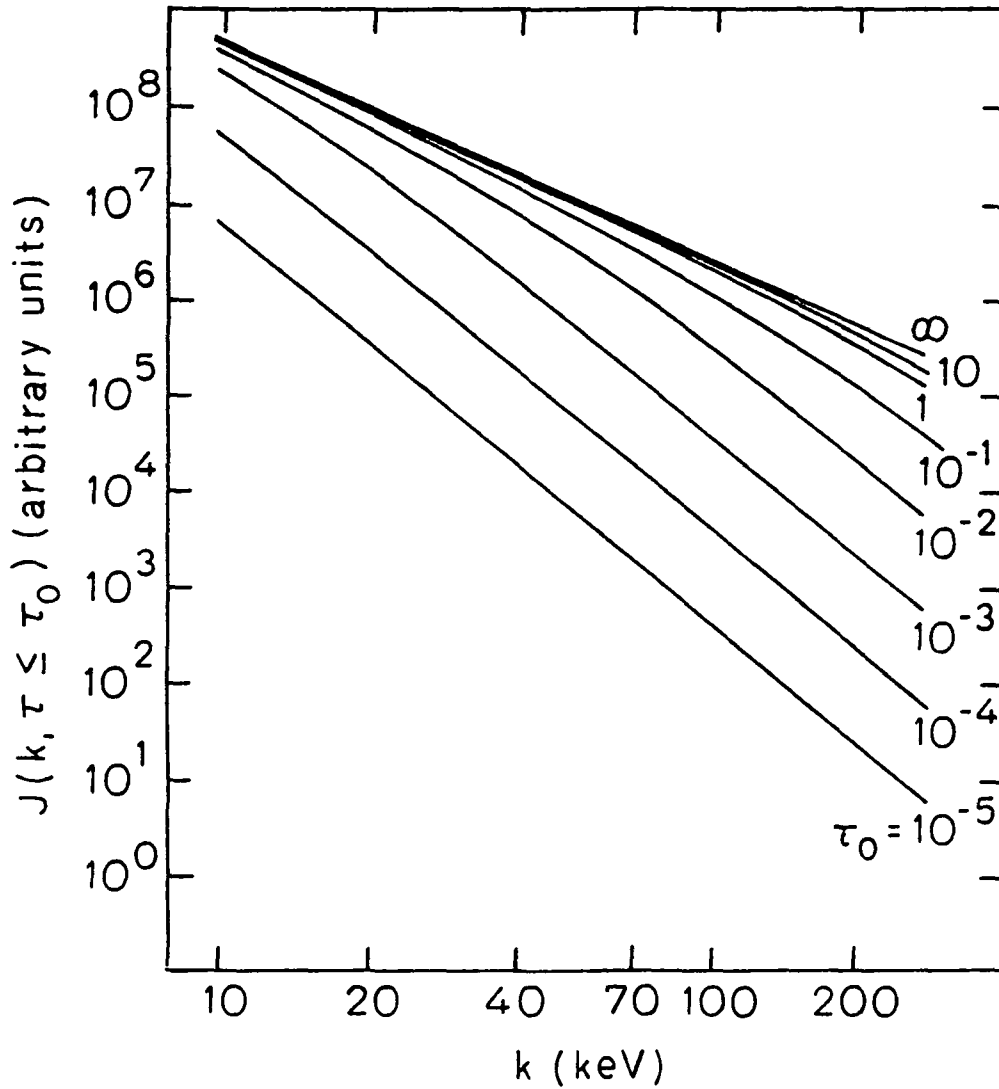


Figure 5.5a.

The emission rate at all energies jumps up at the transition region by an amount equal to the jump in the density. As the electron beam flux begins to drop, with the flux at lower electron energies dropping first, the X-ray emission follows suit. The X-ray emission peaks for each photon energy as the rate at which the electron flux

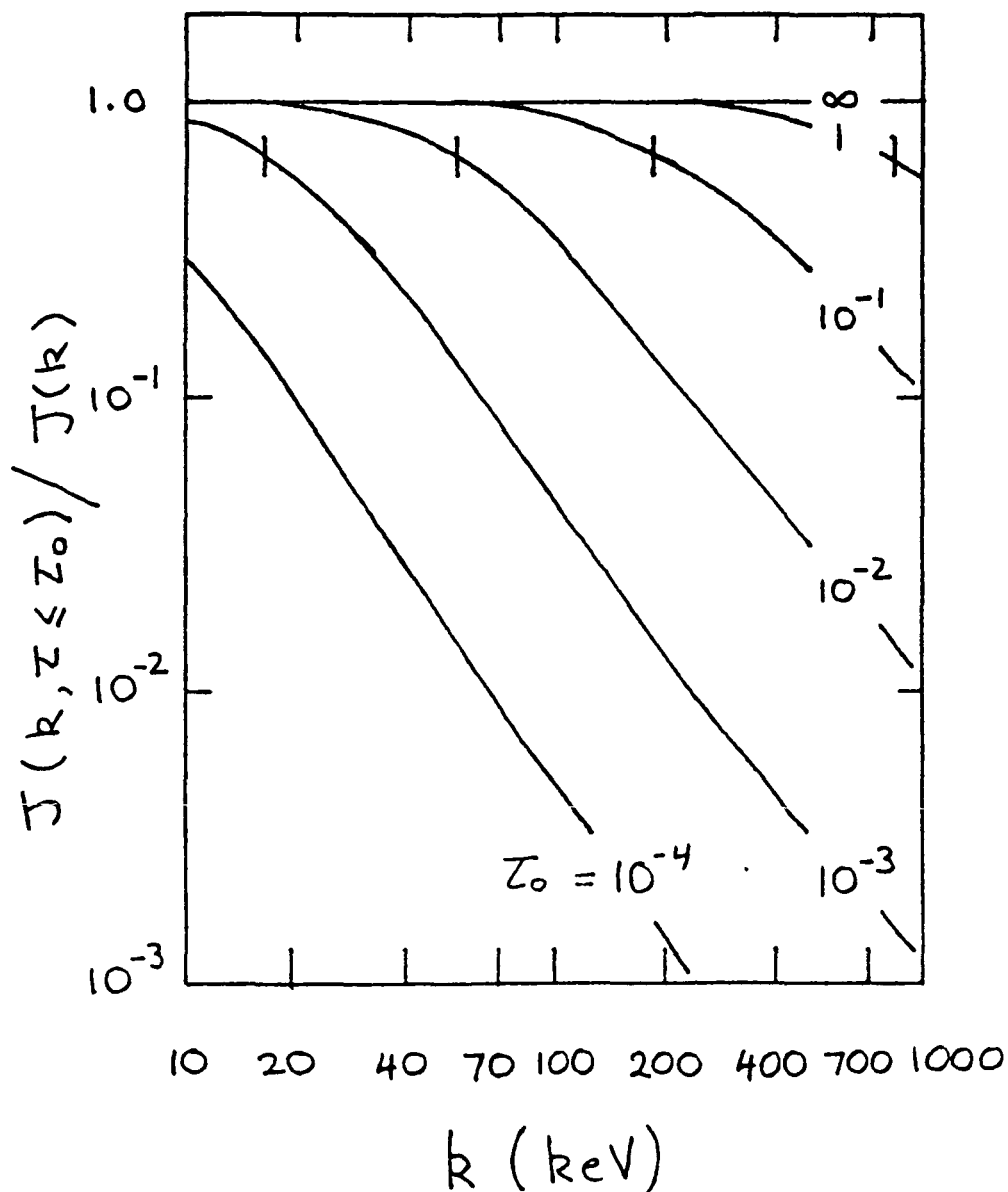


Figure 5.5b The X-ray flux for a source which can be seen only down to a depth τ_0 , as given by equation (5.2.16). This equation is based upon the semi-empirical fit to $I(k, r)$ (equation (5.2.23)). Figure (5.5a) has a whole loop spectrum $J(k) \sim k^{-\gamma}$ with $\gamma = 2.3$ and, in equation (5.2.23), $\delta = 3$. The spectral knee is visible most clearly in the $\tau_0 = 10^{-2}$ curve though it is not very pronounced (it is even less pronounced for larger values of γ and δ). To assist seeing the spectral knee, Figure (5.5b) has the whole loop spectrum folded out. It also has $\delta = 5$. The vertical lines on each curve show the energy for which $\tau_0(k+1)/k^2 = 1$. These are the energies about which the spectral knee for each depth is centered.

Chapter V: X-ray Results

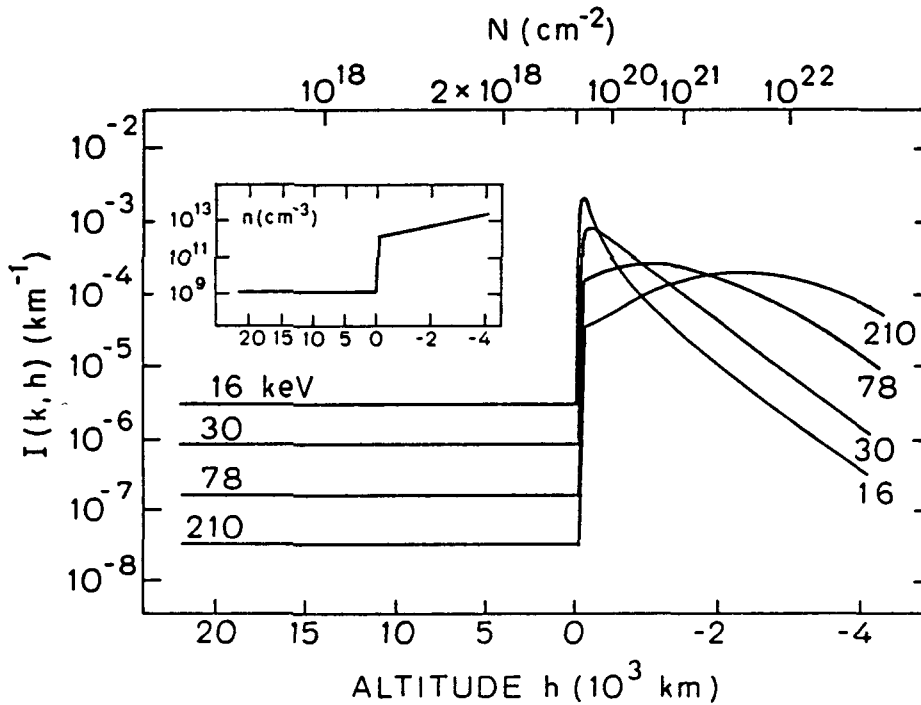


Figure 5.6 $I(k, h)$ vs h for *Model 1*. $I(k, h)$ is the fractional rate of emission per unit altitude h , shown for each of four X-ray energies k . The corona is to the left of $h = 0$ (which corresponds to the transition region) and has positive altitudes, the chromosphere is to the right of $h = 0$ and has negative altitudes. Note the different scales on either side of $h = 0$. Along the top is shown the overlying column depth N for each altitude. The transition region occurs at a depth $2.4 \times 10^{18} \text{ cm}^{-2}$. The inset shows the variation of the plasma number density (Hydrogen masses per cm^{-3}) with altitude within the flare.

falls increases beyond the rate at which the atmosphere becomes more dense. The lower energy photons, therefore, peak higher in the chromosphere. These results confirm the earlier work of Emslie (1981b) and Brown and McClymont (1975).

The rapid jump in $I(k, h)$ upon crossing the transition region does not mean that the coronal part of the loop is relatively invisible when seen against the brightness of the footpoints in the chromosphere. The physical extent of the

Chapter V: X-ray Results

coronal loop is so great in comparison to that of the chromospheric part that the integrated emission coming from above the transition region can be higher than that coming from below. The percentage of the total emission which is produced above the transition region is, for $N_{tz} = 2.4 \times 10^{18} \text{ cm}^{-2}$,

$k \text{ (keV)}$	%
16	10
30	2.8
78	0.45
210	0.09

The percentages for a transition region located at a column depth $N_{tz} = 2.3 \times 10^{20} \text{ cm}^{-2}$ would be

$k \text{ (keV)}$	%
16	94
30	75
78	32
210	8

Consequently, if, say, HXIS were to image a flare which had a column thickness of $2.3 \times 10^{20} \text{ cm}^{-2}$ between the top of the coronal loop and the transition region, almost all the radiation in the 10 – 30 keV channels would appear to be coming from the corona with the footpoints making only a small contribution in its

Chapter V: X-ray results

highest energy channel (22 – 30 keV). However, with increasing photon energy, the footpoints become relatively brighter and at energies of several hundred keV the corona would be all but invisible.

X-ray Spectrum:

Shown in Figure (5.7) is the X-ray spectrum for the whole loop seen along three orthogonal directions, the \hat{x} , \hat{y} , and \hat{z} directions of the global observation frame (*cf.* Figure (5.1)). The spectra are well represented by power laws in photon energy, with spectral indices differing by $\simeq 0.4$ between the vertical and horizontal viewing directions (for comparison with earlier treatments see Brown 1972; Petrosian 1973). In Table III we give the values of the three spectral indices $\gamma_{\hat{x}}$, $\gamma_{\hat{y}}$, and $\gamma_{\hat{z}}$ for this and subsequent models. The behaviour of the \hat{x} , \hat{y} and \hat{z} indices is common to all our models: the \hat{x} and \hat{y} indices are essentially the same and differ from the \hat{z} index by up to 0.5. The close similarity between the spectra seen in the \hat{x} and \hat{y} directions suggests that spectral observations could not distinguish between two similar flares which had the same longitude on the sun's disk (the same Θ in Figure (5.1)) but different orientations (different Φ). However, the difference between the \hat{x} (or \hat{y}) spectra and the \hat{z} spectra would imply a spectral difference between otherwise identical limb and disk-center flares. Our results imply that limb flares should, on the whole, have slightly harder spectra than disk flares though this does not correspond to what is actually seen. Datlowe and his coworkers (Datlowe, Elcan and Hudson 1974; Datlowe 1975; Datlowe and Hudson 1975; Datlowe *et al.* 1977) saw little to distinguish limb flares from disk flares except for a tendency

Chapter V. X-ray results

for limb flares to have slightly softer spectra. One effect which could account for this discrepancy is the contribution of the solar albedo which, though not present with limb flares, may be very significant for disk-center flares (*cf.* § 5.1). Also, for a flux limited sample, the mean spectral index depends upon the relative fluxes in the \hat{z} versus the \hat{x} (\hat{y}) directions (Petrosian 1975).

Figure (5.8) shows the variation of the X-ray spectrum with depth for *Model 1*. Because of the only slight variation in the X-ray intensity with Θ and Φ , the spectra shown here are integrated over 4π steradians of viewing direction. Curves 2 through 7 show the spectra for sources at various depths. The spectrum begins as a typical thin target spectrum, representing the X-rays from a source electron distribution which is essentially unchanged from the injected distribution. The spectral index over the range 30 keV and above is approximately 5.9, 0.9 larger than the electron index δ and generally as one would expect on the basis of less exact modelling (*cf.* Brown and McClymont 1975). However, the thin target spectrum (curve 2) contains a steepening at lower energies. The spectral index for the range 10 – 30 keV is 6.5, a full 1.5 steeper than the electron spectral index and 0.6 steeper than the index for the higher energy range. This slight excess of lower energy photons arises from the fact that the electrons in the beam were injected with a significant amount of collimation ($\alpha_0^2 = 0.4$, *cf.* Table II), and this spectral steepening increases with decreasing α_0^2 . We shall return to this point more fully when we examine the results for *Model 4* and *Model 5*.

This low energy spectral steepening rapidly disappears as the source moves deeper through the loop and it is no longer present in curve 3. Thereafter the low

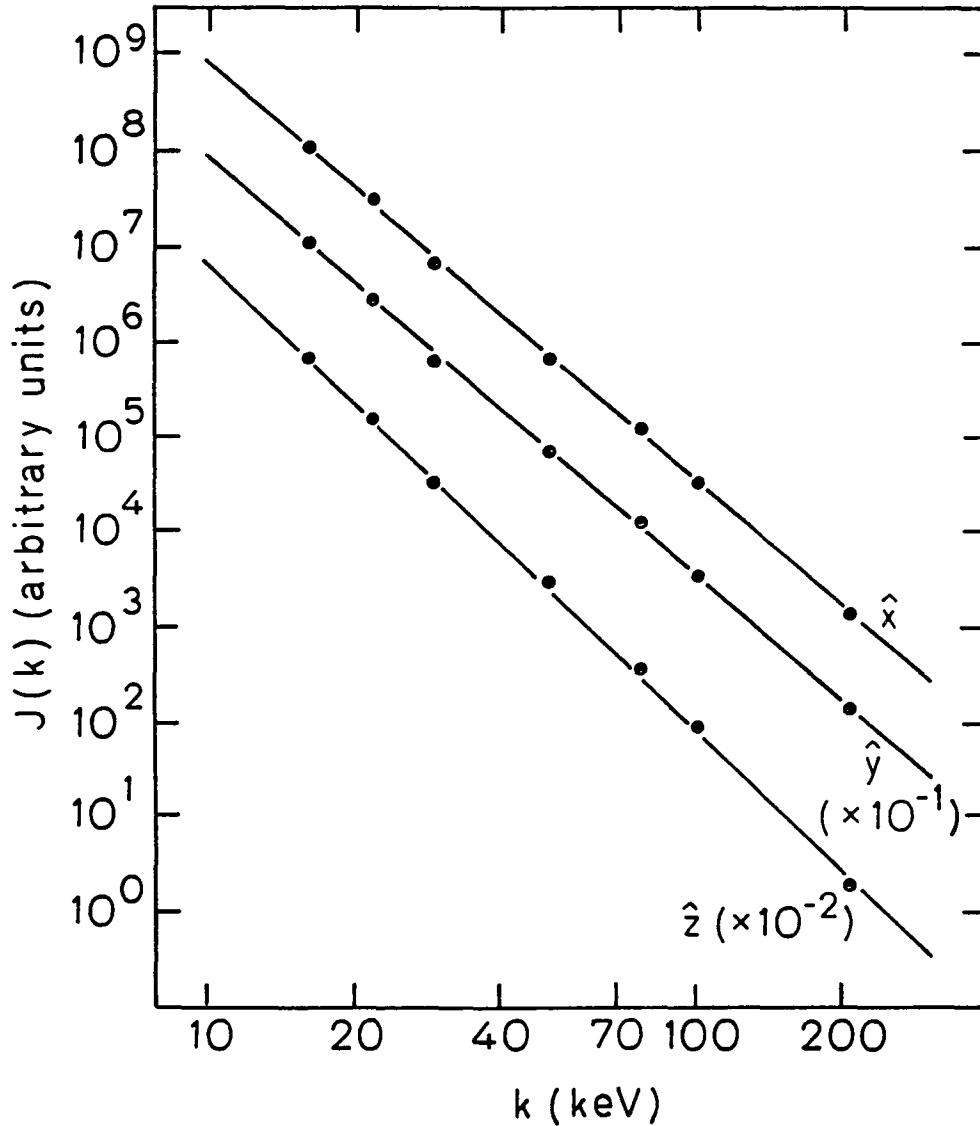


Figure 5.7. The X-ray spectrum $J(k)$ in three mutually orthogonal directions \hat{x} , \hat{y} and \hat{z} , for *Model 1*. $J(k)$ is in units of photons $cm^{-2}sec^{-1}ster^{-1}keV^{-1}$, arbitrarily scaled. The dots show the numerical results and the lines the best fit power law spectrum through them. The spectra are positioned vertically for ease of presentation; the actual intensities in the \hat{y} and \hat{z} directions have been reduced by factors of 10 and 100, respectively.

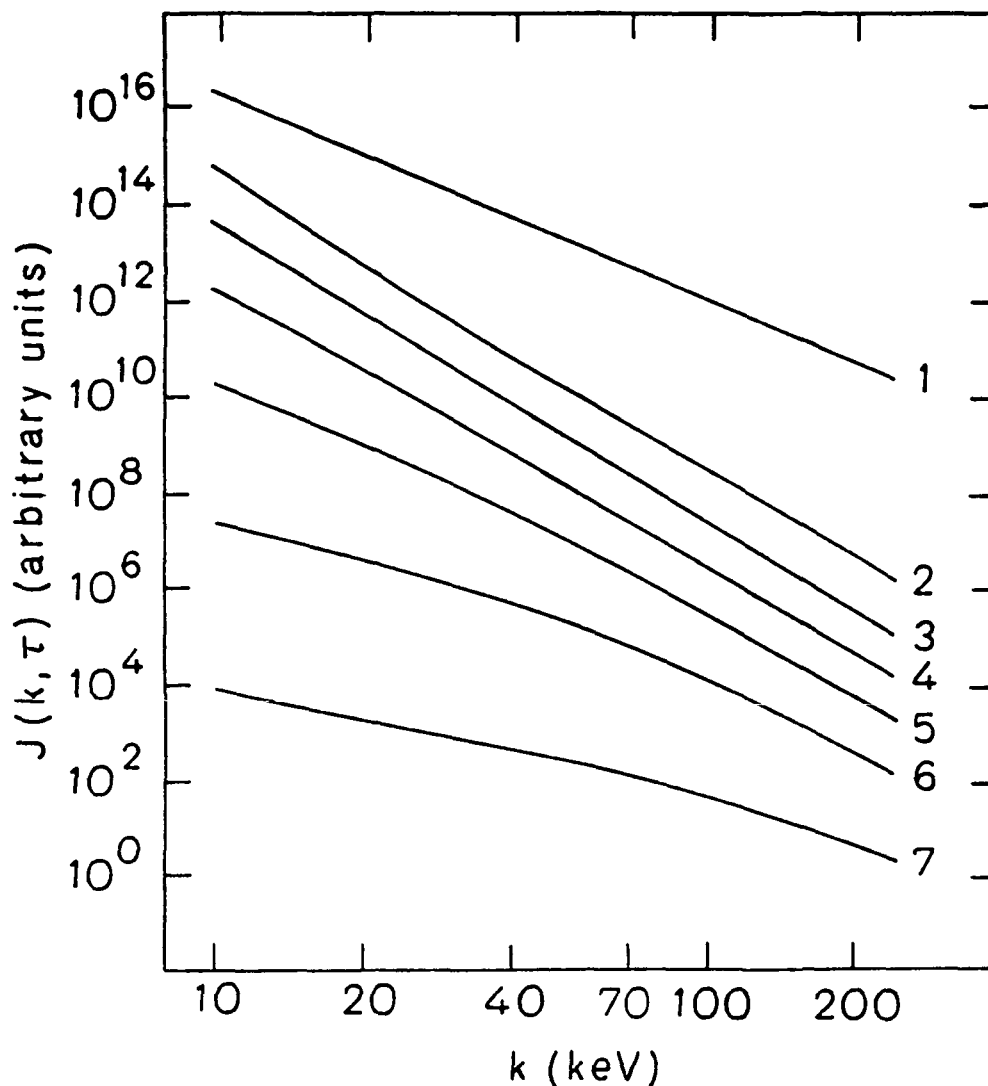


Figure 5.8 The evolution of the X-ray spectrum with depth for *Model 1*. All the spectra are integrated over 4π steradians of viewing angle. Curve 1 is the spectrum for the whole loop and has been moved upward vertically by a factor of 10. Curves 2 through 7 correspond to sources at depths N and each has been moved vertically by a factor f . Curve 2, $N = 3.0 \times 10^{17}$ and $f = 10^0$; Curve 3, $N = 4.6 \times 10^{18}$ and $f = 10^{-1}$; 4, 1.9×10^{19} and 10^{-2} ; 5, 6.8×10^{19} and 10^{-3} ; 6, 4.7×10^{20} and 10^{-4} ; 7, 6.2×10^{21} and 10^{-5}

Chapter V: X-ray results

energy end of the spectrum becomes flatter than the high energy end as the X-rays reflect the reduced penetration of low energy electrons. This turn over in the spectrum moves to higher energies with increasing source depth and the spectrum as a whole falls in step with the drop in the number of high energy electrons initially present in the injected beam.

The spectrum for the whole loop (curve 1) is the sum of the spectra for each depth and it has an index which is $\simeq 0.7$ less than the electron index δ . Even though this spectrum is the sum of many spectra, most of which are not simple power laws, the fact that the break energy in the individual spectra moves through to very high photon energies with sufficient depth means that the overall spectrum is again close to being a single power law. All our models give whole loop spectra which, if they were to be observed by any of the currently available X-ray telescopes, would be unambiguously classified as single power law spectra having indices as given by Table III. The values quoted for $\delta - \gamma_{\text{all}}$ are calculated for the range 16 to 210 keV and are as accurate a fit to the numerical results as are the \hat{x} , \hat{y} and \hat{z} spectra shown in Figure (5.7). A single power law X-ray spectrum is, apparently, unavoidable for a power law injected electron flux and is broadly insensitive to the particulars of the individual models.

There is a slight correlation between the spectral index and the degree of magnetic trapping. However, the spectral index cannot be used to indicate the presence of such trapping unless there are other measurements at hand which can independently determine the electron index. As Table III shows, $\delta - \gamma_{\text{all}}$ lies in the range 0.2 to 0.7 which means that the X-ray spectral index cannot determine the electron index to better than ± 0.3 . This range of uncertainty is not large unless

Chapter V: X-ray results

Table III

The X-ray spectral indices for each model.

MODEL	$\gamma_{\hat{x}}$	$\gamma_{\hat{y}}$	$\gamma_{\hat{z}}$	$\gamma_{\text{top}} - \delta$	$\delta - \gamma_{\text{all}}$
1	4.4	4.4	4.8	1.1	0.7
2	3.3	3.3	3.8	1.0	0.7
3	2.4	2.4	2.8	1.0	0.5
4	4.3	4.3	4.4	1.1	0.7
5	4.3	4.3	4.6	0.9	0.7
6	2.3	2.3	2.7	0.9	0.5
7	4.4	4.4	4.7	0.7	0.6
8	4.6	4.6	5.1	0.8	0.4
9	5.2	5.2	5.5	0.9	0.2
10	4.2	4.2	4.7	0.6	0.7
11	4.5	4.5	4.7	0.7	0.5

The indices are taken over the energy range $16 \text{ keV} \leq k m_e c^2 \leq 210 \text{ keV}$. \hat{x} , \hat{y} and \hat{z} are three orthogonal directions; \hat{x} and \hat{y} are in the plane of the solar surface, \hat{z} is the outward normal. γ_{top} is the index for the top segment of the loop, γ_{all} is the index for the whole loop. Both are integrated over 4π steradians of emission angle.

Chapter V: X-ray results

we wish to calculate anything relating to the size of the electron beam, such as the amount of energy which the beam carries, the rate at which it heats the flaring plasma and evaporates chromospheric material or the size of the reverse current which it engenders. In these cases an uncertainty of 0.5 in the electron index can translate into an uncertainty of more than half a decade in the obtained results.

We hereby add strong support to the argument that the X-ray spectrum is not a good tool for obtaining more than a general measure of the underlying electron population.

X-ray Directivity:

The X-ray anisotropy is only vaguely evident in the variation of spectral index with direction as presented in Figure (5.7) and Table III. A more transparent measure of the anisotropy is the directivity ratio $d(k, \tau)$ defined by equation (5.2.3). There are several effects which contribute anisotropy to the X-rays and several effects which tend to bring about isotropization. Any X-ray anisotropy arises from a combination of the anisotropy in the distribution of the electrons and the anisotropy in the angular distribution of the radiation emitted by each electron. As such the angular distribution of the radiation from each part of the flare loop will tend to reflect whichever of these two distributions is smoothest. If either the distribution of the electrons or the distribution of the emitted radiation from each electron is isotropic then the radiation itself will be isotropic.

Firstly, the electrons do not radiate isotropically. The emission cross-section as a function of the angle η between the electron and the photon has a maximum

Chapter V: X-ray results

which, for non relativistic electrons, is at $\eta \simeq \pi/2$ and which moves toward smaller values of η as the electron energy increases. (For low and intermediate energies see the figures in Tseng and Pratt 1971; for high energies see those in Koch and Motz 1959.) Secondly, the electron distribution is not isotropic. At each depth within the flare the electrons collectively define a preferred direction by their bulk motion within the loop. However, this electron anisotropy is moderated by the fact that the individual electrons each follow helical paths. As every electron path has rotational symmetry about the direction of the magnetic field, the distribution describing all the electrons will display this symmetry as will also the X-rays which these electrons produce. As all electron pitch angles are represented, the electron distribution will tend to be a smooth function in pitch angle. Consequently, only for high energy photons and strongly beamed electrons can we expect the X-ray distribution to be highly anisotropic.

In Figure (5.9) we show the directivity $\Delta(k, \Theta, \tau)$ (*cf.* equation (5.2.1)) for *Model 1* at three photon energies and for a range of source heights. The upper curve in each box is the directivity for the whole loop. Curve 1 is for the top of the loop and shows the degree to which the X-rays reflect the anisotropy of the source electrons. *Model 1* has $\alpha_0^2 = 0.4$ for which the ratio of the flux of electrons at $\mu = 1$ to that at $\mu = 0$ is 2×10^{-3} . At no energy do the X-rays reflect anywhere near that amount of electron anisotropy, though the X-ray anisotropy does increase with photon energy owing to the X-ray cross-sections becoming more directional. As the X-ray source moves deeper through the flare loop the electron distribution broadens and hence the radiation becomes increasingly isotropic, with

Chapter V: X-ray results

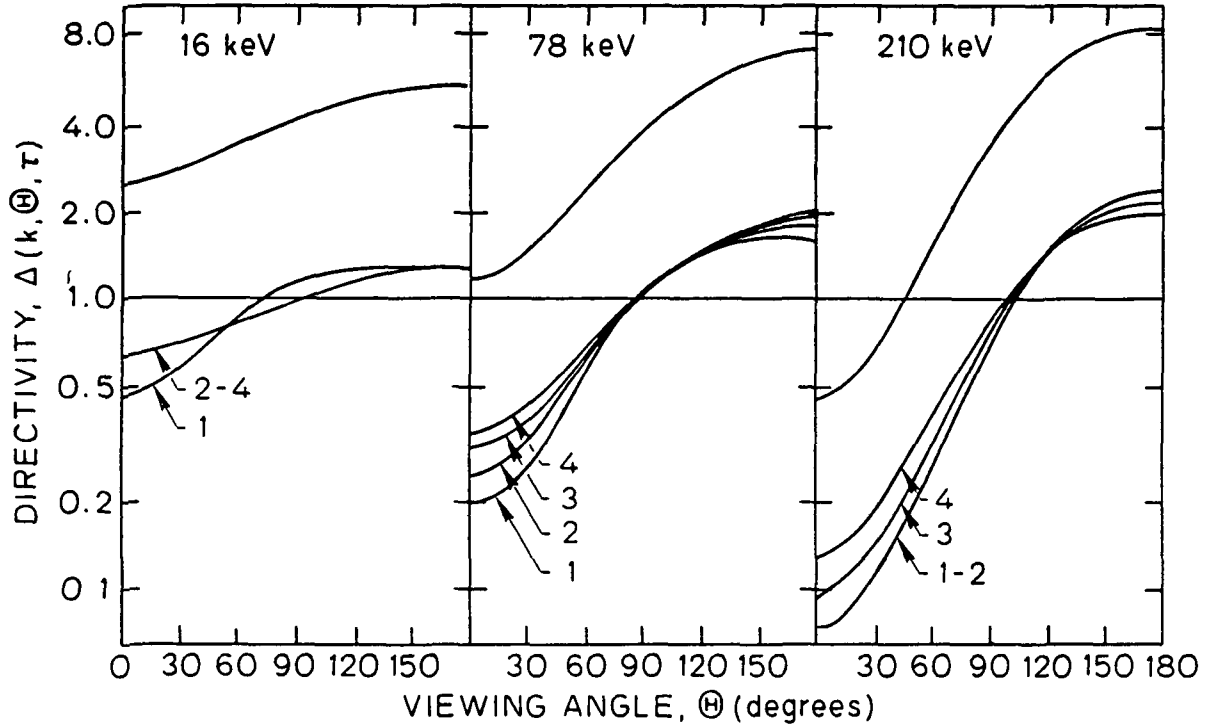


Figure 5.9 The X-ray directivity as a function of viewing angle Θ and for three energies k , for *Model 1*. $\Delta(k, \Theta, \tau)$ is defined by equation (5.2.1). Θ is the polar angle relative to the appropriate polar axis. The upper curve in each box shows the directivity of the flare as a whole, multiplied each time by a factor of four in order that it stand clear of the rest of the diagram. It is measured in the global observation frame for which the appropriate polar axis is the normal to the surface of the sun (*cf* Figure (5.1)). $\Theta = 0^\circ$ corresponds to flares seen at the center of the solar disk and $\Theta = 90^\circ$ to flares seen at the solar limb. Curves 1 through 4 correspond to sources at different depths within the flare. For these the directivity is measured in the local observation frames for which the appropriate polar axes are the directions of the local loop magnetic field (*cf* Figure (5.2)). Curves 1 through 4 correspond to sources at depths N . Curve 1 corresponds to 3.0×10^{17} ; 2 to 6.8×10^{19} ; 3 to 4.7×10^{20} and 4 to 6.2×10^{21} . Therefore the local observation frames for curves 2, 3 and 4 coincide with the global observation frame.

Chapter V: X-ray results

the directivity in the forward direction ($\Theta = 0^\circ$) falling and that in the backward direction ($\Theta = 180^\circ$) increasing.

For a source which is sufficiently deep, the electron distribution at all energies will be nearly isotropic and hence the directivity curves at all energies will be flat. However, the intensity of the radiation from such a deep source will be relatively small, the electron flux having dropped so much by then, and the contribution of such deep sources to the whole loop totals will be negligible. The radiation from the whole loop is therefore not typical of the radiation from the deepest source but is typical of that from a characteristic depth, where that characteristic depth varies with photon energy and is of the same order as the characteristic depth obtained from the intensity curves of Figure (5.3), *i.e.*, $\tau \sim k^2/(k + 1)$. In Table IV we give the directivity ratios $d(k, \tau)$ for many depths and photon energies. As can be seen from Figure (5.9) most of the directivity ratios are the ratio between the counts at $\Theta = 0^\circ$ to the counts at $\Theta = 180^\circ$. We also give the directivity ratios for the loop as a whole and show that these are higher than the ratios for the deepest sources alone.

Polarization:

In the same way that the electron beam can produce anisotropic radiation it can produce polarized radiation. The degree of linear polarization is a combination of the degree of anisotropy of the electron distribution and the degree of polarization of the X-rays that each electron is able to produce. Either an isotropic electron distribution or a situation in which the radiation from each electron is unpolarized will give rise to unpolarized flare X-rays.

Chapter V: X-ray results

Table IV

The X-ray anisotropy for *Model 1* .

Depth	Energy (keV)						
(cm^{-2})	<u>16</u>	<u>22</u>	<u>30</u>	<u>50</u>	<u>78</u>	<u>102</u>	<u>210</u>
3.0 (+17)	2.8	3.4	4.2	6.2	9.5	12.6	31.4
2.1 (+18)	2.7	3.2	4.0	6.1	9.4	12.5	31.3
5.8 (+18)	2.5	3.1	3.9	6.0	9.3	12.4	31.2
2.0 (+19)	2.3	2.8	3.6	5.6	8.9	12.1	30.8
1.0 (+20)	2.1	2.5	3.1	4.8	7.7	10.7	28.9
8.4 (+20)	2.0	2.3	2.8	4.0	5.9	8.0	22.2
1.3 (+22)	2.0	2.4	2.8	3.6	4.8	6.2	14.6
whole loop	2.2	2.6	3.1	4.2	6.0	7.6	17.1

The anisotropy, defined in equation (5.2.3), is the ratio J_{\max}/J_{\min} where J_{\max} and J_{\min} are in the directions of maximum and minimum X-ray flux, respectively. As can be seen from Figure (5.9), these two directions are usually antiparallel.

The degree to which each electron produces polarized radiation is clearly shown by the series of diagrams in Tseng and Pratt (1973) (their Figures 1 - 10) giving the degree of polarization as a function of electron-photon angle η for a wide range of electron and photon energies. For low and intermediate energy

Chapter V: X-ray results

electrons, that is for electrons with energies up to, say, $E \sim 200 \text{ keV}$, the shape of the polarization curves with η , typically, have the shape of a bell. The polarization vanishes for photons emitted in the forward and backward directions ($\eta = 0^\circ$ and 180° , respectively), rises rapidly for more obliquely emitted photons and then holds to a maximum value for a spread of η around 90° . The top of the bell is slightly skewed toward values of η less than 90° , and the higher the electron energy the more skewed toward the forward direction it is. The height of the bell, that is the maximum degree of polarization, increases steadily with photon hardness, i.e., with $x = k/E$, where the numerical value of the degree of polarization is, on the whole, approximately that of x itself. Hard photons (for which x is close to unity) have the potential to be almost 100% polarized whereas soft photons (for which x is small) can only display small degrees of polarization. As discussed in the previous chapter, flares produce only linearly polarized X-rays and, for electrons with low or intermediate energies, the preferred plane of polarization is always the plane parallel to the emission plane.

As the electron energy increases above $\sim 200 \text{ keV}$ the bell shape moves entirely into the forward direction so that the degree of X-ray polarization at $\eta = 90^\circ$ is small. For electrons with energies which are intermediate to high the polarization for photons emitted into the backward hemisphere ($90^\circ < \eta \leq 180^\circ$) is small and is in the perpendicular plane. As the electron energy gets larger ($E \gg 200 \text{ keV}$) that half of the polarization curves which corresponds to backwardly emitted photons begins to develop its own bell shape and for this the preferred plane of polarization is the perpendicular plane. Again, the magnitude of the polarization is roughly

Chapter V: X-ray results

proportional to x though the maximum degree of polarization tends to be lower than is found for the X-rays from lower energy electrons.

The above behavior of the polarization curves should show through in our polarization results. A highly collimated electron beam will give rise to polarization curves which, as functions of viewing angle Θ , will have the characteristic bell shape of the emission polarization curves in η . A broader or more isotropic electron distribution will give rise to an X-ray polarization which will retain most of the smooth and typically bell-like structure of the emission polarization curves but the height of the bell, the maximum degree of polarization, will be lower.

In Figure (5.10) we show the polarization curves for *Model 1* giving four source depths and three photon energies. The abscissa is the viewing angle Θ , the angle between the direction of observation and the direction of the local frame's polar axis. The ordinate is the percentage degree of linear polarization. Curves 1 through 4 are for sources at successively greater depths and the upper curve in each box is the polarization for the loop as a whole.

After the discussion of the previous two pages, the results are easily understood. The electron beam is injected into the top of the loop with an intermediate amount of collimation (*cf.* Table II) and hence the thin target polarization results (curves 1) retain the distinctive bell-like shape though with some lowering of the polarization magnitude. As the source moves deeper, the electron beam broadens, the polarization magnitudes fall and the shape of the curves changes slowly reflecting the increased role being played by beam electrons with $\mu < 0$. The high energy photon results reflect the more complicated structure of the high energy polarization curves.

Chapter V: X-ray results

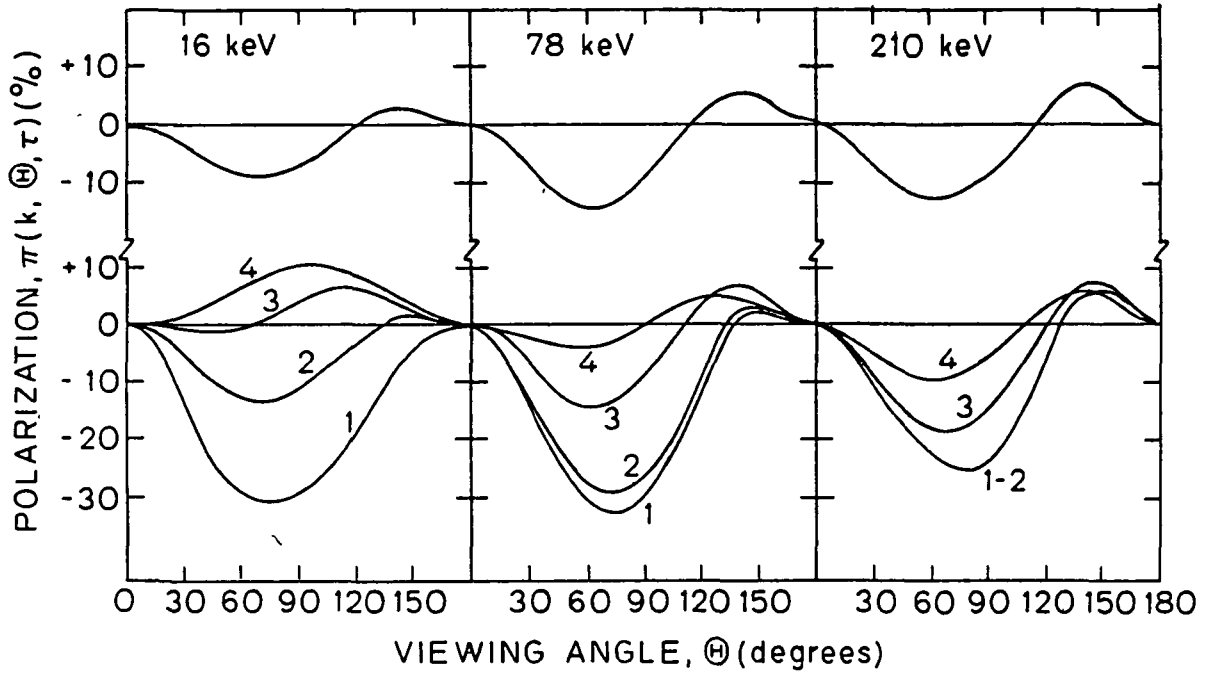


Figure 5.10. The same as Figure (5.9) but for the X-ray polarization $\Pi(k, \Theta, \tau)$ (cf equation (5.2.4)). The upper curve in each box gives the polarization for the loop as a whole. Curves 1 through 4 correspond to depths 3.0×10^{17} , 1.9×10^{19} , 4.7×10^{20} and 6.2×10^{21} .

The values of the maximum degree of polarization at each energy and depth are given in Table V. At each energy the polarization falls with increasing source depth, and the whole loop polarization is that of a characteristic depth which, as with the earlier directivity results, increases with photon energy. For example, Table V shows that, for 16 keV photons the characteristic depth lies somewhere between $2 \times 10^{19} \text{ cm}^{-2}$ and 10^{20} cm^{-2} ($N_0 k^2 / (k + 1) = 4.75 \times 10^{19} \text{ cm}^{-2}$) and for 78 keV photons it is close to $8 \times 10^{20} \text{ cm}^{-2}$ ($N_0 k^2 / (k + 1) = 1.01 \times 10^{21}$). Strikingly, at the very top of the loop where the electron beam has the same

Chapter V: X-ray results

Table V

The maximum degree of X-ray polarization (%) for *Model 1* .

Depth (cm^{-2})	Energy (keV)						
	<u>16</u>	<u>22</u>	<u>30</u>	<u>50</u>	<u>78</u>	<u>102</u>	<u>210</u>
3.0 (+17)	30	30	30	30	30	29	25
2.1 (+18)	25	27	29	29	30	29	25
5.8 (+18)	20	23	26	28	29	28	24
2.0 (+19)	14	18	22	26	28	27	24
1.0 (+20)	6	10	13	19	23	24	22
8.4 (+20)	5 [*]	5 [*]	5 [*]	10	14	16	18 [*]
1.3 (+22)	10 [*]	5 [*]	3 [*]	4 [*]	5 [*]	6 [*]	10 [*]
whole loop	11	12	12	13	14	14	13

The maximum is for polarization parallel to the observation frame unless otherwise indicated by an asterisk.

degree of anisotropy at all energies, the degree of polarization does not begin to vary with photon energy until above 100 keV . Throughout the body of the flare the polarization increases with increasing photon energy reflecting the fact that the electron beam is always more anisotropic at high electron energies than at low electron energies. Looking at the whole loop, the polarization is again insensitive to

Chapter V: X-ray results

photon energy and does not vary significantly over the whole range from 16 *keV* up through 210 *keV*. As any currently obtainable polarization measurements of solar flares have no spatial resolution this insensitivity of the whole loop polarization with respect to photon energy is worth recording. X-ray polarimeters do not need to strive for high energy resolution in order to obtain interesting flare polarization results. If a polarimeter could filter out the low energy hard X-rays so that it was collecting only photons of a high enough energy that thermal contamination was negligible (for example 25 *keV* and above), it could advantageously use the insensitivity of the whole loop polarization to X-ray energy by collecting a wide span of photon energies into its measurements and thereby allowing itself much better counting statistics.

Having energy resolution at the low energy end of the hard X-ray range could also be useful, though, as it would enable an estimate to be made of the degree of contamination by unpolarized X-rays from a thermal source (*cf.* Emslie and Vlahos 1980). Such thermal contamination would be felt most at energies up to about 10 *keV*. If the degree of polarization measured were to increase with photon energy over the range, say, 5 – 20 *keV*, it would be an indication of thermal contamination and would imply that the uncontaminated results at all energies should be close to those found at the higher (20 *keV* or above) energies. There is currently at least one instrument (Lemen *et al.* 1982) which claims to have sufficient accuracy and energy resolution over the range 5 – 20 *keV* that it would be capable of detecting such an effect. The results of a recent observation by this instrument onboard the Space Shuttle Columbia (Tramiel, Chanan and Novick 1984) did show a tendency

Chapter V: X-ray results

for the measured polarization to increase with X-ray energy over this range though the data is not accurate enough for conclusive results to be drawn.

The most significant of the results shown in Figure (5.10) and Table V is that the maximum degree of polarization for the whole loop does not exceed 15%. Earlier calculations based upon much simpler modelling obtained polarizations in the range 30 – 50%, though due acknowledgement was given to the fact that, because of the model simplifications, these values would have to be taken as upper limits and that a full and thorough treatment would probably obtain somewhat lower values (*cf.* § 5.1). The results of just such a full and thorough treatment are now seen to give values considerably lower than the earlier estimates. It appears that the non-thermal flare models need not give rise to polarizations which are an order of magnitude higher than those obtained from thermal models. We shall discuss this point more fully as we look to our other models and see how this maximum figure, which is 15% for *Model 1*, varies from model to model.

Models 2 and 3 – The effects of changing the spectral index.

From Table II we can see that *Model 1*, *Model 2* and *Model 3* are the same except for having different electron spectral indices. By comparing the results from these three models we should be able to ascertain the dependence of the X-ray characteristics upon the electron spectral index.

Figure (5.11) shows the normalised X-ray intensities as a function of column depth for *Model 1*, *Model 2* and *Model 3*. Figure (5.11a) is a reproduction of Figure (5.3). For all three models the X-ray curves retain the same self-similarity which

Chapter V: X-ray results

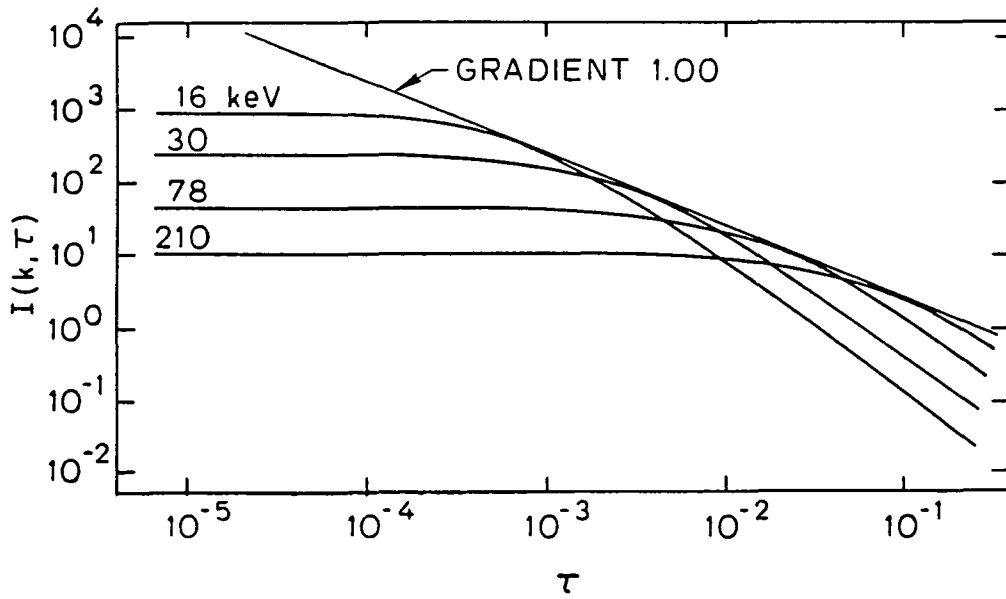
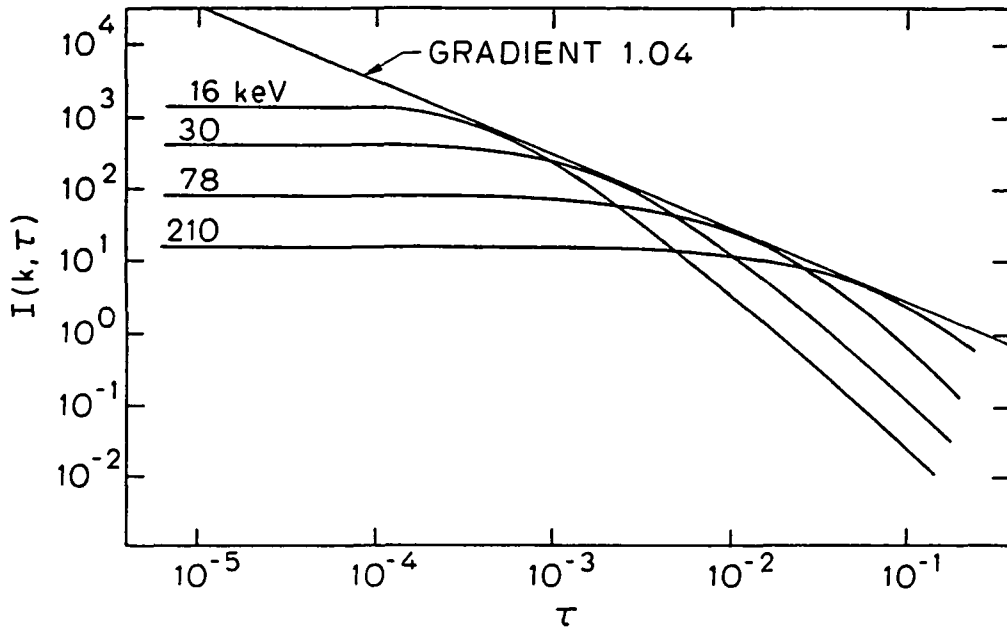


Figure 5.11a, 5.11b

Chapter V: X-ray results

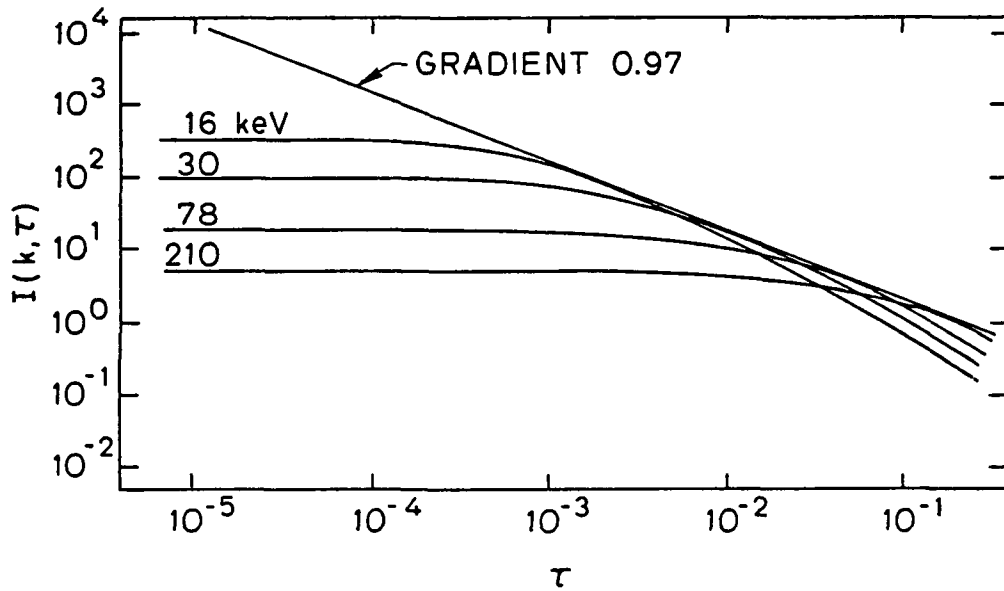


Figure 5.11c. $I(k, \tau)$ vs. τ for *Model 1*, *Model 2* and *Model 3*. Figure (5.11a) is a reproduction of Figure (5.3). The gradients at large τ are -2.5 (*Model 1*), -2.0 (*Model 2*) and -1.5 (*Model 3*)

was present in Figure (5.3). Where Figures (5.11a), (5.11b) and (5.11c) differ is primarily in the gradient of the curves at large column depths. The gradients are 2.5, 2.0, and 1.5, respectively from which we obtained the substitution $\delta/2$ for the exponent in equation (5.2.12)

We can show from our earlier electron results that this is the expected form for the exponent. If we look back to equation (3.3.5) we see that the electron flux at an energy E and a depth τ behaves as

$$F(\eta, \tau) = \frac{\beta^2(\eta)}{\beta^2(\eta + \tau)} F_0(\eta + \tau) \quad (5.2.20)$$

Chapter V: X-ray results

where $\eta = E^2/(E + 1)$. For a particular photon energy k , the X-ray flux generated by the electrons is

$$I(k, \tau) \sim \int_{E=k}^{\infty} h(E, k) \frac{\beta^2(\eta)}{\beta^2(\eta + \tau)} F_0(\eta + \tau) dE \quad (5.2.21)$$

where $h(E, k)$ gives the relative weights of the contributions to the photon flux from electrons with an energy E . $h(E, k)$ is related to the emission cross-sections and is obviously independent of the column depth τ .

The curves in Figure (5.11) show that the power law behavior of $I(k, \tau)$ on τ is to be found at large column depths, that is, for $\tau/\eta \gg 1$, and that it is most clearly pronounced in the lower energy curves. Hence, in equation (5.2.21) we may approximate η with E^2 and $\eta + \tau$ with τ . $F_0(\eta + \tau)$ is obtained from our injected energy spectrum $F_0(E) \sim E^{-\delta}$. $F_0(\eta + \tau) \sim F_0(E^2 + \tau) \sim (E^2 + \tau)^{-\delta/2} \sim \tau^{-\delta/2}$. $\beta^2(\eta + \tau)$ is approximately constant and equal to unity for large τ whereas $\beta^2(\eta) = \beta^2(E) \simeq 2E$ for small η . We have, then,

$$I(k, \tau) \sim \tau^{-\delta/2} \int_k^{\infty} g(E, k) dE \quad (5.2.22)$$

where $g(E, k)$ is a function of E and k but not of τ . We can, therefore, expect the large τ behavior of $I(k, \tau)$ which is shown in Figure (5.11). At large depths, the flux of low energy X-rays falls in accordance with the penetrating power of the electrons. The electrons which can penetrate to relatively large τ were injected at the top of the loop with relatively high energies and are correspondingly much fewer in number.

Chapter V: X-ray results

The general form of equation (5.2.12) is, then,

$$I(k, \tau) = \left(\frac{\delta}{2} - 1\right) \left(\frac{k+1}{k^2}\right) \left(1 + \tau \cdot \frac{k+1}{k^2}\right)^{-\delta/2} \quad (5.2.23)$$

In Figure (5.12) we show a comparison between the curves of Figure (5.11) and the values given by equation (5.2.23), with Figure (5.12a) being a reproduction of Figure (5.4). As mentioned in connection with Figure (5.4), the fact that the 210 keV curve is consistently high indicates that a smaller value of N_0 is appropriate for higher photon energies. The raggedness in the plots, also mentioned earlier, is due to the difficulty in obtaining one value of τ to represent each depth bin well at all photon energies.

From Figure (5.12) we must conclude that equation (5.2.23) represents an accurate fit of a simple equation to the full numerical results and that its accuracy is strong for a wide range of photon energies, source depths and electron indices δ . From Figure (5.12) it appears that the accuracy of equation (5.2.23) increases slightly with increasing δ , *i.e.*, that the accuracy correlates with the strength of the initial premise which was that photons k tend to come predominantly from electrons E with $E \sim k$. It may also be noted here that the envelopes drawn to the curves in Figure (5.12) have gradients which are very nearly equal to -1.0 . Equation (5.2.23) has an envelope with a gradient of -1.0 and this result is independent of k , τ and δ .

The spectral results for *Model 2* and *Model 3* are given in Table III. The behavior of the whole loop spectral index with viewing direction is essentially the same as that shown by *Model 1*. Likewise, the variation of spectral shape with

Chapter V: X-ray results

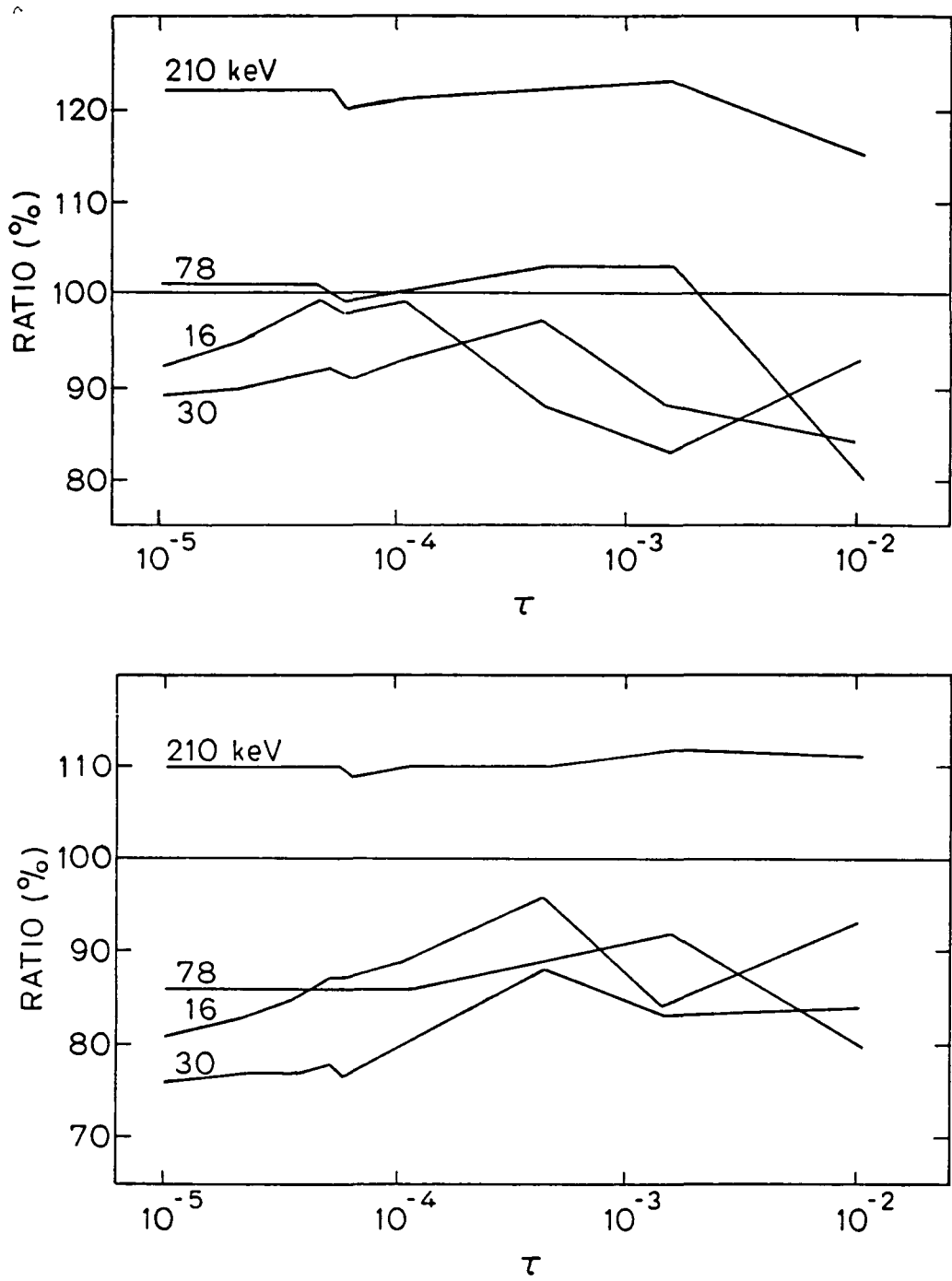


Figure 5.12a, 5.12b.

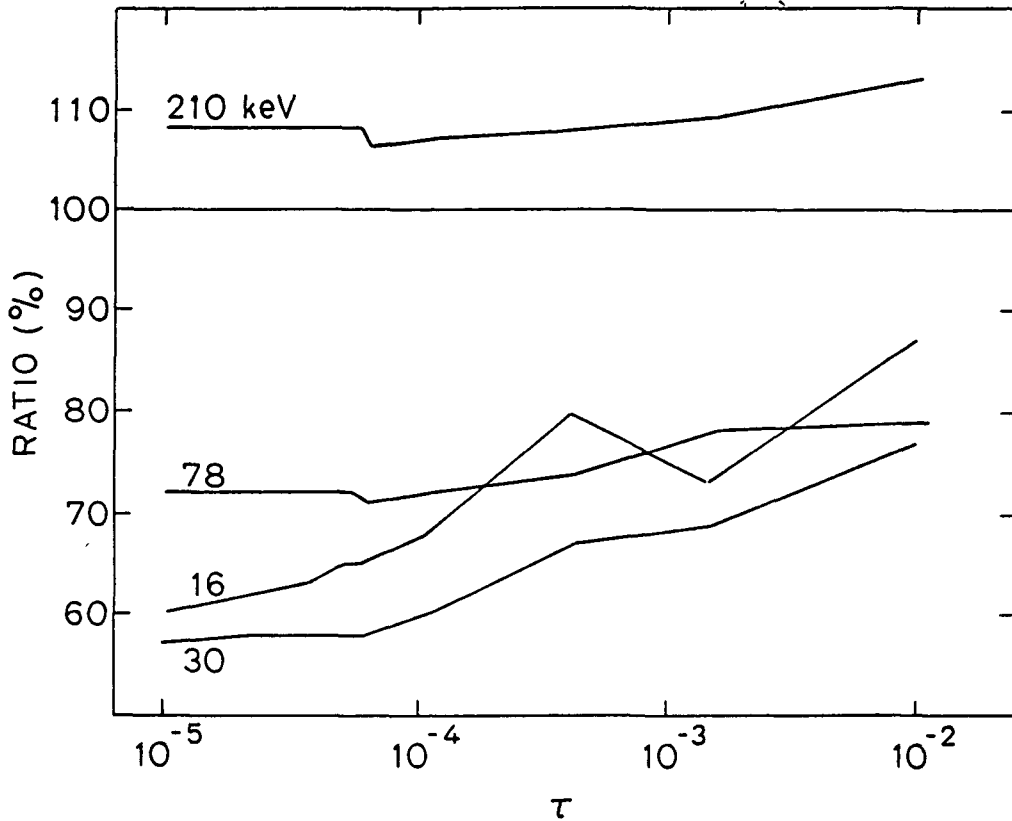


Figure 5.12c. The ratio of $I(k, \tau)$ from the numerical results to $I(k, \tau)$ from equation (5.2.23) for *Model 1*, *Model 2* and *Model 3*. Figure (5.12a) is a reproduction of Figure (5.4).

depth, the spectra show a progression from thin to thick target with the transition energy increasing with depth. Table III shows that the relationship between the thick and thin target indices and the electron index is maintained across the change in δ . The low energy steepening of the thin target spectrum due to the electron beam collimation is present to a similar degree in the results from *Model 2* and *Model 3*, as it is for *Model 1*.

In Figure (5.13) we show the directivity curves for *Model 1*, *Model 2* and *Model 3*, with Figure (5.13a) being a reproduction of Figure (5.9). The directivity

Chapter V: X-ray results

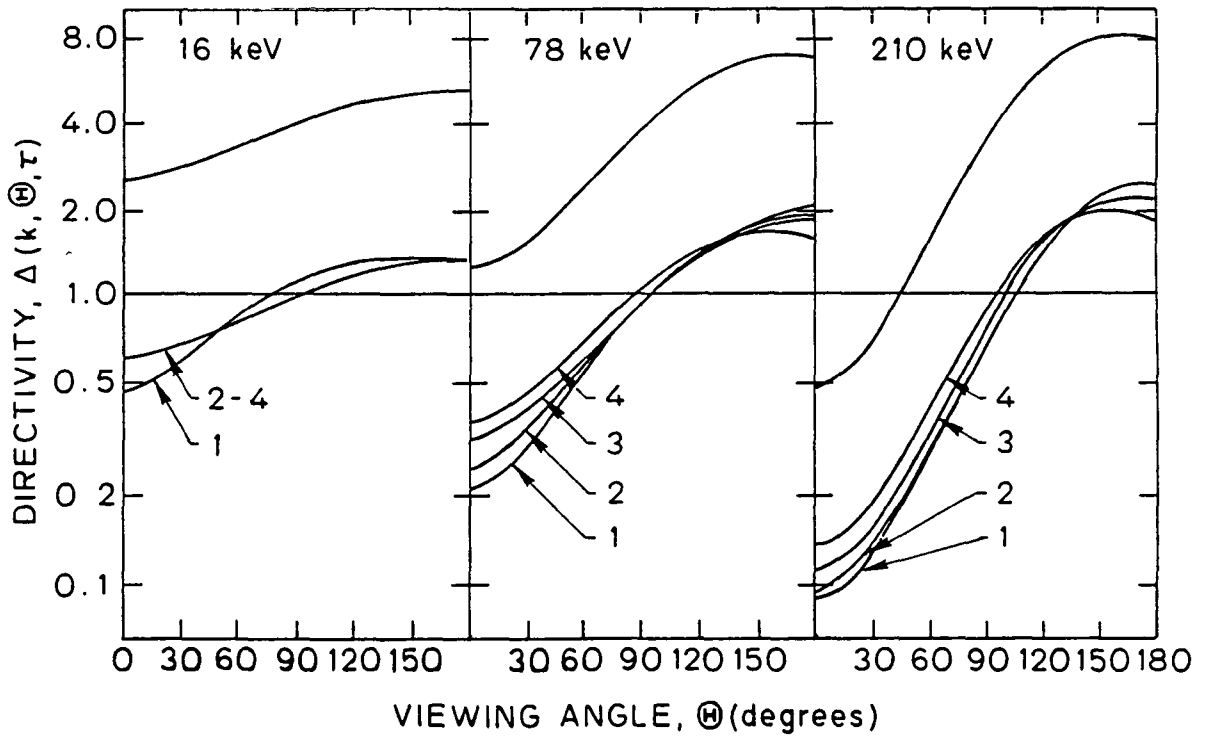
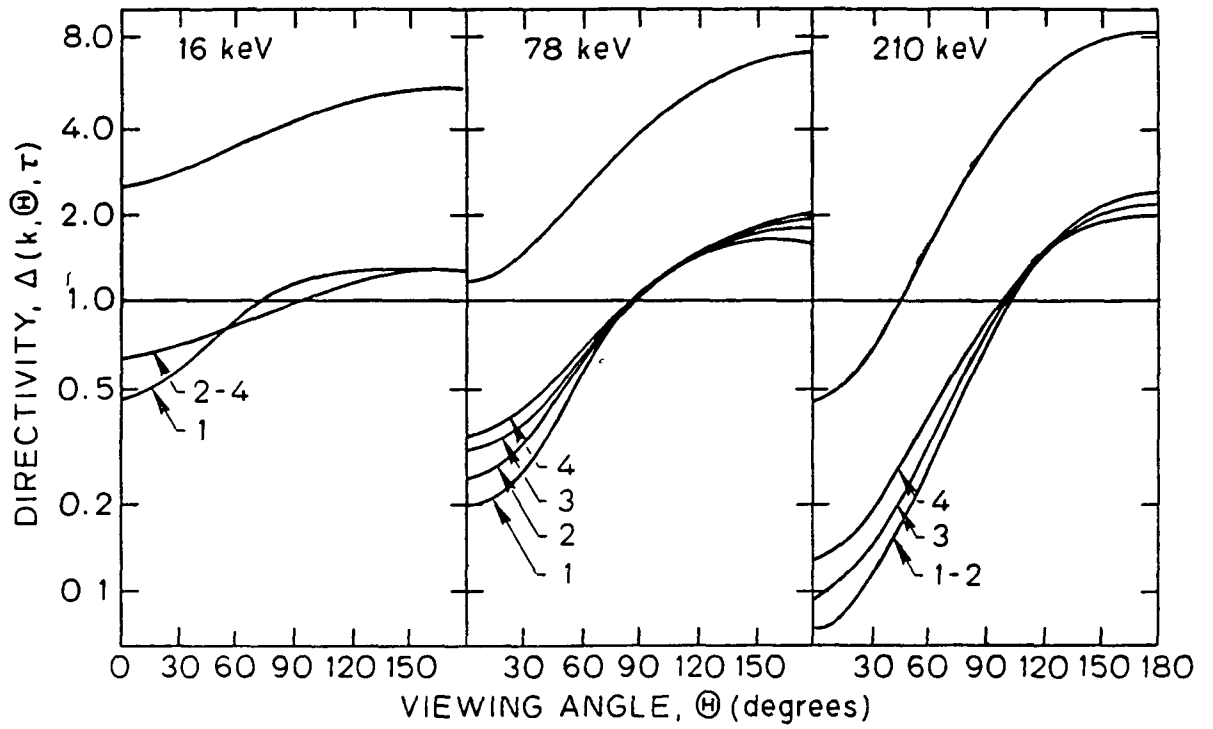


Figure 5.13a, 5.13b

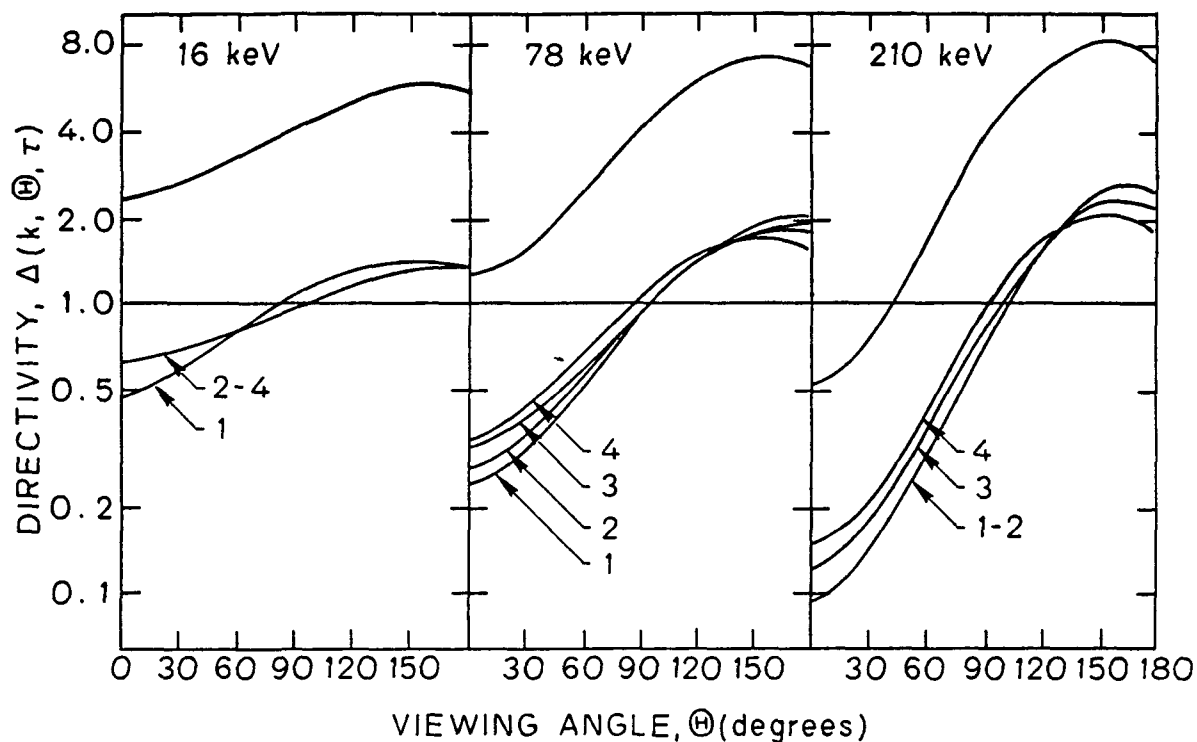


Figure 5.13c The X-ray directivity as a function of viewing angle for *Model 1*, *Model 2* and *Model 3* Figure (5.13a) is a reproduction of Figure (5.9).

results are not strongly dependent upon the electron spectral index or, as is the same, upon the mean photon hardness. The shapes of the X-ray cross-sections (shown graphically by Koch and Motz 1959 and by Tseng and Pratt 1970, 1971) indicate that the emission anisotropy decreases only slowly with decreasing photon hardness and too slowly to be observed in Figure (5.13). Table VI shows the effect on the X-ray directivity of a change in δ . In the range 20 – 100 keV, the directivity falls slightly on changing δ from 5 to 4 but it then rises again on changing δ from 4 to 3. This behavior is real. There are two effects working here, both of which are small but which work on the directivity in opposite directions. Figure (5.11) and

Chapter V: X-ray results

Table VI

The anisotropy of the whole loop (spatially integrated) X-rays.

MODEL (α_0^2)	Energy (keV)						
	<u>16</u>	<u>22</u>	<u>30</u>	<u>50</u>	<u>78</u>	<u>102</u>	<u>210</u>
1 (0.4)	2.2	2.6	3.1	4.2	6.0	7.6	17.1
2 (0.4)	2.2	2.5	3.0	4.1	5.5	7.0	15.7
3 (0.4)	2.3	2.7	3.1	4.2	5.6	7.1	15.1
4 (∞)	1.8	2.1	2.4	3.2	4.1	5.1	10.3
5 (0.04)	2.4	2.9	3.4	4.9	7.1	9.4	24.2
6 (0.04)	2.5	2.9	3.4	4.6	6.4	8.3	19.4
7 (∞)	1.4	1.6	1.9	2.5	3.3	4.0	7.8
8 (∞)	1.2	1.4	1.6	2.1	2.8	3.4	6.6
9 (∞)	1.1	1.2	1.3	1.6	2.1	2.5	4.6
10 (0.04)	1.7	1.9	2.2	3.0	4.0	4.9	8.3
11 (0.04)	1.3	1.5	1.7	2.2	2.9	3.5	5.8

Indicated alongside each model number is the value of the pitch angle parameter α_0^2 .

equation (5.2.23) both show that, for lower δ , the X-ray flux falls off less rapidly with increasing τ than it does for high δ . This means that, for any whole loop

Chapter V: X-ray results

results, the relative contribution from large τ sources is greater for small δ than for large δ . The X-ray directivity decreases with source depth and, for the above reason, the whole loop directivity should fall with decreasing δ . The second effect is that a lower value of δ means flatter electron spectra at all depths and, therefore, a greater relative contribution to the X-ray results from high energy electrons, again at all depths and for all photon energies. At each depth the high energy electrons are more beamed than are the low energy electrons, and at all photon energies the high energy electrons produce more highly beamed radiation (due to the relativistic beaming) than do the low energy electrons. The increased contribution from high energy electrons when δ is low leads to a greater directivity in the X-ray results at all depths and, consequently, to a greater directivity in the results for the whole loop. These two effects, one of which reflects an increased contribution from large τ sources and the other of which reflects an increased contribution from the high energy electrons, together explain the variation in directivity shown for *Model 1*, *Model 2* and *Model 3* in Table VI.

The polarization results for *Model 1*, *Model 2* and *Model 3* (i.e., the polarization as a function of δ) show a different behavior. In Figure (5.14) we show the X-ray polarization as a function of viewing angle, with Figure (5.10) being reproduced as Figure (5.14a). The maximum degree of polarization for the whole loop has, by *Model 3*, fallen almost to zero. To the effects which brought the maximum degree of polarization of *Model 1* down from 30 – 50% (Brown 1972) to around 15% (cf. Table V) – the absence of strong electron beaming and the addition of loop curvature – we must now add the effect of having softer (smaller k/E) photons. The softer photons of *Model 3* are much less strongly polarized than are the harder photons

Chapter V: X-ray results

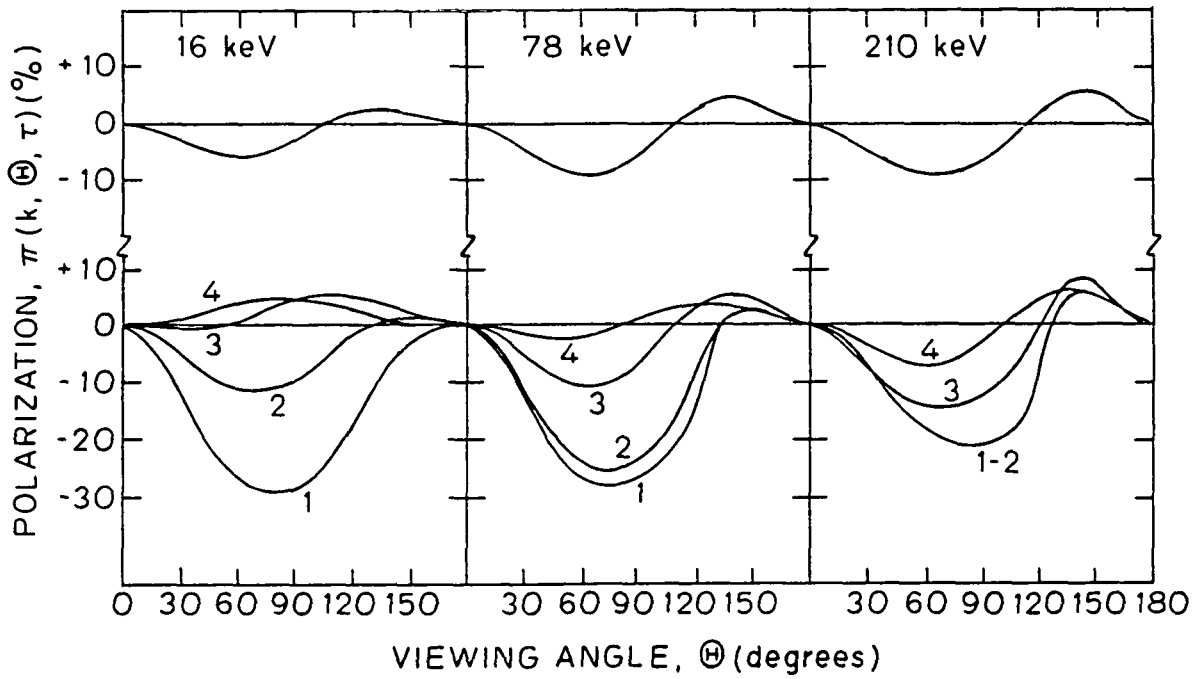
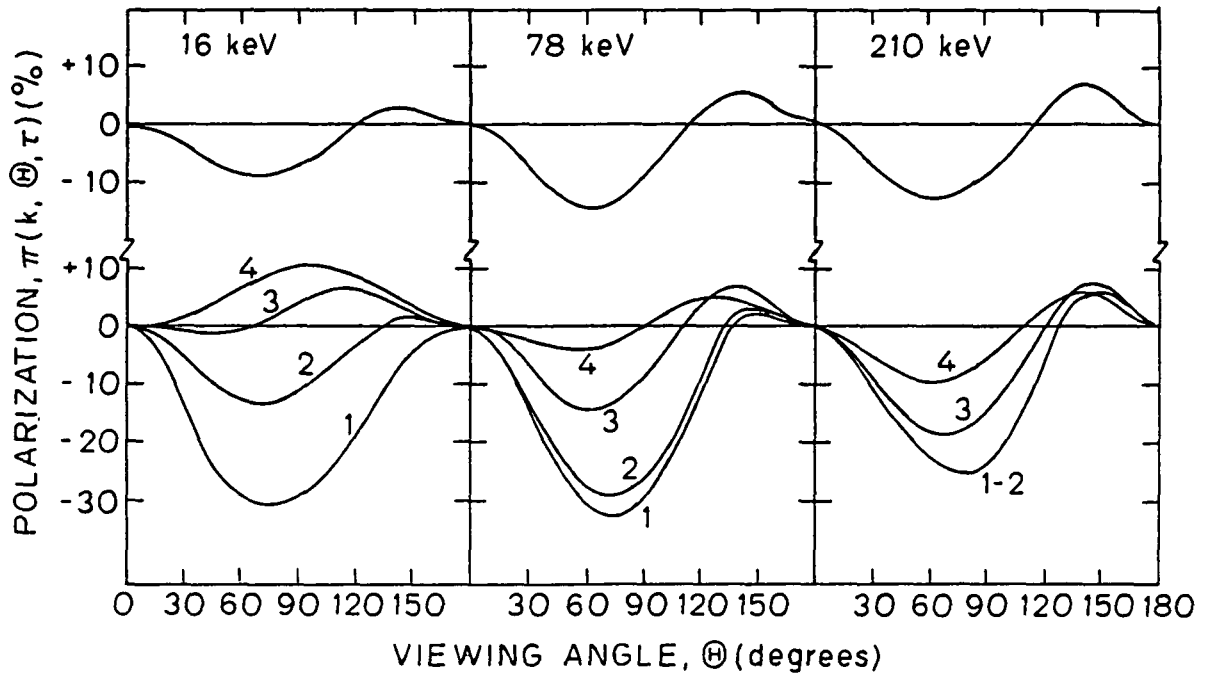


Figure 5 14a, 5 14b

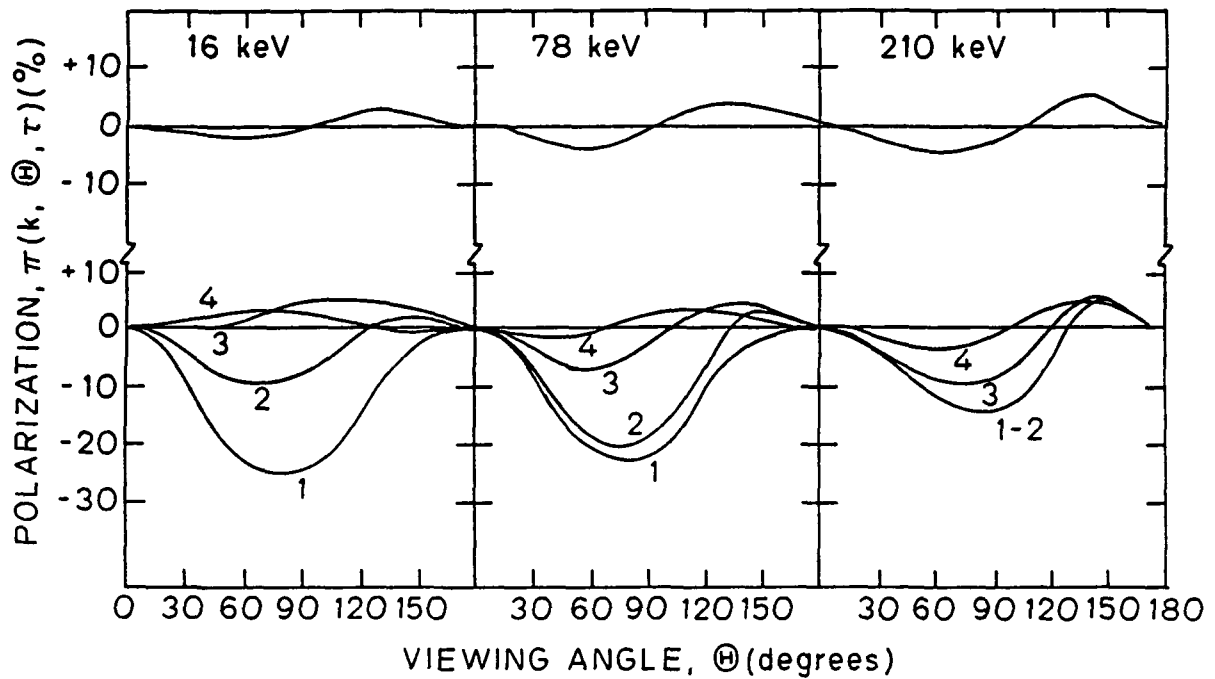


Figure 5.14c The X-ray polarization as a function of viewing angle for *Model 1*, *Model 2* and *Model 3*. Figure (5.14a) is a reproduction of Figure (5.10)

of *Model 1* and the maximum degree of linear polarization for the whole flare is now below 5%. It is no larger than the polarization expected from an isotropic source with the contribution of the photospheric albedo included (Hénoux 1975). This shows clearly the need for a detailed and thorough calculation of non-thermal X-ray results such as has been conducted in this thesis, for these results show that earlier and simpler modelling has given rise to somewhat exaggerated polarization estimates

Chapter V: X-ray results

Models 4 and 5 – The effects of changing the injected electron beaming.

A comparison of the results for *Model 1*, *Model 4* and *Model 5* will allow us to see how the X-ray characteristics depend upon the degree of beaming of the injected suprathermal electrons. Let us briefly recall the electron results of § 3.3.

For *Model 1*, the electrons are injected with a pitch angle distribution which is a Gaussian of moderate width. The distribution broadens as the beam passes down the loop but at all depths the beam is still visible as an excess, though at great depths only a slight excess, of electrons with a pitch angle of 0° over those with a pitch angle of 90° (*cf.* Figure (3.6)).

For *Model 4*, the injected distribution is uniform over the range $0^\circ - 90^\circ$. Those electrons which have a velocity component parallel to the magnetic field begin to move down the loop. Within a short distance the beam establishes a broad Gaussian profile which then remains as the beam penetrates deeper through the loop (*cf.* Figure (3.7)).

For *Model 5* the injected distribution is a very narrow Gaussian; $\alpha_0^2 = 0.04$, which means that the flux per steradian at a pitch angle 30° is already 1/1000th of that at zero degrees (*cf.* Figure (3.5)). This highly collimated beam broadens rapidly within the flare and, after having traversed a depth τ for which $\tau/\eta \sim 1$, is indistinguishable from a beam which had much less collimation at $\tau = 0$.

In Figure (5.15) we compare the fractional emission $I(k, \tau)$ for *Model 1*, *Model 4* and *Model 5* as a function of depth and for several energies. Below a depth τ for which $\tau(1+k)/k^2 \simeq 1$ the models can barely be distinguished on the basis of

Chapter V: X-ray results

Table VII

The maximum degree of X-ray polarization (%).

MODEL	Energy (keV)						
$(\delta, \alpha_0^2, \beta)$	<u>16</u>	<u>22</u>	<u>30</u>	<u>50</u>	<u>78</u>	<u>102</u>	<u>210</u>
(5, 0.4, 1)	11	12	12	13	14	14	13
(4, 0.4, 1)	7	7	7	8	9	9	9
(3, 0.4, 1)	2	2	2	3	4	4	5
(5, ∞ , 1)	9	10	11	11	11	10	8
(5, 0.04, 1)	18	17	17	17	18	17	15
(3, 0.04, 1)	4	4	4	4	5	5	7
(5, ∞ , 2)	15	16	18	18	17	17	13
(5, ∞ , 5)	14	15	15	16	16	15	12
(5, ∞ , 25)	13	12	11	12	14	14	11
(5, 0.04, 5)	9	10	11	11	11	11	9
(5, 0.04, 25)	11	11	13	14	15	16	12

The models are labelled according to the values of the three parameters δ , α_0^2 and $\beta (= B(N_{tZ})/B(0))$.

the intensity of their X-ray emission. Significant differences between the models can only be seen at small values of τ , for which *Model 4* gives a relative excess

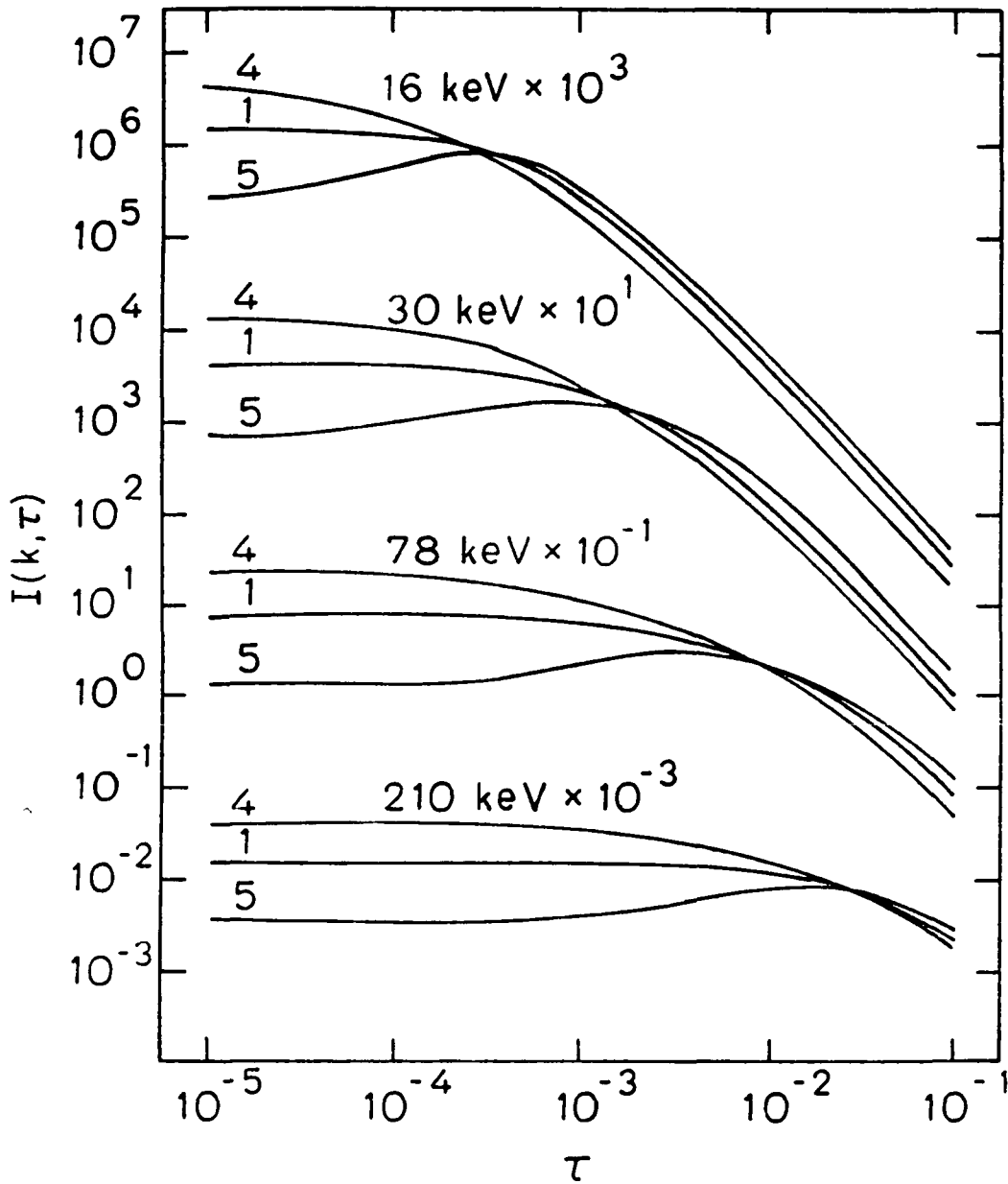


Figure 5.15. $I(k, \tau)$ as given by the numerical results for *Model 1*, *Model 4* and *Model 5*. *Model 1*, *Model 4* and *Model 5* are identical except for having different values of α_0^2 (cf. Table II). For clarity the curves for each energy are moved vertically by the indicated amount. $I(k, \tau \simeq 0)$ for *Model 4* is approximately sixteen times $I(k, \tau \simeq 0)$ for *Model 5*.

Chapter V: X-ray results

of X-rays while *Model 5* produces a considerable deficiency. This may easily be understood. τ is measured along the magnetic field lines and is the column depth traversed by an electron which at all times moves strictly parallel to the loop axis, that is with a pitch angle of zero degrees. Electrons with non-zero pitch angles encounter a greater column thickness of material than is indicated by the value of τ ; with each incremental step $d\tau$ an electron with a pitch angle cosine μ passes by $(N_0/\mu) d\tau$ particles cm^{-2} . This means that electrons with non-zero pitch angles produce more X-rays per incremental increase in the loop length traversed than will electrons with pitch angles zero, in the ratio $1 : \mu$. The broader the electron beam the larger the beam's mean pitch angle and the greater the X-ray emission. The difference in X-ray production rates between the two extremes, *Model 4* and *Model 5*, exceeds a factor of ten at very low column depths. With increasing depth, both models converge toward *Model 1*, which is the best fit of the three to equation (5.2.23) for $I(k, \tau)$. When comparing the results for *Model 1*, *Model 2* and *Model 3*, we saw that equation (5.2.23) was accurate for a wide range of k , τ and δ . We now see that it is also good for a spread of α_0^2 about the median value, becoming less accurate as α_0^2 becomes either large or small.

The swiftness with which the X-ray results for *Model 4* and *Model 5* converge toward those of *Model 1* depends upon the photon energy. This is the origin of the low energy steepening of the thin target X-ray spectra to which we have already drawn attention. At a depth $\tau = k^2/(k+1)$ for k corresponding to 16 keV X-rays, the rate of production of 16 keV X-rays will be roughly the same for all three models. At that same depth τ the rate of production of, say, 78 keV X-rays will still be strongly influenced by the value of α_0^2 . Models with a small value of α_0^2 will

Chapter V: X-ray results

still be underproducing high energy X-rays at a depth where the low energy X-rays are insensitive to α_0^2 . In terms of the X-ray spectrum at each depth this implies that, for *Model 5*, the spectrum for the top part of the coronal loop should be steeper around 16 keV than it is at much higher photon energies. With increasing source column thickness, the position of this steepening moves to higher photon energies, though it is soon overwhelmed by the flattening of the low energy end of the spectrum which comes about from the collisional losses of low energy electrons. For small source column thicknesses, the X-ray deficiency of *Model 5* exceeds an order of magnitude ($I(k, \tau \simeq 0)$ for *Model 4* divided by $I(k, \tau \simeq 0)$ for *Model 5* ~ 16) which means that the spectral index can increase by more than unity. For the top segment of the loop in *Model 5* the spectral index for the range below 22 keV is 6.7 whereas for the range above 30 keV it is 5.8. The results quoted in Table III do not show clearly this low energy steepening because they are obtained from fitting a single power law over too wide a range, namely 16 – 210 keV. We recall that for *Model 1* the index below 22 keV was 6.5 and above 30 keV was 5.9. There should be a marked weakening of this effect in the first segment spectrum of *Model 4*, and this is indeed found in the numerical results. The first segment spectral index below 22 keV minus that above 30 keV is 0.3 for *Model 4*.

This steepening of the low energy end of the thin target spectrum by strongly collimated electron beams is a new result for non-thermal models. It is also a highly significant result, as we shall show clearly in the next chapter when we discuss some recent HXIS data. In the absence of polarization measurements, this spectral steepening is the only means by which the X-ray data can indicate the degree of electron beam collimation. The effect is found at low hard X-ray energies.

Chapter V: X-ray results

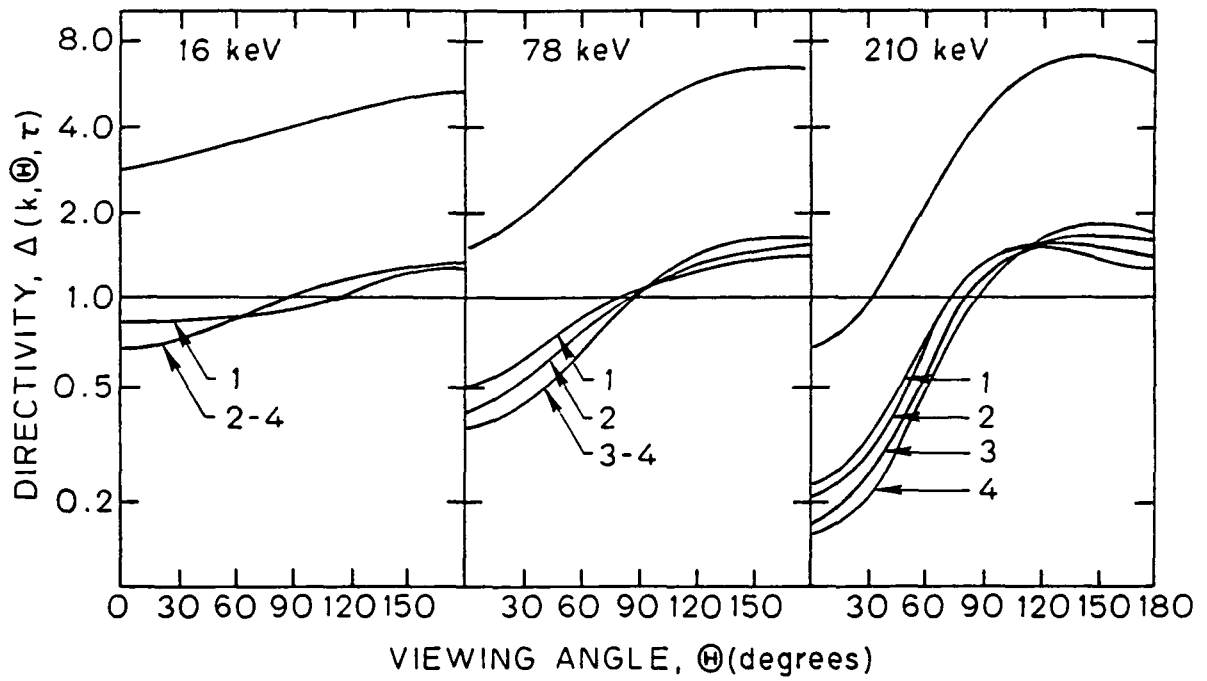
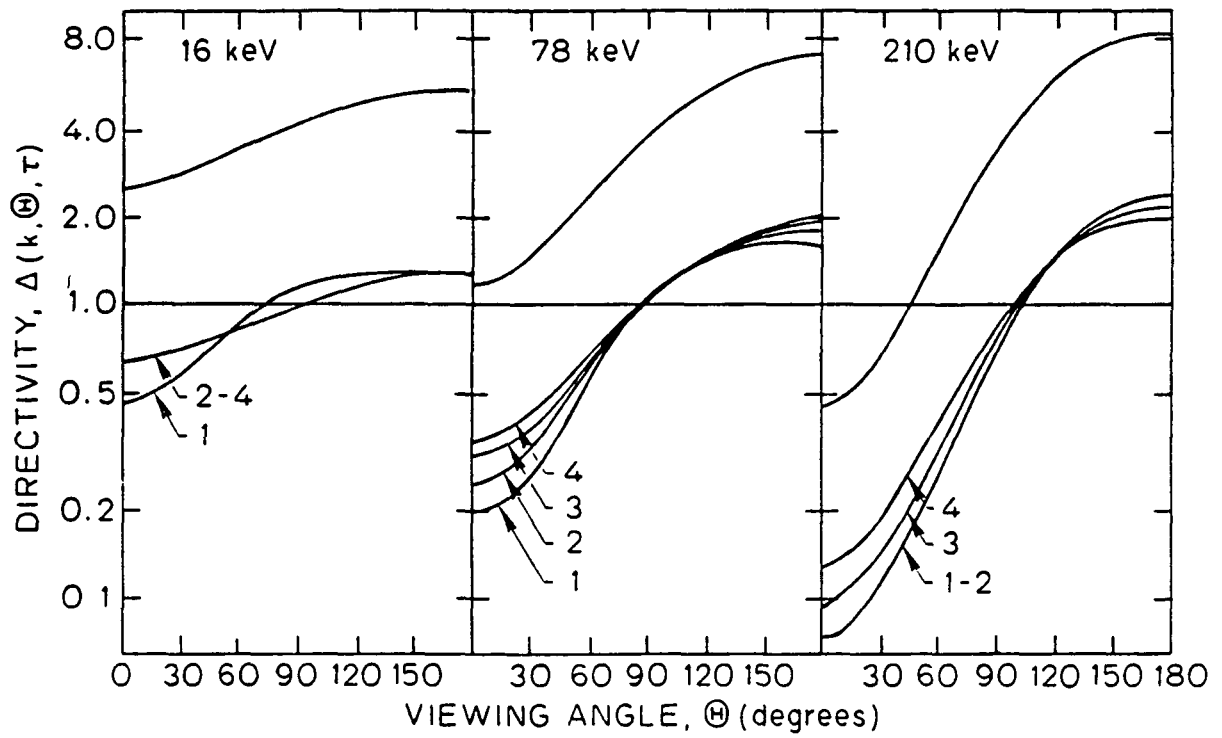


Figure 5.16a, 5.16b

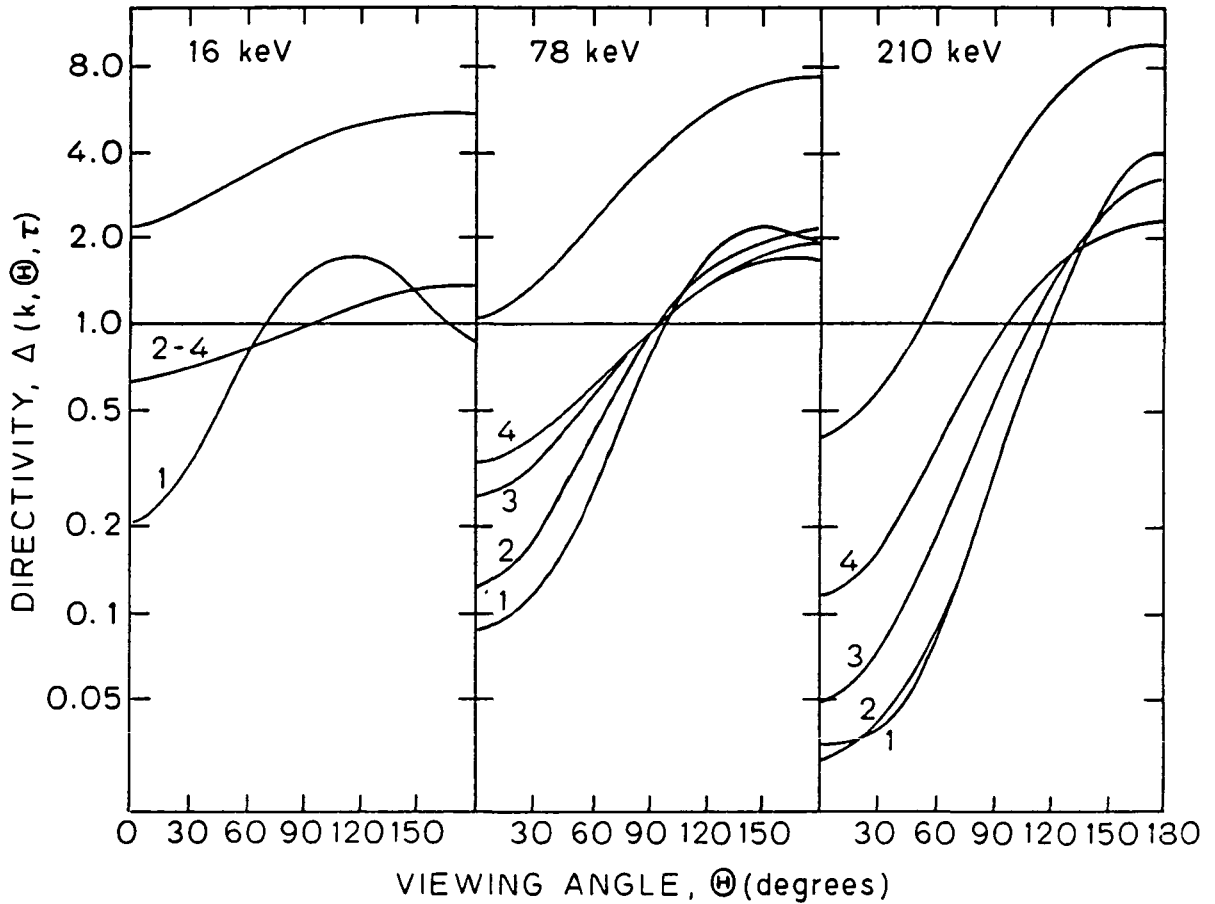


Figure 5.16c The X-ray directivity as a function of viewing angle for *Model 1*, *Model 4* and *Model 5*. Figure (5.16a) is a reproduction of Figure (5.9).

However, it is in precisely this range, 10 – 30 keV X-rays, that HXIS forms its hard X-ray images

Returning to the results for *Model 1*, *Model 4* and *Model 5*, in Figure (5.16) we show the X-ray directivity. As expected, the thin target directivity correlates closely with the pitch angle structure of the electron beam. For *Model 4* (Figure (5.16b)), the X-ray directivity is initially very weak and it strengthens as the source

Chapter V: X-ray results

moves deeper within the flare, thus following the behavior of the electron beam as shown in Figure (3.7). For *Model 5* (Figure (5.16c)), the directivity is initially very strong and it weakens rapidly as the electron beam broadens. Recall that at great depths the pitch angle distribution of an electron beam was independent of the value of α_0^2 . This shows up in the directivity results in that, at 16 and 78 keV, curve 4 (for a source depth of $6.2 \times 10^{21} \text{cm}^{-2}$) is identical for each of the three models. Curve 4 is not quite deep enough for this congruity of the curves to be seen at 210 keV. For *Model 5* the top segment curves (curves 1) show that at low energies the maximum emission occurs for $\Theta < 180^\circ$ and that this peak moves to larger Θ as the X-ray energy increases. Evidence of the initial amount of electron beaming can be found in the directivity results for the whole flare (*cf.* the upper curves in Figure (5.16), and Table VI). Again, these are intrinsic directivity results and it is not clear that any such indication of the electron beaming would show up in actual flare directivity measurements.

The effects of electron beaming show through more clearly in the polarization results. These we show in Figure (5.17). For *Model 4* (Figure (5.17b)), the polarization is, initially, almost entirely in the perpendicular direction and is of order 20 – 30%. As the source moves deeper and the electrons establish a downward moving beam the polarization crosses into the parallel direction. Therefore, whereas the directivity strengthened as the beam was being established, the polarization falls. The strongest polarization for *Model 4* is found at the top of the loop and is in the perpendicular (positive Π) direction.

For *Model 5* (Figure (5.17c)), the highly collimated beam of electrons generates large (70 – 80%) degrees of linear polarization. As the source moves deeper within

Chapter V: X-ray results

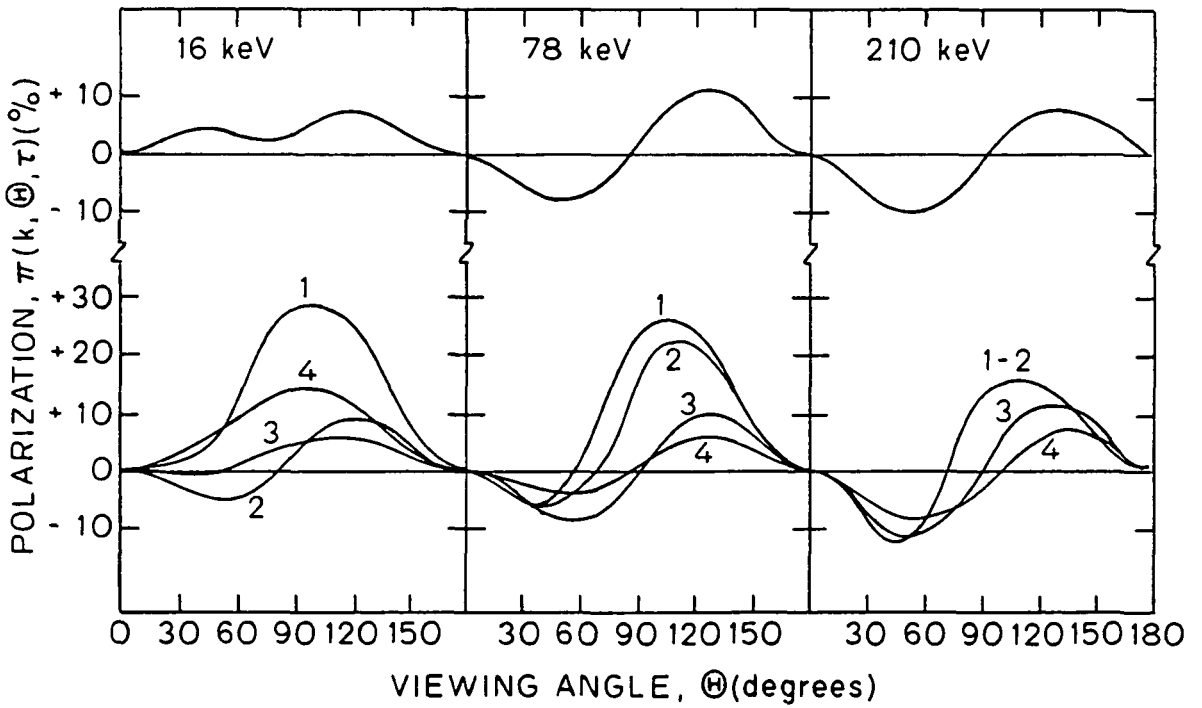
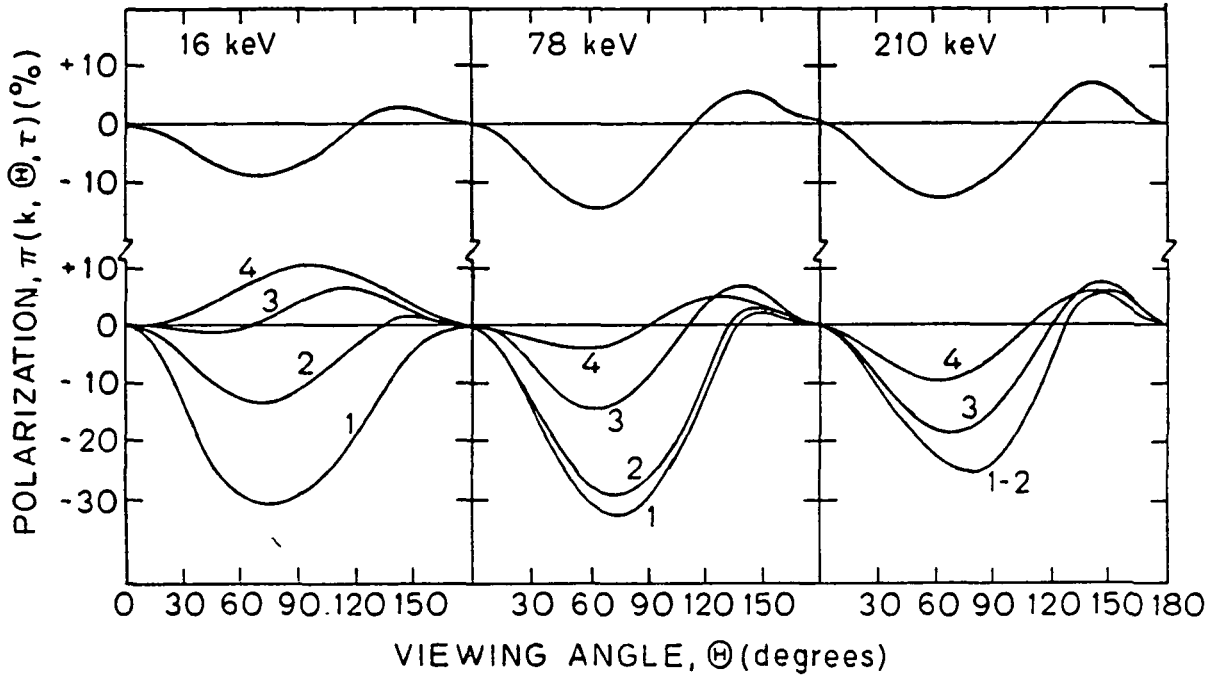


Figure 5.17a, 5.17b.

Chapter V: X-ray results

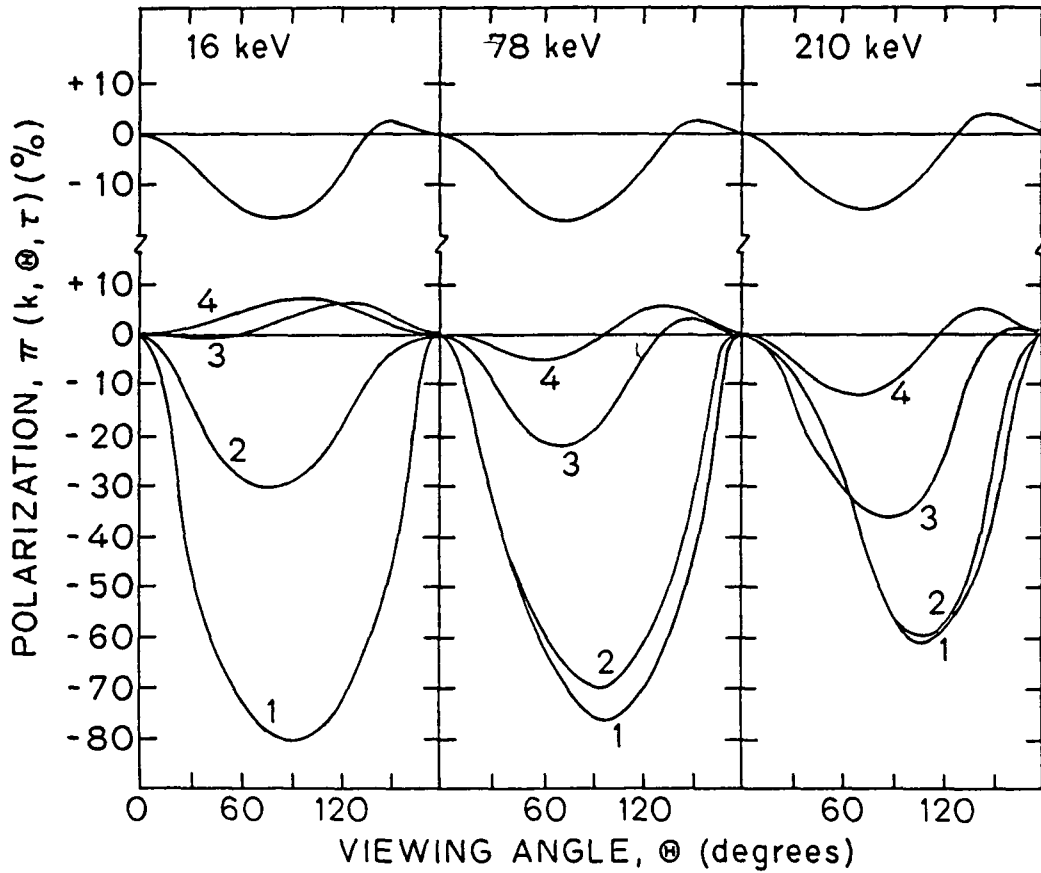


Figure 5.17c The X-ray polarization as a function of viewing angle for *Model 1*, *Model 4* and *Model 5* Figure (5.17a) is a reproduction of Figure (5.10).

the flare, the polarization falls and, beginning with the low energy photons, is eventually very similar to the results of the other two models. The consequences of this convergence in the results are felt most strongly in the polarization curves for the whole flare – the upper curves in each box and Table VII. Even for such a highly collimated beam as is present in *Model 5* the majority of the X-rays are not produced until after the beam has substantially relaxed, that is, until below the depths $\tau \simeq k^2/(k+1)$. The X-rays which are emitted below these depths cannot

Chapter V: X-ray results

contain any information about the initial collimation of the X-ray beam. Hence, even for *Model 5*, the polarization for the whole flare is characteristic of a broad electron beam. From Table VII we can see that the whole loop polarization for *Model 5* is greater than that for *Model 1* but it is still only of the order 15 – 20%, compared with *Model 1*'s $\lesssim 15\%$. For *Model 4*, the polarization is $\simeq 10\%$. For all three models, the polarization changes only slightly with photon energy in the range 10 – 100 keV.

Model 6 – The effects of low δ and low α_0^2 combined.

These results show the response of the whole loop polarization to a change in α_0^2 . The smaller the value of α_0^2 the greater is the X-ray polarization, though even the smallest values of α_0^2 do not give polarizations which are as large as those obtained by the earlier modelling attempts (*cf.* §5.1). High degrees of initial electron beaming generate whole loop X-ray results of at most 20% polarization. A uniformly injected electron beam generates $\sim 10\%$. The results for *Model 2* and *Model 3* showed the response of the whole loop polarization to a change in δ . The smaller the value of δ , the lower the X-ray polarization. *Model 3*, for which $\delta = 3$, gave rise to whole loop polarizations $\lesssim 5\%$, polarizations much smaller than the 10 – 15% for *Model 1* ($\delta = 5$). The results for *Model 6* (Figure (5.18)) show the combined effect of having a highly collimated electron beam and a low value of δ . The polarization is initially large ($\sim 70\%$) in response to the smallness of α_0^2 . With increasing penetration within the flare the electron beam broadens and its energy spectrum flattens. Both the broadening and the flattening contribute to the

Chapter V: X-ray results

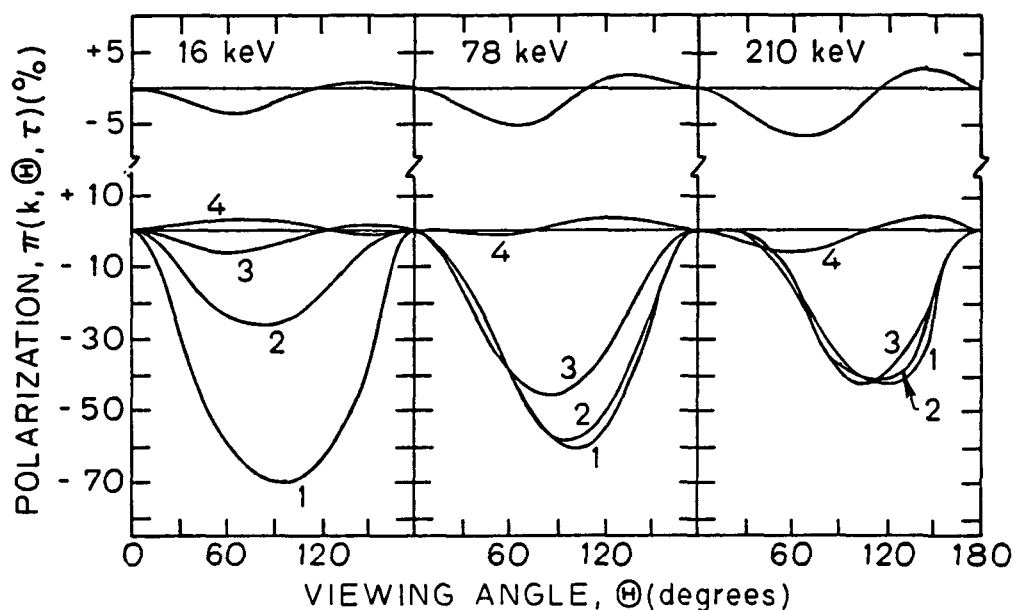


Figure 5.18. The X-ray polarization for *Model 6*. For comparison with *Model 5* (Figure (5.17c)). *Model 5* and *Model 6* both have a highly collimated injected beam ($\alpha_0^2 = 0.04$), but *Model 5* has $\delta = 5$ whereas *Model 6* has $\delta = 3$.

rapid fall off in the degree of X-ray polarization which is observed for increasing source depth. Comparing curves 4 in Figures (5.17c) ($\delta = 5$, $\alpha_0^2 = 0.04$) and (5.18) ($\delta = 3$, $\alpha_0^2 = 0.04$) the polarization is less for *Model 6* than for *Model 5* reflecting the fact that the energy spectrum is much flatter.

By comparing the whole loop polarization curves in Figures (5.17c) and (5.18), and by turning to Table VII, we are able to see which of the two effects, that of a small δ or that of a small α_0^2 , dominates the results for *Model 6*. Clearly, the former effect overwhelms the latter. Despite having a strongly collimated injected beam, *Model 6* shows whole loop polarizations which are as low as $\simeq 5\%$ for a wide range of X-ray energies. The X-ray directivity for *Model 6* is only slightly lower than that for *Model 5*, which means that still many more X-rays are beamed

Chapter V: X-ray results

into the photosphere than escape directly from the flare to the observer. In such a case any measured X-ray polarization from a flare described by *Model 6* will have had to have been contributed by the photospheric albedo (Hénoux 1975; Langer and Petrosian 1977; Bai and Ramaty 1978).

The impetus behind theoretical and observational studies of hard X-ray polarizations has been the belief that non-thermal models predict high degrees of polarization and that thermal models predict very low degrees of polarization. This led to the hope that a passably accurate polarimeter, without the need for an imaging capability, would be able to distinguish unambiguously between a predominance of thermal over non-thermal or of non-thermal over thermal hard X-rays, and, hence, would be able to indicate the nature of the energetic electron distribution. We now see that this underlying belief was not well founded. Our flare models have shown that any observations of large linear polarization can only come from viewing thin target sources, but that from these the X-ray luminosity will be relatively low in comparison with that from the whole flare. Currently available instruments, not having sufficient spatial resolution to be able to take separate measurements from different parts of the whole flare, can only expect to see, at best (high γ , narrow injected electron beam), X-ray polarizations not in excess of 25% and, at worst (low γ , broad injected electron beam), X-ray polarizations of the order of just a few percent. Consequently, only with a very accurate X-ray polarimeter viewing an optimal flare (large γ , highly collimated electron beam, limb position to eliminate any albedo X-rays) would there be a chance of the X-ray polarization indicating any preference for non-thermal over thermal processes.

Chapter V: X-ray results

Models 7 through 11 – The effects of a converging magnetic field.

Of the parameters with which we label our models we have so far left one of them unchanged. We now discuss the response of the impulsive hard X-rays to a change in the magnetic field strength along the length of the loop. A field which increases in strength with distance away from the top of the loop acts as a magnetic bottle trapping the energetic electrons near the regions of lowest field strength. For rapidly increasing magnetic field strengths the electron current moving down through the loop falls in proportion to the increase in field strength, as shown by our results in Chapter III (*cf.* Figures (3.10) and (3.11)). The bottling up of the electrons in the upper reaches of the loop will be reflected by the height distribution of the X-rays in the form of an increasing fraction of the X-rays at each energy coming from the corona.

It is not easy to get a good sense of how much the magnetic field strength varies throughout a flaring loop. There are, as yet, no accurate measurements of the magnetic field strength in the corona. The photospheric fields are measured by Zeeman line splitting (Zirin 1966, pp 367-375), but this technique cannot be extended into the corona because the plasma density there is too low. Photospheric measurements indicate that the magnetic field strength near to sunspots are of the order of $1 - 3 \times 10^3$ Gauss (Zirin 1966, p373; Brown and Smith 1980), but the photospheric fields cannot by themselves give a clear indication of the field strengths in the corona. Flares are associated more with complex photospheric fields than they are with large photospheric fields and they tend to occur where the photospheric magnetic field gradients are steepest (Zirin 1966, p456; Brown and Smith 1980). This means that a simple equating of magnetic field strengths between

Chapter V: X-ray results

the photosphere and corona will not suffice. Neither will the more complex drawing of potential field lines from the photosphere up into the corona suffice. Flares do not occur in potential field geometries. A potential magnetic field structure is a relaxed structure of lowest magnetic energy and as such cannot provide the energy needed to power a flare. There are observational indications that the post flare loops remaining after the gradual phase of a flare are close to being potential field structures and that they represent the relaxation of the magnetic field strength from that which obtained before the flare occurred (Zirin 1966, p456; Kundu 1973; Rust and Bar 1973). For a particular flare burst Kundu (1973) estimated that the chromospheric field strength dropped from roughly 4×10^2 Gauss before the burst to 10^2 Gauss after it. On another occasion Rust and Bar (1973), by modelling potential fields to observed post-flare loop geometries, obtained estimates of the post flare loop strength from 50 – 80 Gauss at the top of a loop to $\simeq 1300$ Gauss at the footpoints near a sunspot. These numbers can be used to give order of magnitude estimates of the magnetic field structure for a flaring loop.

Another method of obtaining estimates of the field variation which, again, applies to quiescent loops rather than flaring loops, uses the gradual phase thermal emissions. Skylab X-ray photographs have shown by high resolution imaging that the loop cross-sectional area changes along the length of the loop (Vesecky, Antiochos and Underwood 1979). Obtaining the emission measure of the thermal radiation as a function of temperature and applying it to models of stable loops has indicated the need for a gradual divergence of the magnetic field by of order 4 – 5, coming mainly at the top of the loop where the temperature exceeds 3×10^6 K (Withbroe 1978; Vesecky, Antiochos and Underwood 1979; Levine and Pye 1980).

Chapter V: X-ray results

Together, all these estimates, which are based upon quiet, *i.e.*, non-flaring loops, indicate that the magnetic field strength may vary by as much as a factor of 20 from the top of the loop to the footpoints. The few measurements taken from burst observations indicate that the loop magnetic field strength can vary widely from flare to flare (Karpen 1980; Marsh *et al.* 1980, 1981) but that the variation with position along a single loop is gradual (Petrosian 1982). As it is likely that the magnetic field strength at the top of the loop is higher before and during an impulsive burst than after it, these impulsive measurements are compatible with the post flare measurements.

From this brief survey we see that we can expect flare magnetic field strengths to increase between the top of the loop and the photosphere by any amount up to a factor of 20 or 30. On this basis, for our models we have selected (constant) values for the parameter $d \ln B/ds$ which give magnetic field strength ratios of 1, 2, 5 and 25 between the top of the loop and the transition region. Because of the large difference in the density between corona and chromosphere, a constant $d \ln B/ds$ throughout the whole length of the model loop implies a large $d \ln B/d\tau$ in the corona and a small $d \ln B/d\tau$ in the chromosphere. The influence of the magnetic field convergence is therefore most manifest in the corona.

In Figure (5.19) we show $I(k, \tau)$ for *Model 4*, *Model 7*, *Model 8* and *Model 9*. The top of the transition region is shown at a value of $\log_{10} \tau \simeq -4.3$ and the chromosphere is to the right. The magnetic field traps the beam electrons in the corona and the degree to which it is effective is directly shown by the X-rays. A small amount of trapping (*Model 7*) leads to a considerable enhancement in the production of coronal X-rays at all photon energies. Increased trapping leads to

Chapter V: X-ray results

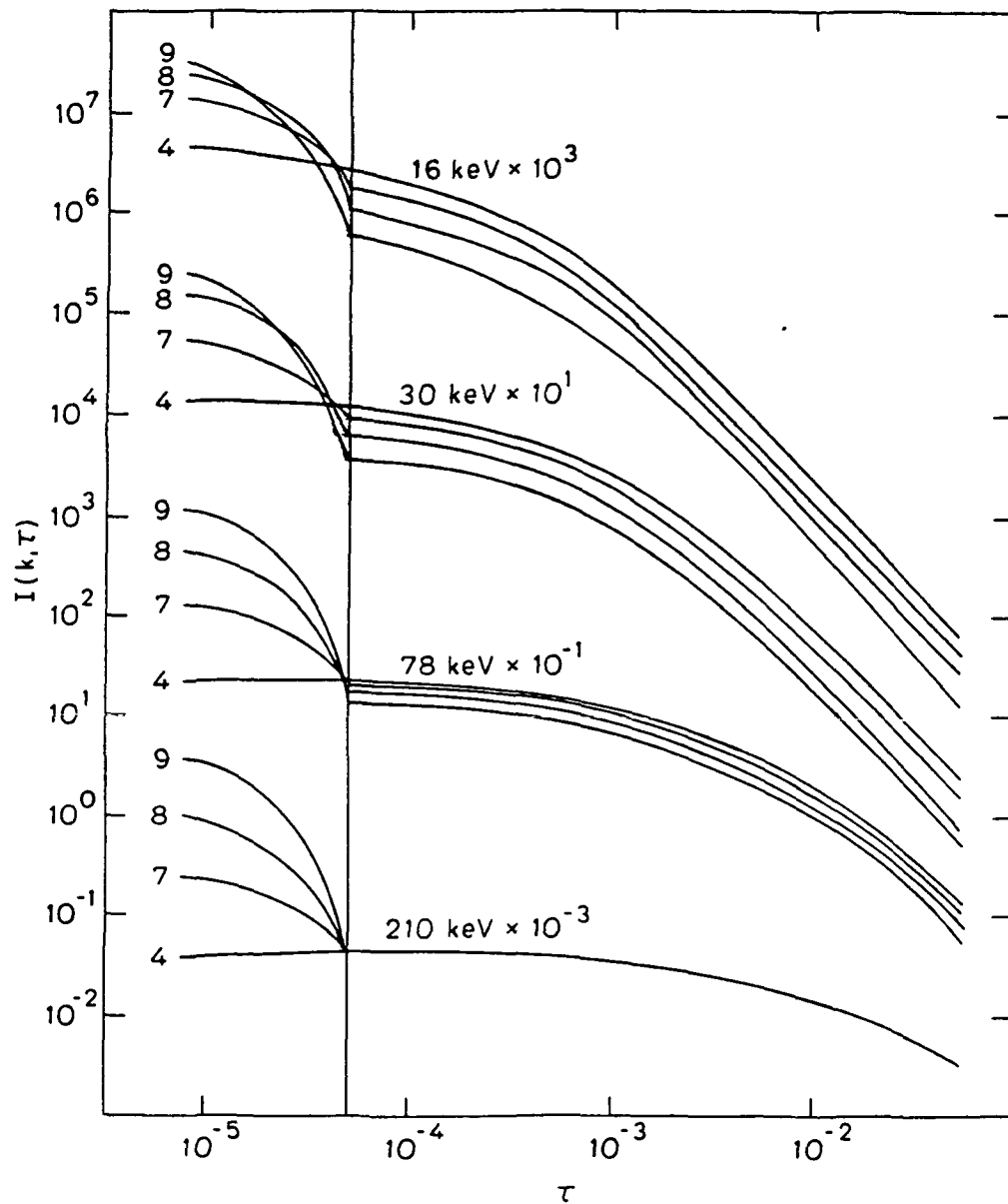


Figure 5.19. $I(k, \tau)$ for *Model 4*, *Model 7*, *Model 8* and *Model 9*. The vertical line at $\log_{10} \tau \approx -4.3$ marks the top of the transition region. The corona is to the left and the chromosphere to the right. The rates at which the coronal magnetic fields converge, given as the ratio of the magnetic field strength at the top of the transition region to that at the top of the coronal loop, are 1 (*Model 4*), 2 (*Model 7*), 5 (*Model 8*) and 25 (*Model 9*). All four models have $\delta = 5$ and $\alpha_0^2 = \infty$.

Chapter V: X-ray results

Table VIII

The coronal X-ray emission as a percentage of the emission from the whole loop.

MODEL	$B(N_{tz})/B(0)$	<u>16</u>	<u>22</u>	<u>30</u>	<u>50</u>	<u>78</u>	<u>102</u>	<u>210</u>
4	1	21	13	8	4	2	1	0.3
7	2	46	35	26	14	7	4	1
8	5	68	58	47	28	15	10	3
9	25	82	76	67	52	35	26	11

The emission as a function of X-ray energy and the rate of magnetic field convergence. Each model has $\delta = 5$ and $\alpha_0^2 = \infty$. The column thickness between the top of the loop and the transition region is $2.4 \times 10^{18} \text{cm}^{-2}$.

increased production of X-rays at the very top of the coronal loop and to a decrease in the production of X-rays at the transition region and in the chromosphere. The behavior of $I(k, \tau)$ with τ below the corona does not change from model to model other than to reflect the reduced percentage of the X-rays which are produced there. The chromospheric density is high enough that the effect of a changing magnetic field strength is not noticeable against the effect of Coulomb collisions, even for the 210 keV X-rays.

Table VIII gives the proportion of the X-ray flux at each energy which is coronal. At low X-ray energies (for example, 16 keV) the coronal proportion initially increases rapidly with the magnetic trapping but then saturates. The

Chapter V: X-ray results

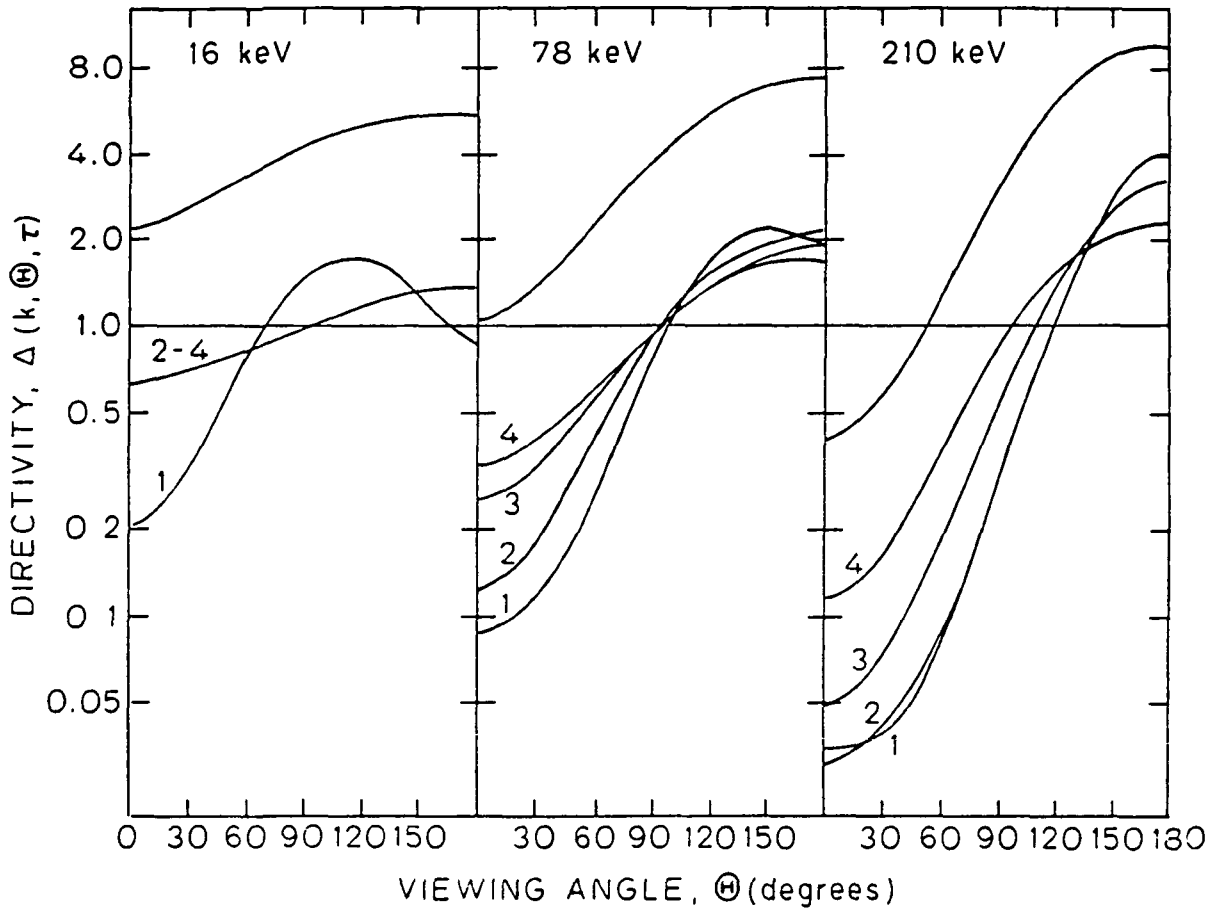


Figure 5.20a The X-ray directivity as a function of viewing angle for *Model 5*, *Model 10* and *Model 11*. These three models each have $\delta = 5$ and $\alpha_0^2 = 0.04$, they differ only in the degree of magnetic trapping (*cf.* Table II). Figure (5.20a) is a reproduction of Figure (5.16c).

large increase in the amount of trapping between *Model 8* and *Model 9* cannot lead to a large increase in the proportion of coronal X-rays simply because the coronal proportion is already so large. The change is more easily seen in the fraction of the X-rays which are produced below the corona, where the production of 16 keV X-rays roughly halves from *Model 8* to *Model 9*. At high X-ray energies

Chapter V: X-ray results

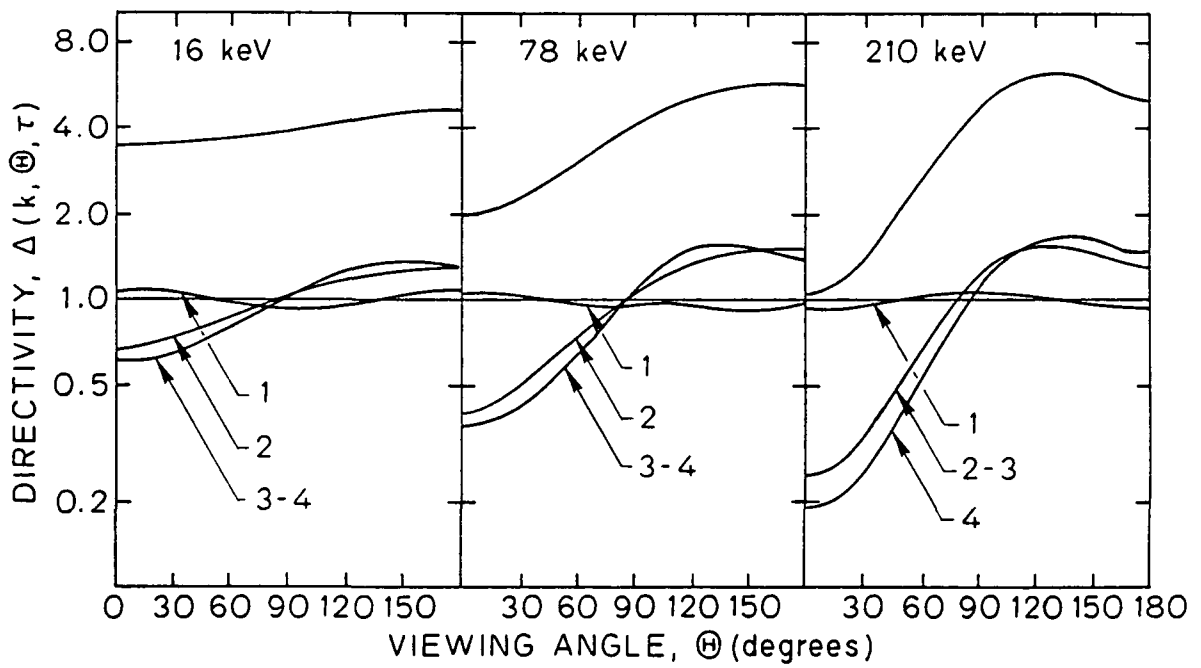
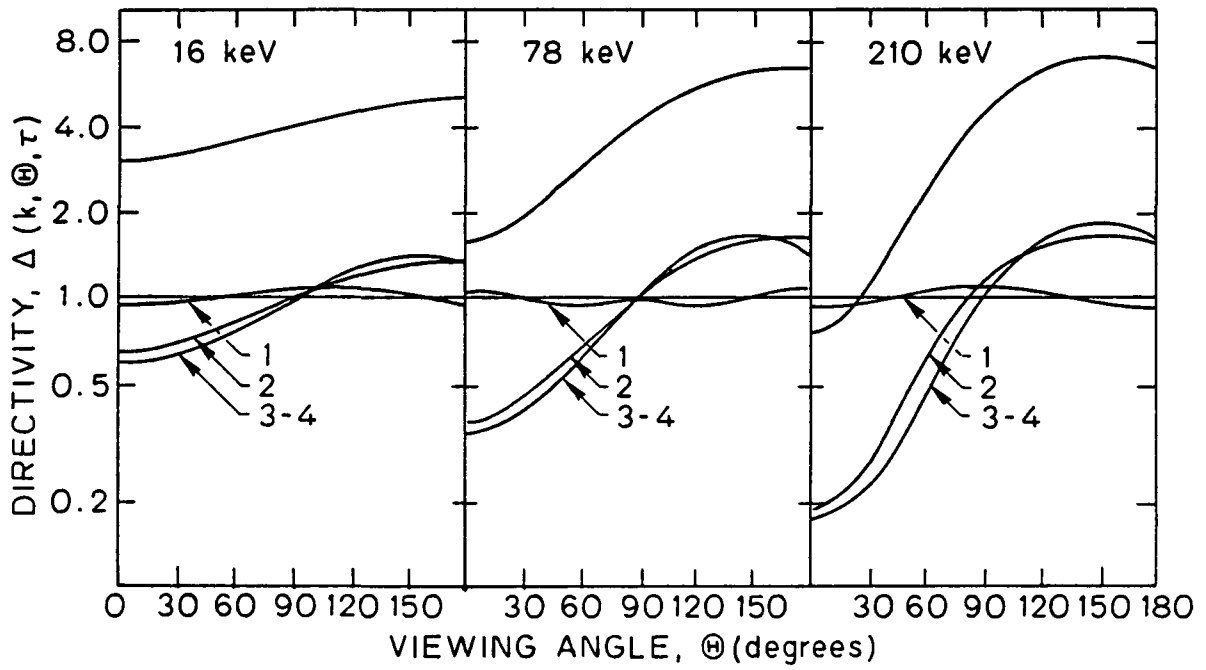


Figure 5 20b, 5 20c.

Chapter V: X-ray results

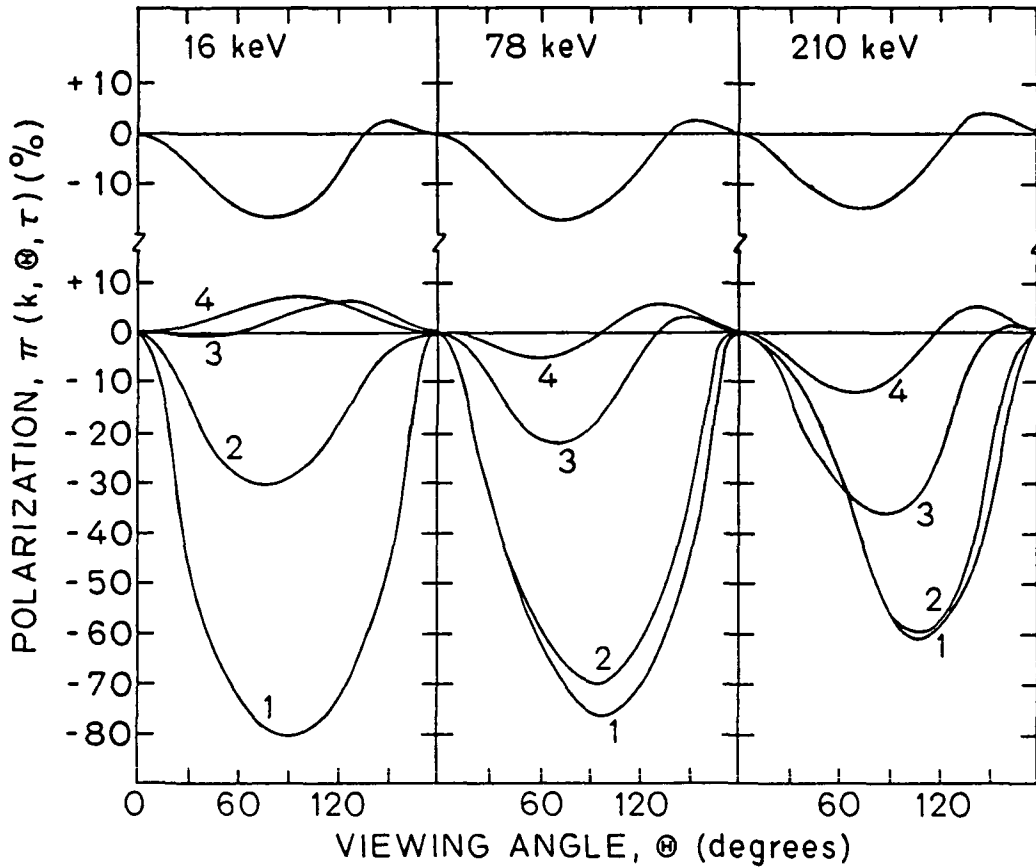


Figure 5.21a

(for example, 210 keV) even a large degree of trapping (*Model 9*) does not cause a large fraction of the X-rays to become coronal, and, hence, the change in $I(k, \tau)$ below the corona between *Model 4* and *Model 9* is only slight. For *Model 9* high energy electrons are efficiently trapped in the corona and cross the length of the loop many times before they eventually escape. However the corona is sufficiently thin to high energy electrons that most of the high energy X-ray emission is still to be found outside the trapping region (*cf.* § 3.3).

Figure (5 20) shows the X-ray directivity for *Model 5*, *Model 10* and *Model 11*. Curve 1 is the X-ray directivity for the top segment of the coronal loop. Curves 2

Chapter V: X-ray results

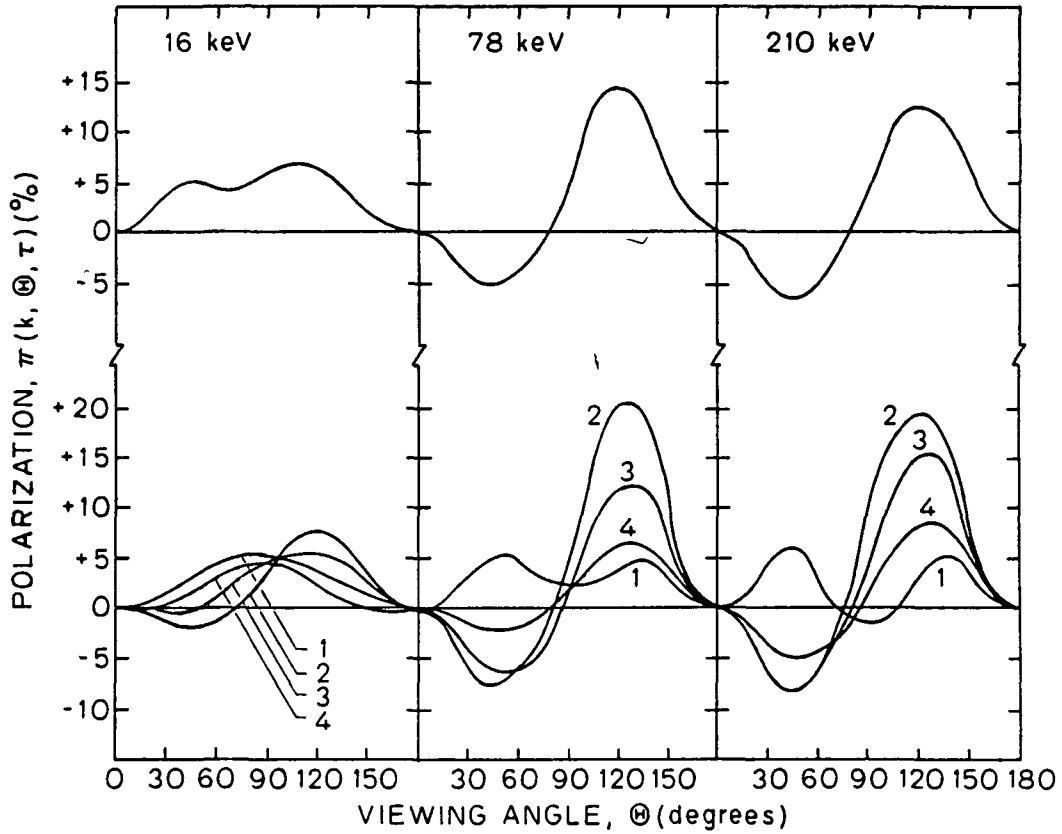


Figure 5.21b

through 4 are for successively deeper parts of the chromosphere. At the top of the coronal loop the directivity is extremely flat at all X-ray energies and the emission is roughly isotropic. Below the corona, the magnetic field is no longer the dominant influence on the electrons. The X-rays become more directional as the electrons establish a downward travelling beam (*cf.* Figure (3.9)). The whole loop directivity (the upper curve in each box) reflects the degree of convergence of the magnetic field to the extent that the emission is primarily coronal or chromospheric. The whole loop directivity at 16 keV is flat whereas that at 210 keV is not.

Chapter V: X-ray results

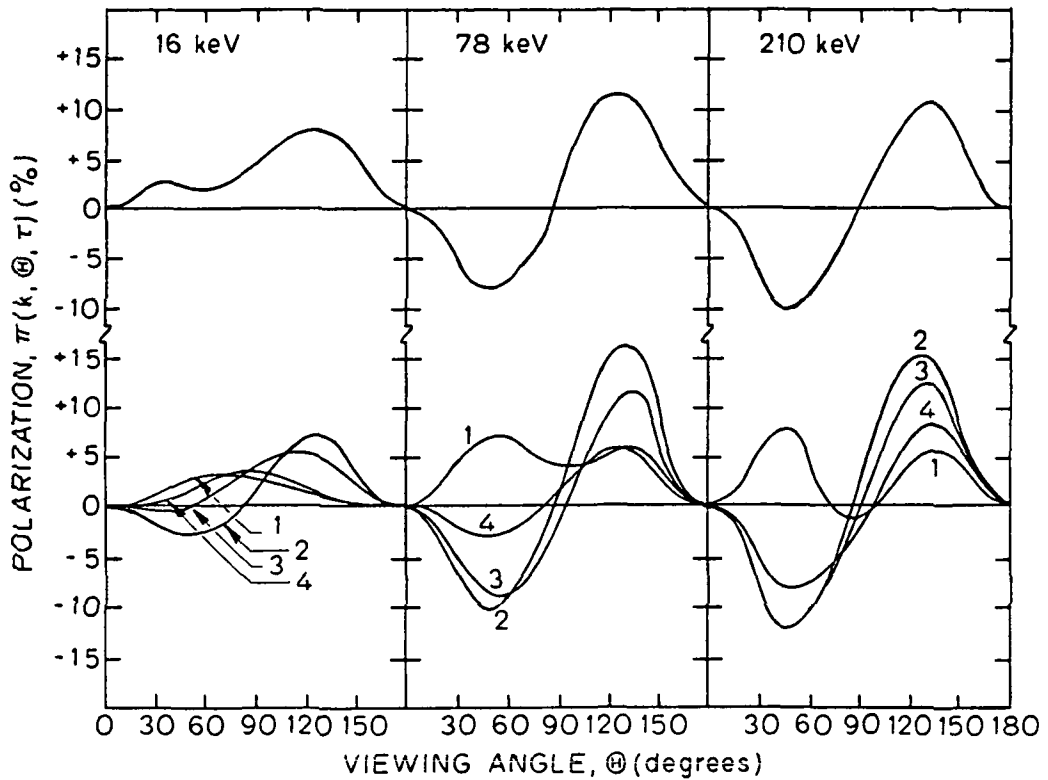


Figure 5.21c The X-ray polarization as a function of viewing angle for *Model 5*, *Model 10* and *Model 11*. Figure (5.21a) is a reproduction of Figure (5.17c).

Figure (5.21) shows the X-ray polarization for the same three models. The complexity of Curve 1 hints to the complexity of the electron pitch angle distribution for a narrow injected beam with a strongly converging magnetic field (*cf* Figure (3.9)) The maximum degree of polarization in the corona is small, being less than 10%. Below the transition region, the X-ray polarization at all energies steadily returns to that of a source without trapping. The whole loop polarization reflects the predominance of coronal or chromospheric emission as the X-ray energy is either low or high.

This brings to a close our discussion of the model results. We have in this chapter presented a sample of the X-ray results for a wide range of non-thermal

Chapter V: X-ray results

models. We have shown how the X-rays respond to variations in the details of the non-thermal models, specifically to changes in the three modelling parameters δ , α_0^2 and $d \ln B/ds$. We have discussed the results in terms of how the X-rays reflect the behavior of the underlying source electrons and have given a quantitative understanding of the accuracy to which the electron model parameters can be inferred from the X-ray measurements.

In the next chapter we shall demonstrate how what has been learned from the X-ray models can be applied to X-ray observations. The general non-thermal model has been thoroughly analyzed and we can now apply our modelling techniques to some of the most recent hard X-ray data. We show that non-thermal models can be obtained which describe the observed flares, and that through these models we obtain much more information from the observations than was heretofore possible.

Chapter VI

Studies of X-ray Observations

We have, so far, covered the early theory and data on solar flare impulsive hard X-rays and have thoroughly discussed the results from our models. We have detailed the relationships between the X-ray characteristics and the model parameters and have quantified the extent to which the X-ray characteristics can reveal the underlying flare model. We showed that none of the X-ray characteristics from a spatially unresolved flare is able to give us precise values for the model parameters. The X-ray spectral index displays no more than a gross correlation with the electron index and can only give an estimate of its value (*cf.* Table III, Chapter V), the extrinsic directivity is difficult either to measure directly or to evaluate indirectly and, even then, is only uncertainly related to the intrinsic directivity, and the total degree of polarization for the spatially unresolved X-rays may be no more than that which is expected from the sum of the direct and reflected (albedo) X-rays from an isotropic source.

Given that spatially unresolved X-ray data is unable to convey precise information about its source, we must look for other ways by which we may use the X-rays to further our understanding of solar flares. We shall now consider the height structures of the X-ray characteristics, specifically the X-ray intensity

Chapter VI: X-ray Observations

and spectrum, and shall show how the results of Chapter V can be used when interpreting spatially resolved X-ray data.

6.1 X-ray height structures.

Preliminary indications from the early use of flare models suggested that thermal and non-thermal flares would have different X-ray height structures. The strongest sources of thermal X-rays would be the regions of hottest plasma, found at the sites where the magnetic energy is released, presumably near the top of the loop. The brightest X-ray emission from a non-thermal beam of electrons would come from regions of high plasma density, that is, from the chromosphere. Consequently, the non-thermal X-rays would be emitted primarily from the footpoints, located low in the solar atmosphere. All the early hard X-ray observations (pre Skylab, the OSO series up to and including OSO-7 for example) were whole sun observations and could not distinguish directly between the impulsive hard X-rays emitted from the top of the loop and from the footpoints. There was only circumstantial evidence to go by. Impulsive hard X-rays show a strong temporal correlation with the burst $H\alpha$ and EUV emissions, both of which come from transition region layers and below. This correlation was taken to indicate a preference for non-thermal X-ray sources. But then occultation experiments showed that some large flares have a measurably large amount of their impulsive X-ray source located at altitudes in excess of $10^4 km$ above the photosphere and therefore in regions of low density (Kane 1974; Roy and Datlowe 1975). This suggested that

Chapter VI: X-ray Observations

the simple thick target, non-thermal model was not sufficient and various thermal and non-thermal models were invoked in order to account for these results.

Brown and McClymont (1975) realized that the height distribution of the X-rays was potentially a good way to distinguish between different flare models. The calculated X-ray height structure is model sensitive and can be compared with observations in order to indicate a preference for those models which give the best agreement. However, the X-ray height structure is sufficiently model sensitive that these X-ray calculations have to be comprehensive for the results to be at all reliable. Brown and McClymont calculated the X-ray height structure for non-thermal models using the Brown (1972) mean scattering treatment of the electron beam and found that the amount of X-ray emission from coronal or low density regions was simply proportional to the coronal column thickness encountered by the electron beam.

The Brown and McClymont results could, then, explain the high altitude X-ray sources but, in so doing, they implied that non-thermal models might not necessarily be distinguishable from thermal models solely on the gross features of the X-ray height structure. In this case more sophisticated modelling would be required. A step was taken in this direction by Emslie (1980, 1981b). His treatment of the non-thermal electron beam used a mean scattering analysis for the effects of collisions but also introduced the effects of a reverse current. His thermal X-ray model included the high energy tail on the isothermal Maxwellian electron distribution from electrons which escape from the confining turbulent fronts and which then together behave like a non-thermal beam. He compared the X-ray height distributions from the two types of model and found both types of model

Chapter VI: X-ray Observations

capable of producing a mixture of coronal and chromospheric emission. He also showed that if these height distributions were convoluted with a filter representing the angular resolution of the best X-ray imaging telescopes, the resulting X-ray height structures from the two types of model would, indeed, begin to lose their dissimilarity. He thus recognised that the instrument resolution then (and now) available is not sufficient for an unambiguous matching of theoretical models to individual observed X-ray height structures and that many observations of large flares will be necessary before the accumulated data can allow a preliminary discrimination between contending flare models.

We are now in a position to advance the theoretical study of non-thermal model hard X-ray height structures more than one step further. Our technique allows us to make the most accurate yet evaluation of the electron beam dynamics and to properly include the influences of Coulomb collisions and the magnetic structure of the flare loop. But we also have complete model flexibility in that we are free to vary continuously all the parameters of the models. This allows us take actual flare observations and to use an iterative approach to obtain a model which best describes the flare. We can use the Chapter V explanations of the general correlations between the X-ray characteristics and the model parameters to indicate a beginning set of parameter values for a trial fit of a model to the flare hard X-ray observations. We can then compare our numerical X-ray results for that trial model with the details of the observational data in order to refine our models to obtain a best fit for that particular flare. This final best fit model would provide a complete description of the structure of the flare including a description

Chapter VI: X-ray Observations

of the injected energetic electron distribution, obtained from agreement of the calculated and observed characteristics of the hard X-rays.

In this chapter we present several studies which use the spatially resolved X-ray data which has recently become available. We select a few flares which have been reported with sufficient data that we can, by applying our modelling techniques, obtain reasonable constraints upon the flare model parameters. We are, of course, limited to the small number of flares for which there is adequate spatial information and then to the accuracy of that data. We certainly hope that in the near future many more reports of high quality spatially resolved data will appear. One thing that our studies will show is that, when using the full power of our modelling technique, we can obtain unique and complete descriptions of flares from the data.

There are, to date, no reports of hard X-ray polarization measurements which include any degree of spatial resolution. In the future, should such data become available, it would greatly improve the determination of how highly collimated the electron beams are when they are injected into the flaring plasma at the acceleration site. This would be of enormous help in understanding the processes which generate the initial electron beams. Without such spatially resolved polarization data, however, the electron population and, hence, the acceleration processes, are not so directly accessible and they must be inferred less directly from the measurements of other X-ray characteristics.

We are similarly without any definite measurement of the degree of convergence of the magnetic field throughout the corona. The effects of any magnetic

Chapter VI: X-ray Observations

trapping are most pronounced in the corona. Magnetic trapping increases the effective column thickness of the coronal X-ray source material beyond that which actually separates the acceleration site from the transition region. It also decreases the interval between the thick and thin target spectral indices for any one model. As a generalisation obtained from a small number of studies, for most flares any increase in the coronal magnetic field from the top of the loop to the transition region is small. Only one of the studies which we are about to present required the use in our models of a coronal magnetic field with increasing strength. That was obtained because one flare was divisible into two regions having very dissimilar X-ray fluxes but similar X-ray spectra. For that one flare, though, we were able to obtain only an approximate lower limit to the degree of magnetic trapping given in the form of the ratio of the magnetic field strength at the top of the transition region to that at the top of the loop. We were not able to put a specific value on the ratio of magnetic field strengths. This general weighting away from strongly converging magnetic fields is compatible with the studies by Withbroe (1978) and Levine and Pye (1980) based upon obtaining the correct differential emission measure to Skylab EUV and soft X-ray measurements. Likewise our generalization is compatible with the recent study by Petrosian (1982) based upon the locations of impulsive microwave sources in which it was concluded that any spatial variation of the coronal magnetic field strength would have to be slight.

The type of spatially resolved X-ray data which we do have available is X-ray flux and spectral data with the beginnings of spatial resolution. There are two sources of such data. One is the Hard X-ray Imaging Spectrometer (HXIS) on board the Solar Maximum Mission satellite (van Beek *et al.* 1980; 1981) which

Chapter VI: X-ray Observations

was launched on February 14th, 1980, has six energy channels covering the range $3.5 - 30.0 \text{ keV}$, is capable of $8'' \times 8''$ angular resolution (corresponding to $\simeq 6000 \text{ km} \times 6000 \text{ km}$ on the surface of the sun), and has a time resolution of 0.5 to 7 s depending on the mode of operation. HXIS is the first instrument to have imaging capabilities at hard X-ray energies but its sensitivity is such that only strong flares with plentiful hard X-ray emission are capable of being imaged in the higher energy channels (Duivjeman, Hoyng and Machado 1982). This severely reduces the value of HXIS data for our modelling technique which requires that the X-rays be of a high enough energy that the possibility of thermal contamination be low. Indeed, only one flare which has been seen by HXIS, that of April 10, 1980, was bright enough and has been thoroughly enough reported to be of use to us here.

The other source of hard X-ray data which has the beginnings of spatial resolution is S. R. Kane and his coworkers. They have data from stereoscopic observations of flares by two telescopes, one an X-ray spectrometer onboard the ISEE - 3 (International Sun Earth Explorer - 3) spacecraft, and the other an X-ray spectrometer onboard the PVO (Pioneer Venus Orbiter) spacecraft. The two telescopes are capable of viewing the sun from widely separated positions and can provide stereoscopic observational data of events which occur within both their fields of view. The ISEE - 3 instrument (initially described by Anderson *et al.* 1978) has undergone recalibration and, in its current condition, is described by Kane *et al.* (1982). It covers the energy range $26 - 3170 \text{ keV}$ in twelve channels, with time resolution better than 0.5 s for the first four channels (up to photon energies of 398 keV) and with somewhat poorer resolution in the higher energy

Chapter VI: X-ray Observations

channels. The PVO instrument was initially described by Kane *et al.* 1979 and redescribed by Kane *et al.* 1982. It covers the range 100 – 2000 *keV* in four energy channels and has time resolution comparable to that of the ISEE - 3 instrument. The estimated uncertainty in the relative responses of the two instruments is given as a calibration uncertainty estimated to be $\lesssim 10\%$ (Kane *et al.* 1982). These two instruments are capable of rudimentary spatial resolution when a flare which is viewed simultaneously by both of them is seen by one telescope as being partially occulted by the solar limb, yet is in full view (unocculted on the solar disk) to the other telescope. Two such observations of one flare provide hard X-ray data from the whole flare and from just that part which was not occulted from either instrument thus dividing the flare into two spatially distinct regions.

6.2 The flare of April 10, 1980.

We turn first of all to one flare which was imaged by HXIS. The flare, which occurred on April 10, 1980, was first reported by Hoyng *et al.* (1981) [hereafter HMD] and has subsequently been studied and presented by Machado, Duivjeman, and Dennis (1982) [hereafter MDD] and Duivjeman, Hoyng, and Machado (1982) [hereafter DHM]. The flare showed soft X-ray type behaviour in the first three HXIS channels (3.5 – 11.5 *keV*) indicating that the flare contained a volume of plasma which was heated at the time of the impulsive burst and which then cooled during the decay phase. The remaining three channels (11.5 – 30 *keV*) showed a short lived hard X-ray burst of duration ~ 20 s. HXIS was able to resolve the flare into three distinct regions (*cf.* Figure (6.1)). Two of these regions (regions A and

Chapter VI: X-ray Observations

C) showed the largest count rates in the hard X-ray channels (11.5 – 30 keV). The other region (region B) produced most of the soft (3.5 – 11.5 keV) X-rays and had weaker emission at hard X-ray energies than regions A and C. Regions A and C were spatially separated with region B between them and all three regions could be clearly separated in the X-ray images, *i.e.*, there was little overlap of region B into the pixels which imaged regions A and C. These three regions each covered an area of $8'' \times 16''$, *i.e.*, each filled two HXIS pixels, though the actual size of the emitting regions may have been much smaller. During the impulsive phase the hard X-ray time profiles of regions A and C showed a strong similarity to each other. HMD compared the positions of regions A and C with H α pictures from Tel Aviv. To within the pointing accuracy of HXIS regions A and C were coincident with the H α kernels. DHM, from an overlay of a magnetogram, placed regions A and C on opposite sides of a neutral line, locating them in regions of different polarity.

Based upon all these observations, the flare structure was described as being a compact loop in the corona (region B in the HXIS field), with footpoints descending into the chromosphere and seen as regions A and C. The footpoints brighten simultaneously in hard X-rays and the loop peaks at a later time in the softer X-rays. HMD give the observed number of counts over a 13.5 second integration time during the hard X-ray burst for regions A, B and C, and these are reproduced here in Table IX. The data clearly shows that the impulsive emission from regions A and C is of a harder character than that from region B. HMD apply their fitting routines to the hard X-ray count data for regions A and C and obtain a best fit power law spectrum for the footpoints of $\gamma = 5.5 \pm 1.0$. The HXIS hard X-ray data

Chapter VI: X-ray Observations

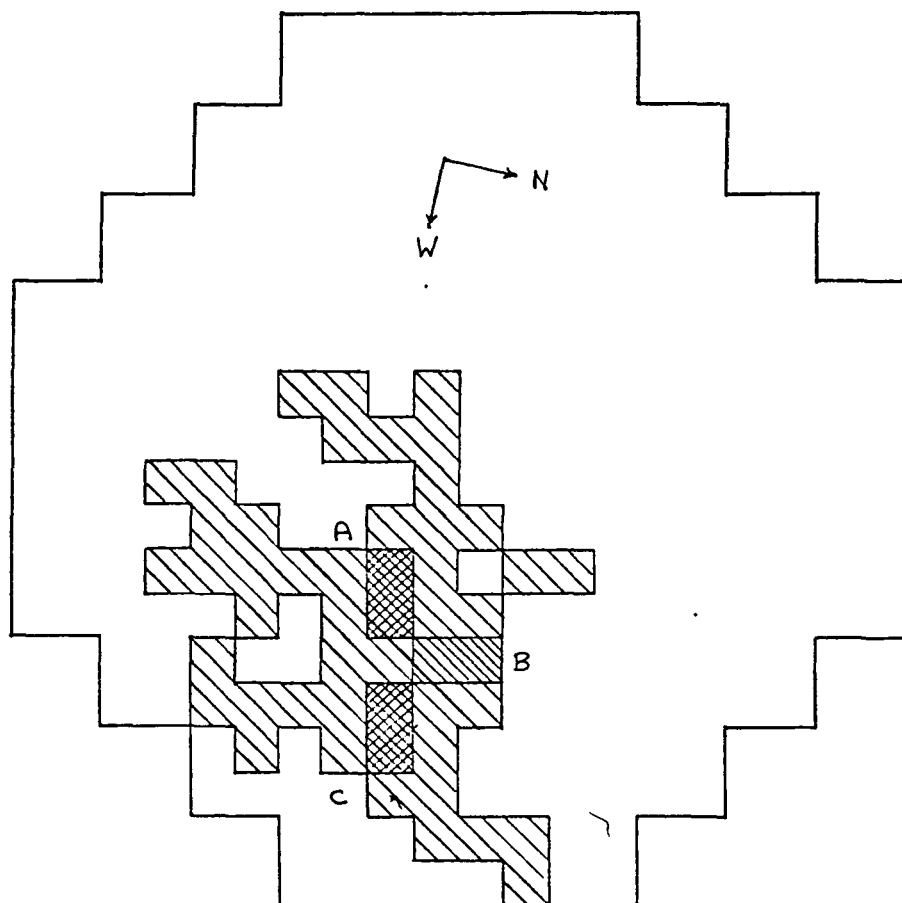


Figure 6.1 The flare which occurred at N12, W42 on April 10, 1980, as seen by HXIS in the energy channel 16 - 22 keV (from Hoyng *et al.* 1981). The location of the regions A, B and C are shown (see text). Each pixel corresponds to an angular resolution of $8'' \times 8''$ which is equivalent to $\sim 6000 \text{ km} \times 6000 \text{ km}$ on the surface of the sun

was not sufficient to rule out a thermal fit to the footpoint spectra, for which fitting a multi-temperature hot plasma to the X-ray data would have required plasma temperatures higher than 10^8 K . The Hard X-ray Burst Spectrometer (HXRBS), also on the SMM satellite, observed the same event (but without any spatial

Chapter VI: X-ray Observations

resolution of the flare) and measured a power law X-ray spectrum for the whole flare with a spectral index of 5.5.

MDD contrasted the emission between the footpoints and the loop in the range 16 – 30 keV and estimated the emission ratio (between footpoints and loop) at these energies to be $\gtrsim 2 : 1$. MDD add that what spatial overlap there may have been in the HXIS images of the three regions would have smoothed the brightness contrast between the regions. (When MDD apply their own modelling to the data they allow for this overlap by subtracting a contribution equal to one third of the loop emission from the footpoints.) This means that in the energy range 16 – 30 keV the footpoints are considerably brighter than the coronal loop and, consequently, that the column thickness of the coronal loop was not large.

MDD and DHM compared the data to the X-ray height structure of the dissipative thermal model of Brown *et al.* (1980) and Brown and Hayward (1981) by using the hard X-ray modelling of Emslie (1981b). They reported that the model predictions were in contradiction with the observations. They then applied a non-thermal thick target model to the data, using the results of Hoyng, Brown and van Beek (1976). They estimated the flux of high energy electrons and the power in the electron beam, and integrated these over the burst duration. They derived an upperlimit to the beam energy of 6×10^{29} ergs in electrons with energies $E > E_0$ for $E_0 = 20$ keV, or, which is equivalent, 10^{30} ergs for $E_0 = 16$ keV. These estimates are within the total flare energy budget of several times 10^{30} ergs but are a large fraction of it. DHM also estimated the loop length to be 3.5×10^9 cms, the column thickness of the coronal loop to be $N_{\text{Corona}} \leq 5 \times 10^{19}$ cm⁻² and the

Chapter VI: X-ray Observations

Table IX

The flare of April 10, 1980.

HXIS Channel (keV)	A+C	B	(A+C)/B
11.5 - 16.0	305	174	1.8
16.0 - 22.0	95	27	3.5
22.0 - 30.0	36	4	9.0

$\gamma_{\text{tot}} = 5.5$ from HXRBS (HMD)
 Impulsive Burst FWHM = 20 seconds (MDD)
 $N_{\text{Corona}} \leq 5 \times 10^{19} \text{ cm}^{-2}$ (DHM)
 loop length = $3.5 \times 10^9 \text{ cms}$ (DHM)
 $0.3 \leq n_{10} \leq 1.4$ (DHM)
 Beam energy 10^{30} ergs above 16 keV (MDD)
 Peak beam flux $2.8 \times 10^{28} \text{ ergs sec}^{-1}$ (MDD)

Sources are: Duijveman, A., Hoyng, P., and Machado, M. E., 1982, *Solar Physics*, **81**, 137, [DHM]. Hoyng, P., Machado, M. E., Duijveman, A., and 21 others, 1981, *Astrophysical Journal Letters*, **244**, L153, [HMD]. Machado, M. E., Duijveman, A., and Dennis, B. R., 1982, *Solar Physics*, **79**, 85, [MDD].

coronal density to be $0.3 \leq n_{10} \leq 1.4$ where n_{10} is the particle density in units of 10^{10} cm^{-3} .

Chapter VI: X-ray Observations

Let us return to the data given by HMD. We shall now apply our modelling technique to this hard X-ray data and shall obtain a best fit of our non-thermal models by finding appropriate values for the physical parameters in the Fokker-Planck Equation. We shall be able to improve substantially upon the rough estimates obtained by the earlier studies.

We shall ignore for now any cross-contamination between regions A, B and C and shall add together the counts for the footpoint regions A and C. This we do because our model considers only half the coronal loop and one footpoint. As region B covers the whole coronal loop we must either halve the counts of region B or include together both footpoints. We take the latter course so that our derived electron beam strengths will be appropriate to the whole flare and not just half. We cannot use the HXIS count data directly to obtain an estimate of the hard X-ray spectral index, as each energy channel has a different counting efficiency and a different energy resolution. However, we can use the channel-by-channel ratios of the counts for B to the counts for A + C to obtain the difference between the best fit spectral indices for B and for A + C. By plotting the $(A + C)/B$ data given in Table IX we obtain $\gamma_B - \gamma_{AC} \simeq 2.5$. We use this with the HXRBS estimate of the index for the whole flare which was $\gamma_{\text{tot}} \simeq 5.5$. We can, then, vary our trial model to obtain the observed flux ratios between the footpoints and the coronal loop (regions A + C and B) in one-keV-wide energy channels at energies of 11.5, 16, 22, and 30 keV. These are the numbers we shall be fitting with our results. Their precision can be no greater than the precision of the quoted X-ray counts which, unfortunately, owing to the smallness of the number of counts in the higher energy

Chapter VI: X-ray Observations

HXIS channels and to the fact that HXIS only gives us three energy channels to work with, is not high.

We now have to use these X-ray data to obtain the parameters and coefficients in the Fokker-Planck Equation. We begin with the fact that both loop and footpoints are well fitted by power law spectra over the range $11.5 - 30 \text{ keV}$ and that the difference in the indices is $\gamma_B - \gamma_{AC} \simeq 2.5$. In § 5.2 we saw that the average difference between thick and thin target spectra for our models was $\simeq 1.7$ and that injecting a very narrowly collimated electron beam (small α_0^2) gave rise to a low energy steepening of the thin target spectrum. $\gamma_B - \gamma_{AC}$, at 2.5, therefore indicates that we should choose a small value for α_0^2 , say, 0.04 for our first modelling attempt. Our model results show clearly that the gap between the thick and thin target indices closes as the amount of magnetic trapping is increased. Therefore, we should also set $d \ln B/ds = 0$.

HXRBS measured a whole loop spectral index of 5.5. To reproduce this we can try an electron spectral index $\delta = 6.0$. We have no clear indication of the column thickness of the coronal loop N_{Corona} other than that obtained by DHM. We shall adopt their value for the distance between the top of the coronal loop and the footpoints ($1.8 \times 10^9 \text{ cm}$) and shall use a uniform coronal density of $2 \times 10^{10} \text{ cm}^{-3}$. This gives a coronal loop column thickness of $3.6 \times 10^{19} \text{ cm}^{-2}$ which is compatible with the DHM estimate. Once we have the results from running our first model we can adjust the coronal density to give better agreement with the HXIS data.

Chapter VI: X-ray Observations

Our first trial model has the parameter set

$$\delta = 6.0;$$

$$\alpha_0^2 = 0.04;$$

$$d \ln B/ds = 0.0;$$

$$N_{\text{Corona}} = 3.6 \times 10^{19} \text{ cm}^{-2}.$$

We ran this to see how well it would fit the HXIS data quite expecting to have to make several iterations before we obtained the best fit model.

We looked at the results from this trial model and found:

1) Our value of $\gamma_B - \gamma_{AC}$ for 11.5 – 30 keV X-rays was 2.9. This was too high and suggested that a larger value of α_0^2 was needed.

2) The spectral index for the whole flare was 5.5 which told us that we did not need to change our value of δ .

3) The X-ray flux ratios between the loop and the footpoints at 11.5, 16, 22 and 30 keV were all between a factor of two or three too high. This meant that the coronal column thickness used was approximately 2.5 times too large and that our coronal density should be reduced by this much. Bearing in mind that a larger value of α_0^2 would increase the loop flux relative to the footpoints flux (*cf.* Figure (5.15)) we reduced the coronal density by a factor of three.

Another iteration beyond this one and we had a good fit to the HXIS data (within the uncertainties in the data) with a model having

Chapter VI: X-ray Observations

$$\delta = 6.0;$$

$$\alpha_0^2 = 0.1;$$

$$d \ln B/ds = 0.0;$$

$$N_{\text{Corona}} = 1.4 \times 10^{19} \text{ cm}^{-2};$$

$$\text{Beam energy } 2.7 \times 10^{29} \text{ ergs above } 16 \text{ keV};$$

$$\text{Peak beam flux } 4.4 \times 10^{27} \text{ ergs sec}^{-1}.$$

Given the way we used the X-ray data to obtain the beginning values for our model parameters and then iterated to converge upon a best fit model, this parameter set is quite unique. There is a small amount of leeway for increasing the value of $d \ln B/ds$ provided we compensate by reducing α_0^2 ; the two changes counteract each other for very small values of $d \ln B/ds$. Any larger values for $d \ln B/ds$ rapidly make the model incompatible with the data as then no value of α_0^2 would be able to reproduce the required $\gamma_B - \gamma_{AC}$. When we scale our model to the MDD peak flux estimate of $25 \text{ photons cm}^{-2} \text{ sec}^{-1} \text{ keV}^{-1}$ at 20 keV we obtain a peak power in electrons with energies greater than 20 keV of $4.4 \times 10^{27} \text{ ergs sec}^{-1}$. This is significantly lower than the MDD estimate of $2.8 \times 10^{28} \text{ ergs sec}^{-1}$ above 20 keV . If we take a FWHM for the impulsive burst of 20 secs (MDD) we obtain a beam energy of $2.7 \times 10^{29} \text{ ergs}$ in electrons with energies greater than or equal to 16 keV . This we can contrast with the DHM estimate of $1.0 \times 10^{30} \text{ ergs}$.

Chapter VI: X-ray Observations

Several points should be emphasized:

1) Our estimate of the column thickness of the coronal loop (that is, the entire coronal loop, not just one half of the arch) is $N_{\text{Corona}} = 1.4 \times 10^{19} \text{ cm}^{-2}$. Active region values of the column depth of the transition region N_{tz} are typically $\sim 3 \times 10^{19} \text{ cm}^{-2}$ (Basri *et al.* 1979). Empirical flare estimates, which are often based upon the later stages of a flare's development by which time there has been considerable evaporation of chromospheric material into the corona, tend to obtain higher values for N_{tz} ($\sim 10^{21} \text{ cm}^{-2}$; Emslie, Brown and Machado 1981). These HXIS results therefore indicate that models of the impulsive stage and of impulsive phenomena should use not late flare model atmospheres but active region atmospheres.

2) DHM and MDD provide rough estimates of the energy and power in the beam and note that their values are smaller than (though they are large fractions of) the total flare budget. One problem which has arisen from previous non-thermal modelling of flares has been the high efficiency required of an acceleration mechanism which puts a large fraction of the total flare energy into the directed motion of the accelerated electrons and not into heating the plasma. The estimate for the required beam energy given by our full Fokker-Planck analysis of the beam dynamics and with the relativistic Coulomb and X-ray bremsstrahlung cross-sections is considerably lower than the estimate given by the less exact methods used by MDD and DHM. The HXIS data upon which our modelling is based is far from precise and as a consequence our value for the beam energy can be no more than an estimate. However, our estimate of the peak beam power is less than the MDD and DHM estimates by a factor of more than six. Properly calculating

Chapter VI: X-ray Observations

the electron beam dynamics may allow a much needed lessening of the efficiency requirement on the acceleration mechanism from a figure of $\gtrsim 20\%$ (Duivjeman, Hoyng and Machado 1982) – a figure worrisomely high – down to a figure of $\sim 3\%$, which is altogether much easier to accommodate.

3) It is the difference between the X-ray spectral indices of the loop and footpoints which allows us to treat the loop as a thin target and the footpoints as a thick target. It is that the difference is greater than 1.5 which provides a measure of the collimation of the electron beam. Under these circumstances the X-ray data can provide a measure of the pitch angle spread of the injected beam even in the absence of spatially resolved polarization measurements. With our full modelling technique the X-ray data shows that the electron beam is neither too highly collimated (an injected beam with all the electrons having a pitch angle of zero would have given a thin target X-ray spectrum which would have been far too steep) nor is it almost isotropic. Our best fit model has a value of $\alpha_0^2 = 0.1$. If we were to allow for the possibility that some of the loop hard X-rays were produced by a hot thermal source, then subtracting those thermal hard X-rays would harden the loop X-ray spectrum and would lead to a larger value of α_0^2 in our best fit model. We then treat our derived value of $\alpha_0^2 = 0.1$ as a lower limit for this parameter. The electron beam is, then, less than highly collimated.

With this study of the flare of April 10th, 1980 we have shown how our modelling technique can be used in conjunction with spatially resolved flare hard X-ray data to derive values for all the model parameters. With our discussion we showed how we incorporated various aspects of the hard X-ray data to arrive at an initial set of values for the model parameters and how the final model parameters

Chapter VI: X-ray Observations

are interrelated in that a change in the value of one parameter can require an adjustment in the values of the others. Thus used, the X-ray intensity and spectral data is able to reveal estimates of the electron beam collimation and the rate of magnetic field convergence as well as the electron spectral index and the column depth to the transition region.

Let us now turn our attention to the second body of data selected for investigation. These come from stereoscopic observations of fortuitously positioned flares by two X-ray telescopes which are separated by a wide viewing angle. Though neither of the X-ray telescopes has imaging capabilities, their relative observing characteristics are well known. Consequently, any flare which is in full view to one device and is partially occulted from the other is effectively resolved into two spatially distinct parts: an upper part which is visible to both devices and a lower part which is seen by only one. Occultation of the lower part of a limb flare is provided by the fact that the chromosphere is relatively transparent to hard X-rays, whereas the photosphere is opaque. The transition from transparency to opaqueness is very rapid as the density scale height at the top of the photosphere is so short (McKenzie 1975).

We shall begin by looking at one flare which was viewed stereoscopically on Oct 5, 1978. Then we shall look at a series of three flares which occurred in rapid succession on Nov 5, 1979 and which came from the same active region. These four flares have been discussed recently by Kane (1983) and have been the subject of earlier studies: Oct 5, 1978 in Kane *et al.* (1979) and Brown, Hayward and Spicer (1981), but see also Kane *et al.* (1982), and Nov 5, 1979 in Kane *et al.* (1982).

6.3 Stereoscopic observations of the flare of October 5, 1978.

We begin with the flare of Oct 5, 1978. This flare occurred in an active region approximately 15° behind the east limb of the sun, which led to the flare being very highly occulted from ISEE - 3 and only slightly occulted from PVO . The angular separation between the two telescopes was 12.5° . ISEE - 3 saw only those parts of the flare which were at altitudes in excess of 25,000 km above the photosphere and PVO those above 700 km[†]. Using these occultation heights, Brown, Hayward and Spicer (1981) have attributed a column thickness of $N_1 \lesssim 10^{19} \text{ cm}^{-2}$ to the upper region seen by ISEE - 3 and a column thickness of $N_2 \gtrsim 5 \times 10^{21} \text{ cm}^{-2}$ to the larger region seen by PVO. This lower limit to N_2 is based upon a quiet sun atmospheric density profile and is in all likelihood a rather conservative estimate. Using active region density profiles (Basri *et al.* 1979), we derive a slightly higher estimate of $N_2 \simeq 10^{22} \text{ cm}^{-2}$. This column depth is large enough to stop those beam electrons which are injected with energies $\lesssim 250 \text{ keV}$, but is not quite large enough to allow PVO to see the entire flare. Our results can be used to obtain not just the source column thickness visible to ISEE - 3, but also that visible to PVO.

The results given by Kane (1983) are in the form of a spectrum for ISEE - 3 and in the form of flux values at mid-channel energies for PVO. The ISEE - 3 spectrum

[†]These estimates of the minimum source heights visible to ISEE - 3 and PVO need not be precisely known, and are not of themselves very interesting. The exact values of the occultation heights depend upon the exact position and orientation of the flare which, because the flare occurred behind the solar limb, are not available. Our work here will give estimates of the column thicknesses of the source regions visible to the ISEE - 3 and PVO telescopes. These can then be used to obtain occultation heights, though to do so requires that we make uncertain assumptions about the density height structure of the flaring plasma. The results are only of use for checking compatibility with the estimates offered by Kane (Kane *et al.* 1979; Kane 1983).

Chapter VI: X-ray Observations

is a fit to the observed counts in the five energy channels from 26 *keV* to 121 *keV*. For comparison with the PVO results at higher X-ray energies, this spectrum is extrapolated with a constant spectral index. The PVO fluxes at mid-channel energies (150, 350, 750 and 1500 *keV*) are obtained from the PVO channel counts by a fitting routine which uses the assumption that PVO sees the same spectral index as does ISEE - 3 (S. R. Kane, personal communication). This is unfortunate because the PVO results themselves do not support this assumption. If we take the quoted PVO fluxes and the given ISEE - 3 spectral index, we can deconvolve the PVO results to obtain the actual counts taken in each of the PVO channels. We can then fit a spectrum through these data points[†]. To the first three PVO channels we obtain a best fit of $\gamma_{\text{PVO}} \simeq 2.3$. If we use just the first two channels, we obtain $\gamma_{\text{PVO}} \simeq 2.1$. The datum for the third PVO channel lies somewhat below the extrapolation of the spectrum taken from the first two channels. This we expect owing to the fact that PVO cannot see the flare all the way down to the photosphere; an increasing amount of the higher energy X-rays are occulted from PVO as well as from ISEE - 3. We shall use the low energy channel estimate of $\gamma_{\text{PVO}} \simeq 2.1$ to indicate a first guess electron spectral index on the basis of PVO being able to see enough of the flare that the X-rays in the first two channels are thick target. We shall then fit our results to the PVO mid-channel count rates and adjust N_2 to give the correct channel 3 flux. The ISEE - 3 data is more accurate

[†] This process of obtaining the original counts from the quoted mid-channel flux values and then recalculating self consistent mid-channel flux values assumes that the PVO detectors have a uniform response function across the width of each channel. Any error introduced by non-uniformity in the detector response functions should not be large for the re-evaluation of the PVO spectrum obtained here.

Chapter VI: X-ray Observations

than the PVO data as it is a spectrum fitted to data from five relatively narrow channels at energies from 26 – 121 keV.

The results to which we shall fit our model are then:

ISEE - 3

A power law spectrum $5.5 \times 10^4 k (keV)^{-3.4}$ photons $cm^{-2} sec^{-1} keV^{-1}$ from 26 to 121 keV, extrapolated up to 750 keV.

$$\begin{aligned} \text{Flux} &= 2.45 \times 10^{-3} \quad @ \quad k = 150 \text{ keV}, \\ &= 1.39 \times 10^{-4} \quad @ \quad k = 350 \text{ keV}, \\ &= 1.04 \times 10^{-5} \quad @ \quad k = 750 \text{ keV}. \end{aligned}$$

PVO

$$\begin{aligned} \text{Flux} &= 0.32 \times 10^{-0} \quad @ \quad k = 150 \text{ keV}, \\ &= 5.25 \times 10^{-2} \quad @ \quad k = 350 \text{ keV}, \\ &= 7.30 \times 10^{-3} \quad @ \quad k = 750 \text{ keV}. \end{aligned}$$

Flux ratios Flux (ISEE - 3)/Flux (PVO)

$$\begin{aligned} \text{Ratio} &= 7.66 \times 10^{-3} \quad @ \quad k = 150 \text{ keV}, \\ &= 2.65 \times 10^{-3} \quad @ \quad k = 350 \text{ keV}, \\ &= 1.42 \times 10^{-3} \quad @ \quad k = 750 \text{ keV}. \end{aligned}$$

Chapter VI: X-ray Observations

We begin by estimating δ . The PVO flux at 150 and 350 *keV* are nominally fit by a spectral index of 2.1, the ISEE - 3 data by an index of 3.4. We anticipate that the PVO observations represent a thick target spectrum up to an energy ~ 500 *keV* and that the ISEE - 3 observations represent a relatively thin target spectrum down to 26 *keV*. We therefore select a first try value $\delta = 2.6$. We can take $N_1 \simeq 10^{19} \text{ cm}^{-2}$ as suggested by Brown, Hayward, and Spicer (1981) for the column thickness of the source material visible to ISEE - 3. We shall need to take $N_2 \simeq \text{several} \times 10^{22} \text{ cm}^{-2}$ in order to make the first two channels of the PVO data be thick target. As the difference in spectral indices ISEE - 3 to PVO is no larger than the average for thin to thick targets for our models we shall also begin with a medium α_0^2 of 0.4 and with $d \ln B/ds = 0$.

When we begin fitting a model to this flare one thing quickly becomes obvious. This is that for ISEE - 3 to see thin target X-rays down to 26 *keV* and for PVO to see thick target X-rays up to 500 *keV*, we would need N_2 to be very much larger than N_1 , sufficiently so that we would then obtain flux ratios $\lesssim 10^{-5}$, that is, about two orders of magnitude lower than was observed. If we decrease N_2 or increase N_1 enough to give a better agreement between the calculated and observed flux ratios, we make either the PVO results almost thin target or the ISEE - 3 results almost thick target, severely reducing the gap $\gamma_{\text{ISEE-3}} - \gamma_{\text{PVO}}$ from $3.4 - 2.1 = 1.3$ to $\lesssim 0.7$. We need to keep $\gamma_{\text{ISEE-3}} - \gamma_{\text{PVO}}$ as high as 1.3 and at the same time achieve the correct flux ratios. One way to do this is to increase the collimation of the electron beam by reducing the value of α_0^2 . This steepens the thin target spectrum and delays the low energy flattening which comes in with increasing column depth. We can also use the fact that the ISEE - 3 spectrum was

Chapter VI: X-ray Observations

a fit to the range 26 – 121 keV and that the flux values at the higher energies (150, 350, and 750 keV) were obtained by extrapolation with constant spectral index. If we increase N_1 the X-rays from the upper part of the flare seen by ISEE - 3 will become intermediate between thick and thin target and the spectrum will develop a gentle knee separating the low energy and high energy ends of the spectrum. The index for the low energy X-rays will be smaller than that for the high energy X-rays. It is the spectrum over the range 26 – 121 keV which needs to have an index of 3.4. The spectrum for the range above 121 keV can be steeper provided we remember that the flux ratios we were given were obtained from the extrapolated ISEE - 3 spectrum above 121 keV and not from the calculated spectrum. We can, then, increase N_1 to increase the ISEE - 3 flux provided we reduce α_0^2 to keep $\gamma_{\text{ISEE - 3}} \simeq 3.4$ for 26 – 121 keV X-rays. We then need to search for one value of N_2 which will simultaneously give the correct spectrum to the PVO mid-channel fluxes and the correct flux ratios between the extrapolated ISEE - 3 spectrum and the PVO counts. If no single value of N_2 will give this, then we need to adjust α_0^2 and N_1 (and maybe also δ) until we find one value which will.

After some experimentation, the model which best fit the flare was:

$$\delta = 2.6;$$

$$\alpha_0^2 = 0.04;$$

$$d \ln B/ds = 0;$$

$$N_1 = 3.8 \times 10^{20} \text{ cm}^{-2};$$

$$N_2 = 2.6 \times 10^{22} \text{ cm}^{-2}.$$

Chapter VI: X-ray Observations

This fitted the ISEE - 3 data between 26 and 121 keV and the flux ratios (between PVO channels and between PVO and ISEE - 3) within $\pm 5\%$ of those we were trying to achieve. There are, again, a couple of comments to be made:

1) Our best fit model has a very small value for α_0^2 . This was obtained from the necessity of keeping a large value for $\gamma_{ISEE-3} - \gamma_{PVO}$ and not having flux ratios which were too small. A large α_0^2 was unable to give a satisfactory fit to the data, for if we had adjusted N_1/N_2 to give the correct flux ratios for a large α_0^2 , we would have needed to settle for $\gamma_{ISEE-3} - \gamma_{PVO} \lesssim 0.7$. If we draw from this a requirement on the size of the errors in the PVO data in order for us to not be able to use the observations to contraindicate a large α_0^2 , then the errors in the PVO data would have to be large; the PVO counting rate in the third channel would have to be in error by a factor of three or more, assuming the counting rate in the first channel to be good. This is well beyond the PVO calibration uncertainty (Kane *et al.* 1982) and beyond the indicated error in the data (Kane 1983). Therefore we are able to conclude that this particular body of data requires a model with a highly collimated injected electron beam. The best fit value to α_0^2 is 0.04.

2) The early estimates of the position of the flare and consequently the amounts of the flare visible to the two telescopes can be revised in the light of our N_1 and N_2 values. The flare occurred behind the left limb of the sun. The only active region close to the limb with which the flare could have been associated was McMath 15587, located $\simeq 15^\circ$ behind the east limb at the time of the flare. If we use our value of N_2 and the atmospheric results of Basri *et al.* (1979), the minimum altitude visible to PVO is approximately 550 km above the photosphere. This places the

Chapter VI: X-ray Observations

flare roughly 14.7° behind the limb as seen from the earth. Our results, then, do not contradict the locating of the flare in McMath 15587. Our value of N_1 , at $3.8 \times 10^{20} \text{ cm}^{-2}$, is substantially above that estimated by Brown, Hayward and Spicer (1981) and suggests that a large volume of flare material was visible to ISEE - 3. Owing to the flare being positioned well behind the solar limb the altitude of the top of the flare loop must have been large for such a large volume of the coronal loop to have been visible. If we assume that that part of the coronal loop visible to ISEE - 3 was of roughly the same length as the part occulted away, *i.e.*, 25 000 km, we obtain densities within the loop of $\gtrsim 10^{11} \text{ cm}^{-3}$. Such high values for the thickness and density of the coronal loop suggest that the flare was seen late in the impulsive stage for which a substantial amount of chromospheric evaporation had taken place.

With this flare we have shown how the need to fit one non-thermal model to the X-ray data from two telescopes has enabled us to obtain a unique set of parameter values and hence to obtain a complete description of the flare. Again, it was having two X-ray spectral indices which were substantially different from each other which allowed us to determine a value for α_0^2 , the parameter measuring the collimation of the electron beam, and $d \ln B/ds$, the measure of the magnetic field convergence. We found that the data required a strongly collimated electron beam and no field convergence. We can also use the same property to show the uniqueness of the derived model. Having PVO see a harder spectrum at high X-ray energies than ISEE - 3 saw at low energy X-rays meant that N_2 had to be large. The flux ratios then required that N_1 be sufficiently large, for which the top volume seen by ISEE - 3 was found to be intermediate to thick target for low

Chapter VI: X-ray Observations

energy X-rays. Keeping the ISEE - 3 spectral index the correct amount above the nominal PVO index then required that α_0^2 be small and $d \ln B/ds$ be negligible. If either of these last two conditions is relaxed the model rapidly ceases to fit the data. Consequently, the model's uniqueness is assured.

6.4 The three similar flares of November 5, 1979.

We shall now discuss Kane's results for the three stereoscopically observed flares of November 5, 1979. The three flares came from the same active region (Hale region 16413) and occurred within a total period of six hours. They were all within full view of ISEE - 3 and were increasingly occulted from PVO, and all three had very similar spectra. Because of their similarity there is a temptation, as noted by Kane, to treat the observations of the three flares as if they were a sequence of three observations of one flare. In this manner Kane obtains three points on a plot of X-ray intensity vs. height, and a spectrum to fit each point. We can attempt to fit these three points using our modelling techniques. The data and results for these three flares are presented by Kane (1983) and were first published in Kane *et al.* (1982).

We shall label the flares in chronological order as flares 1, 2 and 3 (they occur as flares 3, 4 and 5a in Kane (1983)). Flare 1 occurred at a location S 13.4°, E 49.0°. This gave ISEE - 3 a viewing angle of 51.6° and PVO one of 90.0°, the viewing angles having an uncertainty of $\sim 1^\circ$. Both instruments were able to see this impulsive burst in its entirety, and the measurements from the two telescopes were

Chapter VI: X-ray Observations

in close agreement. The ISEE - 3 data from the first 8 channels (26 – 562 *keV*) and the PVO data from the first three channels (100 – 1000 *keV*) are very well fit by a power law spectrum with an index of 3.0. Their respective flux measurements agree to better than 10%. This is consistent with the calibration uncertainty between the two devices. Flare 2 occurred four hours and eight minutes later at a location S 14.2°, E 44.6°. This gave ISEE - 3 a viewing angle of 47.8° and PVO one of 94.3°. Consequently, ISEE - 3 could see the whole flare whereas PVO was able to see only those parts of flare 2 which were more than $\simeq 2000$ *km* above the photosphere. The ISEE - 3 data from 26 – 900 *keV* is well fitted by a power law spectrum with an index of 3.3. The PVO data in the range 100 – 500 *keV* has a slightly lower flux, as may be expected, but is clearly consistent with the ISEE - 3 spectrum. Flare 3 occurred at S 15.4°, E 44.0° almost two hours after flare 2, and the ISEE - 3 and PVO viewing angles were 47.7° and 94.8°, respectively. This allowed PVO to see all those parts of flare 3 which were at more than $\simeq 2500$ *km* above the photosphere. Again, the spectral shapes from the two observations are closely similar, but with the PVO flux now being substantially less than the ISEE - 3 flux. The spectral index based upon the ISEE - 3 26 – 900 *keV* channels was 3.15.

The three flares, as well as having very similar spectral indices (3.0, 3.3 and 3.15) were also of nearly equal intensity to PVO. As the third flare was substantially occulted from PVO this means that the three flares were not of equal intrinsic brightness. From the ISEE - 3 measurements, flare 3 was approximately a factor of ten brighter during the impulsive phase than was flare 1. This, on its own, need not necessarily deter our hopes of treating all three flares as three examples of one

Chapter VI: X-ray Observations

“typical” flare. However, there are other reasons for questioning this approach. For each of the three flares both PVO and ISEE - 3 measured the same spectral index. Yet flare 3 was strongly occulted from PVO which was only able to see $\simeq 7\%$ of the hard X-ray flux. Because PVO and ISEE - 3 measured the same spectral index over the 100 – 500 keV range the flux ratios (PVO to ISEE - 3) at 150 and 350 keV (the PVO mid-channel energies) were the same, *i.e.*, 7%. However, on the basis of our non-thermal model results, we would expect the altitude above which 7% of the 150 keV X-rays were emitted to have been higher than that above which 7% of the 350 keV X-rays were emitted. The PVO to ISEE - 3 flux ratios at these two energies would, in that instance, be different, with the flux ratio at 150 keV being larger than that at 350 keV.

We use the expression obtained in Chapter V for $I(k, \tau)$ (equation (5.2.23)) to see what source thicknesses are required for 7% of the 150 keV and 7% of the 350 keV X-rays. Using the nominal value $\delta = 4$, equation (5.2.23) predicts that 7% of the 150 keV X-rays would come from above a column depth of $1.1 \times 10^{20} \text{ cm}^{-2}$, while 7% of the 350 keV X-rays would need a column depth of $4.4 \times 10^{20} \text{ cm}^{-2}$. These two column depths would normally correspond to the upper chromosphere or above and would be separated by a distance equal to many times the photospheric density scale height. If the levels in the photosphere where the 150 and 350 keV photons are occulted are to differ from each other, they would do so by a distance of order only one photospheric density scale height.

One way that we can reconcile having equal PVO to ISEE - 3 flux ratios at 150 and 350 keV for both flare 2 and flare 3 is to invoke a large amount of magnetic trapping of the electrons. We need to invoke a large enough degree of

Chapter VI: X-ray Observations

trapping that the trapping rate becomes essentially independent of the electron energy for electron energies of 150 keV and above. As we increase the degree of coronal magnetic trapping in our models, a larger and larger percentage of the X-ray flux comes from above the transition region. In our models we would need to juggle both $d \ln B/ds$ and the coronal density in order to achieve flux ratios which are independent of X-ray energy. Kane (1983) quoted altitudes of 2000 km and 2500 km above the photosphere for the occultation altitudes of flares 2 and 3, and flux ratios at 150 and 350 keV of 45% for flare 2 and 7% for flare 3. A large degree of magnetic trapping in our models would be able to make 45% of the very high energy X-rays come from above an altitude of 2000 km . But if, at the same time, only 7% of the same X-rays is to come from above 2500 km altitude, then either the flare loop is exceptionally short (maximum altitude $\approx 2600\text{ km}$) or all of the magnetic trapping is effected in the last 500 km of a loop which is much taller. Neither of these options is quite satisfying and both suggest that there is difficulty in using these three separate flare observations as three examples of one "typical" flare.

What we shall do is this. Because all the relevant electron (Chapter III) and X-ray (Chapter V) results we have given so far have used a constant $d \ln B/ds$, that is, have had the magnetic trapping distributed evenly throughout the coronal loop, we shall not now attempt to model a flare having all the magnetic trapping effective over only a small part of the loop. We shall, instead, construct a model which has a sufficiently strongly converging magnetic field that the X-ray flux ratios are roughly constant across the interval $100 - 500\text{ keV}$, and we shall obtain estimates of the column thicknesses of material visible to PVO for flares 2 and 3.

Chapter VI: X-ray Observations

This will, of course, show that flare 3 presented a much smaller emitting volume to PVO than did flare 2 despite the two flares having very similar occultation heights.

We saw from the electron and X-ray results how a large degree of magnetic trapping is manifested in our models. The downward electron flux or current falls with the increase in the magnetic field strength (*cf.* Figures (3.10) and (3.11)). The electrons bounce backward and forward across the loop with a small probability of escaping from the trapping region with each attempt. There is, then, a small current of electrons which passes out of the trapping region (the region within which the magnetic field dominates the electron beam evolution, *i.e.*, the corona) and into the chromosphere. Because this escaping current is small compared to the downward current at the apex of the loop, the upward current (the current of mirrored electrons travelling back toward the loop apex) is almost as large as the downward current at each point within the coronal loop. The generated X-rays are produced by both the upward and the downward electron flux. For this reason, the X-ray flux at any point within the trapping region is controlled by the behavior of the magnetic field and the total column thickness over the entire trapping region and not just the local field strength and particle density about each point.

The parameters in our models which we need to adjust in order to obtain the correct X-ray fluxes are, then, the amount by which the magnetic field converges over our entire trapping region and the total column thickness of that region. This is in contrast to the more usual technique for adjusting the model parameters which is to adjust these parameters only for the region between the top of the loop and the occultation height. If the trapping region extends below the occultation height,

Chapter VI: X-ray Observations

then what happens to the electron beam below the occultation height affects the production of X-rays above it.

Table VIII and Figure (5.19) show that, for high energy X-rays, if the coronal column thickness is small, the majority of the X-rays can still come from the chromosphere even if the degree of magnetic trapping is large (*cf. Model 9*, Figure (5.19)). In this case, the flux ratios (corona to chromosphere) will still be energy dependent. To obtain flux ratios which are roughly independent of energy we need to have a situation where the large majority of the X-rays are emitted from within the trapping region itself. Consequently, we need not only a large amount of magnetic trapping but also a substantial column thickness for the trapping region, N_{tz} , in order to make the X-ray flux ratios relatively constant over the interval 100 – 500 keV. The 150 keV and 350 keV flux ratios will converge as the coronal column thickness is increased.

In our models we need to find values of $B(N_{tz})/B(0)$ and N_{tz} which are large enough to make the 150 keV and 350 keV flux ratios roughly equal. We use the relative calibration uncertainty between the PVO and ISEE - 3 X-ray telescopes to indicate that the calculated X-ray flux ratios at 150 and 350 keV need be no closer than within 10% of each other. Having them this close guarantees that $\geq 95\%$ of the 150 and 350 keV X-rays will be generated in the corona. We then need to find the depths within the trapping region (corona) above which 45% and 7% of the X-rays are produced. These depths will correspond to the occultation heights for flare 2 and flare 3, respectively.

Increasing either $B(N_{tz})/B(0)$ or N_{tz} will make the 150 and 350 keV flux ratios converge. Therefore the models will be able to give only a lower limit to N_{tz}

Chapter VI: X-ray Observations

for each $B(N_{tz})/B(0)$ or, alternately, a lower limit to $B(N_{tz})/B(0)$ for each N_{tz} . If we reduce N_{tz} , we need to increase $B(N_{tz})/B(0)$ by a commensurate amount in order to keep the flux ratios within 10% of each other. Likewise, if we reduce $B(N_{tz})/B(0)$, we need to increase N_{tz} , except that if we reduce $B(N_{tz})/B(0)$ far enough, the required value of N_{tz} will be so large that the magnetic field will no longer dominate the electron beam evolution and Coulomb collisions will again become important. At this stage the flux ratios will begin to diverge again. We can obtain a rough estimate of this minimum value of $B(N_{tz})/B(0)$ below which no value of N_{tz} is able to give flux ratios which are within 10% of each other.

We ran a series of models (all with $\alpha_0^2 = \infty$) in order to obtain pairs of values $B(N_{tz})/B(0)$ and N_{tz} which gave flux ratios at 150 and 350 keV (the fraction of the total 150 (350) keV emission which is generated in the trapping region) which were within 10% of each other, and which gave a whole loop spectral index of $\simeq 3.2$. One such model had

$$\begin{aligned}\delta &= -2.5, \\ N_{tz} &= 10^{19} \text{cm}^{-2}, \\ B(N_{tz})/B(0) &= 150.\end{aligned}$$

For this model the column thicknesses of material visible to PVO were $\simeq 1.5 \times 10^{18} \text{cm}^{-2}$ (flare 2) and $\simeq 2 \times 10^{17} \text{cm}^{-2}$ (flare 3). Increasing $B(N_{tz})/B(0)$ allowed us to reduce N_{tz} by an approximately equal amount. Decreasing $B(N_{tz})/B(0)$ required that we increase N_{tz} by somewhat more than an equal amount. Another suitable model had

$$\begin{aligned}\delta &= -2.5, \\ N_{tz} &= 5 \times 10^{19} \text{cm}^{-2}, \\ B(N_{tz})/B(0) &= 60.\end{aligned}$$

Chapter VI: X-ray Observations

$(B(N_{tz})/B(0))$ reduced by a factor of 2.5 from the previous model and N_{tz} increased by a factor of 5) for which the source thicknesses were $\simeq 8.6 \times 10^{18} \text{cm}^{-2}$ and $\simeq 1.1 \times 10^{18} \text{cm}^{-2}$, respectively. Further decreasing $B(N_{tz})/B(0)$ required that N_{tz} rapidly increase and from then on no value of N_{tz} gave adequate flux ratios. We therefore estimate the lower limit to the amount of coronal trapping, as given by the ratio of the magnetic field strength at the transition region to that at the loop apex, at ~ 60 .

In this study we used the fact that the PVO to ISEE - 3 flux ratios were constant across an energy interval to indicate that any model constructed to fit the data would need a large amount of coronal trapping of the electrons. The models we used probably do not represent well the actual flares themselves, though we cannot know whether it is more likely that the flares had a highly uneven distribution of trapping throughout the coronal loops or that flare 3 had an exceptionally short loop. The value of the models is primarily to show how our modelling technique is to be used with flare data of this type and to put a numerical value on the amount of magnetic trapping indicated.

6.5 Some recent polarization results.

While this thesis was being written, a preprint was circulated containing some new and very timely results. Tramiel, Chanan and Novick (1984) reported the flight of an X-ray polarimeter onboard the Space Shuttle Columbia and their observations of several solar flares on March 29, 1982. Though their experiment

Chapter VI: X-ray Observations

suffered from a certain amount of detector contamination and though one may raise an objection to their in-flight calibration method, these results are probably the most reliable flare polarization measurements currently available. The authors observed seven flares in all, five of which were grouped within 18 degrees of disk center.

Of the seven flares observed the authors used the two which were closest to disk center for the in-flight calibration of their polarimeter. They assumed that the X-rays from these two flares would be unpolarized by virtue of the flares' being so near to the disk center. This assumption can be challenged. Formally, the measurement of a polarization requires mention of both the polarization vector's magnitude and its orientation. The reporting of its orientation requires the definition of a reference plane and the one usually taken is the plane containing the line of sight and the normal to the sun at disk center. For a flare positioned at disk center, this reference frame cannot be defined. Therefore, neither can the direction of the polarization vector. However, this need not imply that the polarization vector is itself a null vector. A flare produces photons independently of whether or not the photons are seen and their polarization measured. The beam of photons streaming away from the sun in a direction parallel to the local surface normal will have a polarization vector with both a magnitude and a direction, and these can be measured with the same techniques as for any other beam of photons. The measurement of the polarization direction is rendered ambiguous owing to the lack of a reference plane. However, the measurement of the polarization magnitude need not be null. There is, perhaps, a tendency to confuse this behavior of the polarization vector when seen along the polar axis of the reference frame with the necessity that a beam

Chapter VI: X-ray Observations

of radiation be unpolarized when it is emitted in the forward direction in the emission frame. In the emission frame the usual reference plane, which is defined as that containing the direction of motion of the emitting particle and of the photon, cannot be defined owing to the fact that the two required directions are parallel and coincident. However, in this case there is also a physical symmetry whereby the emission process recognizes no preferred plane with which to locate the direction of linear polarization. Hence the net linear polarization, which is the sum of many vectors each having a randomly selected orientation in space, must necessarily be zero.

This confusion may have led to an invalid calibration of the polarimeter. The effect of this would be to redefine the quoted polarization results to be polarizations relative to that of the two calibration flares. The question of what the absolute polarization of these two disk center flares may have been, were it not zero, remains unanswerable. Proceeding with this one qualification, the authors Tramiel, Chanan and Novick measured flare polarizations which were consistent with a random distribution of statistical fluctuations about zero polarization. They interpreted this as indicating a null polarization for all the flares. More particularly, they singled out one of their observations, that of a flare which was well removed from the solar disk and for which they observed separately the early impulsive phase. This flare was also observed by ISEE - 3 which allowed for an independent estimate of the flare's spectral index. For this one flare the authors recorded "no significant polarization", and quoted their results as $3.4 \pm 2.2\%$ for the polarization integrated from 5.0 to 21.1 keV. The results for each energy channel were considerably more noisy and showed an increase in the X-ray polarization with channel energy. If real,

Chapter VI: X-ray Observations

this increase in the polarization with X-ray energy would indicate that the lower energy results were partially contaminated by an admixture of purely thermal (and hence presumably unpolarized) emission. If so, the effect of this contamination upon the integrated (over X-ray energy) polarization results would be to reduce the measured polarization below that which would otherwise have been observed.

We may now look at the implications of this latest low polarization result for our non-thermal flare modelling. The authors accept that a low measured polarization implies that the source electrons are essentially isotropic. They compared their data with the several theoretical results available in the literature, including those contained in Leach and Petrosian (1983) which are drawn from the research contained within this thesis. They found that their data were marginally inconsistent with a model having small α_0^2 and large $d \ln B/ds$, which implied that they were strongly inconsistent with a model having a small α_0^2 and zero $d \ln B/ds$. The authors claimed that their data were consistent with a model having $\alpha_0^2 = \infty$, that is an isotropically injected electron beam.

We are in a position where we can select and use models which are more appropriate to their particular observation than the ones which they drew from Leach and Petrosian (1983). This allows us to give a better indication of how well non-thermal models can fit their results than could the authors. The crucial piece of information which we need in order to fit an appropriate model is the X-ray spectral index. This can be obtained from the ISEE - 3 observations. Over the energy range $11.6 \text{ keV} < E(\text{keV}) < 100 \text{ keV}$ the X-ray spectrum had an index of 3.3. Over the lower energy range $5 - 11.6 \text{ keV}$ the index was 7.2. This strongly suggests that the lower energy photons ($5 - 11.6 \text{ keV}$) were a mixture of thermal

Chapter VI: X-ray Observations

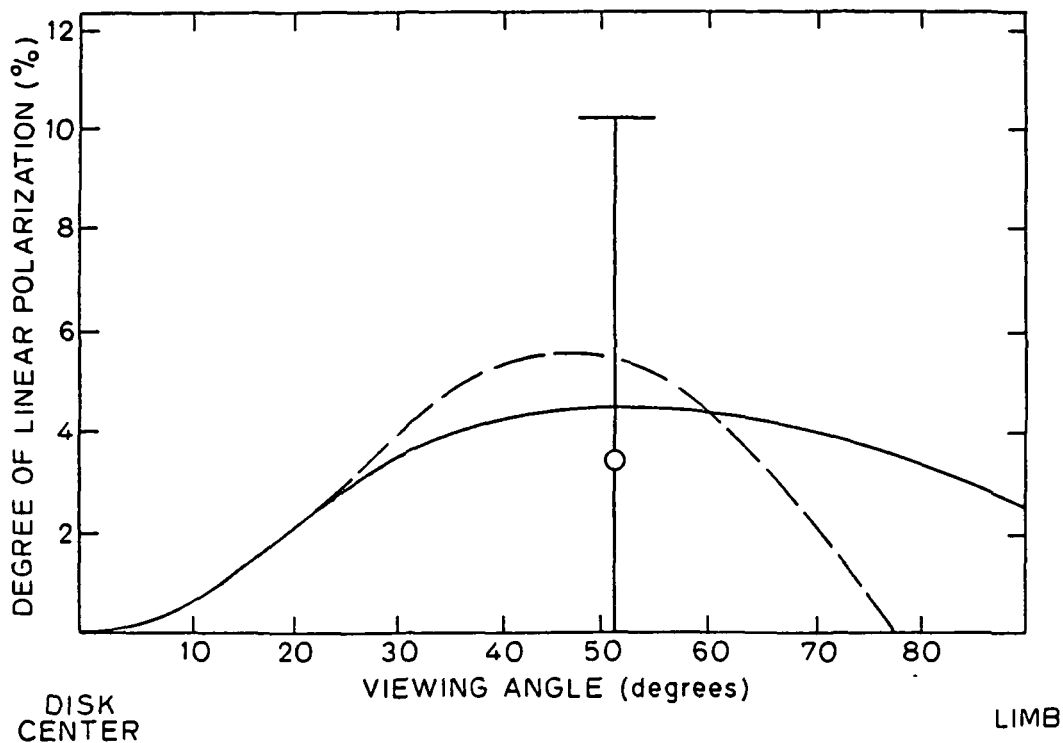


Figure 6.2. A comparison between the measured polarization for the impulsive phase of the flare of March 29, 1982 (taken from Tramiel, Chanan and Novick 1984) and the results from two models. The flare had a spectral index of 3.3 and therefore the two models have $\delta = 4$. The solid line corresponds to a model with $\alpha_0^2 = 0.4$ and a coronal magnetic field of constant strength. The dashed line corresponds to a model with stronger beaming ($\alpha_0^2 = 0.1$) and a magnetic field which increases in strength by a factor of twenty over a coronal column thickness of 10^{19} cm^{-2}

and non-thermal photons and that the integrated result of $3.4 \pm 2.2\%$ polarization is lower than would have been measured had the estimate been made only from the data of the higher energy channels above 11.6 keV .

An X-ray spectral index of 3.3 indicates an electron index at injection $\delta \simeq 4.0$. The results taken from Leach and Petrosian (1983) by Tramiel, Chanan and Novick (1984) were for an electron index of 5, a value steeper by unity than it needed to

Chapter VI: X-ray Observations

have been. We know from the results of Chapter V that flatter electron spectra produce less highly polarized X-rays than steeper electron spectra. Changing from $\delta = 5$ to $\delta = 4$ introduces a marked reduction in the model polarization results. We can compare the Tramiel, Chanan and Novick data with the results from models having $\delta = 4$ and can estimate the maximum amount of electron beaming which will allow the models to remain compatible with the data. The error bars on the data (*cf.* Figure (6.2)) are large enough that we cannot place strict lower limits on α_0^2 . However, we can see from Figure (6.2) that a model with $\alpha_0^2 = 0.4$ and zero $d \ln B/ds$ would be compatible, as would a model with stronger electron beaming and a converging magnetic field ($\alpha_0^2 = 0.1$ and a twenty fold increase in the magnetic field strength over a column depth of 10^{19} cm^{-2}). Figure (6.2) is taken from the recently prepared report by Leach, Emslie and Petrosian (1984) which discusses the Tramiel, Chanan and Novick (1984) results in the light of the results contained within this thesis.

6.6 Summary.

In this chapter we presented four studies which have used the modelling techniques developed in this thesis. In the first three we showed how we can use our method with recent X-ray data to obtain complete descriptions of the flares studied. These descriptions are the most complete descriptions which have heretofore been obtainable using non-thermal modelling techniques in that they contain information pertaining to both the pitch angle distribution of the electron beam and to the magnetic structure of the flaring loop. We have shown that our

Chapter VI: X-ray Observations

modelling technique is flexible and that we can obtain best fit models which are as unique as the precision of the data will allow. With these three studies we showed that the newly available high quality data contains enough information that, properly analyzed, a complete description of the flare can be extracted. In the future it can be hoped that many more reports will become available for study, especially reports containing reliable polarization measurements. This would give us the opportunity to analyze a substantial number of flares with our modelling technique and for a record of many flare descriptions to be accumulated. This could lead to the recognition of classes of flares grouped according to their physical structure and their associated X-ray characteristics, especially according to the pitch angle structure of the injected electron beams. If so, the flare descriptions obtained through our modelling technique could provide the basis for an improved understanding of the acceleration mechanisms which have to date remained quite inaccessible.

Chapter VII

Summary and Conclusions

Now is the time to step back and review this body of work, restate its objectives and highlight our conclusions. We shall begin by recapitulating the ideas from which we took our motivation. We shall follow quickly the path by which the investigation unfolded, and we shall then concentrate one by one on each of our major results. We shall outline how we have used our results in conjunction with some of the very latest high resolution observations and shall indicate how this thesis has fulfilled the objectives which we set for it.

7.1 Summary.

Though the sun as-a-star is quite well understood, the Sun as a unique physical system of its own displays an abundance of complex phenomena which tax prevailing experimental and theoretical ingenuity. Solar flares are among the most energetic and interesting of the sun's phenomena and yet the understanding of the impulsive phase, during which much of that energy is liberated over very short timescales, is still incomplete. The emitted impulsive radiations can be measured

Chapter VII: Summary and Conclusions

from radio through to γ -ray energies, yet some basic questions are still unresolved as is the primary question: How, specifically, do solar flares work?

Many answers could be extracted from observations of the impulsive radiation if we only knew how to make full use of the data collected. From out of a huge stock of observations, the major part of which has been collected over the last couple of decades, the principal idea which has emerged is of highly accelerated electrons streaming through the flaring plasma and redistributing huge quantities of energy. This energy most likely originates as free energy contained in the pre-flare magnetic structure. It is liberated from the magnetic field through a process of reconnection and is used to create a population of extremely energetic electrons. These electrons, which constitute the primary agent of the impulsive phase, then carry the energy throughout the rest of the flare. A small fraction of the flare energy is emitted in the form of impulsive radiation and is most frequently observed in the radio, optical, extreme ultra-violet and X-ray wavebands. Another fraction of the flare energy is carried away by the escape of high energy particles, some more of it is used to drive mass motions, but most of it is redistributed throughout the flare plasma, giving rise to bulk heating and generating the attendant thermal radiation at all wavelengths.

All of these phenomena tell something about the underlying energetic electrons. Once the characteristics of the energetic electrons have been evaluated, the fundamental problem of how those electrons were accelerated can be unravelled. If that can be done, significant progress will have been made toward a more complete understanding of a solar flare as a physical system. Of the various flare phenomena, the impulsive radiations are the most closely related to the energetic electrons.

Chapter VII: Summary and Conclusions

Of these impulsive radiations the X-rays represent the most direct probe into the details of the electrons' population. Learning to read the emitted X-rays is therefore the necessary first step toward removing the obstacles in the way of a better understanding of solar flares.

Yet, despite the large number of observations of the impulsive hard X-rays accumulated over the last two decades, no consensus on the description of the electron population has emerged. Several theoretical models have been developed, each giving priority to one or another aspect of the overall problem, yet no one model has encompassed the full diversity of the X-ray data. Part of this problem has stemmed from an unclear knowledge of the limits of what the observations can tell us. There has been a real need for a thorough-going study of the energetic electrons' behavior within the flare plasma and of the correlations – which must exist – between the measurable and quantifiable hard X-ray characteristics and the characteristics of the electron population that produces them. Now that we have performed just such a study we are better able to obtain the nature of the electron population from the impulsive hard X-ray measurements.

The first part of our study was to understand the behavior of the high energy electrons. Once we had that in hand we could incorporate the relatively well-understood processes of X-ray production and then learn to recognise the behavior of the electrons from that of their X-rays. In Chapter II of this thesis we developed a model for following the evolution of the electron population. We set up the geometry of the flare magnetic structure and discussed the appropriate mechanisms which come into play as the energetic electrons, in the form of a beam which is injected into the top of the flare structure or loop, pass down within this

Chapter VII: Summary and Conclusions

flare structure toward the solar photosphere. We did not confine the electrons to having any particular, preconceived distribution upon injection into the top of the loop. We left ourselves free to invoke any beam distribution necessary and we did this by parameterizing the description of the beam. This gave us two free parameters which we could then fix as needed.

We saw that the primary agent determining the behavior and evolution of the electron beam was Coulomb collisions within the flaring plasma. This necessitated a stochastic treatment of the electron beam dynamics and led to a description of the electron population by way of a single-particle number distribution. We then discussed how to translate the physical paradigm into an equation which would be obeyed by this electron number distribution, and, in the last part of Chapter II, we evaluated the necessary coefficients. We obtained an equation, the Fokker-Planck Equation, from which could be extracted the details of the electron's behavior during the flare's impulsive phase.

In Chapter III we set about solving this equation. Like so many other contemporary plasma physics problems this one did not allow an analytic solution and we were forced to use a large computer in order to obtain the solution in numerical form. We explained how best to rewrite the equation and, from an inspection of its components, we devised a heirarchical approach to obtaining the solution which employed implicit, finite difference techniques and Gaussian Elimination on what is essentially a tridiagonal matrix. We also devised means to assure ourselves that the end product of our labors would be a numerically evaluated function which bore a close likeness to the ideal (because unknown) solution of the exact equation which we had set out to solve.

Chapter VII: Summary and Conclusions

We found an approximation to our Fokker–Planck Equation which did admit to an analytic solution. This approximate equation was based upon the behavior of the Fokker–Planck Equation in a restricted domain of the independent variables. Consequently, we could not be certain that the solution of this approximate equation, extended beyond that domain, would bear a good likeness to either the numerical solution or the ideal solution of the Fokker–Planck Equation. We compared the analytic solution of the approximate equation with the numerical solution of the Fokker–Planck Equation and found them to be in good agreement. We then looked at the behavior of both the analytic solution and the numerical solution in order to understand how the electron beam evolved as it passed down from the acceleration region through the flaring plasma. This understanding of the beam dynamics was a necessary prerequisite for our making sense of the X-ray results which were to be obtained in a later chapter.

Satisfied that we had the evolution of the electron beam adequately described, we needed to incorporate the production of the X-rays, first into our paradigm and then into our computer code. The latter objective primarily required the numerical integration, over several variables, of a kernel which was composed of the electron distribution and the X-ray cross-sections threaded together by a substantial amount of spherical trigonometry. As such it was more a matter of precise bookkeeping than of cracking conceptual nuts. The former objective, that of incorporating the X-ray production into our paradigm, required that we determine what information we wanted to get from the X-rays and that we then use X-ray cross-sections adequate to our needs. In Chapter IV we introduced the Stokes parameter formalism for the X-rays and described briefly the means by which the

Chapter VII: Summary and Conclusions

Stokes parameters could be evaluated from the two cross-sections describing the production of X-rays with either of the two independent linear polarizations.

The several available forms of those two cross-sections are all rather cumbersome and have restrictions on the domains over which their use is justified. We were able to find, for these two cross-sections, expressions which would serve us well over the whole range of electron and photon energies of interest, though these expressions still relied upon an important correction term to ensure their validity over that whole range. These cross-sections are not without some debate as to their accuracy though they have generally been well supported in the literature. Most significantly, they have been given very strong validation by a recent body of work which has used the power of present day, large computers to obtain an accurate numerical evaluation of the cross-sections throughout precisely that domain in which we are interested. We could, then, confidently meld these cross-sections with our electron number distribution and be sure of obtaining, with an accuracy more than adequate to the task, all the information required about the hard X-ray radiation field from the beam of high energy electrons.

At this stage we were fully able to start investigating the correlations between the X-ray characteristics and those of the electrons from which the X-rays had come. But in order to use what we could learn from our X-ray calculations we needed to know more precisely where previous studies, both theoretical and experimental, had left us. We needed to survey the questions that had been raised by other scientists' labors and evaluate the extent to which the intensive study of solar flare hard X-rays had provided us with a firm platform from which to

Chapter VII: Summary and Conclusions

progress. Our investigation in the first part of Chapter V revealed that earlier attempts to model both the dynamics of the electron beam and the X-rays produced therefrom were necessarily rather inexact. They served more to give a qualitative idea of the relationships between the X-rays and the electrons than to give precise values to the electron characteristics derived from the X-ray observations. The observational results were similarly indefinite. Solar flares span such a wide range of sizes and are such complex experimental subjects that the data can often appear to be inhomogeneous.

In the second part of Chapter V we presented a broad outline of the results obtained from our numerical calculations. Our first need was to order the results to make them sensible. To accommodate a wide range of possible flare geometries and any type of injected beam, we had left unspecified many of the model parameters. One advantage gained from looking at the electron results of Chapter III was that we had seen that the important parameter measuring depth within the flare was not the geometric location of any particular region, but its accumulated column depth from the site where the electron beam was injected. This took away the emphases on the coronal density and the coronal loop length, both of which are variables which can take on a wide range of values. It allowed us to specify one parameter, the column thickness of the coronal part of the loop, and this parameter remained fixed throughout all our work. In addition, it meant that the most informative way to present the results on the height structure of the X-rays would be to give them not in terms of the spatial location of the X-ray source but in terms of its column depth within the flare.

Chapter VII: Summary and Conclusions

This left us with three parameters with which we could label our electron models and their X-ray results: the two parameters which we had created to allow the full range of possible injected beam distributions, plus a third which described the magnetic structure of the coronal loop. We created eleven models from eleven sets of this triplet of parameters and described the X-rays that each model produced. As our objective was to learn how to correlate the X-rays with the electrons, we chose one particular set of the triplet of values to represent our standard or reference model, and we naturally dealt with this model first. These results we described in full, giving the X-ray characteristics in terms of the X-ray intensity, spectrum, polarization and directivity, all as functions of photon energy, photon direction and source depth within the flare. We also integrated our results over the entire volume of the flare so that we could give the characteristics of the X-rays as emitted by the flare as a whole. This was desirable because almost all currently available data has this integration already performed and because, by comparing the whole loop results with the results at each depth, we could see how the curvature of the flare loop influenced the X-ray results, something which previous studies had not been able to provide.

Once we had become entirely familiar with the X-rays from this first model we compared them with the results from our other models. This allowed us to see what the individual effects of changing each of our three model parameters were. We were able to see how the X-rays changed in response to a change in the distribution of energy among the energetic electrons, to a change in the degree to which the electrons were collimated by the acceleration mechanism, and to a change in the influence of the magnetic field which defined the flare loop. We then

Chapter VII: Summary and Conclusions

looked at the combined effects of changing two parameters at the same time, to see how the effects from changing each parameter separately would either combine or compete in their influence upon the X-rays produced. This allowed us a clearer idea of the extent to which the X-rays would be able to inform us as to the nature of the underlying electron population.

7.2 Conclusions.

We shall now discuss some of the more important conclusions which have come out from our examination of the X-ray results.

(1) The X-ray intensity as a function of source depth within the flare followed closely the general evolution of the electron beam. This enabled us to find a simple expression which described very well the relative rate of X-ray production as a function of source depth within the flare, for all photon energies. We defined the relative intensity $I(k, \tau)$ to be the fraction of the total X-ray emission at a photon energy k (which is in units of the electron rest mass energy), emitted per unit of our dimensionless column depth parameter τ . ($\tau = N/N_0$ where N is the accumulated column depth traversed by the electron beam and is given in units of cm^{-2} . $N_0 \simeq 5 \times 10^{22} cm^{-2}$ and the normalization is $\int_{\tau=0}^{\infty} I(k, \tau) d\tau = 1$). We initially obtained the function $I(k, \tau)$ from an empirical fit to the X-ray intensity curves obtained from the numerical results of *Model 1*. We then turned to our other models and generalized the expression to describe the hard X-ray height structure at all energies and for most situations. We could not describe easily the

Chapter VII: Summary and Conclusions

X-ray height structure for those models that had a converging magnetic field, but we did obtain a fit which was very good for a broad range of the other two model parameters, that is, a fit which was good for any value of the electron spectral index δ and for all but the most strongly collimated of electron beams. We were able to include models having different degrees of electron beaming within this one expression because the majority of the X-rays are not emitted until after the beam has been substantially decollimated. Only close to the electron acceleration site is the degree of initial electron beaming the dominant influence upon the variation of the X-ray intensity with source height. This means that once the electron beam has penetrated within the flare beyond a characteristic distance, the intensity of the subsequently emitted X-rays is determined only by the electron beam's gross features. This makes the X-ray height structure easy to describe. It also has other important consequences and these we shall discuss in item (5).

Our general expression for $I(k, \tau)$, namely

$$I(k, \tau) = \left(\frac{\delta}{2} - 1\right) \left(\frac{k+1}{k^2}\right) \left(1 + \tau \cdot \frac{k+1}{k^2}\right)^{-\delta/2} \quad (7.1)$$

fits accurately enough to the results from the full Fokker-Planck treatment that we advise its use when modelling to a limited set of X-ray data or to data which is insufficiently accurate to allow reasonably certain limits to be put on the model parameters. In such a situation, using the full Fokker-Planck treatment is expensive and unwarranted. Equation (7.1) can be of great use to those who do not have available either computing facilities or the actual computer code with which our detailed results have been obtained. The expression easily supersedes

Chapter VII: Summary and Conclusions

the general guidelines most people use when, for example, distinguishing between thick and thin target emission or when talking about most of the X-ray emission being either coronal or chromospheric, either from the loop or from the footpoints.

(2) The second important result to come from this work is that the spectrum of the X-rays from a spatially unresolved flare is almost completely insensitive to the particular details of that flare and cannot be used to give an accurate determination of the flare parameters. The X-ray spectrum is the result of having integrated over and, hence, having averaged out, most of the structure of the flare. To generate the spectrum the X-ray source function, which in our system is the product of the X-ray cross-sections with the density of the emitting electrons, is integrated over all electron directions, over all contributing electron energies, and over the entire volume of the flare. The one component which determines the large scale structure of the X-ray spectrum is the energy spectrum of the underlying fast electrons. This means that if we inject electrons with a power law energy spectrum, we obtain an X-ray spectrum which has, almost exactly, a power law structure. Almost all the information on the geometry of the flare or the spatial structure of the beam electrons within the flaring plasma is lost. Any remaining information only manifests itself as slight, smooth modifications on the overall X-ray spectrum. Most X-ray telescopes do not have the necessary energy resolution to detect any real small scale structure on an X-ray spectrum that can fall through several decades in intensity over just one decade in X-ray energy. Furthermore, any structure to the X-ray spectrum which can be detected is not able to release its information about the flare unless we know from independent measurements the initial energy spectrum of the beam electrons.

Chapter VII: Summary and Conclusions

On its own, a flare's X-ray spectrum is unable to give much information about that flare's geometry or about the spatial structure of the energetic electrons. The spectrum is also unable to give definite information about the energy distribution of those electrons. Our results show clearly that there is only a loose correlation between the X-ray and electron spectral indices. This means that if the spatially integrated X-ray spectrum is the only information that we have about the X-rays, then we cannot determine the electron spectral index to better than an uncertainty of ± 0.3 . This may not sound like too large an uncertainty until we wish to estimate the total energy carried by the electron beam or the rate at which the beam evaporates chromospheric material into the corona, in which cases an uncertainty of a half in the spectral index can lead to an uncertainty of half a decade in the beam energy content.

In addition to this uncertainty in the determination of the electron spectral index from the X-ray spectral index, we have to bear in mind that a power law energy spectrum for the electrons is not the only distribution able to give a power law energy spectrum to the X-rays. A non-isothermal distribution of sufficiently hot electrons can be adequate, in which case the spatially unresolved X-ray spectral index cannot even allow us to determine the gross features of the electron distribution. It should then be most clear that the spatially unresolved X-ray spectrum, on its own, is not a good source of information about a flare.

(3) One large step forward can be taken by removing just one level of integration of our source function, that is, by looking at the X-ray spectrum without the spatial integration. Though the spectrum from the entire flare loop is a rather poor source of information, the spectra from different regions of the flare contain

Chapter VII: Summary and Conclusions

structure beyond a simple power law form, structure which is distinctly related to the electron populations which are found in those different regions. This makes the variation of the X-ray spectrum with position along the flare a more appropriate object of investigation.

There is obviously a much closer correlation at each height between the X-ray spectrum and its local source electron distribution than there is between the spatially integrated X-ray spectrum and the electron distribution at injection. And ideally, that part of the loop which we would most like to separate out and to look at in isolation is the very top. For it is here that the electron distribution is closest to that at injection. There has been little room for any beam evolution to erase the information carried by the beam about the conditions in the acceleration region and it is, consequently, here that the X-rays can tell us most directly about the processes involved in the creation of the electron population.

Our models show that the X-ray spectrum from, say, just the top half of the coronal loop, need not be a power law even though the injected electrons had an energy spectrum which was one. The X-ray spectrum for the top of the loop can acquire some shape according to the degree of electron beaming (strong beaming steepens the low energy end of the photon spectrum) and, in the absence of accurate polarization data (see item (5) below) this could be one of the few means by which a determination of the electron collimation could be made.

The local X-ray spectrum can display additional structure, for example by developing a knee which moves to higher energies as the thickness of the top segment of the loop is increased. This is because the rate at which the ambient

Chapter VII: Summary and Conclusions

plasma modifies the distribution of the beam electrons varies with electron energy. A given column thickness of plasma can be relatively thin to high energy electrons (hence high energy photons) and at the same time rather thick to the lower energy electrons which produce most of the low energy photons. This causes the low energy end of the electron spectrum to flatten with increasing source depth while the high energy end stays relatively unchanged. The X-ray spectrum reflects this development by acquiring a knee whereby the lower energy X-rays have a smaller spectral index than do the higher energy X-rays. The position and extent of the knee in the spectrum can indicate the thickness of the source material seen and, especially if the electrons are highly beamed in the beginning, can indicate the presence of a rapidly increasing magnetic field strength along the coronal loop.

(4) Our next result pertains to the directivity of the X-rays and to the observational contribution of those X-rays which are initially beamed away from any observer but are then reflected back toward the observer by the solar photosphere. Our conclusion is that these backscattered X-rays can, in some cases, make a significant contribution to the observations.

The intrinsic directivity of the radiation from a solar flare would be a hard thing to measure. It would require surrounding a flare with many X-ray detectors each of which has the capacity to separate in its measurements the direct X-rays from those which are reflected by the photosphere. This being essentially impossible, we can only make indirect measurements of the variation with direction of the total (direct + reflected) X-ray flux. Other studies have shown that, at an X-ray energy of 30 – 50 *keV* the flux of backscattered photons is approximately 20 – 30% of the flux initially beamed into the photosphere. If the flare has an

Chapter VII: Summary and Conclusions

intrinsic directivity which sends, say, four times as many photons down toward the photosphere as it sends up away from the sun, the contribution to the observations from the backscattered photons could well be as large as the contribution from the photons which are seen directly.

With our modelling techniques we are able to calculate the intrinsic flare directivities but we cannot include the effect of photospheric backscattering. Our intrinsic results show that, at an X-ray energy of 50 keV, the ratio of the flux beamed straight down into the photosphere to that beamed away from it can vary from as low as 1.5 up to ~ 5 (*cf.* Table VI). The intrinsic directivities may then be large enough that the backscattered X-rays make a significant contribution to the observations. The intrinsic results also point to limb brightening of flares and to a hardening (or flattening) of the X-ray spectrum as the position of the flare moves from the center of the solar disk to the limb (*cf.* Table III). This does not agree with the observations, such as they are, and may be another indication that the backscattered photons need to be considered.

(5) Up to now our hopes of being able to distinguish between the so-called “thermal” and “non-thermal” models have rested upon the assumption that the two types of model would give rise to widely differing polarization signatures. Then the measurement of either a high degree of X-ray polarization or an almost zero degree of X-ray polarization for any one flare would be a definitive indication of the appropriate type of model. The difficulty has been with obtaining reliable polarization measurements, not with interpreting them once they have been collected. These expectations no longer hold. We show by our results that, as well as being able to give rise to X-ray polarizations which are clearly higher than

Chapter VII: Summary and Conclusions

those from thermal models, non-thermal models are also able to generate, quite naturally, X-ray polarizations which are every bit as low as those which are to be expected from a thermal source. Consequently large polarization measurements would still point unequivocally to non-thermal flare processes but low polarization measurements are ambiguous and can arise from either type of model. The situation is a little complex.

The degree of X-ray polarization is determined by the convolution of two functions, the distribution of the electrons and the cross-sections for X-ray production. If either the electron distribution is isotropic or the X-ray cross-sections for the two independent linear polarizations are identical, then the resultant degree of X-ray polarization will be zero. The non-thermal models will only give high X-ray polarizations to the extent that both the electron distribution is anisotropic and the two cross-sections are unidentical.

The results from Chapter III showed how a beam of electrons evolves as it passes through the flaring plasma. Any beam, no matter how strongly collimated at injection, becomes increasingly isotropized as it penetrates further down through the atmosphere. Below a depth which depends upon the electron energy followed but which is not large, the beam no longer carries any information about its initial degree of collimation. As mentioned in item (1), it is below this depth that the bulk of the X-rays are emitted. Therefore, the X-ray emission from the whole source will have the character of the emission from a highly broadened electron beam, with only a weak signal remaining to indicate the initial electron collimation. A spatially unresolved measurement of the X-ray polarization must then give rise to a low result. Our calculations using the full Fokker-Planck treatment of the

Chapter VII: Summary and Conclusions

beam evolution show that the highest degree of polarization obtainable from the non-thermal models, even with optimum model parameters, is of the order of 25% (*cf.* Table X). Until X-ray polarimeters with high spatial resolution capabilities are developed we cannot expect measurements of flare polarizations which go beyond this upper range.

But this range is only an upper limit and is for optimum non-thermal model parameters. The X-ray polarization can easily be lower than 25% and as low as the values expected from thermal models. The primary reason is that the degree of X-ray polarization is a sensitive function of the electron spectral index. The cross-sections for bremsstrahlung X-ray production are functions of the photon to electron energy ratio x . Photons are known as being “hard” if the photon energy is nearly equal to that of the electron from which it came, in which case the ratio x will be close to unity. Conversely, photons are “soft” if the photon energy is much less than the electron energy and the ratio x is small. The two cross-sections for the production of X-rays with one or the other of the two linear polarizations behave differently as functions of the variable x and are most similar to each other when x is small. As a consequence, a beam of hard photons, all else being equal, will be more highly polarized than a beam of soft ones.

An electron distribution which has a flat energy spectrum (low spectral index) will give rise to X-rays in which more of the photons are soft than will an electron distribution which has a steep energy spectrum. We must then expect that our models which have the flatter X-ray spectra will also have the lower X-ray polarizations. This we find to be overwhelmingly true. The influence of the electron spectral index upon the degree of polarization is sufficiently strong that it

Chapter VII: Summary and Conclusions

Table X

The maximum degree of polarization (%) for 16 keV X-rays.

δ	α_0^2			
	∞	0.4	0.04	0.01
3	≤ 5	≤ 5	≤ 5	6
4	8	8	11	13
5	10	11	20	21
6	10	16	25	25

can mask the influence of the electron beaming. Our upper limit of 25% polarization is for a highly collimated electron beam with a very steep energy spectrum. If we reduce the electron spectral index δ from 6 to 3, the polarization, again for a strongly collimated electron beam, falls to around 5 – 6%. A sample of our results are given here in Table X. From the literature we see that it is common knowledge that the stronger the beaming of the electrons is, the larger will be the X-ray polarization. However, just how large a degree of X-ray polarization can be obtained from a highly collimated beam of injected electrons is generally over-estimated, and knowledge of the dependence of the degree of X-ray polarization on the spectral index of the electrons is not at all widespread.

The overwhelming message of the conclusions from our research is that the ideas on how to use the impulsive phase hard X-ray signature as a diagnostic tool

Chapter VII: Summary and Conclusions

giving information about the energetic electrons and the acceleration mechanisms in a solar flare need to be rethought. We can learn almost nothing from the X-ray spectrum unless we have spatially resolved data. The intrinsic X-ray directivity is impossible to measure satisfactorily, and the X-ray polarization, even if it is accurately known, may be of no help in discriminating between substantially different physical processes which produce the source electron distributions. Again, this last point will probably be overcome only with the development of polarimeters with good spatial resolution capabilities.

However, making use of spatially resolved data to obtain a description of a flare need not depend upon our being able to measure the spatially resolved X-ray characteristics with the same degree of accuracy with which we can currently measure the unresolved characteristics. We have developed modelling techniques which use the full power of our Fokker-Planck treatment to obtain a good description of a flare from X-ray observations which have only the beginnings of spatial resolution. This is most timely because it is exactly that type of data, X-ray data with the beginnings of spatial resolution, which has started to become available over the last few years. The early results from the Hard X-ray Imaging Spectrometer (HXIS) onboard the Solar Maximum Mission satellite, the Imaging Hard X-ray Telescope (SXT) on the Hinotori satellite and the stereoscopic results from the Pioneer Venus Orbiter (PVO) and the International Sun Earth Explorer - 3 (ISEE - 3) are examples of hard X-ray data containing just an initial amount of spatial resolution. They can give us separate X-ray intensity measurements from two parts of a flare loop; HXIS by imaging and distinguishing between a flare's coronal loop and its footpoints and PVO/ISEE - 3 by viewing a flare which is

Chapter VII: Summary and Conclusions

partially occulted from one of the telescopes by the solar limb but which is in full view to the other. Data such as this allows us to use the modelling techniques which we have developed to obtain values for the flare parameters based upon a best fit of our models to the data. We then know the structure of the observed flare, including the characteristics of the injected electron distribution, and this we can use toward forming an understanding of the acceleration mechanisms themselves.

In Chapter VI we gave several examples of how to use the full power of our modelling techniques in conjunction with the data now appearing. We have drawn from the published literature examples of flares imaged by HXIS or seen stereoscopically by PVO and ISEE - 3. These examples have been reported with sufficient data that we can determine, within just a couple of model iterations, the non-thermal model which is necessary to reproduce the flare. We illustrate how the modelling technique is to be used; we draw from the literature that data which we need and we put it in the required form so that we can set a model to it. We explain how we synthesize this data to estimate simultaneously values for all our model parameters, for a change in one parameter can often necessitate a readjustment of all of the other parameters, and we then explain how we use the results of our computer runs to zero in on a best fit model.

With so few flares being sufficiently well reported we can do no more than show the power of our technique as it is applied to each set of data. In the future, should we be able to use our technique on a greater number of flares, we would hope to discover that there are trends and similarities between all flares or between flares grouped according to a suitable classification. This would give important clues on

Chapter VII: Summary and Conclusions

the mechanisms responsible for the acceleration of the electrons and would be of great assistance in understanding the physics of solar flares.

Our study, which investigated the correlations between the impulsive hard X-rays and the parameters of the flare model which produced them, has gone on to show how to make full use of the X-ray data which is currently being collected. It has shown how this data can give us otherwise unavailable information on the structure of solar flares and, in particular, crucial information bearing upon the population of the energetic electrons.

References

- Abramowitz, M. and Stegun, I. A., 1970, (eds) *Handbook of Mathematical Functions*, 7th ed., Dover, New York, p486, equation 11.4.29.
- Acton, L. W., 1968, *Astrophysical Journal*, **152**, 305.
- Alvarez, H. and Haddock, F. T., 1973, in *High Energy Phenomena on the Sun*, ed. R. Ramaty and R. G. Stone, NASA SP-342, p537.
- Alvarez, H., Haddock, F. T. and Lin, R. P., 1972, *Solar Physics*, **26**, 468.
- Anderson, K. A., Kane, S. R., and 5 others, 1978, *IEEE Transactions*, **GE-16**, 157.
- Anderson, K. A. and Mahoney, W. A., 1974, *Solar Physics*, **35**, 419.
- Anderson, K. A. and Winckler, J. R., 1962, *Journal of Geophysical Research*, **67**, 4103.
- Anderson, K. A. and Winckler, J. R., 1963, *Space Research*, **III**, 839.
- Arnoldy, R. L., Kane, S. R. and Winckler, J. R., 1967, *Solar Physics*, **2**, 171.
- Arnoldy, R. L., Kane, S. R. and Winckler, J. R., 1968, *Astrophysical Journal*, **151**, 711.
- Bai, T. and Ramaty, R., 1978, *Astrophysical Journal*, **219**, 705.
- Banks, P. M., Chappell, C. R. and Nagy, A. F., 1974, *Journal of Geophysical Research*, **79**, 1459.
- Bannerjee, H., 1958, *Physical Review*, **111**, 532.
- Basri, G. S., Linsky, J. L., Bartoe, J. -D. F., Brueckner, G. and van Hoosier, M. E., 1979, *Astrophysical Journal*, **230**, 924.
- van Beek, H. F., de Feiter, L. D. and de Jager, C., 1974, *Space Research*, **XIV**, 447.
- van Beek, H. F., de Feiter, L. D. and de Jager, C., 1976, *Space Research*, **XVI**, 819.
- van Beek, H. F., Hoyng, P., Lafleur, B. and Simnett, G. M., 1980, *Solar Physics*, **65**, 39.
- van Beek, H. F., de Jager, C., Fryer, R., and 21 others, 1981, *Astrophysical Journal Letters*, **244**, L157.
- Bekefi, G., 1966, *Radiation Processes in Plasmas*, Wiley, New York.
- Benford, G. and Book, D. L., 1971, in *Advances in Plasma Physics*, ed. A. Simon and W. B. Thomson, interscience, New York, **4**, 125.
- Bethe, H. A. and Heitler, W., 1934, *Proceedings of the Royal Society, A*, **146**, 83.
- Bethe, H. A. and Maximon, L. C., 1954, *Physical Review*, **93**, 768.
- Bowen, P. J., Norman, K., Pounds, K. A., Sanford, P. W. and Willmore, A. P., 1964, *Proceedings of the Royal Society, A*, **281**, 538.

References

- Brown, J. C., 1971, *Solar Physics*, **18**, 489.
- Brown, J. C., 1972, *Solar Physics*, **28**, 441.
- Brown, J. C., 1973a, *Solar Physics*, **28**, 151.
- Brown, J. C., 1973b, *Solar Physics*, **31**, 143.
- Brown, J. C., 1974, in *IAU Symposium No. 57, Coronal Disturbances*, ed. G. A. Newkirk, Jr., Reidel, Dordrecht, p395.
- Brown, J. C., 1975, in *IAU Symposium No. 68, Solar Gamma, X-, and EUV Radiation*, ed. S. R. Kane, Reidel, Dordrecht, p245.
- Brown, J. C., 1976, *Philosophical Transactions of the Royal Society, A*, **281**, 473.
- Brown, J. C., 1978, *Astrophysical Journal*, **225**, 1076.
- Brown, J. C., Canfield, R. C. and Robertson, M. N., 1978, *Solar Physics*, **57**, 399.
- Brown, J. C., Craig, I. J. D. and Karpen, J. T., 1980, *Solar Physics*, **67**, 143.
- Brown, J. C. and Hayward, J., 1981, *Solar Physics*, **73**, 121.
- Brown, J. C., Hayward, J. and Spicer, D. S., 1981, *Astrophysical Journal Letters*, **245**, L91.
- Brown, J. C. and McClymont, A. N., 1975, *Solar Physics*, **41**, 135.
- Brown, J. C., McClymont, A. N. and McLean, I. S., 1974, *Nature*, **247**, 448.
- Brown, J. C. and Melrose, D. B., 1977, *Solar Physics*, **52**, 117.
- Brown, J. C., Melrose, D. B. and Spicer, D. S., 1979, *Astrophysical Journal*, **228**, 592.
- Brown, J. C. and Smith, D. F., 1980, *Reports on Progress in Physics*, **43**, 125.
- Canfield, R. C., Brown, J. C., Brueckner, G. E., and 8 others, 1980, in *Solar Flares. A Monograph from Skylab Solar Workshop II*, ed. P. A. Sturrock, Colorado University Press, Boulder, p231.
- Chandrasekhar, S., 1943, *Reviews of Modern Physics*, **15**, 1.
- Chandrasekhar, S., 1946, *Astrophysical Journal*, **104**, 110.
- Chandrasekhar, S., 1960, *Radiative Transfer*, Dover, New York.
- Cheng, C. -C. and Spicer, D. S., 1975, in *IAU Symposium No. 68, Solar Gamma, X-, and EUV Radiation*, ed. S. R. Kane, Reidel, Dordrecht, p423.
- Cheng, C. -C. and Widing, K. G., 1975, *Astrophysical Journal*, **201**, 735.
- Chubb, T. A., 1971, in *Solar Terrestrial Physics*, ed. E. R. Dyer, Part 1, Reidel, Dordrecht, p99.

References

- Chubb, T. A., Kreplin, R. W. and Friedman, H., 1966, *Journal of Geophysical Research*, **71**, 3611.
- Chupp, E. L., Forest, D. J. and Suri, A. N., 1975, in *IAU Symposium No. 68, Solar Gamma, X-, and EUV Radiation*, ed. S. R. Kane, Reidel, Dordrecht, p341.
- Cline, T. L., Holt, S. S. and Hones, E. W., 1968, *Journal of Geophysical Research*, **73**, 434.
- Cohen, R. S., Spitzer, L. Jr. and McRoutly, P., 1950, *Physical Review*, **80**, 230.
- Craig, I. J. D., 1975, in *IAU Symposium No. 68, Solar Gamma, X-, and EUV Radiation*, ed. S. R. Kane, Reidel, Dordrecht, p187.
- Craig, I. J. D. and Brown, J. C., 1976, *Nature*, **264**, 340.
- Crannell, C. J., Frost, K. J., Mätzler, C., Ohki, K. -I. and Saba, J. L., 1978, *Astrophysical Journal*, **223**, 620.
- Culhane, J. L., Willmore, A. P., Pounds, K. A. and Sanford, P. W., 1964, *Space Research*, **IV**, 741.
- Datlowe, D. W., 1975, in *IAU Symposium No. 68, Solar Gamma, X-, and EUV Radiation*, ed. S. R. Kane, Reidel, Dordrecht, p191.
- Datlowe, D. W., Elcan, M. J. and Hudson, H. S., 1974, *Solar Physics*, **39**, 155.
- Datlowe, D. W. and Hudson, H. S., 1975, in *IAU Symposium No. 68, Solar Gamma, X-, and EUV Radiation*, ed. S. R. Kane, Reidel, Dordrecht, p209.
- Datlowe, D. W., O'Dell, S. L., Peterson, L. E. and Elcan, M. J., 1977, *Astrophysical Journal*, **212**, 561.
- Debye, P. and Huckel, E., 1923, *Zeitschrift für Physik*, **24**, 185.
- Donley, M. B., 1979, (ed.) *The SALT Handbook*, The Heritage Foundation, Washington.
- Donnelly, R. F. and Hall, L. A., 1973, *Solar Physics*, **31**, 411.
- Donnelly, R. F. and Kane, S. R., 1978, *Astrophysical Journal*, **222**, 1043.
- Donnelly, R. F., Wood, A. T. Jr. and Noyes, R. W., 1973, *Solar Physics*, **29**, 107.
- Drake, J. F., 1971, *Solar Physics*, **18**, 152.
- Duijveman, A., Hoyng, P. and Machado, M. E., [DHM], 1982, *Solar Physics*, **81**, 137.
- Elcan, M. J., 1978, *Astrophysical Journal Letters*, **226**, L99.
- Elwert, G., 1939, *Annalen der Physik*, **34**, 178.

References

- Elwert, G., 1968, in *IAU Symposium No. 35, Structure and Development of Solar Active Regions*, ed. K. O. Kiepenheuer, Reidel, Dordrecht, p444.
- Elwert, G. and Haug, E., 1969, *Physical Review*, **183**, 90.
- Elwert, G. and Haug, E., 1970, *Solar Physics*, **15**, 234.
- Elwert, G. and Haug, E., 1971, *Solar Physics*, **20**, 413.
- Emslie, A. G., 1978, *Astrophysical Journal*, **224**, 241.
- Emslie, A. G., 1980, *Astrophysical Journal*, **235**, 1055.
- Emslie, A. G., 1981a, *Astrophysical Journal*, **244**, 653.
- Emslie, A. G., 1981b, *Astrophysical Journal*, **245**, 711.
- Emslie, A. G., 1981c, *Astrophysical Journal*, **249**, 817.
- Emslie, A. G. and Brown, J. C., 1980, *Astrophysical Journal*, **237**, 1015.
- Emslie, A. G., Brown, J. C. and Donnelly, R. F., 1978, *Solar Physics*, **57**, 175.
- Emslie, A. G., Brown, J. C. and Machado, M. E., 1981, *Astrophysical Journal*, **248**, 337.
- Emslie, A. G. and Noyes, R. W., 1978, *Solar Physics*, **57**, 373.
- Emslie, A. G. and Rust, D. M., 1980, *Solar Physics*, **65**, 271.
- Emslie, A. G. and Smith, D. F., 1984, *Astrophysical Journal*, (in press).
- Emslie, A. G. and Vlahos, L., 1980, *Astrophysical Journal*, **242**, 359.
- Evans, R. D., 1955, *The Atomic Nucleus*, McGraw-Hill, New York.
- Fainberg, J. and Stone, R. G., 1974, *Space Science Reviews*, **16**, 145.
- Falciani, R., Landini, M., Righini, A. and Rigutti, M., 1968, in *IAU Symposium No. 35, Structure and Development of Solar Active Regions*, ed. K. O. Kiepenheuer, Reidel, Dordrecht, p451.
- Fano, U., 1959, *Physical Review*, **116**, 1156.
- Fano, U., Koch, H. W. and Motz, J. W., 1958, *Physical Review*, **112**, 1679.
- de Feter, L. D., 1975, in *IAU Symposium No. 68, Solar Gamma, X-, and EUV Radiation*, ed. S. R. Kane, Reidel, Dordrecht, p283.
- Fronsdal, C. and Überall, H., 1958, *Physical Review*, **111**, 580.
- Frost, K. J., 1969, *Astrophysical Journal Letters*, **158**, L159.
- Frost, K. J. and Dennis, B. R., 1971, *Astrophysical Journal*, **165**, 655.
- Gasiorowicz, S., Neumann, M. and Riddell, R. J. Jr., 1956, *Physical Review*, **101**, 922.

References

- Ginzburg, V. L. and Syrovat'skii, S. I., 1964, *The origin of Cosmic Rays*, Macmillan, New York.
- Gluckstern, R. L. and Hull, M. H. Jr., 1953, *Physical Review*, **90**, 1030.
- Gluckstern, R. L., Hull, M. H. Jr. and Breit, G., 1953, *Physical Review*, **90**, 1026.
- Haug, E., 1972, *Solar Physics*, **25**, 425.
- Haug, E., 1976, *Solar Physics*, **45**, 453.
- Haug, E., 1979, *Solar Physics*, **61**, 129.
- Haug, E., 1982, *Space Science Reviews*, **33**, 83.
- Heitler, W., 1954, *The Quantum Theory of Radiation*, 3rd ed., Oxford University Press, London.
- Hénoux, J. C., 1975, *Solar Physics*, **42**, 219.
- Heyvaerts, J., Priest, E. R. and Rust, D. M., 1977, *Astrophysical Journal*, **216**, 123.
- Holt, S. S. and Cline, T. L., 1968, *Astrophysical Journal*, **154**, 1027.
- Holt, S. S. and Ramaty, R., 1969, *Solar Physics*, **8**, 119.
- Hoyng, P., Brown, J. C., Stevens, G. and van Beek, H. F., 1975 in *IAU Symposium No. 68, Solar Gamma, X-, and EUV Radiation*, ed. S. R. Kane, Reidel, Dordrecht, p233.
- Hoyng, P., Brown, J. C. and van Beek, H. F., 1976, *Solar Physics*, **48**, 197.
- Hoyng, P., Knight, J. W. and Spicer, D. S., 1978, *Solar Physics*, **58**, 139.
- Hoyng, P., Machado, M. E., Duijveman, A., and 21 others, 1981, *Astrophysical Journal Letters*, **244**, L153, [HMD].
- Hoyng, P. and Melrose, D. B., 1977, *Astrophysical Journal*, **218**, 866.
- Hoyng, P., Melrose, D. B. and Adams, J. C., 1979, *Astrophysical Journal*, **230**, 950.
- Hudson, H. S., 1972, *Solar Physics*, **24**, 414.
- Hudson, H. S., 1973, in *High Energy Phenomena on the Sun*, ed. R. Ramaty and R. G. Stone, NASA SP-342, p207.
- Hudson, H. S., 1978, *Astrophysical Journal*, **224**, 235.
- Hudson, H. S., Jones, T. W. and Lin, R. P., 1975, in *IAU Symposium No. 68, Solar Gamma, X-, and EUV Radiation*, ed. S. R. Kane, Reidel, Dordrecht, p425.
- Jackson, J. D., 1975, *Classical Electrodynamics*, Wiley, New York.

References

- de Jager, C. and de Jonge, G., 1978, *Solar Physics*, **58**, 127.
- de Jager, C. and Kundu, M. R., 1963, *Space Research*, **III**, 836.
- Joseph, J. and Rohrlich, F., 1958, *Reviews of Modern Physics*, **30**, 354.
- Kahler, S. W., 1975, in *IAU Symposium No. 68, Solar Gamma, X-, and EUV Radiation*, ed. S. R. Kane, Reidel, Dordrecht, p211.
- Kahler, S. W. and Kreplin, R. W., 1971, *Astrophysical Journal*, **168**, 531.
- Kahler, S. W., Spicer, D. S., Uchida, Y. and Zirin, H., 1980, in *Solar Flares. A Monograph from Skylab Solar Workshop II*, ed. P. A. Sturrock, Colorado University Press, Boulder, p83.
- Kane, S. R., 1969, *Astrophysical Journal Letters*, **157**, L139.
- Kane, S. R., 1972a, *Solar Physics*, **27**, 174.
- Kane, S. R., 1972b, *Space Science Reviews*, **13**, 822.
- Kane, S. R., 1973, in *High Energy Phenomena on the Sun*, ed. R. Ramaty and R. G. Stone, NASA SP-342, p55.
- Kane, S. R., 1974, in *IAU Symposium No. 57, Coronal Disturbances*, ed. G. A. Newkirk, Jr., Reidel, Dordrecht, p105.
- Kane, S. R., 1983, *Solar Physics*, **86**, 355.
- Kane, S. R. and Anderson, K. A., 1970, *Astrophysical Journal*, **162**, 1003.
- Kane, S. R., Anderson, K. A., Evans, W. D., Klebesadel, R. W. and Laros, J. G., 1979, *Astrophysical Journal Letters*, **233**, L151.
- Kane, S. R., Anderson, K. A., Evans, W. D., Klebesadel, R. W. and Laros, J. G., 1980, *Astrophysical Journal Letters*, **239**, L85.
- Kane, S. R., Crannell, C. J., Datlowe, D. W., and 8 others, 1980b, in *Solar Flares. A Monograph from Skylab Solar Workshop II*, ed. P. A. Sturrock, Colorado University Press, Boulder, p186.
- Kane, S. R. and Donnelly, R. F., 1971, *Astrophysical Journal*, **164**, 151.
- Kane, S. R., Fenimore, E. E., Klebesadel, R. W. and Laros, J. G., 1982, *Astrophysical Journal Letters*, **254**, L53.
- Kane, S. R., Frost, K. J. and Donnelly, R. F., 1979, *Astrophysical Journal*, **234**, 669.
- Karpen, J. T., 1980, Ph. D. Thesis, University of Maryland (NASA Technical Memorandum 82013).

References

- Kindel, J. M. and Kennel, C. F., 1971, *Journal of Geophysical Research*, **76**, 3055.
- Kiplinger, A. L., Dennis, B. R., Emslie, A. G., Frost, K. J. and Orwig, L. E., 1983, *Astrophysical Journal Letters*, **265**, L99.
- Kirkpatrick, P. and Wiedmann, L., 1945, *Physical Review*, **67**, 321.
- Koch, H. W. and Motz, J. W., 1959, *Physical Review*, **31**, 920.
- Korčák, A. A., 1967a, *Soviet Astronomy - A. J.*, **11**, 258.
- Korčák, A. A., 1967b, *Soviet Physics - Doklady*, **12**, 192.
- Korčák, A. A., 1971, *Solar Physics*, **18**, 284.
- Korčák, A. A., 1974, *Comments on Astrophysics and Space Physics*, **6**, 57.
- Krall, N. A. and Trivelpiece, A. W., 1973, *Principles of Plasma Physics*, McGraw-Hill, New York.
- Kuckuck, R. W. and Ebert, P. J., 1973, *Physical Review*, **A7**, 456.
- Kuiper, T. B. H., 1973, in *High Energy Phenomena on the Sun*, ed. R. Ramaty and R. G. Stone, NASA SP-342, p540.
- Kundu, M. R., 1961, *Journal of Geophysical Research*, **66**, 4308.
- Kundu, M. R., 1963, *Space Science Reviews*, **2**, 438.
- Kundu, M. R., 1973, in *High Energy Phenomena on the Sun*, ed. R. Ramaty and R. G. Stone, NASA SP-342, p104.
- Kundu, M. R., 1983, *Solar Physics*, **86**, 205.
- Kundu, M. R., Schmahl, E. J. and Velusamy, T., 1982, *Astrophysical Journal*, **253**, 963.
- Langer, S. H., 1978, Ph. D. Thesis, SUIPR Report # 761, Stanford University, Stanford.
- Langer, S. H. and Petrosian, V., 1977, *Astrophysical Journal*, **215**, 666.
- Leach, J. and Emslie, A. G., 1980, *Bulletin of the American Astronomical Society*, **12,4**, 893.
- Leach, J., Emslie, A. G. and Petrosian, V., 1984, in preparation.
- Leach, J., Langer, S. H. and Petrosian, V., 1984, in preparation.
- Leach, J. and Petrosian, V., 1981, *Astrophysical Journal*, **251**, 781.
- Leach, J. and Petrosian, V., 1983, *Astrophysical Journal*, **269**, 715.
- Lee, C. M., Kissel, L., Pratt, R. H. and Tseng, H. K., 1976, *Physical Review*, **A13**, 1714.
- Lemen, J. R., Chanan, G. A., Hughes, J. P., and 5 others, 1982, *Solar Physics*, **80**, 333.

References

- Levine, R. H. and Pye, J. P., 1980, *Solar Physics*, **66**, 39.
- Lewis, M. B., 1969, in *Kinetic Processes in Gases and Plasmas*, ed. A. R. Hochstim, Academic Press, New York.
- Liboff, R. L., 1969, *Introduction to the Theory of Kinetic Equations*, Wiley, New York.
- Lin, R. P., 1974a, *Space Science Reviews*, **16**, 189.
- Lin, R. P., 1974b, in *IAU Symposium No. 57, Coronal Disturbances*, ed. G. A. Newkirk, Jr., Reidel, Dordrecht, p201.
- Lin, R. P., 1975, in *IAU Symposium No. 68, Solar Gamma, X-, and EUV Radiation*, ed. S. R. Kane, Reidel, Dordrecht, p385.
- Lin, R. P., Evans, L. G. and Fainberg, J., 1973, *Astrophysical Letters*, **14**, 191.
- Lin, R. P. and Hudson, H. S., 1971, *Solar Physics*, **17**, 412.
- Lin, R. P. and Hudson, H. S., 1976, *Solar Physics*, **50**, 153.
- Luhman, J. G., 1976, *Journal of Atmospheric and Terrestrial Physics*, **38**, 605.
- MacDonald, W. M. and Walt, M., 1961, *Annals of Physics*, **15**, 44.
- Machado, M. E., Avrett, E. H., Vernazza, J. E. and Noyes, R. W., 1980, *Astrophysical Journal*, **242**, 336.
- Machado, M. E., Duivjeman, A. and Dennis, B. R., 1982, *Solar Physics*, **79**, 85, [MDD].
- Makishima, K., 1982, in *Proceedings of the Hinotori Symposium on Solar Flares*, ISAS, Tokyo, p120.
- Mandel'stam, S. L., Beigman, I. L. and Tindo, I. P., 1975, *Nature*, **254**, 462.
- Marsh, K. A. and Hurford, G. J., 1980, *Astrophysical Journal Letters*, **240**, L111.
- Marsh, K. A., Hurford, G. J. and Zirin, H., 1980, in *IAU Symposium No. 86, Radio Physics of the Sun*, ed. M. R. Kundu and T. E. Gergely, Reidel, Dordrecht, p191.
- Marsh, K. A., Hurford, G. J., Zirin, H. and Hjellming, R. M., 1980, *Astrophysical Journal*, **242**, 352.
- Marsh, K. A., Hurford, G. J., Zirin, H., and 4 others, 1981, *Astrophysical Journal*, **251**, 797.
- Marshak, R., 1941, *Annals of the New York Academy of Sciences*, **41**, 49.
- Mätzler, C., Bai, T., Crannell, C. J. and Frost, K. J., 1978, *Astrophysical Journal*, **223**, 1058.
- McKenzie, D. L., 1972, *Astrophysical Journal*, **175**, 481.

References

- McKenzie, D. L., 1975, *Solar Physics*, **40**, 183.
- Melrose, D. B. and Brown, J. C., 1976, *Monthly Notices of the Royal Astronomical Society*, **176**, 15.
- Møller, C., 1932, *Astrophysical Journal*, **14**, 531.
- Moore, R., McKenzie, D. L., Švestka, Z., and 13 others, 1980, in *Solar Flares. A Monograph from Skylab Solar Workshop II*, ed. P. A. Sturrock, Colorado University Press, Boulder, p341.
- Mott, N. F. and Massey, H. S. W., 1949, *The Theory of Atomic Collisions*, 2nd ed., Oxford University Press, London.
- Nakada, M. P., Neupert, W. M. and Thomas, R. J., 1974, *Solar Physics*, **37**, 429.
- de la Noë, J., Boishot, A. and Aubier, M., 1973, in *High Energy Phenomena on the Sun*, ed. R. Ramaty and R. G. Stone, NASA SP-342, p602.
- Noyes, R. W., 1973, in *High Energy Phenomena on the Sun*, ed. R. Ramaty and R. G. Stone, NASA SP-342, p231.
- Ohki, K. I., 1969, *Solar Physics*, **7**, 260.
- Olsen, H. and Maximon, L. C., 1959, *Physical Review*, **114**, 887.
- Olsen, H., Maximon, L. C. and Wergeland, H., 1957, *Physical Review*, **106**, 27.
- Orwig, L. E., Frost, K. J. and Dennis, B. R., 1980, *Solar Physics*, **65**, 25.
- Penrose, R., 1960, *Physics of Fluids*, **3**, 258.
- Peterson, L. E., Datlowe, D. W. and McKenzie, D. L., 1973, in *High Energy Phenomena on the Sun*, ed. R. Ramaty and R. G. Stone, NASA SP-342, p132.
- Peterson, L. E. and Winckler, J. R., 1959, *Journal of Geophysical Research*, **64**, 697.
- Petrosian, V., 1973, *Astrophysical Journal*, **186**, 291.
- Petrosian, V., 1975, *Astrophysical Journal*, **197**, 235.
- Petrosian, V., 1982, *Astrophysical Journal Letters*, **255**, L85.
- Phillips, K. J. H., 1973, *Observatory*, **93**, 17.
- Pines, D. and Bohm, D., 1952, *Physical Review*, **85**, 338.
- Pintér, S., 1969, *Solar Physics*, **8**, 142.
- Pizzichini, G., Spizzichino, A. and Vespignani, G. R., 1974, *Solar Physics*, **35**, 431.
- Pounds, K. A., 1970, *Annals of Geophysics*, **28**, 555.

References

- Pratt, R. H. and Tseng, H. K., 1975, *Physical Review*, **A11**, 1797.
- Ramaty, R., 1969, *Astrophysical Journal*, **158**, 753.
- Ramaty, R., 1973, in *High Energy Phenomena on the Sun*, ed. R. Ramaty and R. G. Stone, NASA SP-342, p188.
- Ramaty, R., Colgate, S. A., Dulk, G., and 9 others, 1980, in *Solar Flares. A Monograph from Skylab Solar Workshop II*, ed. P. A. Sturrock, Colorado University Press, Boulder, p117.
- Ramaty, R. and Petrosian, V., 1972, *Astrophysical Journal*, **178**, 241.
- Rosenberg, H., 1976, *Philosophical Transactions of the Royal Society, A*, **281**, 461.
- Rosenbluth, M. N., McDonald, W. M. and Judd, D. L., 1957, *Physical Review*, **107**, 1.
- Roy, J. R. and Datlowe, D. W., 1975, *Solar Physics*, **40**, 165.
- Rust, D. M. and Bar, V., 1973, *Solar Physics*, **33**, 445.
- Rust, D. M., Hildner, E., Dryer, M., and 10 others, 1980, in *Solar Flares. A Monograph from Skylab Solar Workshop II*, ed. P. A. Sturrock, Colorado University Press, Boulder, p273.
- Santangelo, N., Horstman, H. and Horstman-Moretti, E., 1973, *Solar Physics*, **29**, 143.
- Smith, D. F., 1974, *Space Science Reviews*, **16**, 91.
- Smith, D. F., 1975, *Astrophysical Journal*, **201**, 521.
- Smith, D. F., 1980, *Solar Physics*, **66**, 135.
- Smith, D. F. and Auer, L. H., 1980, *Astrophysical Journal*, **238**, 1126.
- Smith, D. F. and Lilliequist, C. G., 1979, *Astrophysical Journal*, **232**, 582.
- Snyder, H. S. and Scott, W. T., 1949, *Physical Review*, **76**, 220.
- Sommerfeld, A., 1931, *Annalen der Physik*, **11**, 257.
- Somov, B. V. and Tindo, I. P., 1978, *Cosmic Research*, **16**, 555.
- Spicer, D. S., 1976, *N. R. L. Report 8036*.
- Spicer, D. S., 1977, *Solar Physics*, **53**, 305.
- Spitzer, L. Jr., 1962, *Physics of Fully Ionized gases*, 2nd ed., New York, Interscience.
- Starek, B., Aiginger, H. and Unfried, E., 1972, *Physics Letters*, **39A**, 151.
- Starfelt, N. and Koch, H. W., 1956, *Physical Review*, **102**, 1598.
- Stokes, G. G., 1852, *Transactions of the Cambridge Philosophical Society*, **9**, 399.

References

- Stone, R. G. and Fainberg, J., 1973, in *High Energy Phenomena on the Sun*, ed. R. Ramaty and R. G. Stone, NASA SP-342, p519.
- Sturrock, P. A., 1968, in *IAU Symposium No. 35, Structure and Development of Solar Active Regions*, ed. K. O. Kiepenheuer, Reidel, Dordrecht, p471.
- Sturrock, P. A., 1980, in *Solar Flares. A Monograph from Skylab Solar Workshop II*, ed. P. A. Sturrock, Colorado University Press, Boulder, p411.
- Sturrock, P. A. et al. 1980, *Solar Flares. A Monograph from Skylab Solar Workshop II*, ed. P. A. Sturrock, Colorado University Press, Boulder.
- Švestka, Z., 1966, *Space Science Reviews*, **5**, 388.
- Švestka, Z., 1975, in *IAU Symposium No. 68, Solar Gamma, X-, and EUV Radiation*, ed. S. R. Kane, Reidel, Dordrecht, p427.
- Švestka, Z., 1976, *Solar Flares*, Reidel, Dordrecht.
- Sweet, P. A., 1969, *Annual Reviews of Astronomy and Astrophysics*, **7**, 149.
- Syrovat'skii, S. I. and Shmeleva, O. P., 1972, *Soviet Astronomy - A. J.*, **16**, 273.
- Takakura, T., 1975 in *IAU Symposium No. 68, Solar Gamma, X-, and EUV Radiation*, ed. S. R. Kane, Reidel, Dordrecht, p299.
- Takakura, T., Tsuneta, S., Ohki, K., and 6 others, 1983, *Astrophysical Journal Letters*, (in Press).
- Tanaka, K. and Zirin, H., 1973, in *High Energy Phenomena on the Sun*, ed. R. Ramaty and R. G. Stone, NASA SP-342, p26.
- Tanaka, Y., 1983, *Solar Physics*, **86**, 3.
- Thomas, R. J., 1975, in *IAU Symposium No. 68, Solar Gamma, X-, and EUV Radiation*, ed. S. R. Kane, Reidel, Dordrecht, p25.
- Tindo, I. P., Ivanov, V. D., Mandel'stam, S. L. and Shuryghin, A. I., 1970, *Solar Physics*, **14**, 204.
- Tindo, I. P., Ivanov, V. D., Mandel'stam, S. L. and Shuryghin, A. I., 1972a, *Solar Physics*, **24**, 429.
- Tindo, I. P., Ivanov, V. D., Valníček, B. and Livshits, M. A., 1972b, *Solar Physics*, **27**, 426.
- Tindo, I. P., Mandel'stam, S. L. and Shuryghin, A. I., 1973, *Solar Physics*, **32**, 469.
- Tindo, I. P., Shuryghin, A. I. and Steffen, W., 1976, *Solar Physics*, **46**, 219.

References

- Tolhoek, H. A., 1956, *Reviews of Modern Physics*, **28**, 277.
- Tomblin, F. F., 1972, *Astrophysical Journal*, **171**, 377.
- Tramiel, L. J., Chanan, G. A. and Novick, R., 1984, *Astrophysical Journal*, (in press).
- Tseng, H. K. and Pratt, R. H., 1970, *Physical Review*, **A1**, 528.
- Tseng, H. K. and Pratt, R. H., 1971, *Physical Review*, **A3**, 100.
- Tseng, H. K. and Pratt, R. H., 1973, *Physical Review*, **A7**, 1502.
- Tseng, H. K. and Pratt, R. H., 1974, *Physical Review Letters*, **33**, 516.
- Tucker, W. H., 1975, *Radiation Processes in Astrophysics*, MIT Press, Cambridge.
- Vasiček, D. J., 1973, NCAR Cooperative Thesis # 30, University of Colorado and HAO, NCAR.
- Vernazza, J. E., Avrett, E. H. and Loeser, R., 1973, *Astrophysical Journal*, **184**, 605.
- Vesecky, J. F., Antiochos, S. K. and Underwood, J. H., 1979, *Astrophysical Journal*, **233**, 987.
- Vette, J. I. and Casal, F. G., 1961, *Physical Review Letters*, **6**, 334.
- Vorpahl, J. A., 1972, *Solar Physics*, **28**, 397.
- Vorpahl, J. A., 1973, in *High Energy Phenomena on the Sun*, ed. R. Ramaty and R. G. Stone, NASA SP-342, p221.
- Vorpahl, J. A., Gibson, E. G., Landecker, P. B., McKenzie, D. L. and Underwood, J. H., 1975, *Solar Physics*, **45**, 199.
- Vorpahl, J. A. and Takakura, T., 1974, *Astrophysical Journal*, **191**, 563.
- Vorpahl, J. A. and Takakura, T., 1975, in *IAU Symposium No. 68, Solar Gamma, X-, and EUV Radiation*, ed. S. R. Kane, Reidel, Dordrecht, p237.
- Widing, K. G. and Cheng, C. -C., 1974, *Astrophysical Journal Letters*, **144**, L111.
- Wild, J. P., Sheridan, K. V. and Neylan, A. A., 1959, *Australian Journal of Physics*, **12**, 369.
- Wild, J. P., Smerd, S. F. and Weiss, A. A., 1963, *Annual Reviews of Astronomy and Astrophysics*, **1**, 291.
- Winckler, J. R., May, T. C. and Massey, A. J., 1961, *Journal of Geophysical Research*, **66**, 316.
- Withbroe, G. L., 1978, *Astrophysical Journal*, **225**, 641.

References

- Wolff, R. S., 1973, in *High Energy Phenomena on the Sun*, ed. R. Ramaty and R. G. Stone, NASA SP-342, p162.
- Wood, A. T. Jr. and Noyes, R. W., 1972, *Solar Physics*, **24**, 180.
- Wu, T., 1966, *Kinetic Equations of Gases and Plasmas*, Addison-Wesley, New York.
- Zirin, H., 1966, *The Solar Atmosphere*, Blaisdel, Waltham.
- Zirin, H., 1978, *Solar Physics*, **58**, 95.
- Zirin, H., Pruss, G. and Vorpahl, J. A., 1971, *Solar Physics*, **19**, 463.
- Zirin, H. and Tanaka, K., 1973, *Solar Physics*, **32**, 173.